2-1-2015

A proposed segmented precast concrete spherical cap: geometry, structural stability and construction

Maha Kenawy

The American University in Cairo

School of Sciences and Engineering

A PROPOSED SEGMENTED PRECAST CONCRETE SPHERICAL CAP: GEOMETRY, STRUCTURAL STABILITY AND CONSTRUCTION

A Thesis Submitted to

Department of Construction and Architectural Engineering

in partial fulfillment of the
requirements for the degree of
Master of Science

by

Maha Kenawy

under the supervision of

Dr. Khaled Nassar
Dr. Mohamed Abdel Mooty

September 2014

ABSTRACT

University Name	The American University in Cairo
Thesis Title	A Proposed Segmented Precast Concrete Spherical Cap: Geometry, Structural Stability and Construction
Student Name	Maha Mohamed Kamal Kenawy
Thesis Supervisors	Dr. Khaled Nassar Dr. Mohamed Abdel Mooty

Summary

This study proposes the design and construction of a concrete spherical cap composed of uniformly-shaped precast doubly-curved panels based on spherical division techniques. A numerical structural analysis is conducted to study the failure behavior of the segmented structure and the capacity of the joints by using finite element modeling techniques to model the concrete material behavior, boundary conditions and intermediate joints of the precast panels. An experimental analysis is conducted to verify the capacity of the structure and the reliability of the modeling techniques, and to study the feasibility of the proposed panel prefabrication and assembly method. The results of this study demonstrate that the proposed precast system and connection design perform efficiently when compared to the monolithically-cast counterpart, particularly under uniform loading conditions. Additional insights on the properties and solution parameters of finite element modelling of concrete shell structures are presented based on the structural analysis of this work. The study concludes the ability of the proposed geometric design and construction method to enhance the prefabrication and construction efficiency with little effect on the structural capacity within the context of the selected geometry and conducted load tests, and recommends further parameters to study for design and construction optimization.

TABLE OF CONTENTS

LIST OF FIGURES

LIST OF TABLES

LIST OF EQUATIONS

Eq. (23)	Modified critical load of a concrete cap by Dulácska [42]
Eq. (24)	Modified concrete modulus of elasticity for creep [42]
Eq. (25)	Creep factor by Dulácska [42]
Eq. (26)	Design buckling load of concrete spherical caps [44]
Eq. (27)	Minimum shell thickness of concrete shells by ACI Committee 344 [5] reported in [85]
Eq. (28)	Design buckling load of ACI Committee 344 [5] in the standard buckling load format by [85]
Eq. (29)	Design buckling load by Medwadowski [85]
Eq. (30)	Inelasticity of concrete factor in Medwadowski [85]
Eq. (31)	Safety factor for buckling governed failure [85]
Eq. (32)	Safety factor for material governed failure [85]
Eq. (33)	Ultimate biaxial compressive strength of concrete [116]
Eq. (34)	Ultimate compressive strength of concrete for a state of biaxial compression superimposed on hydrostatic stress state [116]
Eq. (35)	Ultimate compressive strength for a state of uniaxial compression superimposed on hydrostatic stress state [116]
Eq. (36)	Concrete stress-strain relationship [40]
Eq. (37)	Maximum concrete compressive strain [40]
Eq. (38)	Concrete modulus of elasticity [47]
Eq. (39)	Meridional force at the foot of the spherical cap [94]
Eq. (40)	Von Mises equivalent stresses [8]

1. INTRODUCTION

The dome is one of the most efficient and inherently stable structures by virtue of its spatial form and load-carrying mechanism. The dome, or spherical cap, is a doubly-curved shell structure; a non-developable surface that is stronger and more stable than other singly curved shell structures.

In addition to the stable form, shell structures, in general, carry applied loads by an efficient mechanism known as the membrane action, as opposed to the generally less efficient bending action in framed structures. The membrane action consists of in-plane normal and shear stresses only, which enables a shell with a small thickness to absorb very large loads with relatively low in-plane stress resultants. Consequently, shell structures have a high strength-to-weight ratio compared to other structural systems, and are able to cover large spans with very small thicknesses.

In general, bending stresses may develop in some regions of structural shells to satisfy equilibrium requirements, but they are generally of local effect, and are limited to the vicinity of loads or deformation incompatibilities, thus leaving the shell behaving mostly as a pure membrane. For dome structures, for instance, these effects are inevitable in the vicinity of the boundary, where, geometrically speaking, the dome diverges from the form of a complete sphere, or structurally speaking, from the clamped boundary condition assumed by the membrane theory. Hence, the dome requires a supporting structural member to absorb the large horizontal thrust at its boundary. The supporting member is commonly referred to as the dome ring.

Reinforced concrete domes, in particular, are used to cover large-span halls and stadiums, liquid retaining structures, and containment structures where usually only a vertical support is available. Consequently, a reinforced concrete dome is almost always bounded by an edge ring beam to absorb the horizontal force and provide lateral support to the structure, which can be considered equivalent to a tie in frame structures [44]. As mentioned above, the presence of the ring beam at the boundary gives rise to a bending

field between the shell and the ring in order to satisfy deformation compatibility at the boundary. A conventional analysis of the dome behavior, thus, requires an analysis of the membrane effects and the bending effects, followed by a superposition of both to find the total shell forces. The analysis must consider the dome-ring interaction, the edge bending edge effects, and the straining actions on the ring beam resulting from the shell hoop and radial forces, and the resulting torsional moment on the ring, so that the structural members can be designed accordingly.

However, unlike other structural systems, the design of shell structures is not mainly governed by material strength requirements for the calculated level of stresses in the shell, which is usually very low. Instead, a mostly governing criterion is the stability of the shell, more commonly referred to as the resistance to buckling failure. The buckling phenomenon refers to a form of instability of thin shells subjected to compressive forces. The reason why it is paramount for the design of thin-shells is that the loss of stability means that a small change in a system parameter (the load for example) results in a major change in the existing state of the system (large deformations) [44]. Consequently, buckling failures of thin-shells are usually sudden, catastrophic and accompanied by very large deflections, making the resistance to buckling one of the major factors in the design of the shell. A huge number of research studies were, consequently, devoted to studying the stability of shells, and understanding their behavior, modes of failure and failure limits in order to provide reliable design guidelines for engineers. Stability of the shell is highly dependent on its geometric parameters; the rise-to-span ratio and the radius-to-thickness ratio. This fact makes the thickness of the shell a paramount factor affecting the shell stability, and gives rise to a characteristic of the shell known as ‘imperfection sensitivity’. The imperfection sensitivity of shell structures infers that the buckling load of the shell is significantly reduced by the presence of initial geometric imperfections in the shell form including thickness variations and changes in the radius of curvature.

As a direct consequence of this sensitivity, the construction method of the shell structure has become a major factor in the design process. This is because the shell

requires elaborate and highly accurate formwork, careful casting process and quality control, and very skilled labor to minimize the inevitable form imperfections as much as possible.

The demanding nature of shell construction, and of particular concern here dome construction, has led to undermining the efficiency of the very strong structure, causing a recent decline in using domes, in general, and resorting to other structural systems. At the same time, it also led engineers to search for alternative construction methods that can increase the efficiency of the construction process including reusable formworks and prefabrication techniques, which aim to reduce the difficulties associated with the elaborate and labor-intensive construction of concrete shell structures. Of concern to this study, prefabrication techniques were applied to concrete shell structures in building complete shell segments or partial shell elements that are assembled to create the final membrane structures. These techniques, however, did not find as much popularity with shell structures as they did in skeletal structures due to the accompanying design and construction difficulties that were generally not given due research attention, as will be discussed in the literature review. The use of these techniques is reconsidered in this study while different design and construction methods are proposed for overcoming the associated disadvantages, and enhancing the overall structural and construction efficiency.

2. OBJECTIVE

The objective of this study is to develop a precast concrete spherical cap structural system which eliminates the disadvantages associated with the construction of cast in-situ concrete shells while maintains the structural efficiency of the double-curvature shell structure.

The motive for this work is the documented efficiency and popularity of precast construction in concrete skeletal structure, while at the same time, that type of construction was rarely applied to shell structures due to the introduced geometric difficulties that arise with dividing shells and obstruct the reusability of precasting molds, and the uncertainty of the structural behavior of segmented shells with the introduced intermediate joints. Consequently, this study aims to partially address the issues associated with segmental construction of concrete shells in a simple yet difficult to geometrically standardize structure; the dome. Accordingly, the scope of work is thus divided into four parts.

The first part of this study addresses the geometric considerations of the structure and attempts to explore the different possible divisions of the dome, determine the optimum division for the present application, which is defined as the division that produces the least number of unique panels for the whole structure, and thus increases the efficiency of the prefabrication process through the reusability of molds. It is attempted to clarify the various relationships between the division type, and the number of panels, panel sizes and weights, so as to provide the engineer with helpful geometric relationships that can help determine the best geometry for each application.

The second part attempts to study the structural behavior of the proposed segmented dome-ring structure using finite element modelling. Initially the structural behavior of the dome as cast monolithically is studied to provide a reference for comparison, and then the inter-panel joints are introduced to the model to study their effect on the stability behavior and overall capacity of the structure. The study initially used linear elastic modeling to verify the model and provide an estimate for the capacity

of the structure. Next, the modeling was extended to include large displacement, inelastic material properties, concrete cracking, various boundary and loading conditions, and various panel contact parameters to represent the effect of segmentation and the introduced joints to the structure.

The third part of the study presents a construction plan for the proposed structural system, and investigates the behavior of the structure during construction. Different scaffolding configurations are explored for supporting the construction and a final temporary supporting plan and assembly sequence are presented. This was done in collaboration with a numerical analysis that considers the arising deflections in the panels under their temporary support conditions. The section aims to provide a feasible assembly sequence for the general application of the structural system, and also for the constructed scale model.

The final part of this study is an experimental analysis on a 1:10 scale model of the structure. The main objective is to determine the ultimate load capacity and failure mode of the proposed segmented structure. Additionally, the experimental investigation also serves to provide insight on the feasibility of mold design and fabrication, the problems associated with the assembly of the structure's panels, and the overall behavior of the structure during construction. Three different loading tests are performed on the structure, and the results are compared to those of the finite element analysis and analytical formulas provided in the surveyed literature. The problems that arose during each stage of the experimental analysis were documented for consideration, and proper recommendations to address those problems were made accordingly.

In the following chapter, the timeline of the development of concrete shell construction and analysis in the literature is presented. In the first section, the development of concrete shell construction is discussed starting from conventional in-situ concrete construction methods and through the different attempts by various engineers to optimize the construction and find more efficient techniques. The significance of one particularly relevant structure 'the geodesic dome' shall be discussed in relation to shell construction applications, and finally some of the prefabricated shells will be reviewed. Although a few project reports and research studies discussed the process of constructing the shell segmentally using prefabricated units, the idea did not seem to be extensively applied nor structurally analyzed to provide a sound and reliable basis for a standardized design of a segmental concrete shell that takes into account geometry optimization, structural stability and ease of construction.

The second section of the chapter discusses the stability of shell structures, and particularly concrete spherical caps, in due depth. As mentioned above, the stability of shells is a paramount and mostly the major concern of shell design. The stability behavior of shells happens to be significantly affected by geometric form imperfections, geometric nonlinearity, material behavior, boundary conditions, among other factors. It is seen that that until today, research studies continue to seek proper definition of the properties of concrete spherical caps, and the effects of the concrete material and its associated nonlinearities on the short-term and long term capacity of these caps. It is also seen that virtually no studies were found on the stability behavior of segmental concrete domes, or the use of numerical models to simulate their behavior. Consequently, although the present study only deals with a specific geometry, it also serves to promote attention toward the possibilities of panelizing concrete domes, and experiment with different possible methods for the numerical modeling of segmented concrete shell structures.

3. LITERATURE REVIEW

3.1. Modern History of Concrete Shell Construction

3.1.1. The Concrete Shell Structure

The era of reinforced concrete shell design started in 1920s. According to a historical review of concrete shell development by Peerdeman [89], the completion of the Carl Zeiss Planetarium dome in Germany (1925) marks the beginning of modern large-span thin reinforced concrete shell structures, where engineers took advantage of the tensile capability of reinforcing steel to overcome concrete shell tension problems which previously posed limitations on shell thicknesses and spans. The Carl Zeiss Planetarium dome, shown in Fig. 1, is 60 mm thick and covers a span of 25 m and is bounded by a ring beam to absorb the horizontal thrust in the lower region of the dome [53]. The dome had a triangular steel grid in-place acting as both a framework and shell reinforcement that was then coated by shotcreting over the wooden formwork; a construction system that was later awarded a patent, Zeiss-Dywidag system [18]. After the success of Zeiss-Dywidag system; the triangular steel grid system encased by concrete, it was used in the construction of many shell structures in Europe and the United States through the 1930s.

Fig. 1: Carl Zeiss Planetrium (www.wikimedia.org)

At that time, the steel grid system of Carl Zeiss began to take a life of its own by laying the foundation for the geodesic dome, fully developed and patented by

Buckminster Fuller. The development and significance of the geodesic dome shall be discussed in the following section.

The trending of shell construction, though, can be traced to post world war II, where the low cost of labor, shortage of materials, and need for many new buildings provided a suitable atmosphere for the flourishing of shell construction [89]. Consequently, although shell construction was a "labor intensive" process, the material efficiency of the shell was a needed advantage that led to the popularity of shell structures throughout the world in the between 1950s and 1970s.

A shift towards shell slenderness, free curved edges with no ring beams, and elegance of form was seen at that time, inspired by prominent shell engineers such as Felix Candela, who built over 300 shells in two decades [89]. Candela is responsible for the trending of the hyper parabolic shell form, referred to as the hypar shell, in the 1950s, with the most famous design being the Los Manantiales restaurant in 1958, which was later copied by many other engineers and has been studied for its structural efficiency even till today [22]. The famous structure (shown in Fig. 2) consists of four intersecting hypar shells of a 40 mm thickness and a span of 30 m [36]. The horizontal forces are absorbed by tension rods connecting the supports under the ground level [22]. Candela's work, then, sponsored the rising of the value of concrete shell structures in architecture, with architects using shells for commercial construction purposes, rather than the previously industrial and military nature of shell construction.

Fig. 2: Los Manantiales restaurant by Felix Candela (www.structurae.co.uk)

Along with free-form exploration, shell engineers started looking for ways to save construction time and costs, and eliminate the form and surface finish problems associated with the elaborate formwork of shell structures. A preliminary attempt was by the Italian engineer Pier Luigi Nervi in constructing airplane hangars between 1939 and 1942 as large cylindrical shells with stiffening ribs over a maximum span of 50 m. The hangar design was based on a steel grid that was encased with cast-in-situ concrete. However, the problems associated with pouring concrete over wooden formwork and the subsequent form imperfections in the first set of hangars (1935- 1938) led Nervi to pursue a completely different construction approach for the second set (1939- 1942); prefabrication. The stiffening ribs were designed as lightweight lattice ribs made of prefabricated parts on-site that were assembled in a fast and efficient erection process, and cast-in-situ concrete was only used at maximum stress locations. At the joints between the precast elements, the steel was welded and high strength in-situ concrete was poured in the stitches [41].

Another later attempt by the same engineer was the use of ferrocement in the construction of double-curved shell roofs for the 1960 Olympic Games. Nervi used ferrocement (layers of steel meshes coated with cement mortar creating thin sheets) as prefabricated moulds for the shell construction, where the prefabricated ferrocement molds were assembled then filled with cast-in-situ concrete [41]. Prefabrication techniques were also used by French engineer Nicolas Esquillan who, beside the use of prefabricated elements, used reusable movable formwork for in-situ concrete casting of shell segments [89].

The need for such efficient construction methods was amplified in the late 1960s where the labor costs increased. According to Peerdeman [89], the curved formwork supported on steel framework of shells had become too expensive and time-consuming, compared to other structural systems.

The use of standardized construction techniques and resuable formwork showed significant progress when Swiss engineer Heinz Isler developed the ‘bubble shell’ in the early 1950s, in collaboration with Bösiger Construction Company. The bubble shell is a

shell construction technique of standardized sizes and resuable formwork allowing for an efficient and economic construction process. The standardized bubble shell comprising a prestressed ring beam and four supports for transferring the vertical load was used mainly for industrial units. Isler constructed about 749 bubble shells between 1956 and 1985, and standard reusable formwork was developed for the construction, in collaboration with the Bösiger Construction Company, for shell spans mostly between 14X20 m and 25X25 m with thicknesses of 80-100 mm [34].

Beside the bubble shells, Isler is also famous for free-form shells, where he ditched edge beams and experimented with different free-forms, most prominently the structurally efficient inverted hanging membrane shells. Based on his experience with shell structures, Isler has written guidelines for engineers concerning stability of shell structures, and the design and construction factors that reduce the shell capacity, which will be discussed in the next section as part of the literature on stability of concrete shells.

Shell construction, however, experienced a falling out in the 1970s when the construction of shells became too expensive compared to other structural systems with regard to the associated cost of labor and formwork, and also the associated difficulties in conducting proper analysis of the structural behavior of shells [89]. Consequently, according to Peerdeman [89], the large-scale usage of shells died out, and the only shells that were built were those with standardized cost-saving construction techniques and shell structures built for industrial purposes.

One auspicious technique that arose to achieve fast and economical shell construction was the use of inflated membranes to act as formwork for the construction of reinforced concrete domes. The system was developed in the 1940s (a patent by Wallace Neff in 1942), but was extensively applied in the 1970s [89] when the Monolithic Dome concept was developed by Barry, Randy, and David South (patent in 1979). The monolithic dome was based on using an airform or a fabric form sprayed with a layer of polyurethane foam to provide form rigidity, support the placement of reinforcement and concrete, and provide insulation for the structure if needed, then steel rebar is attached to the form and concrete is sprayed. The method (shown in Fig.3) allows for a very fast

construction process and the airform can be deflated and reused multiple times. Consequently, the monolithic dome system has gained popularity, was used for construction of houses and commercial facilities, and is still in use today due to both the efficient construction and the structural strength of domes [2].

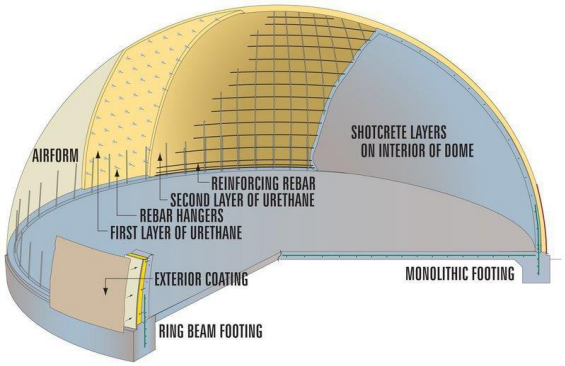

Fig. 3: The Monolithic Dome [2]

Another construction technique was the segmental construction of shells where the shell was divided into elements that were efficiently assembled, eliminating the elaborate formwork and the demanding construction process. The grid shell, which was built of linear or curved triangular or quadrilateral elements and was made to behave as a shell membrane using internal tie rods, was developed in the 1960s by Frei Otto and was commonly built of steel and timber [89].

The next type of grid shell is the famous geodesic dome which was fully developed by Richard Buckminster Fuller and his collaborates, and laid the base for the technique of using spherical subdivision for panelizing dome structures.

3.1.2. The Geodesic Dome

As mentioned above, one approach to facilitating dome construction, although not extensively applied to concrete systems, was the geodesic dome. The geodesic dome can be defined as "a three-way grid of great circles" [90] or as defined by Fuller's 1954 patent "A framework of generally spherical form, in which the main structural elements form a substantially uniform overall pattern of great circle arcs intersecting in a three-way grid" [90]. This grid is accomplished by "creating a spherical version of a planar polyhedron and subdividing its faces with a grid". More literally, it is a spherical grid of triangles with unique division patterns. These division patterns vary greatly and some of them have incredibly important characteristics in terms of manufacturing and assemblage practicality. The first person to recognize the value of spherical polyhedral and subdivision grids to architectural construction is Buckminster Fuller, the inventor of the geodesic dome; and most subdivision techniques used today in many more fields than structural systems were developed in the late 1940s and 1950s by Fuller and his associates to build geodesic domes [90]. The importance of Fuller's work lies in his highly creative results that still favored manufacturing techniques.

Examples of early geodesic domes include the US pavilion, Expo '67 in Montreal (shown in Fig.4), Epcot center at Disney world in Orlando, and La Géode Theater in Paris. Geodesic domes were built in many sizes and diverse materials including wood, plastic sheets, metal sheets, foam panels, cardboard, plywood, bamboo, fiberglass and concrete. The concept of the geodesic dome, or uniform spherical subdivision in general, was extended to a lot of other fields than construction including astronomy, weather prediction, materials science, virology, computer architecture, and dimple patterns on golf balls.

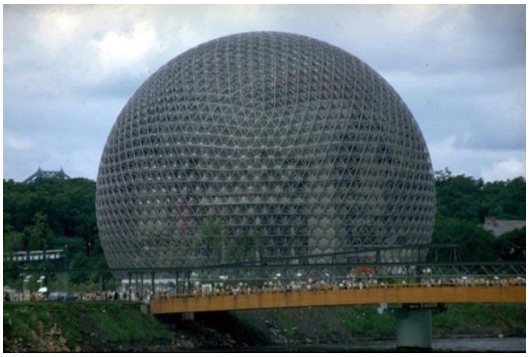

Fig. 4: US pavilion, Expo '67 in Montreal (www.columbia.edu)

The stability and rigidity of the geodesic structure is inherited from the original basic platonic solid of the design, most frequently an icosahedron, tetrahedron or octahedron (solids with equilateral triangular faces). The icosahedron, in particular, is the most used polyhedron for spherical subdivision [90] since it provides the highest number of identical regular triangular faces, which translates in construction applications to efficient prefabrication and reusing of molds. The search for the most optimum subdivision technique is, however, not as straightforward. Much experimentation was conducted by Fuller, his collaborates and his successors on finding optimum spherical subdivision techniques. In fact, whole books were written on the matter including Divided Spheres (latest publication in 2012) which explores mainly the different techniques of spherical subdivision and produces comparisons between their different characteristics that provide an industrial edge in various applications. Divided Spheres [90] is referenced in the methodology section of this study quite frequently, since it was used for selecting the optimum geometry for the dome in this study. Another significant work on the matter was Joseph D. Clinton report for NASA, 1971 [35] on the formulation of mathematical models for the subdivision of polyhedral and the structural applications of the resulting "spherical space frames".

3.1.3. The segmental Precast Concrete Shell

Although the research on the structural applications of spherical subdivision presented an auspicious for space frame structures, as seen in the development of lattice structures, particularly lattice domes built as space frames of steel members, it did not seem to find much application with concrete shell structures.

As previously mentioned, prefabrication of shell elements started as early as the 1940s in attempts of engineers to optimize the shell construction process, and later the prefabrication of small shell parts developed to a prefabrication of large shell segments such as the Stuttgart Federal Garden Fair shell in 1977, which is made of eight large prefabricated shell segments [89]. However, standardized prefabrication of shell concrete elements did not seem to have had much research support or application. The use of prefabrication techniques was being applied to skeletal concrete structures. In framed structures, the use of standardized precast concrete members highly increases the efficiency of construction. The prefabrication process allows both a high level of quality control of the precast panels, and a speedy erection process with no formwork, and minimum faslework.

The application of precasting techniques to curved spatial structures is not as straightforward, though, especially with the dome whose structural efficiency arises from its complete form. Thus, dividing the dome into individual panels introduces some other construction difficulties and new structural loads to be taken into account in the analysis process. Another structural concern raised by the prefabrication technique is preserving the continuity of the final structure, i.e. achieving full transfer of the loads across the joints between the precast concrete panels.

A third concern in panelizing dome construction is the cost of manufacturing the panels themselves. The efficiency of the precast construction is achieved through standardization of modules, meaning that the structure is divided into groups of identical parts that are fabricated using the same mold. The more standardized building parts are, the more times molds are used and the fabrication process is optimized. In dome structures, as mentioned in the previous section, this panelization process is not as simple

or direct as most skeletal structures. A large span dome is not readily divisible into groups of maneuverable parts with convenient weights and identical shapes. Consequently, using precasting techniques in constructing concrete domes requires more planning and analysis effort in order to optimize the manufacturing and assembly process, and preserve the strength and stability of the final structure.

The first geodesic concrete dome is the Cinerama theatre, California in 1963, although about 2000 geodesic domes of different materials were built prior to that project [65]. The dome has a diameter of 41 m, a rise of 15.7 m and consists of 316 precast concrete hexagonal and pentagonal panels of 16 different sizes, requiring 35 different configurations for the panels' steel reinforcement. The author noted the very high dimension precision required for the production of the panels, along with proper curing to minimize drying shrinkage. The dome was supported by a post-tensioned ring beam cast monolithically with the supporting wall of the structure. For the panels' assembly, a wooden deck was placed at the ring beam level with steel scaffolding on top of the platform to support the placement of the panels, which weighed about 2.85 tons, using cranes [65].

Another segmented precast concrete dome with a different division pattern was featured in literature in 1969 [37]. The author described the construction process of a 45.7 m diameter reinforced concrete dome from precast panels, with minimum formwork and equipment for erecting the structure. The dome division pattern was in both radial and circumferential directions giving six differently sized prefabricated units. The precast panels are connected by cast-In-place slots of concrete, and the ring beam was also made of 16 precast concrete segments tied together with cast-in-place concrete slots. The construction of the system was implemented using only steel falsework and no formwork. However, no design basis was provided and no stability analysis was carried out.

A barrel vaulted roof, designed by Studio Nervi of Rome in collaboration with South African architect Colyn & Meiring, was reported in 1977 [1] to be constructed of 892 light-weight reinforced concrete shell panels covering a span of about 85.3 X 85.3 m. The shell panels are equilateral triangles of 28 different unique sizes; the lengths of the

panels range between 3.5 and 4 meters, while the thickness ranges between 0.46 and 0.76 m, resulting in a total panel weight between 1.5 to 6.5 tons [1]. The roof is supported on four arch beams transferring the loads to the supports, as shown in Fig.5 [1]. The report indicates that the construction of the shell panels was supported on 364 steel frame towers that were braced horizontally.

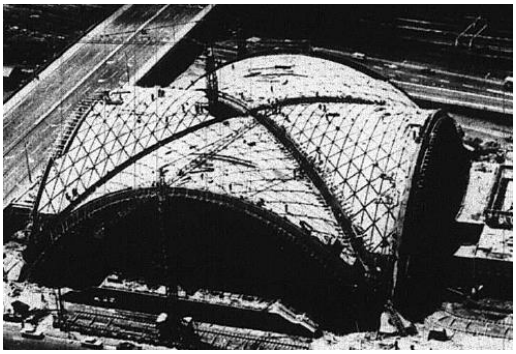

Fig. 5: 1977 barrel vaulted roof of concrete triangular panels [1]

In 1982, another segmental concrete shell design was implemented with no formwork, as well [74]. The shell had a square base plan, thus making it easier to divide the shell surface into substantially equal square precast concrete elements, as shown in Fig.6 [74]. The authors described the construction of the concrete shell using only one module, i.e. identical precast concrete elements. They noted, however, that the curvature angle of the dome elements increased as the elements got closer to the dome apex, yet they were able to overcome this non-consistency by allowing some variance in the width of the joints between the precast elements. These joints were later filled with cast-in-place concrete.

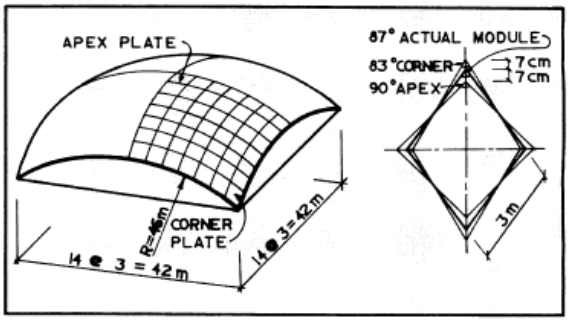

Fig. 6: Panels of the segmented concrete shell reported by Kaplunovich and Meyer [74]

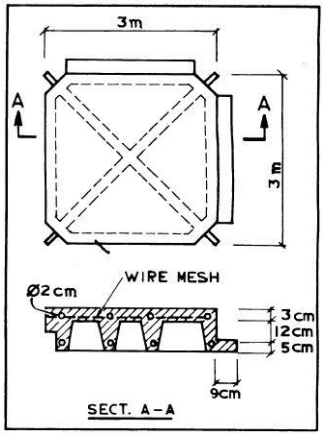

Fig. 7: Stiffened precast concrete panel in [74]

The precast concrete panel of the shell was stiffened by ribs along its edges and the two diagonals. The 30 mm thick top part was reinforced with welded wire fabric, while the ribs were reinforced with 20 mm steel bars, as shown in Fig.7 [74]. Two flanges were integrated onto two perpendicular edges of the element as shown in the figure. These flanges acted as resting beds for the neighboring elements to be supported on the already installed one. The design of the joints also required the protrusion of the reinforcing steel bars of each panel, and then the bars of adjacent panels were welded together before filling the joint with concrete as mentioned above.

Kaplunovich and Meyer [74] proposed a construction process which used temporary falsework consisted of four corner ties, as shown in Fig.8 [74], for stiffening the edge beams against temporary horizontal thrust forces that developed during the early stages of construction where the assembled elements resembled cantilevered arches [74].

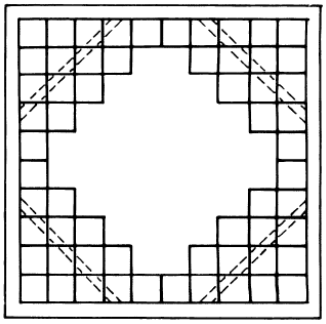

Fig. 8: Shell Plan showing corner ties and assembly of corner panels [74]

The concrete precast elements were then placed starting from the corners where each unit rested directly onto the flange of a previously installed unit, supported completely by a cantilever bending action. After installing each unit, the reinforcing bars were tied to the bars of the previous unit, and then the joint is filled with cast-in-situ concrete. Consequently, the elements were supported by two actions: the cantilever bending of the elements and the arching action of each corner arch, until enough elements were assembled to connect the four corner arches allowing for the shell membrane action.

The authors discussed in detail the deflections of the shell elements, particularly those induced during the construction stage when the assembled precast elements worked as cantilevers before enough elements are assembled to produce the dome action. They noted that the deflections of each element were different during each stage of the construction process, which also emphasized the need for comprehensive construction stage analysis. The authors used one of the scale models they developed to measure the deflections of the individual shell panel during the construction process and created histograms for the deflection patterns at each stage. Fig. 9 and Fig.10 [74] present an explanation of the deflection pattern vs. the assemblage history of the typical shell panel.

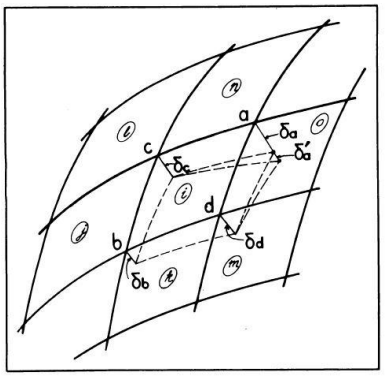

Fig. 9: Deflection of a typical shell panel [74]

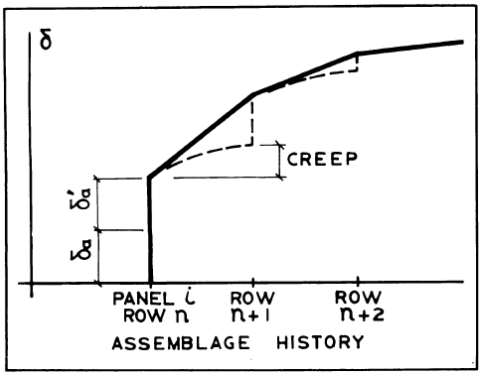

Fig. 10: Deflection histogram of point a in Fig. 9 [74]

The authors, however, did not conduct a stability analysis of the shell, and indicated that such analysis, along with the appropriate analytical formulas, is needed for standardizing the design and construction procedure.

In other later works, a trend of using segmented shell structures for low-cost and efficient small-scale housing was noted. Examples are the construction method proposed by Habib, 1993 [55] of a hyperbolic paraboloid shell roof built of ferrocement flat triangular panels, and the construction of geodesic domes made of polystyrene panels encased by a reinforced concrete layer [66].

Frank J. Heger [62] discussed the design of a precast concrete dome used for water and waste water tanks, regarding the resistance to buckling as the primary design parameter. The dome was constructed of differently sized precast elements combined with monolithic circumferential rings between each row of precast panels; these circumferential rings were considered to be the only source of effective circumferential stiffness. Heger dicussed the reduced buckling resistance of the precast dome, compared to its monolithic counterpart, due to the rotational flexibility of joints, and the absence of continuous reinforcement across the joints. This reduction in capacity was taken into account with a recommended correction factor.

A few large-scale segmented shell structures were reported in the literature in the past few decades. The 1997 aircraft museum in Duxford consists of a singly curved

vaulted roof over a 90 m span, shown in Fig.11. The structure is segmented in a way that creates identically shaped and curved precast reinforced concrete elements, except for those at the edges of the structure which have various different shapes. The elements are designed in a stiffened T-shape with a 100 mm thick topping slab. After element assembly, a wet connection is created at the concrete stitches between the elements by placing steel reinforcement and in-situ concrete. The construction was supported by temporary scaffolding that held the elements in place until hardening of the concrete connections [39].

Fig. 11: Aircraft museum in Duxford (www.wikimedia.org)

Another prefabricated shell project is the canopy shed system of Shawnessy light rail transit station, Canada, in 2003, although on a smaller scale. The canopy system, shown in Fig.12 [6] consists of only two segments prefabricated and connected through a bolted connection at the upper part of the shell, to a slightly curved base using reinforced ribs, and to a tie beam across the open base (see Fig.12 [6]). The segments are fabricated from fiber-reinforced ultra-high performance concrete allowing a very small thickness (minimum thickness = 20 mm). 3D models of the canopy molds were built and their deflections analyzed using finite element methods. The reusability of the molds was advantageous in this project since the shed system consisted of 24 canopies [39].

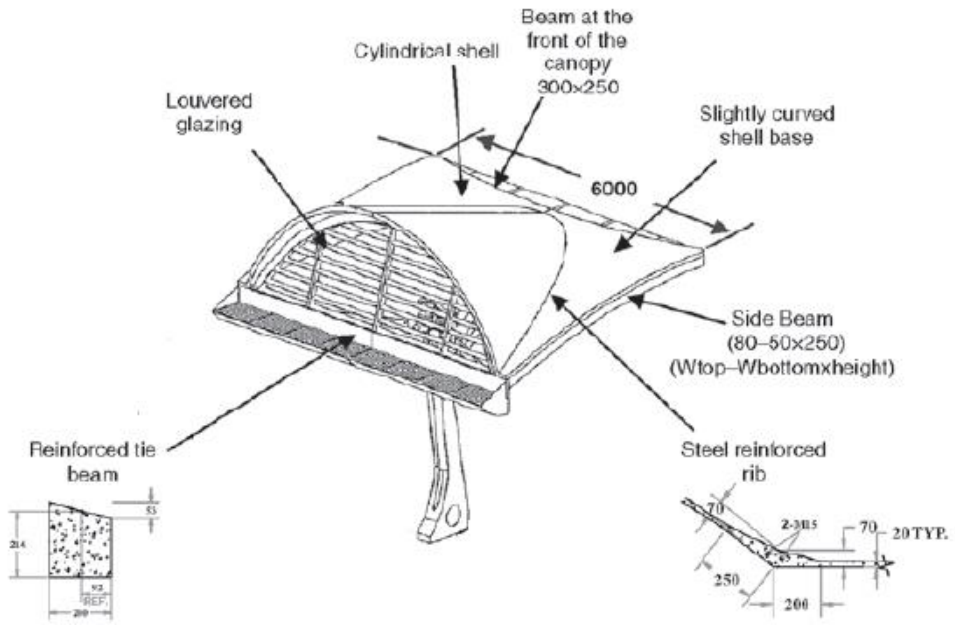

Fig. 12: Schematic of one canopy of shed system of Shawnessy light rail transit station, Canada [6]

Through the few studies and projects that include prefabrication of concrete shells it is possible to understand the associated problems with the analysis, design and construction, which allows for the consideration of these issues in the design of the structure of the present study. As mentioned in the beginning of this subsection, the application of prefabrication techniques to concrete shell structures is not as straightforward as it is with structures of skeletal forms. Based on the surveyed literature, the major issues to account for are summarized as follows:

- Accurate estimations of the effects of the joints between the precast shell elements on the overall behavior of the structure are not readily available and are difficult to quantify [39], [74], although reported to affect both the deflection state and the stability behavior [62], [74]. Another connection related problem is the requirement of high precision elements to obtain strong connections that ensure the continuity and stability of the structure, while, at the same time, some adjustment may be needed during the assembly of the panels [39].

- Reusability of molds is usually very limited since the shell panels usually have different forms and sizes [39]. The use of re-adjustable molds based on height-adjustable pins that can create different shapes of curved elements was reported in the literature [52], [95], [96], [97], with detailed experimentation on the possibilities of these flexible molds, although not discussed here in detail.
- Due to the variable natural of shell structures, each structure has differently shaped panels and optimum connection types, making it difficult to standardize the design and construction procedures [39].

The following section focuses in-depth on the timeline and recent development of stability analysis of spherical shell structures, and particularly concrete spherical caps. However, it is noted that almost no studies were available which provided stability analyses on segmental concrete spherical shells. This could be attributed to the fact that that type of construction never found much application due to the reasons mentioned above. However, this study believes that the proposed construction method, supported by a comprehensive structural analysis, may present an efficient, fast and economical alternative for the construction of concrete dome structures of relevant geometry. Therefore, the major part of this work is to study the development of the stability analysis of concrete spherical caps.

3.2. Stability Analysis of Concrete Shells

3.2.1. Stability Theory of Shells

Shell structures have much higher membrane stiffness than bending stiffness, allowing them to absorb very high membrane strain energy without excessively deforming. An instability failure of the shell occurs when, loaded in compression, the shell's stored membrane energy is converted into an equivalent amount bending energy, requiring very large deflections [23]. Farshad [44] provided a simplified definition of buckling as "a special mode of instability of equilibrium which may occurs in deformable bodies subjected mostly to compressive loadings".

The two distinctive types of buckling are bifurcation buckling and nonlinear collapse. Bifurcation buckling is refers to a theoretical mode of buckling in which, upon reaching theoretical buckling load level, the shell deformations begin to grow in a new pattern or a secondary path that is different from the axisymmetric prebuckling load-deflection path (primary path). If the post-bifurcation load-deflection curve has a negative slop, the new deformation grows unboundedly and failure occurs [23]. Bifurcation buckling load is based on the linear elastic theory of shells and is predicted by an eigenvalue analysis. Consequently, true bifurcation buckling for real imperfect structures does not exist. What it represents is a theoretical upper bound for the buckling of shells that was used for calculating convenient approximations of the failure load, and as a basis for modifications and comparisons of experimental results, in research attempts to account for the factors that cause the shell to fail before reaching its theoretical buckling limit.

The other type of buckling is nonlinear collapse, (also known as limitation of equilibrium [44]) in which the stiffness of the structure changes over the loading history and is, consequently, based on geometrically nonlinear analysis. In nonlinear collapse, the structure initially deforms slowly as the load increases, and as it approaches the maximum load, the deformation rate increases i.e. the stiffness of the structure decreases gradually until it reaches the maximum load point where the stiffness is zero (known as neutral equilibrium). At that point, if the load is maintained, the structure experiences a

dramatic failure where the structure theoretically has a negative stiffness (negative slope of the load-deflection curve). In shell structures, this type of failure is commonly known as 'snap-through' [23] which, according to Bushnell [23], was derived from earlier experiments on shallow spherical caps and arches, where, upon reaching the neutral equilibrium point on the load-deflection path, the structure snaps to a nonadjacent postbuckling configuration that resembles the original configuration but in an inverted form [23]. The development of nonlinear theoretical models since the 1940s marks the launch of the research phase that attempted at justifying the significant discrepancy between experimental analysis results on shell buckling and the values predicted by the theoretical models of the linear elastic theory. The geometric nonlinearity is, however, only one of many factors that are seen to significantly affect the failure load and mode of spherical caps. The following subsections attempt to review these factors as documented in the surveyed literature.

In the Buckling of shells chapter of *Thin Plates and Shells, Theory: Analysis and Applications* [110] the elastic buckling of shells was illustrated using an ideal cylindrical shell under uniform axial loading. The perfect shell load deflection path is shown in Fig.13 [110].

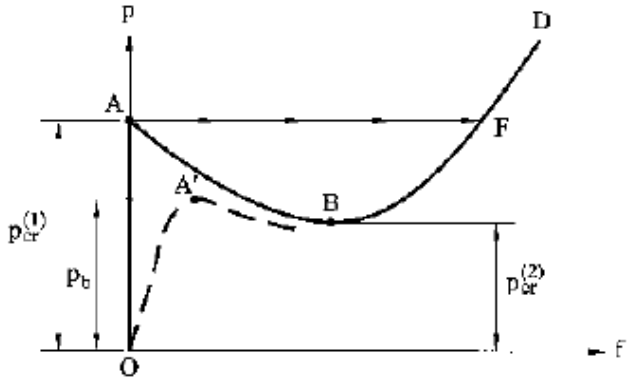

Fig. 13: Load-deflection path of the perfect shell [110]

According to the figure, the perfect shell (solid line) starts in a membrane state of stress with no deflections until it reaches point A, where no adjacent stable buckled configuration exists (AB branch has a negative slope). Thus, the structure "jumps" from

the stable prebuckled configuration through the unstable state (branch AB) to the new stable buckled configuration at F on branch BD. This transition represents what is referred to as ‘snap-through’ buckling. The analysis of that problem in general requires a geometrically nonlinear analysis [110], [54], unlike buckling of rods or plates where stable buckled configurations are found in the vicinity of the bifurcation point with no dramatic jumps.

What makes the buckling of shells problem even more challenging is that real shells are inevitably imperfect, and the critical buckling load of the shells was found in most of the documented literature to be extremely insensitive to the geometric imperfections that present prebuckling deformations imposed on the shell. As shown in Fig.13 [110] in a dashed line, the load-deflection part of the imperfect cylindrical shell has a critical load A’ (where the snap-through jump occurs) that appears significantly lower than the critical load of the perfect shell A.

Based on the previous analysis, three distinct values of the critical loads for thin shells are differentiated; the first is the upper load limit (represented by point A in the figure) obtained through linear differential equations; the second is the lower load limit (point B in the figure), representing the largest load at which the perfect shell is stable when considering large deflections, which requires solving the complicated geometrically nonlinear theory of shells problems. It is stated that all the available results for the lower critical load of the perfect shell are obtained using numerical models since it is impossible to obtain the exact analytical solution [110].

The third critical load limit is that of the imperfect shell (the buckling load of the real shell) which happens to occur somewhere between the upper and lower limits of the perfect shell, and is extremely sensitive to geometric imperfections and boundary conditions. This has been seen through the large scatter of the experimental analysis results of buckling loads of shells, and, as stated in [110], theoretical analysis of imperfect shells also imposes challenges because it is impossible to accurately account for all shell anticipated imperfections. Consequently, a large discrepancy has always been reported between the results of theory and experiments of buckling of shells [110].

While solutions based on the geometrically nonlinear shell theory are stated to be too computationally demanding to apply for design purposes to calculate shell failure loads [110], the linear stability theory is not adequate for predicting the buckling behavior of shell structures. It is useful, however, in demonstrating the different factors that affect the buckling load and their interactions, when combined with corrections and coefficients that may be derived based on experimental analysis results to supplement the analytical relationship prescribed by the linear theory and provide valid design tools.

Guran and Lebedev [54], on the other hand, state that precise experiments of buckling of spherical caps provide good agreement with theory, but significantly differ from actual critical load values in engineering practice in general. The authors agree on attributing these differences to inadequacy of mathematical models to describe the behavior of the real structure, because the critical load values are sensitive to shape imperfections, boundary conditions and production of the shell that may have significant effects on the material behavior. Research has, then, been concerned with answering the question of how to account for each possible imperfection in each shell in order to provide applicable numerical models for real systems.

A more integral analysis of the behavior of shells is noted in recent studies. Pan and Cui [87] presents a clear distinction of the failure modes of perfect spherical caps; a material failure resulting from stresses reaching the yield condition followed by a subsequent plastic collapse, and predicted by stress analyses, and an elastic buckling leading to collapse, and predicted by stability analyses. The ultimate strength of the shell is defined as the minimum of the two. For a maximum yield stress σ_y of the shell material, the maximum allowable pressure is presented in Eq. (1) [87]:

$$p_y = 2\frac{\sigma_y t}{R} \tag{1}$$

Thus, p_y is compared with the classical elastic buckling load pcr to determine the failure mode of the perfect spherical shell. From that comparison, the authors formulated the condition that determines the buckling mode as presented in Eq. (2) [87]:

$$\frac{t}{R} > \frac{\sqrt[\sigma y]{3(1-\nu^2)}}{E} \tag{2}$$

If that condition holds, then the classical buckling load is higher than the material failure load, indicating that the shell failure is a result of material yielding. Hence, an elastic-plastic buckling analysis is needed (usually for thick-walled spherical shells) [87].

3.2.2. Stability Analysis of Spherical Caps

The previous section aimed to touch on the various issues concerning stability theories of thin-shell structures in general. The purpose of this section is to present a quick survey of research efforts and their development over the past few decades regarding simplifying the procedures and improving the reliability of the prediction of critical loads of spherical caps of various parameters. The section investigates the experimental analysis, and the consequently developed numerical models that aim to bridge the gap between theory and experiment, understand the behavior of spherical caps, and provide approximate methods to quantify the different factors affecting the capacity of spherical caps for design purposes.

As previously mentioned, in stability analyses of spherical shells, and spherical caps in particular, experimental analysis results proved the existence of a large gap between theory and experiment. More seriously, some of the actual built structures with presumably sufficient strength safety margins have undergone unforeseeable failure due to this gap [86], [101]. Consequently, the research direction in the decades that followed was to understand the factors that cause the actual spherical cap to fail long before it reaches its calculated critical buckling pressure prescribed by the linear elastic theory of shells. The factors that were seen to be studied the most over the past eight decades are the geometric nonlinearity, boundary conditions, material nonlinearity, and geometric and loading imperfections.

Studying the effect of the nonlinearity of the shell material, for instance, is a widely challenging topic that is only as advanced as the available material constitutive models for numerical analysis. Material nonlinearities, and specifically time-dependent properties, can significantly affect the capacity of thin shell structures. As for the material at hand, the more recent studies of concrete shells predominantly investigated the effects of creep, and the vulnerability of concrete shells of different geometric parameters to creep buckling. Miscounted for in earlier structures, concrete creep strains are shown in the literature to significantly reduce the long-term capacity of concrete shells.

In experimental studies of concrete shells, and shells in general, material effects are not studied in isolation due to the inevitable presence of geometric and loading imperfections. Quantifying the effect of imperfections on the shell capacity requires accurate quantification of these imperfections, their types, locations and amplitudes. In fact, most reported shell experimental tests have attributed the early failure of the shell model to the presence of geometric imperfections. These included accidental changes in shell thickness, variations in the radius of curvature and others.

3.2.2.1. An Overview of the Buckling of Spherical Shells

The buckling load of a complete spherical shell under uniform external pressure was first calculated in 1915 by Zoelly R. [121] based on the linear elastic theory (small deflections assumption), as (Eq. (3) [121]):

$$P_{cr} = \frac{2E}{\sqrt{3(1-v^2)}} \left(\frac{h}{R}\right)^2 \tag{3}$$

Where E is the modulus of elasticity, v is Poisson's ratio, R is the radius of the spherical shell, and h is the thickness of the shell. For a Poisson's ratio of 0.2, the equation reduces to Eq. (4):

$$P_{cr} = 1.179\ E \left(\frac{h}{R}\right)^2 \tag{4}$$

The same value was calculated by Van der Neut in 1932 [107] for unsymmetric buckling.

Experimental buckling tests that followed showed very low bucking loads when compared to the classical value, and research investigations were conducted to explain discrepancies between theory and experiments. Since the elastic theory worked well for plates, the research has focused on determining the effects of curvature and spherical shape imperfections that cause the large reduction in buckling capacity. The gap between

the theory and experiment was also attributed to the geometric nonlinearity and initial imperfections. Consequently, researchers used the large deflection theory and developed various methods to account for initial imperfections of spherical shells.

T. von Karman and H. S. Tsien, 1939 [113] used energy principles in deriving the lowest buckling load (equivalent to that defined as the lower bound in the previous section). The energy approach assumed that the minimum buckling load coincides with the position of minimum total potential energy on the load-deflection curve, if one existed [99]. The authors predicted a theoretical value of the lower bound of the buckling load as (Eq. (5) [113]):

$$\mathrm{P\,cr} \;=\; 0.365\ \mathrm{E}\left(\frac{\mathrm{h}}{\mathrm{R}}\right)^{2} \tag{5}$$

This value compared more favorably with experimental data at that point [67], [31], and it was recommended for design practice. Volmir, 1963 [112] calculated the geometrically nonlinear lower-bound buckling load for the elastic shell under external pressure, using the nonlinear stability theory, to be about 25% of the upper limit predicted by the linear stability theory (Eq. (6) [112]), a value that is even lower but close to that calculated by the authors in [113]:

$$Pcr\ (lower\ limit) = 0.31\ E\ \left(\frac{h}{R}\right)^{2} \tag{6}$$

At that point, research studies focused on providing a relationship between the buckling load and a normalized geometrical parameter that depends on the rise-to-thickness ratio of the shell and was found to govern the buckling of shallow spherical caps. The shell geometrical parameter is calculated by Bushnell [23] as (Eq. (7) [23]):

$$\lambda = 2\left[\sqrt[4]{3(1-\nu^2)}\sqrt{\frac{H}{h}}\right] \tag{7}$$

where H is the shell rise, h is the thickness, and ν is poisson's ratio.

Bushnell showed qualitatively that the prebuckling and buckling behavior of spherical caps depends on their shallowness (for the same thickness) by constructing the load-deflection curves for clamped spherical caps with different shallowness, shown in Fig.14 [23], governed by the shallowness parameter λ and corresponding to both linear (dashed) and nonlinear (solid) theory predictions. The circles on the linear load-deflection path represent the classical buckling pressure for the complete spherical shell. The figure shows the following:

- For $\lambda < 3.5$, the nonlinear load-deflection path shows no loss of stability.
- For $3.5 < \lambda < 6$, axisymmetric snap-through buckling occurs.
- For $\lambda > 6$, the bifurcation load is lower than the axisymmetric snap-through load.
- For $\lambda > 7$, prebuckling behavior closely follows that predicted by the linear theory, and the non-uniform prebuckling behavior occurs near the clamped edge, which causes buckling at about 80-90% of the classical buckling value of a complete spherical shell [23].

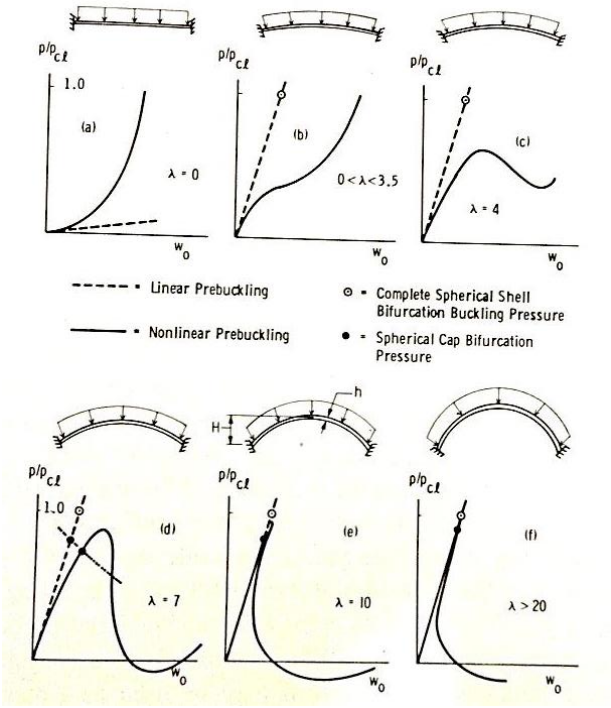

Fig. 14: load-deflection curves for clamped spherical caps with different shallowness parameters [23]

Marcinowski, 2007 [83] determined critical pressures and full equilibrium paths of shells for values of the shell parameter between 3.5 and 12 using a finite element method approach that proved to be in good agreement with the qualitative descriptions of Bushnell [23] above and other previous studies [21], [114], [103]. Based on Marcinowski's work, a shell with $\lambda = 10$ (close to that of the present study) has a lower limit point on the buckling equilibrium path (mostly used in other studies to represent critical buckling load) equal to 0.134 of the classical value of the linear elastic full spherical shell.

Farshad [44] also presented an approximate relation that determines the buckling mode of a spherical cap, characterizing the buckling as either a global phenomenon that includes the whole shell or a snap-through buckling confined to a local region, depending on the shell thickness, radius and central angle. According to Farshad, the whole shell buckles up to a base radius $ro > 3.8\sqrt{R\,h}$ at which the shell buckling becomes a local phenomenon.

Other theoretical studies, such as those of B. Budiansky [21], Weinitschke [114], G. A. Thurston [103], Caseman [30], Archer [14]; Keller and Wolfe [75], continued the work aiming at deriving a relationship between the shell geometrical parameter λ and the buckling pressure. The results of Budiansky [21], Weinitschke [114], Thurston [103] and Caseman [30] are shown in Fig.15 constructed by Seaman [99] where the normalized buckling load (as a ratio of the classical linear buckling load) is plotted against the shell geometrical parameter. Although most of these studies are reported to have provided accurate predictions of axisymmetric buckling loads of perfect clamped spherical shells through various numerical methods, the results did not match the experimental results obtained during that period [49], [99].

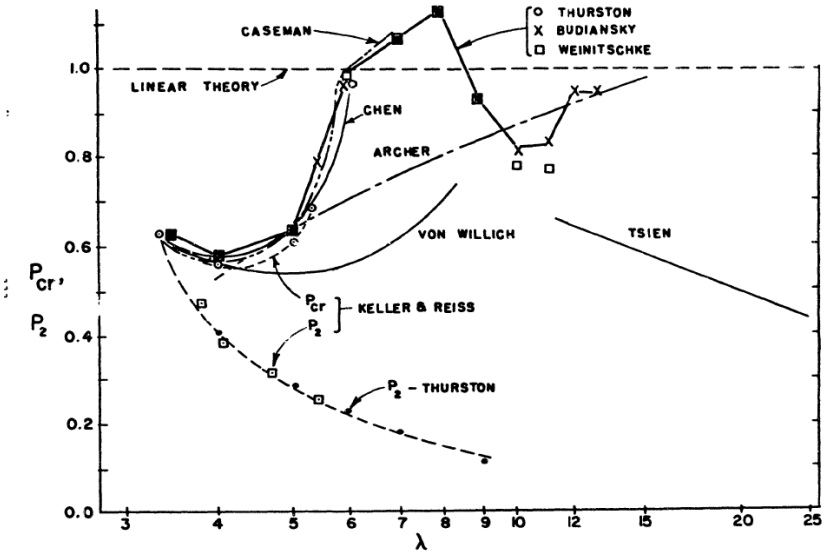

Fig. 15: Comparison of theoretical buckling loads predicted by various authors, compiled in reference [99]

Examples of those experiments are the investigations by Tsien [106]; K. Kloppel and Jungbluth [77]; Kaplan and Fung [72]; Homewood, Brine, and Johnson [63]; Thurston [102]; Parmerter [88]; and Thurston and Penning [104] which resulted in significantly lower loads than the values predicted theoretically for various shell parameter values. The results of some of these experiments are shown in Fig.16 compiled by Seaman [99].

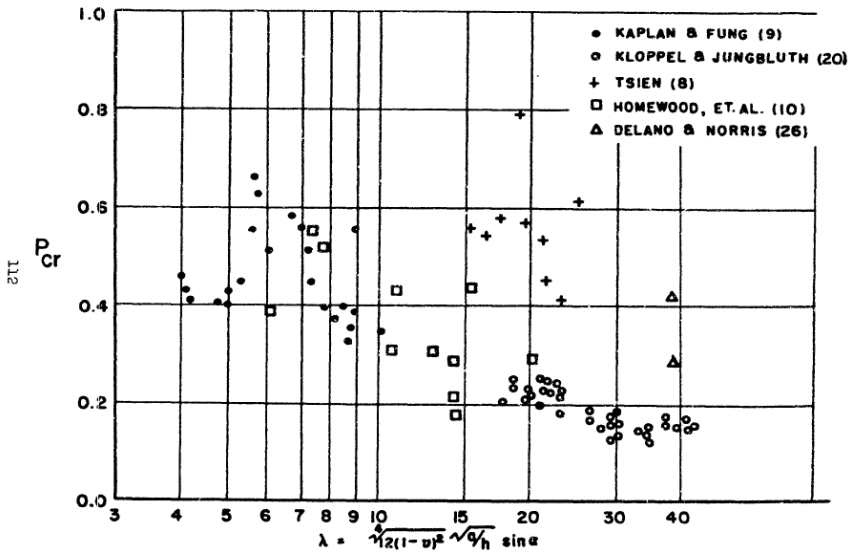

Fig. 16: Comparison of experimental buckling loads predicted by various authors, compiled in reference [99]

A relatively large scatter is noticed in Fig.16 of different studies compared by seaman [99] among others, which Seaman attributed to the differences in shell material, testing apparatus and procedures and boundary conditions of each study, while Bushnell [23] attributed them mainly to the imperfection sensitivity of shells. Bushnell presents a plot of the surveyed studies versus the shell parameter in Fig.17 from Kaplan [73], which includes most of the studies compared in [99], in addition to more data points from another study by Bellinfante [17].

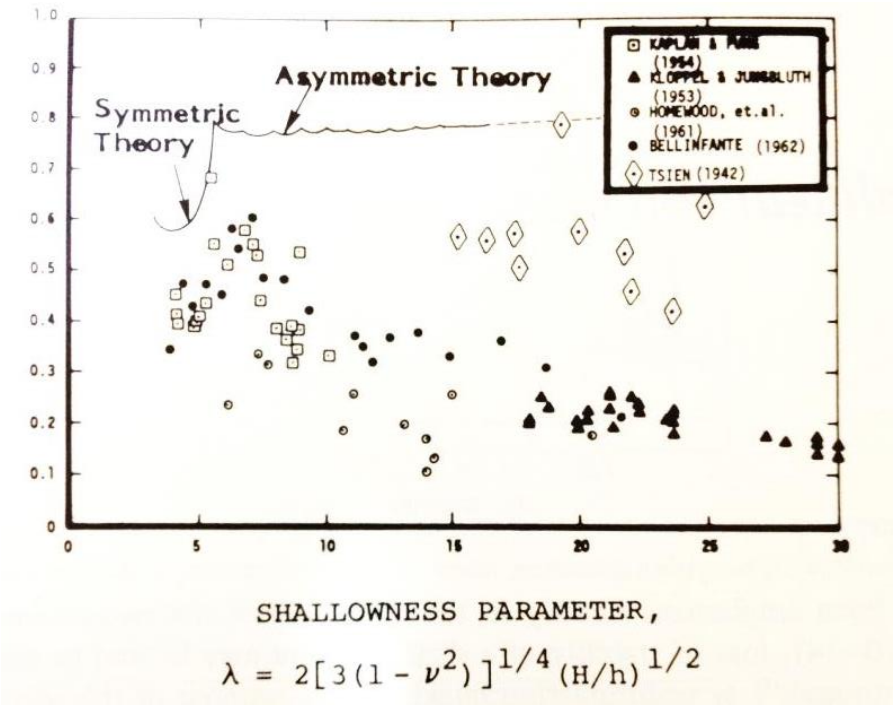

Fig. 17: Comparison of buckling loads predicted by various authors, compiled in reference [73]

For the purpose of this study, the spherical cap to be analyzed has a shallowness parameter slightly larger than 10 (equals 10.7). From the Fig. 16 [99] and Fig. 17 [73], the normalized external buckling pressure for structures with shallowness parameter between 10 and 15 appears to almost always fall between 10% and 40% of the classical buckling load.

Seaman's experimental work [99] was performed on plastic shells that buckled elastically and concluded that the buckling of spherical shells for a large range of the shell parameter λ between 3.5 and 25 occurred due to a geometric instability and not due to material yield or local effects for the elastic shell. However, the author also concluded that the minimum buckling load is related to the depth parameter (α) (which is half the central angle of the cap) rather than the shell parameter. The results of Seaman [99] (presented in Fig.18 [99]), provide the experimental buckling load versus the shell parameter which he calculated as (Eq. (8) [99])

$$\lambda = \sqrt[4]{12\,(1-\nu^2)}\sqrt{\frac{R}{h}}\sin\alpha \tag{8}$$

These results show similar values to previous investigations previewed in Fig. 17 [73]; however, with a narrower scatter which the author attributed to the unchanged conditions of the test proving the reproducibility of buckling loads. Seaman's experiments included both load controlled and displacement controlled tests.

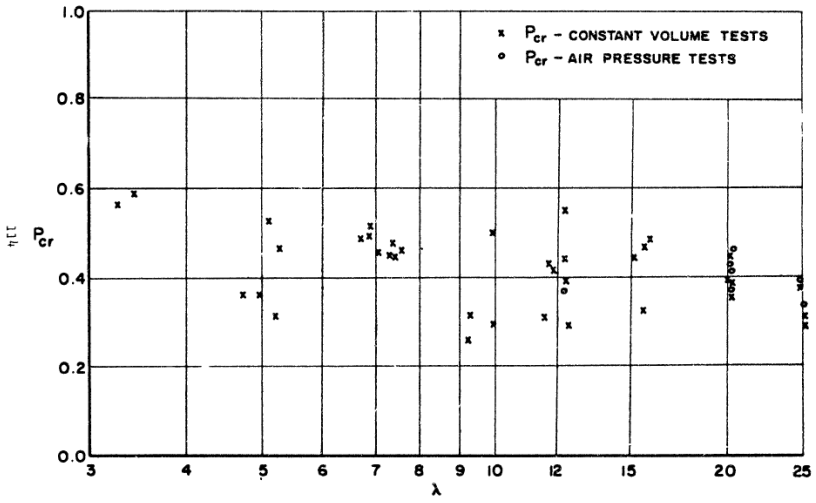

Fig. 18: Buckling loads predicted by Seaman [99]

Later, a study by Huang [64] numerically derived a solution for unsymmetric buckling of shallow spherical caps based on the initiation of unsymmetric deflections in the form of circumferential waves. Huang's model is reported to provide closer values to experimental results, with the difference attributed to geometric imperfections [32].

For design purposes, determination of the shell buckling loads is paramount because it mostly governs the thin shell capacity, while it is obvious that accounting for the initial imperfections and other effects in the design stage would be extremely difficult and unjustifiably expensive. According to the authors in [67], shell buckling investigations moved toward a trend that presents a "modification" to the linear theory. This approach works by calculating the buckling load using the classical linear elastic

equation of the perfect shell, then combining factors that account for the reduction in the buckling load resulting from imperfections and inelastic behavior [67]. The result is statistically derived design curves using a sufficiently large amount of experimental data, or conservative design recommendations involving empirical reduction factors (in case the problem lacks availability of sufficient test data to provide a statistical design load). Based on the latter approach, the author presents an empirical equation for the buckling of the spherical cap under external pressure problem (Eq. (9) [67]):

$$P_{cr} = \alpha \frac{E h^2}{R^2} \tag{9}$$

Where α is a coefficient calculated in Eq. (10.a) and (10. b) [67]

For $250 \leq \frac{R}{h} \leq 800$,

$$\alpha = \frac{1}{2.36} \sqrt[8]{(\frac{100h}{R})^3} \tag{10.a}$$

For $\frac{R}{h} \leq 250$,

$$\alpha = 0.3 \tag{10.b}$$

These coefficients are recommended for high-quality manufactured shells. However, if less accurate manufacturing conditions are inevitable and imperfections are expected to be in the order of its thickness, the coefficient is reduced even further by 1.5-2 times [67].

Gonçalves and Croll [49] suggested that Q^*_I, presented in Eq. (11) from [49] and calculated by the authors, be used as a capacity reduction factor in the design procedure

that takes into account boundary condition induced nonlinearity and geometric imperfections.

$$Q_I^* = \frac{7.34}{\lambda^2} \tag{11}$$

Wunderlich and Albertin [117] presented a draft proposal for calculating the critical load of spherical caps for application in the Euro code. The design curves are based on the author's study that included the effects of various boundary conditions, imperfection and material plasticity on the capacity of the spherical cap under uniform external pressure fabricated of steel or materials that exhibit similar behavior. Wunderlich proposed an elastic imperfection factor α, which represents a reduction factor for the capacity of the shell dependent on the imperfection amplitude determined by three quality classes that define the level of shell imperfections. The author also studied the interaction of the material plasticity with various boundary conditions and introduced a material reduction factor for the critical load limit [117].

In design codes, in general, the design of spherical caps follows the previously discussed trend of applying reduction factors to the classical theoretical value. These reduction factors are to account for the nonlinear behavior arising from boundary conditions, geometric imperfections and material nonlinearity. For concrete spherical caps, in particular, the paramount significance of the material properties highly supports following that approach, which allows designers to count for concrete plasticity, cracking, creep and other properties in an efficient manner using empirical relationships. Consequently, the development of these relationships is considered an integral part of the research on the capacity of concrete spherical caps and shall be reviewed in detail in a later section. The following subsections shall try to look at each field of the spherical cap stability analysis research individually to provide a general research background idea of each, before investigating them in the context of concrete spherical shells.

3.2.2.2. Imperfection sensitivity

According to the authors in [54], the assumptions made while establishing simplified 2-D nonlinear models of shells oversee deviations that are present in the shape of the shell mid-surface, which is used for building the 2-D idealization, or in the thickness of the shell. Small deviations in these parameters can have a great effect on the value of critical loads. Another implication of the presence of shape imperfections is that they change the distribution of strain along the normal to the mid-surface utilized for the 2D idealization. Hence, these irregularities may introduce complicated stress distributions that cannot be properly modeled with 2D approximation models. These stress distribution and their possible adjacent material plasticity effects [54] can, thus, result in significant discrepancies between the theoretical approximate model and the real shell structure in practice [54].

Various forms of geometric imperfections were studied in the literature. W. L. Chen [33] investigated the effect of symmetric shape imperfections on the critical load (grooves at mid-height of the shell), and the author's results suggested merely that a complex correlation exists between the geometric imperfections and buckling loads [99]. According to Seaman [99], the only conclusion about the effect of geometric imperfections on buckling loads by 1962 was that they are complex and difficult to accurately account for in both theoretical and experimental work [99]. Seaman attempted to categorize and quantify the present imperfections in thirty nine plastic shells that were buckled under unchanged conditions, but no clear relationship between the imperfections and the critical loads was established.

In 1963, Krenzke and Kiernan [81] performed tests on 200 spherical glass shells with different imperfections and derived Eq. (12) [81] for the buckling load based on their results:

$$p_{cr} = 0.84\, E \left(\frac{h}{R_i}\right)^2 \tag{12}$$

Where R_i is a modified radius that suggested that the buckling load depends on the local curvature and the thickness of what is defined as the geometric imperfection region or the critical arc length L_c as shown in Fig.19 from reference [67], where Lc is calculated from Eq. (13) [67]:

$$L_c = 2.42\ h\ (Ri/h)^{1/2} \tag{13}$$

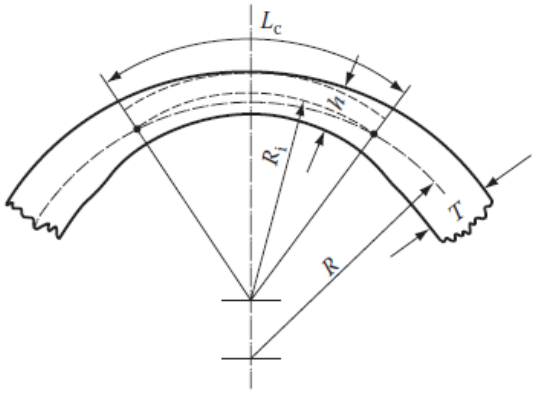

Fig. 19: Definition of the imperfection zone and critical arc length in reference [67]

In the more recent study in [87], a modification of Krenzke and Kiernan 1963's formula was proposed [81]. The authors noted that the formula may be limited to the authors' results since the imperfection sensitivity and required degree of reduction depends on t/R. They, thus, presented a modification of the equation in Eq. (14) [87]:

$$p_{cr} = 0.84\ E \left(\frac{t_{cr}}{R_{cr}}\right)^2 \tag{14}$$

Where R_{cr} is defined as the outer local radius in a critical arc of the local imperfection shown in Fig. 20 (taken from reference [87]), and t_{cr} is the mean thickness at the local imperfection arc.

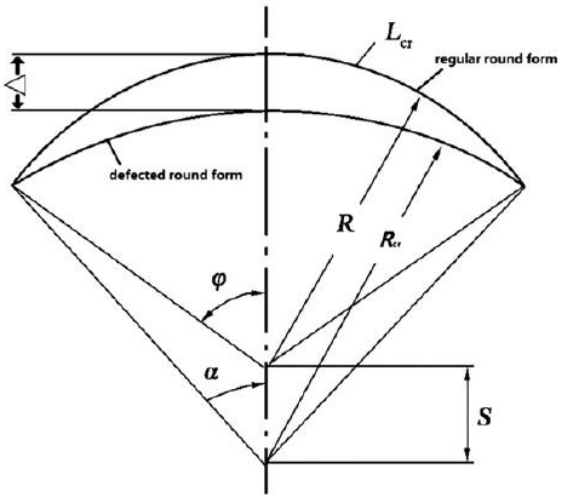

Fig. 20: A circular dent imperfection as defined in reference [87]

A similar approach for quantification of the geometric imperfections was provided by the ACI committee 334 report [4] where the geometric imperfections are reported to cause a change in the principal radii of curvature of the shell surface. If the radius of curvature is larger (the shell is flatter), then membrane forces are greater and the critical buckling load is lower.

Similarly, Zarghamee and Heger [119] stated that the buckling load is severely affected by imperfections characterized by a significant change of R/t over a large region. They claimed that buckling of a shell with imperfect regions is governed by the lowest buckling load of the imperfection region itself assumed to be clamped at the boundaries calculated from Eq. (15) and Eq. (16) [119].

$$P_{cr} = 0.7\ P_{cl} \tag{15}$$

$$P_{cl} = 1.1\ E_t/R_{imp} \tag{16}$$

Where R_{imp} is the local radius of curvature over the imperfection region (Based on krenzke and Kiernan [80], and E_t is the tangent modulus of elasticity

This imperfect region was approximated to have a diameter of $4.3\sqrt{(Rt)}$ by Bushnell [26], [27], and $2.5\sqrt{(Rt)}$ by Krenzke and Kiernan [80].

Dulácska [42] presented a general graph that differentiates between the limits of buckling loads for the imperfect shell with an imperfection of amplitude w_o (denoted as P_{cr}^{lin} and P_{cr}^{u}, respectively). Fig. 21 [42] shows the comparison of the load-deflection paths of both shells for a radially pressured spherical shell, while Fig. 22 [42] presents a quantitative description of that reduction with the increase of the normalized imperfection amplitude (w_o/t) for various shells and loadings. Dulácska presented an empirical equation for the calculation of the imperfection amplitude w_o for concrete shells, as shall be discussed in the relevant part of this section.

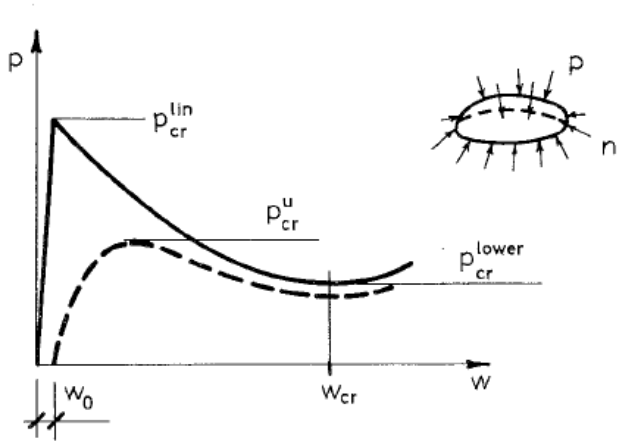

Fig. 21: Load-deflection path of elastic perfect and imperfect shells [42]

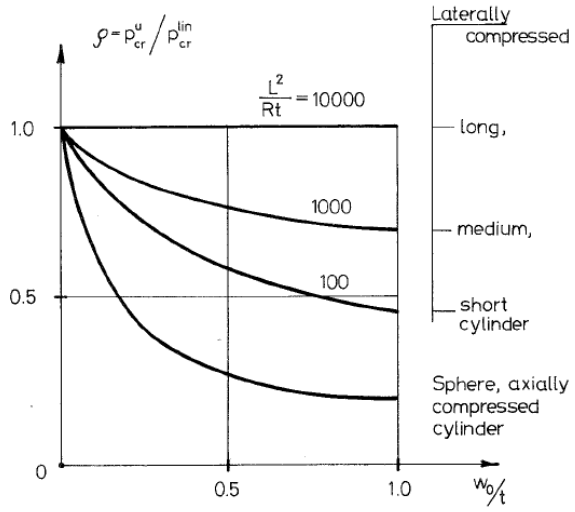

Fig. 22: Reduction of buckling load due to initial imperfections in various shells [42]

Instead of calculating the buckling load of an approximated imperfection region, Scordelis [98] used the actual buckled geometry of the shell and imposed it as an initial imperfection on the shell in an unstressed state. Hence, the deformed shape obtained in a previous analysis, i.e. the first buckling mode of the shell, was used in a separate analysis in an unstressed state to represent the imperfect shell. The results showed a reduction of about 50% in the ultimate load capacity.

While all the surveyed studies agreed that the discrepancies between the theoretical predictions and experimental results are chiefly influenced by geometric imperfections, some researchers believed that the major value of elaborate nonlinear modeling of imperfections is just to improve our understanding of the nature of the problem, and these should be later used to develop simpler methods for accounting for the shell imperfections for design purposes [49]. This is due to the fact that analytical studies of imperfection sensitivity of shell buckling loads, such as those in references [21], [102] and [105], are restricted to limited imperfections shapes and did not provide adequate explanation of the scatter in the experimental results [49].

Consequently, the approach of Gonçalves and Croll [49] was to adopt simpler approaches that provide bounds to the influence of geometric imperfections on buckling

loads of shells. The author explains that that approach is suggested to be of higher value for design purposes, since the shell imperfections are not pre-known in the design stage.

To accomplish so, the authors in [49] tested axisymmetric geometric imperfections in the form of the buckling modes. The effect of these imperfections on the buckling load of a shell of a geometric parameter of 10 (similar to that of the shell of this study) is shown in Fig. 23 [49]. The author noted that geometric imperfections in the form of the lowest buckling mode have the greatest effect on buckling pressure of the shell.

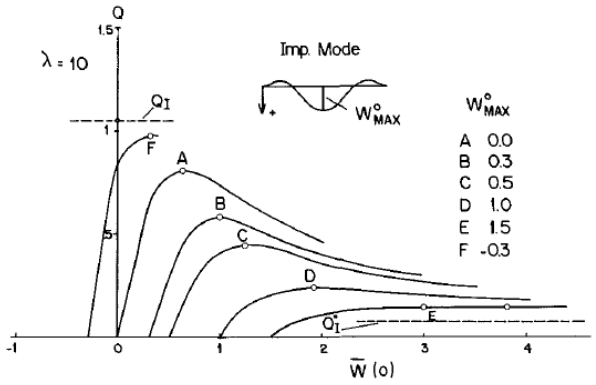

Fig. 23: Load-central deflection curve for an imperfect shell with λ = 10 [49]

Accordingly, a lower bound factor for the buckling of a spherical cap irrespective of the level of imperfection, and after numerically incorporating the effects of geometric imperfections in the form of buckling modes and linear vibration modes, was provided in the previously stated Eq. (11) [49] (restated here):

$$Q_I^* = \frac{7.34}{\lambda^2} \tag{11}$$

This value is shown to bound previous experimental work that was discussed above, as shown in Fig. 24 from [49] comparing data points of Kaplan [72], Thurston [104], Tillman [105] and Yamada [118] with the resulting values of Eq. (11) by the authors in [49].

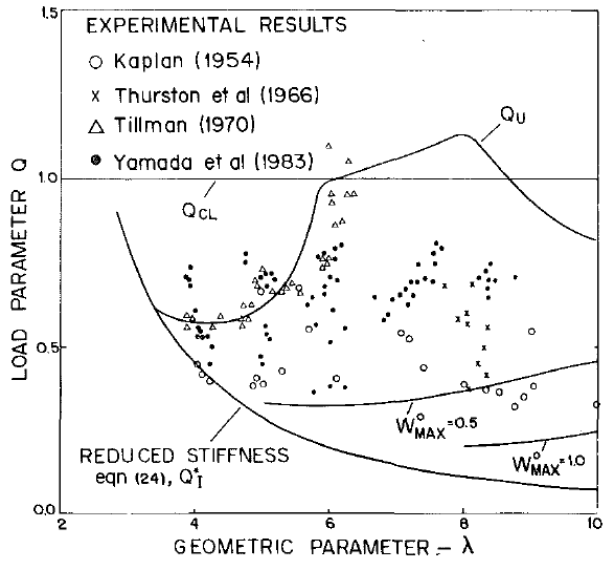

Fig. 24: Comparison of experimental buckling loads of various authors compiled by the author in [49]

Although the buckling loads are radically reduced using the approach in [49] with the increase of the geometric parameter (a buckling load of only 6% of the classical value for a spherical cap with a shell parameter approximately equal to 10), it is seen to be adopted by a few other researchers stating that it provides a way around the difficult-to-quantify geometric imperfections, resulting in a truly lower bound for the buckling of shells. Budiansky and Fitch [20] also stated the viability of studying the post-buckling behavior to predict the buckling of the same structure when it has an initial geometric imperfection. Grigolyuk and Lopanitsyn [51] discussed the presence of drastic changes in the limit points on the postbuckling equilibrium paths and the variations of load-deflection curves in general with small changes in a thickness parameter of the shell (h/R) studied in the range between 1/20 and 1/200. The study results suggest that these values may provide information about the critical loads of imperfect shells [51].

The work of Khakina and Zhou [76] supports the claim that studying the postbuckling behavior may eliminate the effects of geometric imperfections altogether. The author noted that while initial buckling is highly sensitive to imperfections, the post-buckling load is independent of initial imperfections, since curves for shells with

different imperfections tend to meet at the post-buckling load [76]. Thus, the author presented a modified buckling load that considers the rise-to-span ratio effect on reduction of the shell capacity based on an analytical study and a finite element simulation, where the post-buckling load is used as the limit load to ensure that the shell capacity is not overestimated. The derived buckling load is given in Eq. (17) [76].

$$q_{cr} = \frac{0.032\ EL^{1.86}}{H^{0.5}} \left(\frac{h}{R}\right)^{2.5} \tag{17}$$

Where L is the span, and H is the rise of the spherical cap

The calculated buckling loads in that study [76] for spherical caps with rise-to-span ratios between 1/8 and 1/40 ranged between 14-27% of the classical buckling load. However, the formula was not stated to be limited to that range and was used in the study for values rise-to-span ratios as large as ¼. For the shell of the present study with a H/L ratio of about 1/5.9, the formula results in a buckling load of 58% of the classical buckling load value, which is seen to be relatively high compared to most experimental results in the surveyed literature.

3.2.2.3. Boundary conditions

Although not many studies have focused on quantifying the effects of the shell boundary on its buckling load, the boundary conditions were stated in almost all of the shell stability analysis literature as one of the major factors affecting the shell capacity.

Some studies referred to the differences between the boundary conditions of the spherical cap analytical model (most of the time the shell is assumed to be clamped at the boundaries) and that of the real cap, which is probably a deformable ring. Idealized boundary conditions are used to calculate critical loads in mathematical models. Thus the inevitable differences between the real boundary and the idealized one, however small, may have a significant effect on the value of the critical loads [54]. This effect is

particularly significant in cases where buckling initiates near the edge due to a particular state of stresses at the region.

Bushnell [23] discusses the bifurcation buckling of externally pressurized spherical caps with edge rings, and shows that the buckling mode varies depending on the size of the ring. Bushnell concludes, based on a survey of earlier experiments and theoretical results calculated using different versions of the specialized computer program B0S0R5 developed by Bushnell, that for shells with shallowness parameters between 9 and 16 with all types of edge conditions (from free to clamped) edge buckling is the mode of buckling, which primarily occurs due to large circumferential compression near the edge where meridional bending is most significant [23]. The author also concludes that the buckling pressure is sensitive to the eccentricity of the edge ring, which, as Bushnell explains, is due to the effect of that eccentricity on the prebuckling circumferential compression near the edge [25].

Other studies looked at the issue differently, considering the clamped spherical shell to be an imperfect boundary condition compared to that of the whole sphere. Thus, the nonlinearity near the shell edge and the reduction in the shell capacity were attributed to the clamped boundary. Huang [64] concluded that the critical load of clamped shells is lower than those with boundaries free to displace radially, since the latter conforms to the behavior dictated by the membrane theory.

This observation is noted in Fig. 25 from [119] of the buckling loads of radially free, simply supported and clamped spherical shells, derived analytically for spherical caps. The figure shows a buckling load of the clamped shell is 80% of that of the shell free to displace radially.

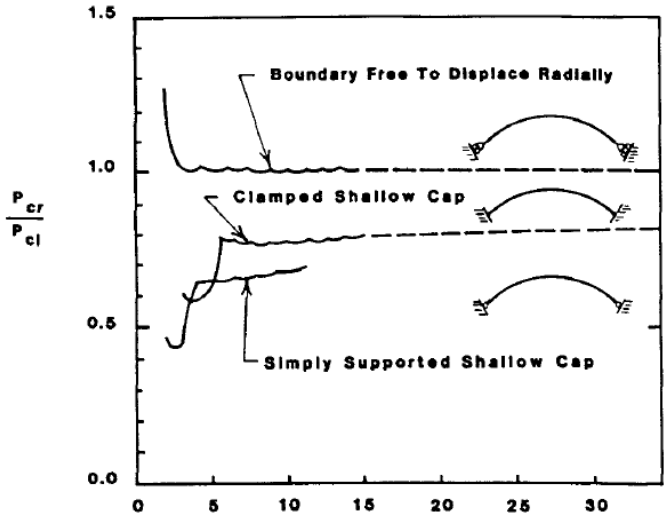

Fig. 25: Comparison of theoretical buckling loads of spherical shells with various boundary conditions [119]

That effect was labeled as a 'loading imperfection' by the authors in [49]. The reason is that the edge prevents the cap from having a state of uniform membrane compression like the complete spherical shell. Consequently, stress non-uniformity is produced in the vicinity of the boundary resulting in the nonlinear prebuckling behavior of spherical caps. Accordingly, the authors in [49] regarded the nonlinear models of clamped shells as imperfect forms of the classical bifurcation model.

The loading imperfection effect became clear when studied simultaneously with geometric imperfections of buckling mode shapes. The study in [49] found that in shells of various shell parameters where a negative geometric imperfection is almost equal to the inherent loading imperfection produced by the boundary, the shell closely follows the bifurcation model [49].

However, as mentioned above, very few studies primarily investigated the effect of the shell edge on the buckling, and almost none were found to accurately quantify that effect. However, it is considered to be accounted for in the shell design within the reduction factors applied to the linear idealized buckling load, as it will be discussed shortly.

3.2.2.4. Material Behavior

The behavior of the shell material is one of the main factors affecting the capacity of the shell. In a general discussion of the behavior of shell structures, it is observed that shells with elastic-plastic materials (and with relatively large thicknesses) exhibit a snap-through buckling mostly after the shell material has started yielding, while thinner elastic shells may exhibit bifurcation before yielding of the shell material [117]. The material inelastic behavior may also be introduced by the presence of shape imperfections, as previously discussed, or result from residual stresses of shell production methods themselves. Although, as stated in [54], the current technologies do minimize these effects, the accompanying strains cannot be entirely eliminated from shell production processes, and are difficult to accurately determine or account for.

As previously noted, earlier shell buckling experimental analyses were performed on thin elastic shells, which buckled elastically before reaching the material yield point. However, to account for the inelastic behavior that may result from the previously discussed effects, it was suggested to replace the elastic modulus of the shell material by the secant and tangent moduli of the material, along with another manufacturing reduction factor that was introduced to account for other residual stresses and workmanship [87]. This leads to Eq. (18) [87]:

$$p_{cr} = 0.84\, C_z \sqrt{E_s E_t} \left(\frac{t_{cr}}{R_{cr}}\right)^2 \tag{18}$$

It should be noted that the authors in [87] used the equation to calculate buckling pressures for titanium spheres under external pressure.

The case is almost entirely different with concrete shells where a highly inelastic behavior is an inherent property of the shell material characterized by the nonlinear stress-strain relationship, difference in behavior and capacity in compression and tension states of stress, cracking, shrinkage, creep strains and other time-dependent effects. Consequently, in order to realistically study the behavior of the shell material at hand, an

entire section was dedicated to studying the failure of concrete shells, and particularly spherical caps. As it will be discussed, the bulk of concrete shell stability studies attempts to incorporate the effects of concrete inelastic behavior when determining the shell capacity, and provide empirical methods to account for that behavior in the design of concrete shell structures.

3.2.3. Stability Behavior of Concrete Spherical Caps

The previous section presented a discussion of research efforts on quantitatively determining accurate predictions of the classical problem of spherical cap buckling. The surveyed studies discussed effects of the geometric nonlinear behavior, boundary conditions, and initial geometric imperfections. The effect of material nonlinearity was quickly touched upon, but was not discussed in detail. This is due to the fact that the concrete material has very distinctive behavior characterized by various nonlinearities that are different from most other materials. Consequently, the research studies on concrete shells have taken a different path of their own, as previously pointed out. This section attempts to review a few of the studies that consider issues concerned only with the behavior of the concrete shell.

3.2.3.1. Overview of the Stability Analysis of Concrete Shells

The research on concrete shells started with the trending of reinforced concrete construction as early as the 1940s and 1950s. The research aim was clear: to analytically simulate the behavior of the concrete material and, subsequently, provide reliable design guidelines for concrete shell construction, safe against buckling that was largely affected by the concrete nonlinearities. It should be noted, however, that this section may not represent the complete picture for concrete shell research. Rather, a quick survey of studies concerned with nonlinearities relevant to the present study.

The problem of the applying data derived from elastic analysis to non-elastic materials was pointed out by Griggs [50] since theoretical solutions of shell behavior were based on assumptions of elasticity, and, up until 1971, nearly all model tests were done on models of ideally elastic materials that possess a linear stress-strain relationship, which fail to predict the behavior of concrete shells. In 2010, Chang et al. [32] restated the same issue with concrete shell buckling analysis, citing that very few studies were performed using concrete, which has a nonlinear stress-strain relationships, cracking, and time-dependent creep deformations and shrinkage [32].

Griggs [50] investigated the effect of concrete plasticity, tension cracking and creep. The author's technique was to conduct the same experimental tests on shells of identical geometry but different materials; plastic and reinforced mortar, in order to

determine the differences in behavior from the elastic shells commonly used in experiments. Griggs's experimental work showed that single curvature barrel mortar shells buckled at 50% of the buckling load of corresponding rigid PVC and Plexiglas shells. A numerical simulation showed that failure of mortar shells was preceded by longitudinal cracks in the shell surface. These cracks largely reduced the transverse stiffness of the shell and caused the early failure, explaining the discrepancy between the elastic and the mortar shells [50].

A similar study was performed on spherical caps where mortar shells exhibited asymmetric buckling failure with an "explosive" reversal of curvature and complete disintegration in the buckled zone, while Plexiglas shells buckled elastically. When compared to the classical value, Plexiglas shells buckled at about 60% of the classical buckling load, while mortar shells at 37% [50].

Among the first attempts to remedy that discrepancy was the use of a modified modulus of elasticity, referred to as the tangent modulus, which represents the effective modulus of elasticity at the buckling membrane stress level. Griggs's usage of the tangent modulus resulted in improving the agreement of the results, where buckling of mortar shells was at about 49% of the classical value (5/6 of the buckling load of Plexiglas shells) [50]. The author concluded that in concrete shells cracking may initiate the buckling failure. Thus, if elastic models are used, the tensile strains should be monitored and failure assumed to occur if they exceed the tensile strength of concrete. The author also recommended the use of a tangent modulus at the buckling stress level to properly account for the concrete nonlinearity and give a lower bound on the buckling load.

Another experimental investigation of clamped reinforced mortar spherical caps in reference [82] with a shell parameter of 4.85 resulted in very similar predictions: the cap buckled at 40.2% of classical value using the initial modulus of elasticity, and 54.5% ($C = 0.638$) when using the tangent modulus at the buckling stress level, as presented in [32].

Another set of experiments was performed on unreinforced microconcrete shallow spherical caps by Vandepitte et al. in [109] following the research tradition of determining the buckling load of spherical caps in relation to the shell geometric

parameter, which allows for the comparison with previous experimental and analytical predictions. The buckling value provided in [109], however, seems to be generally higher than the analytical predictions of T. von Karman and H. S. Tsien [113], and Volmir [112]. The discrepancies of the results with the classical value were explained by the commonly discussed initial imperfections, boundary conditions and geometric nonlinearity, next to other factors specific to concrete only; these include the lack of material homogeneity and the possible inaccuracy of the value of Young's modulus [109]. The buckling pressure of the spherical cap was given in Eq. 19 [109]:

$$P_{cr} = CE\left(\frac{h}{R}\right)^2 \tag{19}$$

Where the mean value of C = 0.621 for spherical caps with prestressed rings (which represents 53% of pcr linear) and C = 0.539 for those with rings that aren't prestressed (which represents 46% of the pcr linear)

Isler [69] presented a report that discusses specific construction factors that affect the stability of concrete shells; namely quality of cast in-situ concrete, control of shell thickness, creep effects and cracks. Isler restated the variability of the quality of shell concrete due to workmanship, fabrication of formwork and other casting conditions of the mostly curved shell surface. The configuration of the shell mostly resulted in a lower quality concrete compared to slabs, for example [69], and a variable shell thickness which is hard to control in casting in-situ concrete. The author noted that the buckling load is very sensitive to changes in the thickness. These particular effects are relevant to the scope of this study since the proposed construction method shall significantly minimize problems associated with concrete quality and thickness uniformity as shall be discussed and verified experimentally later.

Isler stated that the increased deformations caused by cracking directly affect the shell stability, which he interpreted as a reduction in the elastic modulus to less than 50% [69]. It should be noted though that no theoretical derivations were presented in Isler's

report and it was directly based on his expertise on the subject. Isler also discussed a subject which was not clearly explained in other parts of the literature, and may have an effect on stability of concrete shells; namely the layering of reinforcement. Isler illustrated that using a double-layer of reinforcement reduces the bending deformations (the rotation angle is almost half of that when using one layer of reinforcement as shown in Fig. 26 [69], and these deformations are what may initiate instability [69].

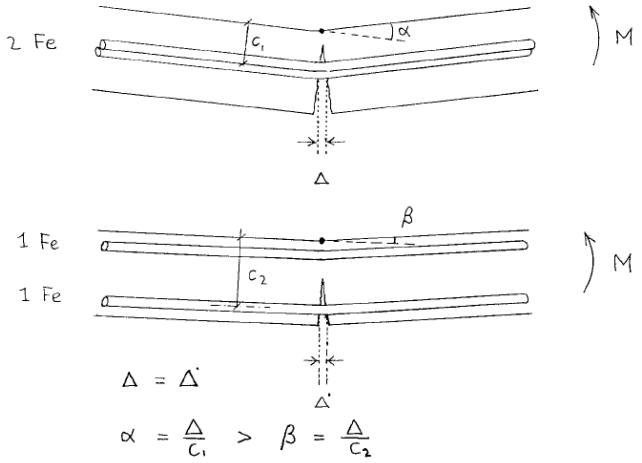

Fig. 26: Effect of using two reinforcement layers on bending deflections of the shell [69]

It is noted by Scordelis [98] that in 1950's and 1960's a lot of experimental work was conducted on buckling of spherical shells in order to improve the reliability of theoretical models. At that point, finite element (FE) analysis programs for thin shells were built on the assumption that shell is made of linear, homogenous and uncracked material [98]. In 1967, the first application of FE analysis to cracked reinforced concrete beams was conducted by Ngo and Scordelis. And then, according to Scordelis, the 1970's and 1980's witnessed development of computer programs for the nonlinear analysis of reinforced and prestressed concrete shells through studies conducted by many researchers, a list of whom is provided in Scordelis [98] and is summarized to study geometric nonlinearity, concrete material nonlinearity, cracking, creep, shrinkage and temperature effects, material constitutive models, failure theories and nonlinear numerical solution techniques, among other topics [98].

According to Scordelis [98], in 1973, a research program of reinforced concrete shell structures at the University of California, Berkeley was initiated, stemming from the demand for larger shell spans, smaller thicknesses and complex shell geometries. The research focus was to develop analytical models to include the geometric nonlinearity, the material nonlinear and time-dependent behavior and edge beam effects, and various computer programs were written and developed for that purpose; the final one NASHL1 (with contributions from the University of Barcelona, Roca) in 1988. Scordelis describes the analysis method and underlying assumptions and parameters of NASHL in [98].

A rather extensive research by Zarghamee and Heger [119] proposed a comprehensive design procedure for shallow concrete domes with R/t >= 500 and prestressed edge rings based on the available literature on dome stability and a computer analysis using BOSOR5 computer program for shell analysis developed by Bushnell. The design accounts for the effects of geometric imperfections (conceptually represented as spherical caps with different radii of curvature than the nominal radius of curvature of the shell), geometric nonlinearity, and material nonlinearity (plasticity, cracking and creep).

The authors' design procedure, based on earlier literature and proposed modifications for concrete shells, is based on the assumption that "the buckling of the shell is governed by the buckling strength of the imperfection least resistant to external pressure" [119]. That critical imperfection is defined as one with a significant change of radius of curvature (a difference of 40% at most) over a diameter of 2.5 $\sqrt{Rt}$ (of the buckle size order of magnitude) and may reduce the buckling capacity to 50% [119]. Thus, the design procedure includes a strength reduction factor for imperfections βimp = 0.5 if the previous imperfection geometry is satisfied, or $\beta imp = (R/Rimp)^2$ otherwise. That factor is combined with a capacity reduction factor $\phi = 0.7$, and a reduction factor for creep, plasticity and cracking βc. The critical load is thus reduced to Eq. (20) [119] :

$$P_0' = 0.66\ \phi\beta_{imp}\ \beta_c\ E\ \left(\frac{h}{R}\right)^2 \tag{20}$$

Where the factored design load (both live and dead loads) on the shell are less than P_0'

The details of the design procedure and calculation of the reduction factors are explained in [119]. The authors noted that although the analytical model did not include cracking, the effect of cracking was included by examining the prebuckling stresses and assuming the occurrence of failure when they exceed the concrete tensile strength. It should be noted that, according to the authors, the selected range of shallow thin domes (R/t >= 500) is based on the fact that for this radius-to-thickness range the shell tensile stresses and resulting cracks are not high enough to reduce the buckling load significantly as the dome approaches failure, i.e. the failure is initiated by buckling not material failure. This point is particularly of interest for this research because the structure in this research has a much higher R/t ratio than this limit (equal to 82.4), hence a material induced failure was predicted and the state of the stresses was monitored in both the numerical and experimental model. That relationship between buckling and concrete material plasticity was concluded by Zarghamee and Heger [119]. The authors state that the buckling nominal membrane stress is far below the concrete compressive strength, and that imperfections and creep increase the effective R/t ratio even further, thus causing more reduction in the buckling nominal stress. Consequently, concrete plasticity is not expected to reduce the buckling loads of thin spherical shells with R/t >500. At the same time, if R/t <500, material failure should be the concern and buckling is not expected to govern the design [119].

Dulácska [42] derived an equation for calculating the buckling load of reinforced concrete shells that includes geometric imperfections, quality of concrete and reinforcement ratio, concrete and steel plasticity, cracking and creep. Dulácska listed the material differences that arise when analyzing concrete shells from elastic ones and result in a lower critical load than that of the homogenous shell: plasticity of concrete and steel, creep of concrete under compression, cracking under tension, and reinforcement ratio, quality and position (especially after concrete cracks). Dulácska's derivation begins with the "upper critical load" that represents a reduction of the classical linear buckling load by a factor ρ that depends on the magnitude of initial imperfections (see reference [42]

for details). In general, the initial imperfections were divided into accidental imperfections w_o'' and bending imperfections calculated by the bending theory of shells using linear elastic analysis w_o'. Dulácska proposed Eq. (21) for calculating the accidental imperfections [42]:

$$w_o'' = 0.05h + \frac{a}{\frac{R/h}{1000} + \frac{1000}{R/h}} \left[\frac{R}{2000}\right] \tag{21}$$

Where **a** is a coefficient that accounts for the type of the erecting formwork (equal to 1 for rigid forms and 6 for slipforms)

The total value of the imperfections is then calculated in Eq. (22) [42] reflecting the low probability of the maximum values of both bending and accidental imperfections happening at the same location.

$$w_o = \sqrt{{w_o'}^2 + 1.4\, w_o' w_o'' + {w_o''}^2} \tag{22}$$

Dulácska [42] then included the influence of concrete creep through an empirical modification of the concrete modulus of elasticity in the buckling load equation, combined with a reduction factor for cracking effects β, and a third factor ζ that accounts for the effects of plastic deformation, which results in Eq. (23) [42]:

$$p_{cr} = \zeta\, \beta\, P_{cr,rc}(\phi) \tag{23}$$

Where $P_{cr,rc}(\phi)$ is the critical load of the homogenous elastic shell (including the effects of concrete creep)

The design procedure is then completed by inclusion of a unique safety factor also calculated by the author.

More recently, an experimental and theoretical investigation of the behavior of thin concrete spherical caps was reported at the University of South Wales, Australia [32]. The authors emphasized the necessity of studying the concrete spherical cap behavior and develop analytical models to account for geometric nonlinearity, initial imperfections and material nonlinearity due to creep and temperature effects. The authors referenced reports of modern concrete caps that collapsed during or after construction [86], [101].

Chang et al. [32] noted that all failure analyses of spherical caps under radial pressure are based on the occurrence of a snap-through buckling at the critical load while very little research has studied localized material failure that can occur during buckling of a concrete spherical cap due to nonlinear stress-strain relationships, and the combined bending and membrane stresses in the shell, and result in earlier failure than predicted by analytical models. Consequently, the authors developed an analytical model that extends a localized failure mode of concrete slabs to the local failures observed in concrete or mortar spherical caps in the literature; hence treating failure of concrete caps as a local phenomenon instead of a global elastic instability.

The authors used their analytical model to calculate the failure load of spherical caps reported in the literature in references [109], [82], and compared it with the reported specimen experimental failure loads, resulting in a very good correlation with the literature results with a mean ratio between experimental failure load and the model obtained load (pt/pu) equal to 1.0 for the caps in [109] (23 with non-prestressed ring and 11 with a prestressed ring) with coefficients of variance 12.0% and 9.1% respectively. A similar correlation was obtained with the mortar specimens of [82] (2 spherical caps) with a pt/pu ratio of 1.06 and a coefficient of variance of 3.0%.

In 2011, the same authors conducted an experimental analysis [31] of the failure of shallow concrete dome with a larger scale than usual (a thickness of 30 mm and a base diameter of 3000 mm), where the concrete spherical cap, loaded by water pressure, failed at about 31% of the classic critical load (corresponding to C = 0.368). The authors noted that the maximum stresses at the failure zone were well below the concrete strength; thus, failure indicated a local unsymmetric buckling affected by geometric nonlinearity,

material nonlinearity, imperfections and bending effects near the edge. the results of the experiment was compared to a study using a FE model on the computer program ABAQUS where only geometric nonlinear behavior was considered, but not the inelastic concrete behavior nor geometric imperfections. Using the initial modulus of elasticity of concrete, the model results were very far from the experimental results, while after using the secant modulus of elasticity at the peak stress of the stress-strain curve, the results were very close as shown in Fig. 27 from [31]. However, the author note that the only indication of this similarity is that the secant modulus of elasticity can be used to provide a simplified estimate of the critical load of thin shallow concrete spherical caps.

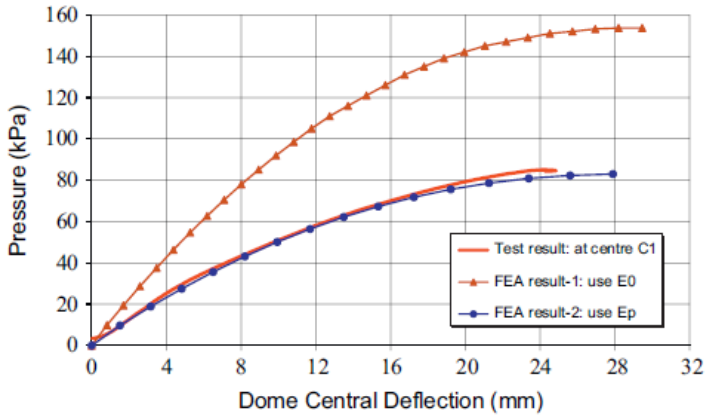

Fig. 27: Comparison of the load-central deflection of experimental and numerical results in [31]

3.2.3.2. Effects of Creep on the Long Term Behavior of Concrete Shells

The long-term capacity of concrete spherical caps under constant load is not included within the scope of this research. However, for the sake of completion, the effects of creep deformations and their effects on the capacity of concrete that were cited in the surveyed literature are included here. Consequently, it should be noted that the reported studies may not present the complete picture of the development of studying concrete creep, but rather serve to cite these effects when looking at the overall stability behavior of concrete shells.

The effects of material creep on shallow spherical concrete shells were stated throughout literature in references [119], [108], [56], [57], [58]. In concrete structures in

general, creep affects behavior at the serviceability limit states (increases deformations). In thin-walled shallow concrete domes characterized by buckling failure, creep deformations are critical for safety. This is because creep causes reduction in dome height accompanied by an increase in compressive stresses, which, as reported by Hamed et al. [56], can cause localized damage, or creep buckling (loss of stability slowly over time) or crushing failure of concrete before buckling occurs.

In order to account for creep, many earlier studies suggested using a modified modulus of elasticity that incorporates the reduction in the capacity of the shell. The ACI 334 committee report [4] approximated creep effects on shell buckling as follows: Besides using a reduced value of E (by determining the tangent modulus of elasticity), E is divided by a multiplier (not less than 2) for long term deflections.

Vandepitte et al. [109] replaced E in the buckling formula developed based on the study tests by a tangent modulus σ/ε_t, where σ is the constant shell stress calculated by the membrane theory, and ε_t, is the value of the total strain at failure. The authors' work concluded that that formula, combined with the modified formula developed in the same research, predicts a correct buckling pressure under a constant load applied for a long duration. Vandepitte and Lagae's experimental buckling tests of unreinforced microconcrete domes [108] showed significant reduction in buckling capacity under sustained loading (about 67% reduction in buckling load): While short-term loading resulted in a buckling load of 46% of classical buckling, the sustained load caused dome collapse under only 33% of its buckling pressure.

Isler [69] explained the effect of creep on stability as an increased flattening of a shallow shell until the curvature is zero, which was referred to in the beginning of this chapter as the "neutral equilibrium" state. Based on the elastic theory, if the load is maintained, the shell will snap-through. However, for a concrete shell, Isler stated that the load is then resisted only by the bending stiffness in the buckling area. Isler stated that shell buckling is, thus, very sensitive to creep effects, and that sensitivity is amplified by the presence of initial geometric imperfections.

Zarghamee and Heger [119] also stated that creep deformations cause continuous reduction of critical buckling load with time, and that the magnitude of creep strains is

dependent on concrete strength, volume-surface ratio (higher creep effects in thinner shells), duration of the load, age of the concrete at loading and average humidity during load application. The authors in [119] explained the imperfection-creep-cracking interaction mechanism as long-term creep deformations in the imperfect zone that constantly reduce the curvature and the critical buckling pressure. At the same time, these deformations increase the membrane and bending stresses thus resulting in tensile stresses near a region of a geometric imperfection, which may continue to grow and cause a loss of buckling resistance.

However, the proposed design procedure in [119] was based on results by the program BOSOR, which used the rate-of-creep method for analysis of creep effects. This method was reported in [58] to possibly lead to inaccurate results for concrete shells because it assumes that the rate of creep approaches zero as time increases, thus, it may underestimate the effect of concrete creep where stresses gradually increase with time [58].

As previously discussed, the influence of concrete creep was also included by Dulácska [42] through an empirical modification of the concrete modulus of elasticity in the buckling load equation. The modified modulus is presented in Eq. (24) [42].

$$E_c = \frac{E}{1 + \phi_c} \tag{24}$$

Where ϕ_c is the creep factor which depends on the thickness of the structure, concrete mix properties and environmental factors.

Dulácska [42] presented an approximation for the creep factor in "normal circumstances" in Eq. (25) [42]:

$$\phi_c = \frac{40}{10 + f_c'} \tag{25}$$

The problem with predicting creep effects lies in the fact that creep strains depend on the level of stresses, interaction with shrinkage and thermal strains, and aging of concrete [56], [57], [58]. The authors in [56] noted that there is very limited research on shrinkage and creep effects on concrete shell structures and shallow domes. The authors acknowledge the literature on creep buckling of shells of other materials than concrete using a "rate-of-creep" method which, as discussed, works well for non-aging materials with an almost linear creep behavior, but is not suitable when applied to concrete structures, particularly concrete domes where significant variations in internal stresses are caused by creep of concrete [56].

An analytical model was developed in [32] to study the effects of concrete creep and shrinkage on the geometric nonlinear behavior of concrete domes, without including material nonlinearity, cracking or geometric imperfections. A later study by the same authors [57] developed an analytical model which accounted for material nonlinearities, beside geometric nonlinearity, creep and shrinkage. An experimental study [57], [58] was conducted for validating the analytical model by the authors. The study included applying long-term constant pressures of 43.5% and 49% of the short term buckling pressure of the domes (derived experimentally from a short-term control specimen). The dome loaded with 43.5% of its instantaneous buckling load (reported in [58]) failed after 240 days indicating an even lower capacity with a failure pressure between 15% and 24% of the classical buckling load only. These results show the significant effects of creep on the capacity of the dome, and also show good agreement with the axisymmetric analytical model developed by the authors which predicted creep buckling after 260 days, as shown in Fig. 28 from reference [58], where the solid line represents the theoretical prediction while the dots represent the experimental deflections.

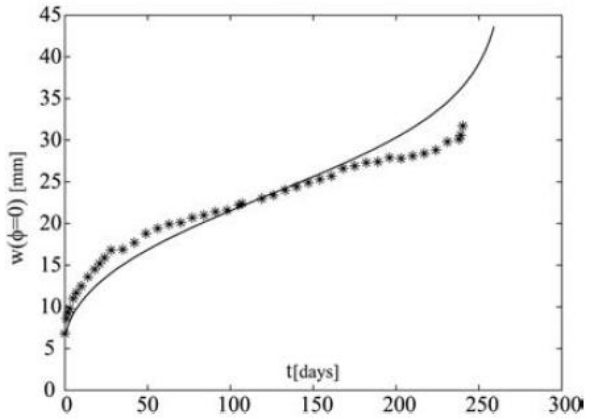

Fig. 28: Experimental and theoretical time variation of creep deflections at the center of the dome in [58]

The authors also noted that the peak measured deflection in the dome was higher than that of the short-term loaded specimen, indicating that, under moderate long term loading, the structure loses its stability with relatively large deflections caused by creep and geometric nonlinearity. The measured strains at the time of failure, well below the strain capacity, also indicate the failure was a loss of stability rather than a material failure.

3.2.3.3. Concrete Shell Design Guidelines

As discussed in the previous section, the design of spherical caps adopts the approach of introducing reduction factors to the classical linear buckling value. This is also the dominant approach for the design of concrete spherical caps, where empirical design formulas based on reduction factors are presented as proposals by research studies, recommendations by relevant organizations and groups, and guidelines by relevant design codes.

In the Design and Analysis of Shell Structures [44], Farshad states that thin concrete domes with large spans are highly susceptible to buckling failure that stability considerations are of the main design governing factors of concrete domes. Farshad presents an approximate formula claimed to be suitable for designing spherical concrete shells, since, as previously illustrated, experiments have revealed much lower buckling

loads than the theoretical values, which are attributed to their sensitivity to imperfections. Farshad stated that some building codes recommend reduction parameters for the theoretical value for the purposes of shell design that provide predictions between 0.05 and 0.1 of the classical value. Accordingly, the presented buckling pressure formula that is recommended for design purposes of the spherical concrete shell is given in Eq. (26) in [44]:

$$P_{cr} = 0.05\, E \left(\frac{h}{R}\right)^2 \tag{26}$$

Medwadowski [85] reports the Eq. (27) recommended by the ACI Committee 344 report [5] (*Design and Construction of Circular Prestressed Concrete Structures*) for the minimum thickness for spherical caps, taking into account the reduction in buckling load caused by geometric nonlinearity, creep effects, and imperfections.

$$h\,\min = R\, \frac{\sqrt{\gamma(g+p)}}{k\, E_c} \tag{27}$$

(with a minimum thickness of 76.2 mm for cast-in-situ concrete domes)

The safety factor γ is assumed to incorporate the effects of creep. ($\gamma = 4$ for storage areas, and higher for public areas). The factor k depends on the rise-to-span ratio and the radius-to-thickness ratio (taken equal to 0.25 for rise-to-span ratios between 1/10 and 1/6 and radius-to-thickness ratio less than 800). The equation was put in the standard buckling load formula in Eq. (28) by Medwadowski [85] using $\gamma = 4$ and k = 0.25 reproducing the same equation as Eq. (26) presented in [44].

$$P_{design} = 0.05\, E \left(\frac{h}{R}\right)^2 \tag{28}$$

This value is only 4% of the classical linear buckling value (including the safety factor).

Medwadowski [85] presented an overview of the guidelines of buckling design of concrete shells, particularly those presented by the International Association of Shell Structures (IASS) in 1979 [68] and subsequent modification proposals including those by the author. Medwadowski [85] provided an equation for the buckling load based on the procedure of IASS [68], Kollár modification proposal in 1993 [78] and other suggested modifications by the author [85]. The procedure starts with calculating the classical buckling load then applying a reduction factor as presented in Eq. (29) from [85]:

$$P_{des.} = \frac{\alpha_1 \alpha_2 \alpha_3 \alpha_4}{\gamma} P_{cr.} \tag{29}$$

This reduction is composed of:

- α_1: Imperfection sensitivity factor that is based on proposed modifications of earlier empirical equations referenced in Dulácska [42] and Kollár [78]
- α_2: Creep factor that is calculated based on a creep modulus of elasticity, in a similar manner to that of those presented in the previous subsection, to account for concrete creep effects.
- α_3: Cracking and reinforcement factor, which is equivalent to β in Dulácska's equation [42], with subsequent modifications the author referenced in Kollár [78]. These factor depends on calculating the ratio *n* representing the ratio between the elastic modulus of steel and creep modulus of concrete (modified elastic modulus), and the reinforcement ratio μ = As/Ac. The value of *n*μ is then used to get the value of the factor Ψ from Fig. 29 (taken from reference [42]). The factor Ψ is then used in combination with the calculated imperfection amplitude to calculate the cracking and reinforcement factor. Medwadowski [85] believed, however, that the most conservative case, when considering buckling, is to consider the shell uncracked and unreinforced; i.e. use a value of Ψ = 1 and a corresponding α_3 = 1. The author stated

that results using this factor correlated well with the earlier experimental test results of Vandepitte et al. [109].

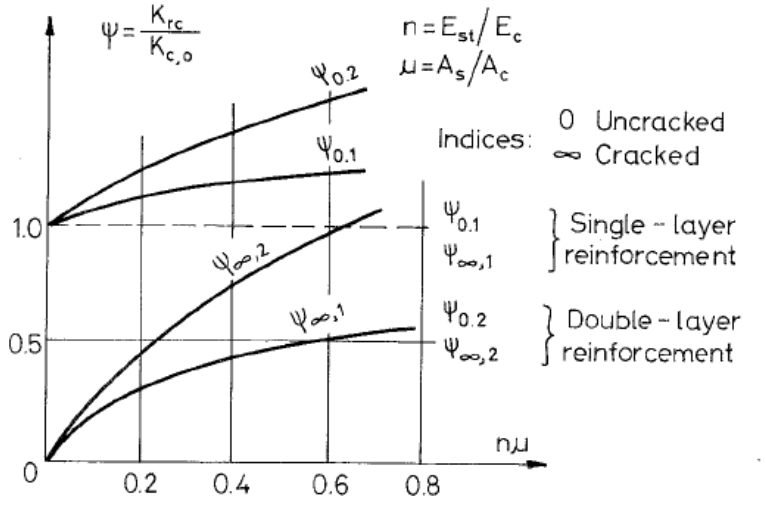

Fig. 29: Values of reinforcement reduction factor for different reinforcement conditions of the concrete shell [42]

- α_4: Inelasticity of concrete factor: the value of the material nonlinearity reduction factor is based on empirical developments by Dulácska and Kollár [79]. The final form is presented by Medwadowski [85] in Eq. (30):

$$\alpha_4 = \sqrt{\frac{1}{1 + \left(\frac{p_o}{p_{ult}}\right)^2}} \tag{30}$$

Where p_{ult} is the ultimate load of the shell and p_o is the buckling load calculated so far using factors α_1, α_2, and α_3. The paper provides empirical equations or recommended values for each of the factors, in order to calculate a reasonable value

of the buckling load of concrete shells that includes material nonlinearity, creep effects and sensitivity to imperfections.

- γ: a safety factor based on an empirical equation suggested by the author [85] in Eq. (31) and (32):

  for $\alpha_1 p_{cr} < 2\, p_{ult}$ (conservatively, the buckling mode of failure governs)

$$\gamma_{buckling} = 2.5 + \exp(-1.5\frac{w_o}{h}) \tag{31}$$

  While for $\alpha_1 p_{cr} > 2\, p_{ult}$ (the material failure governs, so the shell is insensitive to imperfections)

$$\gamma_{material} = 1.75 \tag{32}$$

  Where p_{ult} is the ultimate load of the shell based on material strength, and p_{cr} is the buckling load

3.2.3.4. Stability of Segmented Concrete Shells

There is very limited research on the stability of segmental shells, specifically shells made of precast concrete segments. The authors in reference [119], previously discussed, stated in their buckling analysis of monolithic concrete shells that buckling of precast domes is affected by panel arrangements and connections between precast elements. Heger [62] proposed a correction factor of the buckling load of monolithic concrete domes to be used for determining the buckling resistance of a precast dome. That correction factor was based on the dimensions of the panels and the thickness of the monolithic ring between panel rows in his design. Heger also discussed other relevant design considerations for segmental precast construction; for instance, camber of the precast panels to counteract deflections that arise during the construction process,

providing precast joints with tensile capacity to increase buckling resistance, and prestressing of the ring beam to minimize edge bending effects and cracking, although no thorough analysis was conducted for quantifying these effects.

Most of the cited precast concrete shells in the literature present specific projects that used scale models to predict the behavior of the precast structure [48], [74]. This is mainly due to the fact that there are many extra parameters that affect the behavior, such as the connections between the precast elements, the subsequent the load transfer concerns and the additional strains introduced to the system due to member deflections during each stage of the construction process. Consequently, for this type of segmental construction, the conventional shell analytical models may not be sufficient to predict the overall behavior of the structure, as reported by Kaplunovich and Meyer [74].

The same authors emphasized the need for viable analytical methods for the analysis and design of these segmental shells which take into consideration all the new variables added to the design equation. These methods should also be able to provide a comprehensive analysis at each stage of the construction.

The conclusion is that the capacity of segmental precast concrete shells is affected by the same factors of the monolithic concrete domes, with the addition of other factors that come into the equation with the geometry of the segmental shell. As previously discussed, the geometric nonlinearity, boundary conditions, material nonlinearity and time-dependent effects are critical factors that dictate the shell's buckling capacity. Geometric imperfections are also critical because of the inevitability of construction inaccuracies, the stated sensitivity of the shell buckling load to geometric imperfections, and the interaction of these imperfections with other effects such as creep.

The major element added to segmental shells is the presence of joints between the precast panels. In general, the behavior of joint is the most important consideration in precast concrete structures [43]. Precast joints must be designed to properly transfer forces between structural members, and provide stability, continuity and robustness. The additional forces that are generated in the joints of precast structures due to relative

displacement and rotation between the elements should be taken into consideration in the design of precast connections.

Precast structural joints can be compression, tension and/or moment joints, depending on the type of forces they transfer and the failure behavior of the structure. Although concrete shallow domes are mainly characterized by membrane compression forces, the presence of a bending field is inevitable, particularly near the shell edge. Consequently, the concrete dome precast joints should be designed as moment resisting joints.

In general, tension joints are characterized by lapping of projecting reinforcement bars or loops through a full anchorage length, and the addition of transverse bars in the joint to resist the transverse component of the diagonal strut formed between the projecting bars. Moment-resisting connections are designed to ensure a ductile failure, i.e. the limiting strength of the connection shall not be governed by shear friction between the precast elements. The moment-resisting connection can be created using different methods that include grouting of projected reinforcement, bolting of steel sections or plates, threaded bars and couplers, or welding to steel sections or plates, which is known to provide a minimized joint length and immediate structural stability [43]. Placing steel ties continuously across the connections over the entire structure is also sometimes considered in order to provide structural continuity and prevent progressive collapse.

Although a large number of research studies investigate the behavior of connections between concrete precast structural members in many different structures, almost none were found to deal with the presence of such connections in shell structures. Studies such as those by Vidjeapriya [111], Julander [70], Fleischman [45] ,[46], Zhang and Fleischman [120], Sullivan [100], Wells [115], Porter [91], Brackus [19] on different types of precast concrete structures provided a reference for incorporating the behavior and different parameters of the structural joints between precast concrete members into the numerical analysis using finite element models, and constructing these joints in experiment scale models. These studies, among others, were used as the basis for modeling the behavior of the connections between the concrete precast panels, bearing in

mind the differences in geometry and loading mechanisms. To avoid redundancy, these studies are, however, not discussed here in detail, since they do not particularly deal with concrete shell structures. Instead, they are referenced in the relevant sections of the methodology chapter of this study.

Based on surveyed literature, it's seen that the construction of concrete domes from precast elements can constitute a very competitive alternative that combines both the structural efficiency of the dome, and the prefabrication quality and fast construction advantages of the precast structures. It is also concluded that the application of a division pattern that produces the largest number of identical units provides the construction advantage of mold reusability and increase the overall design and construction competitiveness of the system.

A final conclusion is that very few studies attempted to investigate the structural behavior of segmental shells, as differentiated from those cast monolithically, although the need for such analysis was stated by many authors. It is seen that this scarcity is due to the unpopularity of precast shell construction, mainly attributed to the introduced factors to that are difficult to account for in the analysis, as discussed previously. Consequently, the literature on concrete spherical cap buckling is used as a reference for comparison with the results of this study. At the same time, the literature on modeling of concrete precast joints is used as a reference for modelling the extra effects introduced to the shell structure through the joints. The purpose is to assess the structural integrity of the proposed segmental dome system, compare its capacity to that of the corresponding monolithically cast system, and incorporate the parameters of that comparison within the larger context of design and construction efficiency, in order to construct a conclusion about the overall efficiency of the proposed structure.

4. METHODOLOGY

4.1. Geometric Design of the Dome Structure

4.1.1. Creating the Design

4.1.1.1. Selection of the polyhedral framework

Based on the literature on spherical subdivision, particularly the properties of spherical polygons and the different ways of using them to create uniform subdivisions presented in *Divided Spheres: Geodesics and the Orderly Subdivision of the Sphere* [90], the icosahedron was selected to be the optimum framework for creating a subdivision pattern for the dome, since it has the largest number of uniform faces of all other polygons, and will, hence, almost always provide a more uniform subdivision compared to other frameworks. Fig. 30 shows both a planar and a spherical version of the icosahedron that was used as the base for creating the subdivision, and is later cut to produce the desired spherical caps in this research. These models were created using the CAD software SOLIDWORKS [38], which was also used later to create a solid model of the dome and the panel molds, as will be discussed later.

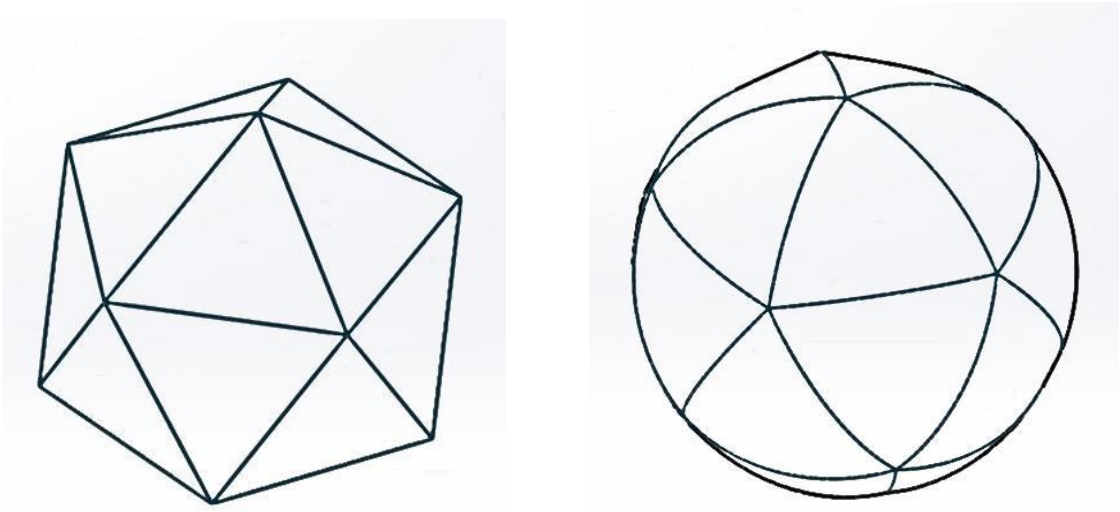

Fig. 30: A planar and a spherical icosahedron

The next step was determining the optimum subdivision scheme for the purpose of this research. The author in [90] presents three main subdivision "classes" and state that each class is more suited for particular applications, based on the characteristics of the patterns produced using each technique. In this research, the most important characteristic of the subdivision is the division uniformity, i.e. producing the least number of unique subdivisions on the sphere. For the dome analyzed in this research, this guarantees the most frequent use of the precasting molds, and thus, the most optimum prefabrication process.

Eventually, class II (triacon) subdivision (as referred to in [90]) was selected for the design for that specific reason; the advantage of having the least number of unique panel sizes. As discussed by the author in [90], there are many different size variations of class II subdivision technique, which are called 'division frequencies'. The division frequency is defined as the number of divisions on each edge of the base polyhedron (the icosahedron in this case) [90]. Different division frequencies produce different panel sizes and total number of panels. The resulting panels of the different division frequencies are presented and compared in a parametric study presented in the next chapter, while the selection of the most optimum for each different application shall be determined by the engineer based on the requirements of each specific project.

4.1.1.2. Cutting the spherical cap

The next step was the selection of the cutting plane for the sphere to create the desired spherical cap needed for the purpose of this analysis. The location of the cut (which determines the spherical cap central angle) was selected as the plane which will result in the least disruption of the spherical polygon's geometry, and mostly match the icosahedron edges and subdivision lines, consequently preserving the uniformity of the panels. The base panels of the dome were further adjusted, as shall be discussed shortly, to produce the plane spherical base required for the dome applications.

Two different spherical caps were cut out of the total subdivided sphere and are selected to be the spherical dome configurations used for the analysis. The two cuts produce two domes that differ significantly in depth. The first dome, shown in Fig. 31

before the division process, has a half central angle of about 63.435^0, which represents five faces of a spherical icosahedron.

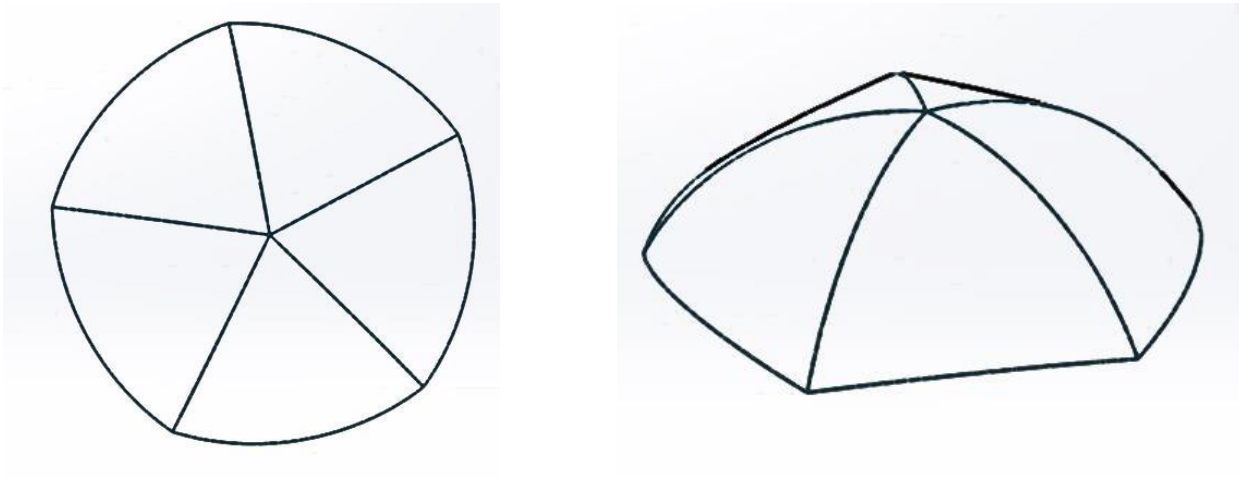

Fig. 31: Deep spherical cap

The second dome, shown in Fig. 32, is considerably shallower and has a half central angle of about 37.38^0. This cut, though, is not directly based on the icosahedron face edges, but rather on the spherical division lines. Both domes are later divided following the class II division procedure explained in reference [90].

The former dome (the deeper) is labeled as (DD), while the latter (the shallower) is referred to as (DS). It should be noted that the DS is analyzed thoroughly in the numerical analysis section of this research, and is also selected for the experimental analysis, while DD was investigated only in some preliminary numerical analyses.

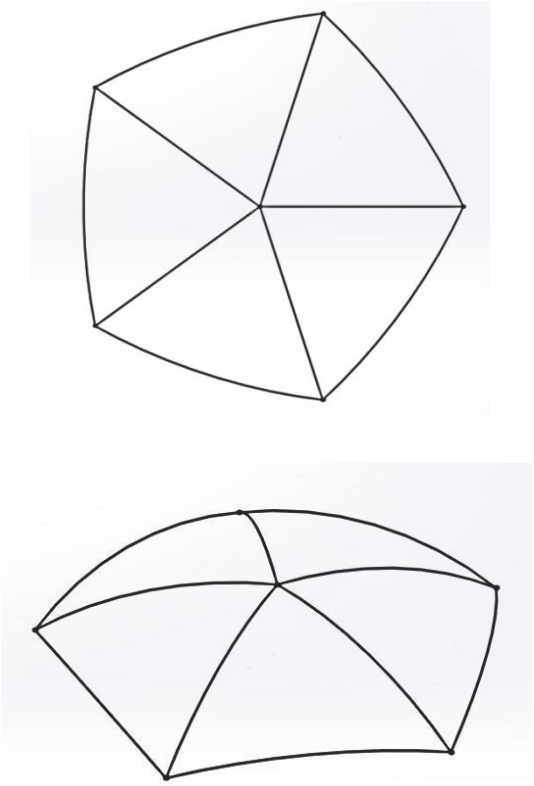

Fig. 32: Shallow spherical cap

It should also be noted that the dome shapes shown in the figures here are the preliminary shapes cut directly from the spherical icosahedron, before adjustment of the dome base for design purposes.

4.1.1.3. Dividing the dome

The next step was the division of the dome. As explained in the literature review, the division technique of [90] is based on selecting a working unit of the dome which can be subdivided then replicated to create the whole structure, thus creating the largest number of uniform divisions. Even though the domes have different depths, they're both based on a spherical icosahedron and shall both be divided using class II division, which is based on the diamond shaped working unit, as shown Fig. 33 (from reference [90]) which illustrates class II subdivision frequencies. '2v' frequency corresponds to division the diamond work unit into two identical spherical triangles. An important note here is that when each of the two identical triangles is re-divided, the resulting right triangle is known as the least common denominator (LCD) (a quarter of the diamond unit). The LCD is a right-angle triangle which has two mirror versions that recreate the entire surface of the sphere. Dividing the sphere into LCDs is technically not one of class II division frequencies; however, it is used in this research as one of the possible subdivision patterns, as it produces the most uniform division, in general. As the diamond is divided more, frequencies 4v, 8v, 16v and 32v result as shown in the figure.

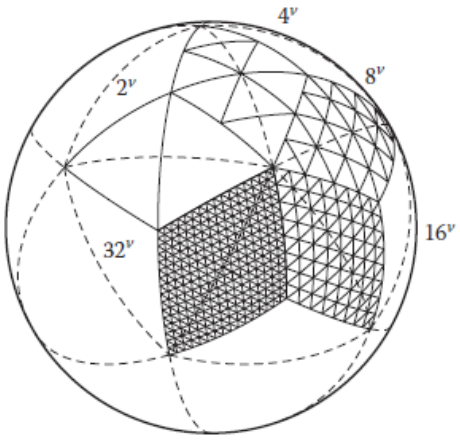

Fig. 33: Class II subdivision frequencies [90]

It is noted that the number of unique panels based on this subdivision class for all division frequencies is the least among all other classes. This is desirable quality in terms of precast concrete construction because the repetitive use of prefabrication molds results in a more efficient and cheaper construction process.

4.1.2. Geometric Design Optimization

As mentioned earlier in this chapter, two dome configurations were selected for analysis based on the foregoing division class (SD and DD). The work done in this part of the section presents a parametric study of both domes that attempts to clarify and compare the design parameters for each dome configuration, division frequency, and span.

The parameters considered in this study are the total number of panels for each division frequency, the number of unique panels, the average size of the panel, and the average panel weight for different shell thicknesses. The purpose is to present a visual representation that can be later further developed to help the designer select the configuration and division frequency most suitable for the specific design application and resources.

For that purpose, an algorithm was developed using MATLAB [84] to generate the relevant geometric data. Initially, the code can be used to generate the panel sizes corresponding to the user input for the desired configuration (shallow or deep), division frequency (LCD, 4v or 8v), and the span to be covered, as prompted at the start of the program. At this stage, the output of the program is the corresponding total number of panels needed for the construction of the dome, and the absolute sizes of all the unique panels for the input division frequency and span. It should be noted that the sizes are expressed in units of area; the thickness is assumed to vary according to the engineer's judgment and the design application.

The same MATLAB code was used to generate graphical relationships between the following parameters for both the DS and DD configurations:

- The total number of panels to be handled for each division frequency
- The number of unique panels resulting from each division frequency
- The average absolute panel size for each span (ranging between 10 and 50 meters) and each division frequency

- The absolute panel weights for each division frequency, constructed for spans between 10 and 50 m, and for a group of thicknesses ranging between span/70 to span/250

The purpose of constructing these graphs would be to help the designer at the preliminary design stage to compare different size options, and determine the appropriate panel size and weight for their particular design application. The resulting graphical relationships are presented in the geometric results section of the next chapter. The developed MATLAB code is presented in Appendix A.

4.1.3. Construction of the Dome Model

The next step was the selection of the specific dome parameters for the purpose of the numerical and experimental analysis of this research, and constructing a 3D CAD model for the dome. The initial selection of the dome parameters was based on the following factors:

- Moderately large span for dome applications, judging based on the reviewed dome structures in the literature
- Relatively large thickness that reduces the shell's susceptibility to premature buckling, also judged from the previewed structures. The selection criteria for the thickness of the dome are presented in detail in the section 3 of this chapter (Design and Construction Plan). For now, it should be noted the selected initial thickness is considered of a conservative value, compared to those found in the literature. A governing factor in selecting the thickness was the convenience of casting the scale model, as detailed later in section 4 of this chapter (Experimental Analysis of the Dome). A smaller thickness would have been very difficult to achieve with the available resources in a 1:10 geometric scale.
- The division frequency was selected based on convenience as well; an optimal division between requiring a least number of unique panel molds, and a reasonable panel size to be handled.

  The parameters of the selected dome for the numerical and experimental analysis are presented in table 1.

Table 1: Selected shell parameters for the analysis

Configuration	Shallow dome (DS) (half central angle = 37.38)
Span (m)	25
Division frequency	4v
Thickness (mm)	250

The CAD software SOLIDWORKS was used to construct 3D models of the dome panels. All panel models were created using only four points in the three coordinate axes space. These points define the vertices of all spherical triangles (panels) in a half-diamond work unit shown in Fig. 34 from reference [90], and the coordinates of which are also extracted from the appendices of [90].

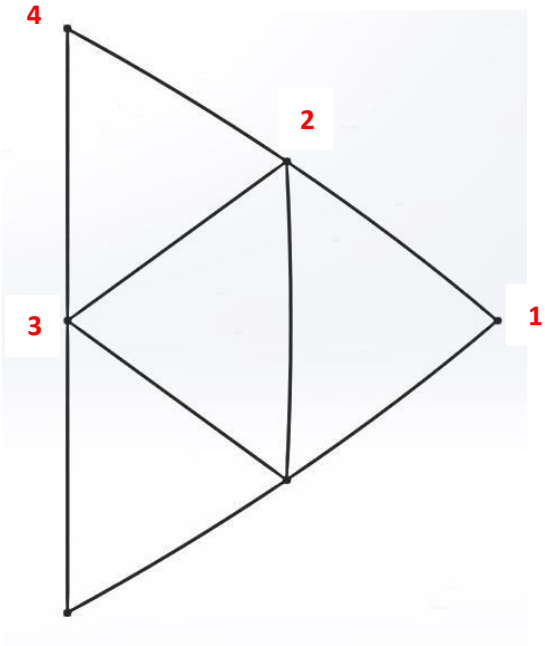

Fig. 34: Half-diamond work unit [90]

SOLIDWORKS features were used to create separate solid models of each panel with the required thickness (an example is shown in Fig. 35). These panels were then assembled in a SOLIDWORKS assembly file creating a full 3D model of the dome, shown in Fig. 36.

Thus, the dome model was constructed using repetitions of three different panels of two unique sizes only (two of the three panels are enantiomorphs (mirrors) of each other).

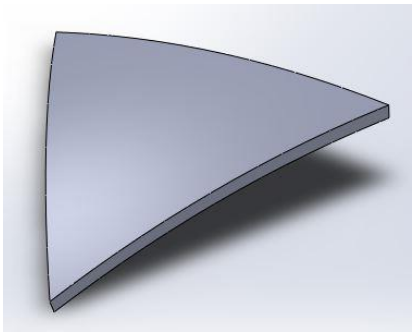

Fig. 35: A panel 3D model

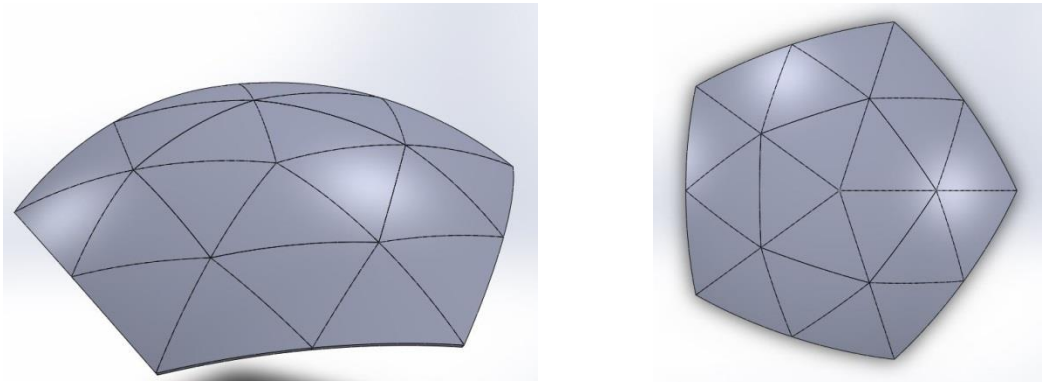

Fig. 36: Full shell 3D model generated using SOLIDWORKS

The next design step was the modification of the shape of the base panels to generate the circular horizontal plane required for the dome and boundary beam design. The base panels were directly extended to complete the spherical shape of the dome and fit the edge of the ring beam. Fig. 37 shows the base panel shape before and after the adjustment, and the final model of the adjusted dome is shown in Fig. 38

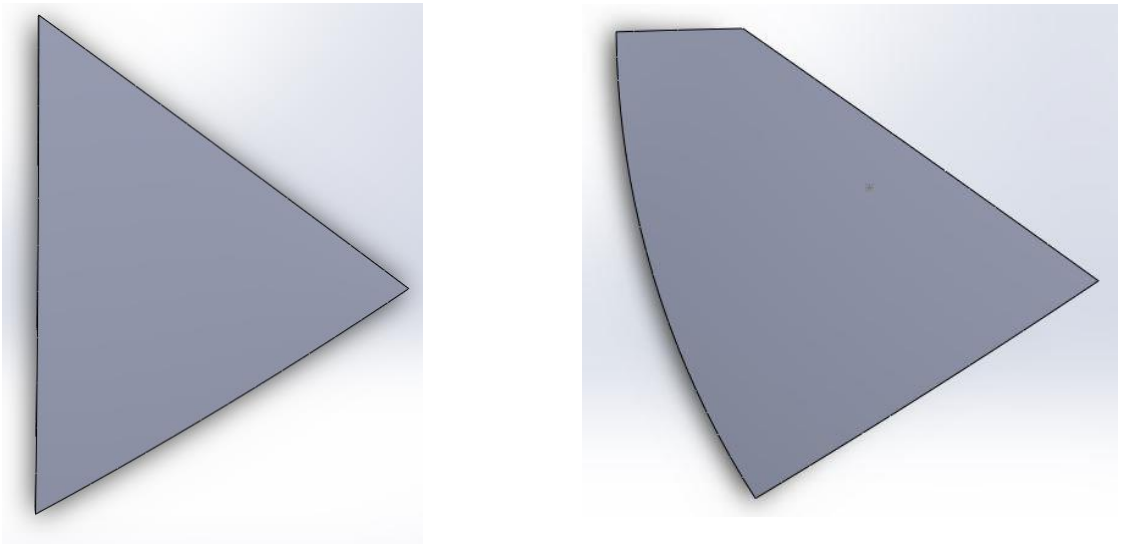

Fig. 37: Base panel before and after modification

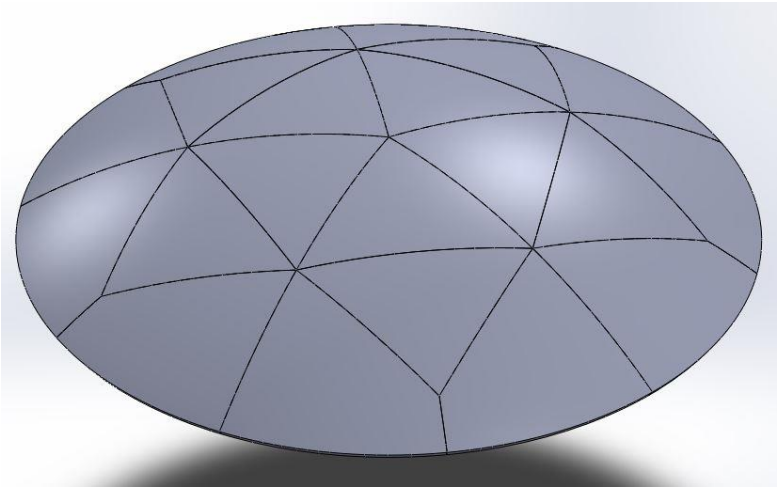

Fig. 38: Final model of the adjusted shell design

Another CAD model was created for the boundary beam, shown in Fig. 39. It is conventional for the boundary beam in dome construction to have a slanting edge that fits the edge of the dome (Fig. 40); in this research, the beam section was modified to both fit the panel edges and provide additional restraint for the panels, given that the panels and the beam are not to be cast monolithically (Fig. 41).

Fig. 39: Ring beam model

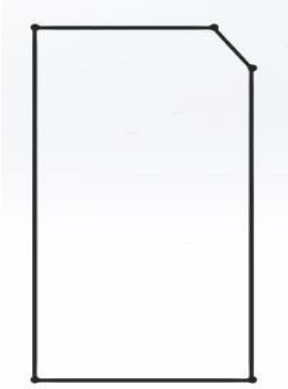

Fig. 41: Conventional dome ring beam

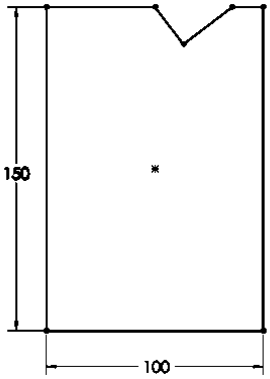

Fig. 40: Adjusted dome ring beam design

The final model of the dome and the ring beam assembled together is shown in Fig. 42:

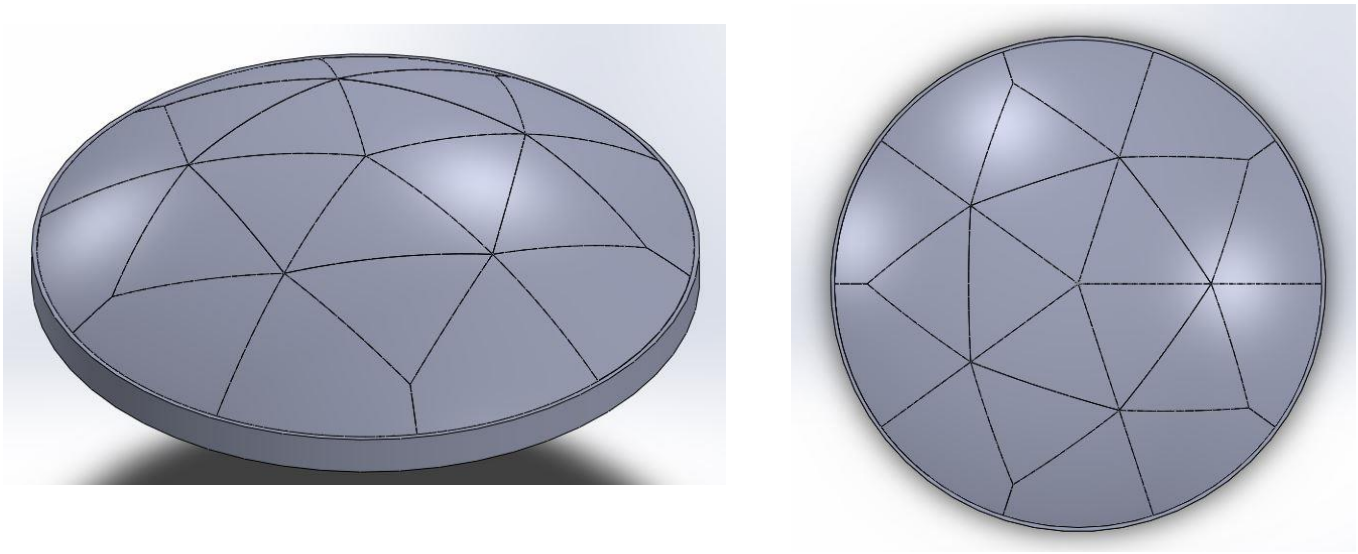

Fig. 42: Final model of the dome panel and ring beam assembly

The previous models were used for the following:

- Extraction of the volume and mass properties of the scale model of the dome, the ring beam and the panels for the purpose of the experimental analysis material surveying.
- The panel models were used for designing the fabrication molds used in the experimental analysis, as will be explained later in this chapter.

The next section of this chapter presents a detailed numerical analysis of the prototype dome of the parameters listed in this section, while the following sections present structural design and construction plans for the prototype, and the experimental analysis procedure and parameters of the scale model.

4.2. Numerical Analysis of the Structure

Several finite element models of the shallow dome configuration were built using the general purpose finite element software ANSYS [13], and utilizing different element types, material properties, loading conditions, boundary conditions, and connection properties. These models were loaded up to failure in order to determine the capacity and the failure behavior of the dome under the different conditions, and define the factors that most affect the structural behavior of the dome.

Most of the models in this study were initially loaded with uniform gravity loads, since it is the relevant loading conditions for the application of this structure. Other loading conditions were also investigated including the most commonly studied normal external pressure case, and a more critical concentrated crown load case.

The structural analysis was accomplished on different stages to take into account the effect of each geometric, material or connection parameter on the global behavior of the structure. The analysis started with determining the linear elastic buckling using the eigenvalue buckling analysis on ANSYS to obtain an idea of the buckling capacity of the proposed geometry, and verify the appropriateness of the modeling parameters. The second stage of the analysis was modeling the effects of geometric nonlinearities on the buckling capacity of the elastic spherical shell; which was the subject of many previous works in the reviewed literature. The third stage of the analysis aimed to include the effects of concrete nonlinearities on the failure behavior of the structure.

The following stage was modeling the effects of boundary conditions. Different boundary parameters were adopted in different models in an attempt to understand the effect of the boundary ring beam on the failure behavior of the structure. These parameters ranged from modeling a completely fixed boundary, to modeling of the ring beam as solid elements integrated into the FE model. A discussion of the effects of boundary modeling on convergence of the solution is included in this chapter.

The following stage was to understand behavior of the intermediate joints introduced to the structure through the proposed segmented design and construction procedure. Different parameters for modeling the behavior of concrete stitches between

the precast panels were used in the analysis, based on approaches or results of other similar studies of precast connections in the literature. These different parameters are discussed in this chapter, while the results are compared to each other and to those of the experimental analysis in the next chapter. This part of the analysis is particularly valuable as it presents an application of precast connection modeling techniques to modeling segmented concrete shell structures, and the reliability of the selected variables is then evaluated based on the results of the experimental analysis of a scale model of the connected precast concrete panels of the dome.

The failure of the dome was determined differently from one model to another. For linear elastic models, the failure (in this case the eigenvalue buckling) of the dome was determined by the program itself as a factor (multiplier) of the load applied to the structure. In the geometric nonlinear models using nonlinear shell elements, very large gravity loads were applied to the structure and the solution was run with the determined optimum number of load steps and equilibrium iterations until it convergence difficulties were faced and the solution terminated. At that point, a restart of the solution is issued while the nonlinear stabilization feature is activated in order to achieve convergence and verify the failure of the structure. The use of nonlinear stabilization is detailed shortly.

For the combined geometric nonlinear and material nonlinear analyses using solid elements, large gravity loads were applied to the structure, and failure was determined when the solution stopped converging with the minimum possible load increment application, the displacement showed a rapid increase under very small loads, and the strains/stresses were verified to reach material limits. A convergence sensitivity study was also conducted in order to determine the optimum meshing, load stepping and solution parameters, and attempt to verify that the termination represents a real structural failure and not a numerical instability.

4.2.1. Linear Elastic Buckling Analysis

The first stage of determining the stability limits of the structure was to conduct an eigenvalue buckling analysis using a FE model on ANSYS. At this stage, the models are built using shell element SHELL281. SHELL281 is suitable for modeling thin to moderately thick shell structures. The element has eight nodes with 6 DOFs at each node (UX, UY, UZ, ROTX, ROTY and ROTZ). The quadrilateral shaped version of the element was used in this analysis. SHELL281 is shown in Fig. 43 [10].

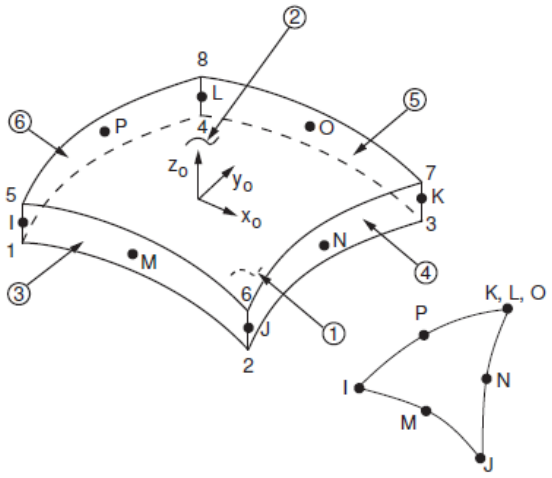

Fig. 43: SHELL281 element on ANSYS [10]

A shell section is defined as one layer of a 0.25 m thickness. The material properties were input as elastic isotropic properties of uncracked concrete with the modulus of elasticity = 22 GPa and Poisson's ratio = 0.2. The density is used as 2500 kg/m3 to represent the density of reinforced concrete. Different boundary conditions were applied:

- The 6 DOFs restrained along the whole perimeter
- Translational DOFs (UX, UY, UZ) restrained along the whole perimeter
- A bounding ring beam was modeled using BEAM189 line element along the perimeter. The beam has the same material properties as the dome and is hinged at 8 locations symmetrically around the perimeter. The beam section is input as 0.75 m width

and 1.5 m depth. Fig. 44 shows the elements for this model with the ESHAPE command which displays the model section dimensions.

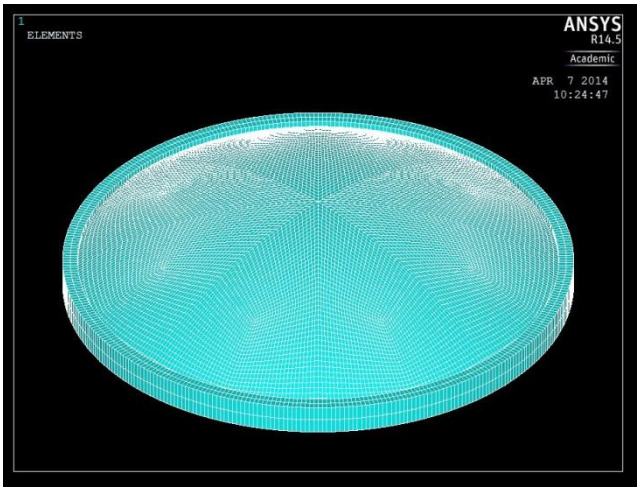

Fig. 44: Shell FE model using SHELL281 and BEAM189 elements

At this stage of the analysis, the structure was loaded in two different ways:

- Unit pressure load normal to the surface of the shell element. This loading condition, together with a completely fixed boundary, shall produce a very close buckling load to that predicted by the linear elastic stability theory for a complete spherical shell.
- Vertical gravity load (gravitational acceleration = 9.81 m/s2). The buckling load in this case is a multiple of the structure's weight. For the present structure, this loading condition represents the serviceability loads (dead and live loads).

The followed solution procedure is ANSYS eigenvalue buckling which starts with a small displacement solution followed by an eigenvalue analysis and an expansion of the buckling mode. As previously mentioned, the failure of the structure was determined by the software as a factor/multiple of the applied loads. As discussed in the literature review, the linear elastic analysis procedure is generally suitable as a starting point for understanding the behavior pattern and order of magnitude of elastic buckling loads.

Both dome configurations (previously referred to as the shallow dome configuration (SD) and the deep dome configuration (DD)) were modeled and loaded at this stage. Starting from the next stage, only the shallow dome, which was selected for the experimental analysis, is modeled and analyzed for failure.

4.2.2. Geometric Nonlinear Elastic Analysis

The large displacement analysis was conducted using SHELL281 nonlinear layered shell. The shell section and linear isotropic material properties were defined as the previous analysis stage. Only the shallow dome SD was modeled at this stage with and without a boundary ring beam using BEAM189 nonlinear line element.

The applied loads were large vertical gravity or normal pressure loads whose value was taken nearly the same value as the linear elastic buckling load. Due to geometric nonlinearity, the structure was expected to lose its stability before reaching the applied loads.

ANSYS large displacement analysis procedure was used. The default nonlinear solution method in ANSYS is the Newton-Raphson method in which the load is applied incrementally in a number of substeps. In each substep, the difference between the applied loads and restoring forces (out-of-balance load vector) is determined to check for convergence. If convergence is not achieved, the process is repeated iteratively and a new solution are obtained until convergence is achieved based on the specified convergence criteria [12]. Other convergence enhancement techniques were used as well, such as bisection (activated by default), line search and automatic time stepping. Automatic time-stepping allows the user to input an initial number of load substeps, and minimum and a maximum number of substeps that designate the maximum and minimum step size. The program starts applying load increments of the initial size, and then increases the step size until it reaches the maximum allowable size. However, if convergence difficulties were faced, the program will start bisecting the step size and iterating the solution until it convergence or the minimum allowable step size is reached.

The Newton-Raphson method alone, however, faces convergence difficulties in nonlinear buckling analyses in which the structural collapses or snaps-though as the tangent stiffness matrix becomes singular. In such cases, ANSYS recommends either the use of nonlinear stabilization together with the Newton-Raphson method, or the other alternative method to Newton-Raphson; the arc-length method. Nonlinear stabilization was used in this analysis as shall be discussed shortly.

Throughout the analysis, the number of substeps (or the time increment size) has varied greatly from one model to another depending on the material properties, the value of the applied load, the boundary conditions and other modelling parameters.

The number of equilibrium iterations was also variable between different runs. The initial number of iterations was input as the program's default (15 equilibrium iterations per substep). In case the substep did not converge, the number of equilibrium iterations (together with the number of subtsteps) was increased and the solution restarted. During the analysis, increasing the number of equilibrium iterations over 200 was seen to cease to enhance convergence.

Failure of the structure at this stage of analysis was initially identified as the load increment at which the solution did not converge after reaching the minimum allowed step size. This failure was verified by using the nonlinear stabilization feature in ANSYS.

Numerical stabilization is used to overcome convergence difficulties in unstable problems where small load increments result in large displacements. It is defined in the ANSYS structural analysis guide as "an artificial damper" that applies an artificial damping force to each node of the element which reduces the displacement at the node so numerical stabilization is achieved [12]. A 'damping factor' is used to calculate the stabilization force based on a user specified energy dissipation ratio or a directly input damping factor. ANSYS specifies the energy dissipation ratio to be between 0 and 1, with the larger energy dissipation ratio resulting in a larger stabilization force and, in turn, a stiffer response of the structure. In this research, different values of energy dissipation ratios were tried in order to determine the smallest possible value to achieve convergence while, at the same time, not result in excessive stiffness. An energy dissipation value of 0.01 was determined to be the smallest value which achieved convergence of the solution. Although this value is relatively large, ANSYS structural analysis guide recommends using the larger values for global instabilities (as opposed to local instabilities) and for shell elements (as opposed to solid elements).

Although nonlinear stabilization has achieved convergence of the solution and helped verify the point at which the structure loses its stability as discussed in the results, this method is unable to correctly track negative stiffness (the negative slope portion of

the load deflection curve), which would have been an issue had the post-buckling behavior of the elastic shell been significant in this research. However, since the analysis is only concerned with the failure point of the structure, the nonlinear stabilization provided satisfying results.

The Newton-Raphson method (together with nonlinear stabilization where needed) has proven to be the most efficient throughout the entire analysis process. The other alternative, the arc-length method, was initially used a few times in some of the models in order to determine the most suitable method. The arc-length method has the advantage that it can circumvent global instability and track unloading (i.e. zero or negative load-deflection slope), and consequently, it is used to explore postbuckling behavior of structures. However, the arc-length method is not compatible with automatic time-stepping or line search. Instead, in order to accurately track the limit load, the reference arc-length radius and its minimum and maximum multipliers may have to be readjusted a few times. Consequently, the trial and error effort exerted in deciding the number of the load substeps (which determines the arc-length radius) and the arc-length range (minimum and maximum multipliers) with no significant improvement in the results has made it the less preferable option in this analysis. In such cases where the failure point is of significance, ANSYS suggests that the standard Newton-Raphson method with bisection may be more convenient to determine buckling load values [8].

4.2.3. Modeling of Concrete Nonlinear Behavior

The next step of the analysis was to include the effects of the concrete material behavior on the capacity and failure mode of the structure. Initially, the type of element used at this stage of the analysis is SOLID65 element for both the dome and the beam. SOLID65 is a solid element in the ANSYS library for 3D modeling of structures. The element is capable of cracking in tension and crushing in compression. It is also capable of plastic deformation and creep. Thus, it is able to model the behavior of the concrete material marked by a much lower strength in tension than compression. The element includes a rebar capability that is able to model the behavior of concrete reinforcement, which can be defined in three different orientations, is capable of tension and compression and is defined in this study to be smeared throughout the element. SOLID65 element has eight nodes with three DOFs at each node (UX, UY and UZ). SOLID65 element is shown in Fig. 45 [10].

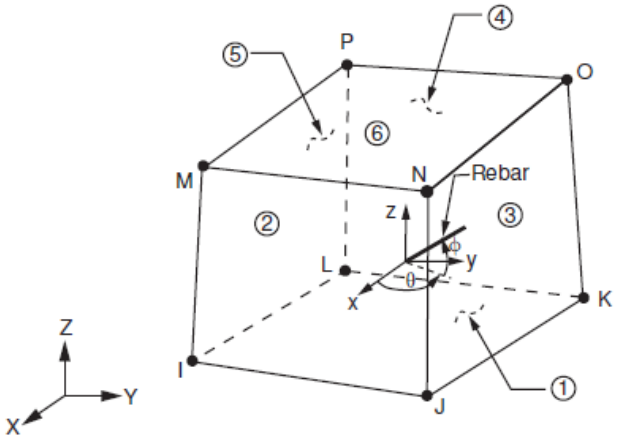

Fig. 45: SOLID65 element in ANSYS [10]

Using the rebar capability of SOLID65 assumes a perfect bond between the concrete and steel reinforcement. The real constant set for SOLID65 includes the volume ratio of the reinforcement which is defined as the rebar volume over the total volume of the element. In this analysis, the volume ratio of the reinforcement was used as 0.005 in the two directions of the shell.

The material properties of the SOLID65 elements are input as linear isotropic properties, concrete material properties and multilinear isotropic von-Mises rate-independent plasticity. The isotropic properties are input as the previous section with elastic modulus of 22 GPa and poisson's ratio of 0.2. for the concrete material properties, the failure surface is defined due to a multi-axial stress state based on five input strength parameters; the ultimate uniaxial tensile strength (f_t), the ultimate uniaxial compressive strength (f_c), the ultimate biaxial compressive strength (f_{cb}), the ultimate compressive strength for a state of biaxial compression superimposed on hydrostatic stress state (f_1), and the ultimate compressive strength for a state of uniaxial compression superimposed on hydrostatic stress state (f_2) [9]. However, ANSYS theory reference [8] states that the failure surface can be specified by two parameters only (the ultimate tensile and compressive uniaxial strength) while the other three parameters default to those determined by Willam and Warnke's constitutive model for the triaxial behavior of concrete [116] in Eq. (33), (34) and (35):

$$f_{cb} = 1.2\, f_c \tag{33}$$

$$f_1 = 1.45\, f_c \tag{34}$$

$$f_2 = 1.725\, f_c \tag{35}$$

In this research, the tensile strength of concrete was input as 10% of its compressive strength (equal to 2.5 MPa). The crushing capability, however, was disabled in most of the models. In the initial stages of the analysis, a few solutions were run with the concrete crushing enabled and a crushed stiffness factor of 0.001. At the beginning of the solution, ANSYS displayed a message clearly stating that using concrete crushing in a large displacement analysis may result in erroneous results, and the solution was found to terminate earlier than solutions where crushing was turned off. Crushing was suggested in most of the relevant literature ([71], [16], [70], [93]) to cause convergence difficulties and premature failure of the model. By disabling crushing, the concrete cracks whenever

a principle stress component exceeds the tensile strength, while the remaining parameters are suppressed [8].

Other parameters for the concrete material are the open and closed shear transfer coefficients which represent the conditions are the crack face and ranges between 0 and 1 with 0 representing a smooth crack and a complete loss of shear transfer while 1 represents a rough crack where no loss of shear transfer has occurred [8]. It was stated in some of the reviewed literature [71], [70] that convergence problems were encountered during the solution when the shear transfer coefficient value was less than 0.2. In this research, the values used are 0.2 and 0.7 for the open and closed cracks shear transfer, respectively.

KEYOPT(7) for SOLID65 was set to 1, which includes tensile stress relaxation after cracking and is recommended by ANSYS and most of the relevant references [70], [93], [100] in order to achieve convergence. A tensile stress relaxation factor of 0.6 (ANSYS default value) was used in the analysis.

According to the concrete material model, the concrete behavior is assumed to be linear up to cracking/crushing. Thus, the concrete material properties were combined with plasticity models in order to model concrete plastic deformation. In most of the reviewed literature, the plasticity models used in combination with concrete are the multilinear kinematic hardening, multilinear isotropic hardening, and Drucker-Prager plasticity. In this research, the mulilinear isotropic hardening plasticity model was used.

The typical concrete stress-strain curve (shown in Fig. 46 from reference [15]) is linear up to about 30% of the maximum compressive strength, followed by a nonlinear portion up to the peak compressive strength where the curve starts to descend into the softening region, and finally crushing occurs at the ultimate strain. In tension, the stress-strain curve is approximately linear up to the maximum tensile strength point, after which the concrete cracks and the strength degrades gradually to zero [15].

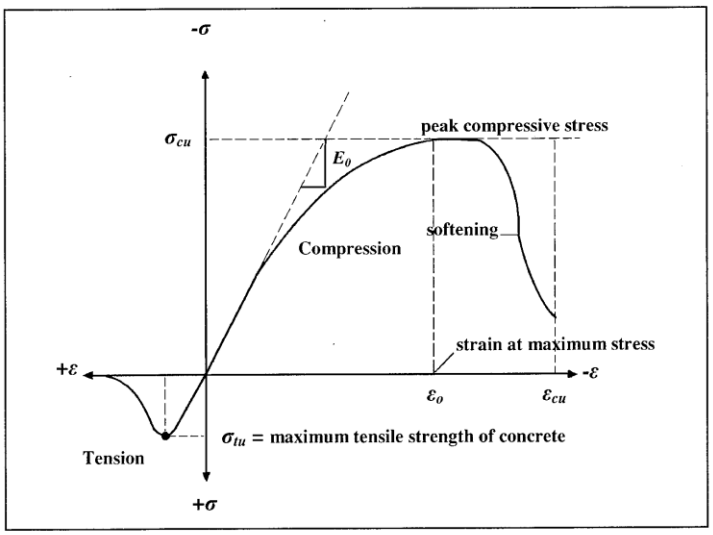

Fig. 46: Typical concrete stress-strain curve [15]

The concrete compressive stress-strain curve is approximated in the analysis by Eq. (36) and (37) referenced in [40] and Eq. (38) referenced in [47]:

$$f = \frac{\mathrm{Ec}\,\mathrm{\varepsilon}}{1 + \left(\frac{\mathrm{\varepsilon}}{\mathrm{\varepsilon}o}\right)^2} \tag{36}$$

$$\mathrm{\varepsilon}o = \frac{2f'\mathrm{c}}{Ec} \tag{37}$$

$$Ec = \frac{f}{\mathrm{\varepsilon}} \tag{38}$$

Where f and $\mathrm{\varepsilon}$ are the stress and strain at any point, respectively, $f'\mathrm{c}$ is the maximum compressive stress, and $\mathrm{\varepsilon}o$ is the strain at the maximum compressive stress.

Five data points were generated using these relations to compose the multilinear linear idealization of the concrete stress-strain curve in compression. The descending portion of the concrete curve after reaching the peak compressive strength is usually

idealized as a horizontal line, shown in Fig. 47 as the idealized curve in blue. In one study of the reviewed literature [93] the stress-strain curve assumed a total increase of 0.05 MPa after reaching the peak compressive stress up to the ultimate strain (0.0035) and was reported to overcome possible convergence problems [93]. This relationship was used in this analysis and is shown in Fig. 47 as the adjusted curve in red (although both curves appear to be almost identical).

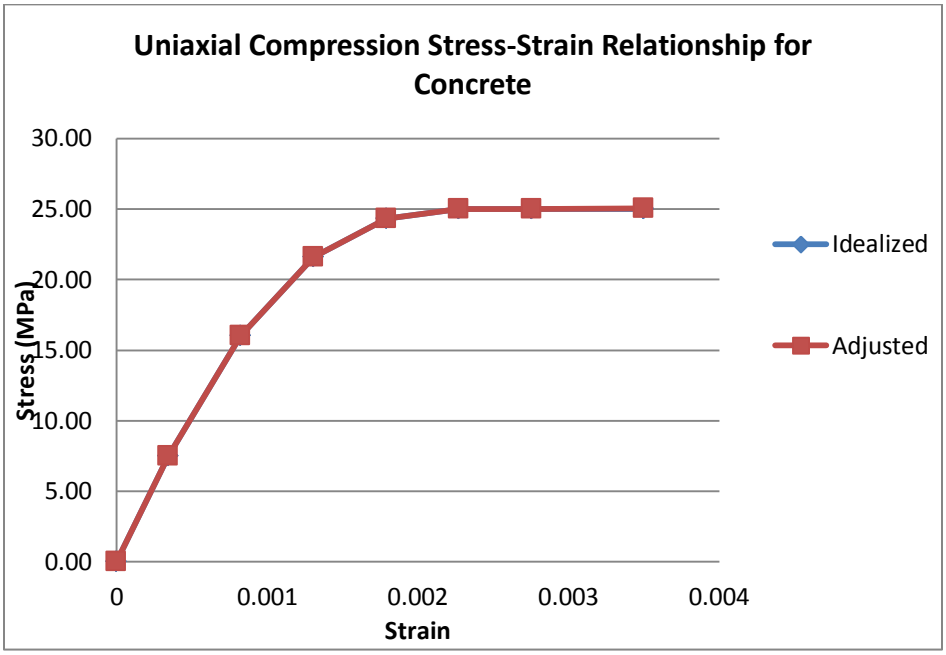

Fig. 47: Idealized and adjusted concrete stress-strain curve

The modeled steel reinforcement material properties are elastic-perfectly plastic using the bilinear isotropic hardening Von Mises plasticity material model. The linear isotropic properties are the modulus of elasticity which is equal to 210 GPa and poisson's ratio equal to 0.3. The parameters of the bilinear isotropic hardening plasticity are the yield stress which is equal to 400 MPa and the tangent modulus of elasticity, which is assumed as 5% of the yield stress of steel in order to avoid convergence problems.

Solution Methods and Convergence Sensitivity

The ANSYS default nonlinear solution method (the Newton-Raphson method) was used as in the previous part of the analysis with automatic time-stepping and the line search feature. However, in some of the models the line search method was turned off and, instead, the adaptive descent feature recommended for concrete nonlinearities was used. The line search method is a convergence-enhancement tool which multiplies the calculated displacement increment by a program-calculated scale factor between 0 and 1 when a stiffening response is detected [8]. ANSYS recommends the line search method for force loaded structures when the solution displays an oscillatory convergence pattern.

Adaptive descent is defined by ANSYS theory guide as a technique that switches to a "stiffer" matrix when convergence difficulties are faced and then switches back to the full tangent when the solution returns to a convergent pattern, which accelerates convergence. Plasticity and concrete element with tensile stress relaxation are some of the nonlinearities that make use of the adaptive descent technique. ANSYS structural analysis guide does not recommend activating both line search and adaptive descent simultaneously. When adaptive descent is on, the program uses the tangent stiffness matrix as long as the iterations remain stable. When divergence is detected, the program restarts the solution using a weighted combination of the secant and tangent stiffness matrices until a convergent pattern is resumed [8]. ANSYS states that adaptive descent usually enhances the program's ability to achieve convergence for complicated nonlinear problems for the elements which support using that feature, which include SOLID65.

In the beginning of the analysis early convergence difficulties were faced with the SOLID65 concrete element. This was initially tackled through increasing the maximum number of equilibrium iterations per substep and increasing the allowed convergence tolerance. The default convergence criterion in ANSYS was based on force convergence tolerance of 0.001. When convergence difficulties were encountered the convergence tolerance limit was increased to 0.005, and sometimes to 0.01 close to the failure load, which accelerated convergence of the solution, along with increasing the maximum number of equilibrium iterations.

At that stage, the failure load was defined at the point where the solution did not converge with the smallest possible substep size allowed in ANSYS, the determined optimum mesh size from initial mesh sensitivity studies, and a maximum number of equilibrium iterations equal to 1000 per substep. Preceding that point, ANSYS gave a few warning messages that one or more elements have become highly distorted, and then terminated the solution. In the next part of the analysis, a convergence sensitivity study was conducted in an attempt to verify that the solution termination represented true structural failure, as shall be discussed shortly.

4.2.4. Effects of boundary conditions

As discussed in the first chapter, concrete domes are usually bound by stiffening members, most commonly boundary ring beams, to absorb the large horizontal thrust that results at the base of the dome. In most shell numerical analysis literature, the boundary is completely fixed (all degrees of freedom are restrained) or hinged (only translational degrees of freedom are restrained) as the focus is the shell behavior alone. These conditions assume that the ring beam is infinitely rigid. In conventional construction, though, the boundary is always a deformable body and its deformations in response to the shell forces have a large effect on the structure's capacity. Boundary conditions were reported in literature to cause the discrepancy between the results of numerical and experimental analyses of spherical shells, besides other factors discussed previously. It is also one of the reasons why engineering practice tends to adopt large safety factors for concrete domes.

This study attempted to model the boundary beam effect. In general, modeling the ring beam has proven to cause convergence difficulties and has resulted in lower limit loads than modeling a completely restrained perimeter, as expected. However, some modeling techniques have proven to be more efficient than others, and can be reasonably claimed to produce closer values to the actual failure load of the dome than analyses using the infinitely rigid boundary.

The following methods were used in several attempts to model the effect of the boundary beam on the capacity of the concrete dome-ring structure:

- An infinitely rigid boundary that prevents both translation and rotation at the base of the dome (UX, UY, UZ, ROTX, ROTY, ROTZ) was assigned. This technique has been applied to models of the dome using SHELL281 as reference case to which all other boundary cases were compared.
- A hinged boundary that restrains translational degrees of freedom only (UX, UY, UZ) was assigned. This technique was applied to models of the dome using SHELL281 elements and models using SOLID65 elements.
- The ring beam was modeled with the line element BEAM189, in combination with SHELL281 for the dome. In some analysis the SHELL281 element was given linear

elastic material properties, while in others it was assigned multilinear isotropic hardening plasticity, and the layers feature of the element was used to provide a layer of steel reinforcement with elastic-perfectly plastic properties (with nearly the same volume ratio of SOLID65 total reinforcement in previous analyses) in order to include the material plasticity effect as well. The line ring beam was symmetrically hinged at eight locations around the perimeter of the dome.

- The ring beam was modeled as SOLID65 elements in combination with SOLID65 elements for the dome as well. At the connection between the dome and the beam, all degrees of freedom are coupled, meaning that the dome and the ring act continuously as one structure (as in the case of a monolithic dome with embedded steel reinforcement doweling from the beam section). Fig. 48 shows a picture of the meshed model of both the dome and the ring beam using SOLID65 elements.

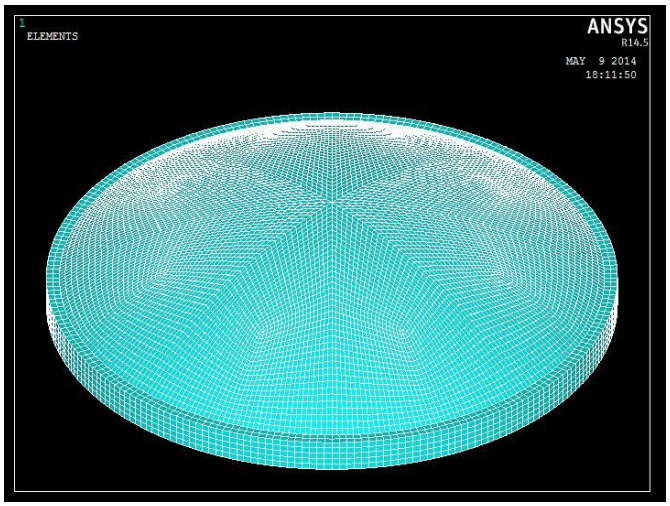

Fig. 48: Shell FE model using SOLID65 elements

The beam was initially hinged at eight line locations at its bottom surface that correspond to the point locations in the previous line element analysis. However, such restraining condition has proved to cause excessive stress concentrations and large element distortion at the restrained locations, which caused the analysis to terminate prematurely. In order to overcome the stress concentrations at the restrained nodes and element distortion, the size of the restrained zone was increased (more nodes were

restrained against translation at the assumed column locations). A plot of the base plane of the model is shown in Fig. 49.

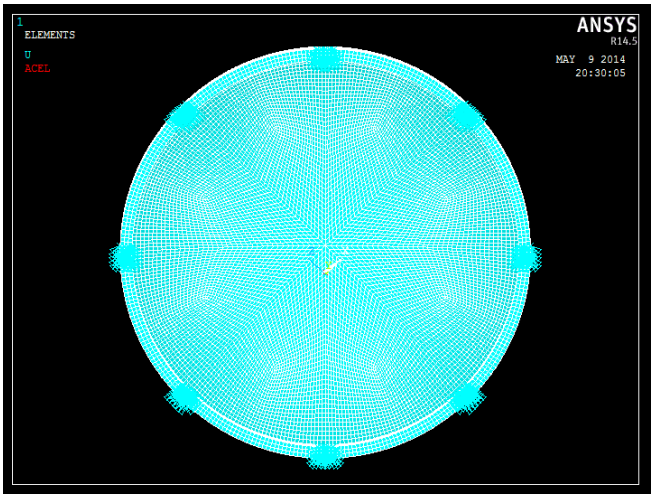

Fig. 49: Base of shell FE Model showing column restraining locations

In another model, the whole base of the beam was restrained against translation in the Y direction (vertical), while the assumed column locations were restrained against translation in X, Y and Z directions. In yet another run, the base of the beam was restrained against vertical displacement along the whole boundary, while only one column location was restrained against horizontal displacement to prevent rigid body motion. This way the beam is permitted to almost freely displace horizontally overcoming all stress concentrations at the various straining locations in previous models. The final model at this stage, however, which demonstrated the best performance was when the whole base of the ring beam was restrained against translation in X, Y, and Z, which allowed the beam section to rotate under the effect of the horizontal force and torsional moment, while the base of the beam is restrained against translation at all times.

Solution Parameters and Convergence Sensitivity

As will be discussed in detail in the next chapter, the failure loads of the models that included the ring beam were a lot less than those with a restrained boundary. At this point, in order to verify that the failure of the models represents a true structural failure and not a merely a numerical instability, a convergence sensitivity study was conducted utilizing many different solution parameters and model properties. The purpose of the study was to experiment with all the solution settings and model properties recommended by ANSYS and in the literature for enhancing convergence. The optimal parameters were determined as those delaying loss of convergence until a large displacement is detected for small load increments, accompanied by exceeding the strain limits of the concrete material. It should be noted that, unlike shell element models, the nonlinear stabilization feature is not supported by SOLID65 concrete element. Thus, this investigation was necessary in order to verify the model results.

Based on the reviewed literature, the following material parameters were found to enhance convergence and were adopted in this study:

- Including concrete tensile stress relaxation with a tensile crack factor of 0.6.
- Crushing was disabled in most of the models. However, it was turned on in some of the models to investigate its effect on convergence with a crushed stiffness factor of 0.001.
- Cracking was used in all the models. However, it was documented to cause early loss of convergence in some of the literature; thus, cracking was also disabled in some of the models in order to investigate that effect.
- Using a steel tangent modulus of 5% of its yield stress (which equals 20 MPa).

In addition to the previous material properties, the following was performed in the convergence sensitivity study:

- The first attempt at enhancing convergence was to increment the load more slowly. As discussed before, the automatic time-stepping feature was used in the analysis. The maximum number of substeps was used as 2,000,000,000 per load step.

- Another attempt at enhancing convergence was to refine the model mesh. Although it was difficult to locally refine meshes of the present models, several models of globally finer meshes were investigated. The process was repeated until refining the mesh no longer affected the results significantly. The selected mesh was used for the rest of the analysis.
- As discussed before, the Newton-Raphson method was used in most of the analysis. In this part of the analysis, a few solutions were run using the alternative nonlinear solution method: the arc-length method. The arc-length method was used a few times with various number of substeps and minimum and maximum arc-length multipliers of 1e-20 and 20, respectively.
- The adaptive descent feature recommended by ANSYS to enhance convergence for SOLID65 type nonlinearities was turned on in some of the models. This feature is used with the default Newton-Raphson method. However, it is not recommended with the line search feature, so line search was turned off in these solutions.

  The performance of all the models in this part of the analysis was evaluated and the optimal solution parameters were used for the rest of the analysis models.

- The next stage was building a more elaborate model of the dome-ring system utilizing ANSYS contact elements technology, whose use is discussed in detail in the following section. Utilizing contact technology, the connection between the dome and the ring beam is modeled as an initially bonded asymmetric flexible surface-to-surface contact using CONTA174 and TARE170 elements in the ANSYS. A debonding feature is combined with these elements with user-specified parameters. This allows for separation or sliding to occur between the contacting surfaces at the interface should the normal or tangential stresses exceed those specified by the user. Contact elements were used extensively in this research as the main method adopted for the simulation of the behavior of the joints between the precast elements in the proposed dome structure. At this point though, a contact condition was provided only at the boundary between the dome and the supporting ring beam. A coefficient of friction between the two surfaces was used equal

to 0.7. The maximum normal and tangential stresses for debonding were used initially as those of the steel (Tensile yield strength of steel, and shear strength of steel assumed as 0.6 of its tensile strength, respectively) assuming that reinforcement bars extend across the joint and are in perfect bond with the concrete (no reinforcement slip). In other models, the maximum stress limits were input as the maximum tensile stress of the concrete and the shear strength of the concrete (assumed as $0.8\sqrt{fc}$, where fc is the concrete compressive strength). This case assumes a bond slip between the steel and concrete, or the absence of reinforcement across the joint. Consequently, only the cast-in-situ concrete in the joint is acting to prevent separation at the joint. It should be noted that no specific contact material cohesion parameters were assigned.

4.2.5. Modeling failure of the concrete stitches between the dome panels

Contact elements on ANSYS with or without debonding features were used to model the behavior of various types of precast concrete connections in most of the reviewed literature [111], [70], [45], [46], [120], [100], [115], [91], [19].

In this research, surface-to-surface contact element CONTA174 and target element TARGE170 define the interfaces between the dome panels and are enabled to model debonding of the two panels at the joint. The contact and target elements overlay the faces of 3D SOLID65 elements. A number of 30 symmetric contact pairs (i.e. each surface is designated as both a contact and target surface) is created on the interfaces between panels, and in some of the analysis models, at the interface between the boundary panels and the supporting ring beam

According to ANSYS contact technology guide, symmetric contact is less efficient than asymmetric contact. It may be required to reduce penetration, or when the distinction between the contact and target elements is not clear, but it is more expensive in terms of CPU time. In this research, the use of symmetric contact was selected since the connection between the panels is expected to produce symmetric behavior, and the contacting elements were identical in terms of flexibility/rigidity and mesh density. However, it should be noted that ANSYS contact technology guide [11] states that, in such cases, the symmetric contact may not improve the results and, thus, will only be more expensive in terms of CPU time. Thus, at the contact between the dome and the boundary beam, both asymmetric and symmetric contact pairs were tried in order to judge the improvement in the solution (if any). In asymmetric contact, contact elements overlay the base of the lower dome panels, while target elements overlay the interfacing edge of the ring beam.

There are many different parameters to set for ANSYS contact conditions. ANSYS contact technology guide [11] states that the default parameters are usually sufficient for most contact analyses. In this research, many of the contact parameters were set to their defaults, while other parameters were changed as deemed appropriate for the type of connection at hand, and based on similar analyses in the literature.

The type of contact in ANSYS varies depending on the type of problem through the use of KEYOPT(12). In this research, the contact is selected as 'bonded initial contact', which is a type of bonded contact where the surfaces are initially in contact. ANSYS guide [11] recommends the use of this type of contact, coupled with the debonding feature, to simulate debonding of the surfaces; an approach that was also adopted in most of the relevant literature.

Hence, in this research failure of the stitch between the panels was modeled using ANSYS debonding feature through defining a cohesive zone material (CZM) model which defines a constitute relationship between normal and/or tangential pressure at the interface, and the corresponding separation across the joint. Debonding using the CZM follows a failure mechanism that gradually degrades the material elasticity between the contacting surfaces at the interface [29].

The cohesive zone material (CZM) has a bilinear behavior, and the constitutive relationships can be defined by separation/sliding distance or separation/sliding energy [29]. The CZM model allows three different modes of debonding; normal separation, tangential separation and a mixed mode of both normal and tangential separation [11]. In this research the mixed mode failure was used by defining the maximum separation and sliding distances, along with the maximum normal and tangential stresses at the interface. ANSYS states that after debonding occurs, standard contact behavior follows [11].

The input of the CZM includes six different inputs. These are: maximum normal contact stress (σ_{max}), contact gap at the completion of bonding (u_{cn}), maximum tangential stress (τ_{max}), tangential slip at the completion of bonding (u_{ct}), artificial damping coefficient (η), and a flag for tangential slip under compressive normal contact stress (β) [9].

In this research a maximum separation and sliding values between 5 and 20 millimeters was used in different models to investigate their effects on failure. Different input values for the normal and tangential stresses were also used in different models to represent different bonding cases between the concrete and reinforcing steel at the joint.

The value of the maximum stress was initially taken as the tensile strength of concrete (σmax = 2.5 MPa), as done in similar previous research involving debonding of precast concrete elements [91], [70], and the maximum tangential stress was input as the shear strength of the concrete, approximated as 0.8 $\sqrt{fc}$, where fc is the concrete compressive strength (τmax = 4 MPa). These values represent a case ignoring the steel reinforcement across the joint, and depending on the strength and cohesion of the concrete at the joint to hold the panels in place. However, as previously noted, no cohesion parameters were input in this study. In the second case of debonding the yield and shear strength of steel (approximated as 0.6 of the yield strength) were input as the limiting normal and tangential stresses for the CZM, respectively. This case is interpreted to assume a perfect bond with no slip between concrete and steel reinforcement across the joint, and consequently, may overestimate the capacity of the joint.

The artificial damping coefficient of the CZM is used to overcome convergence problems that may arise due to modeling of debonding. The damping coefficient has units of time and is suggested to be less than the smallest time step size so that the maximum traction and separation are not exceeded in debonding calculations. In this research, although the time step size was always variable, an artificial damping coefficient value of 0.0001 was selected to be appropriate for the analysis as it is maintains convergence, does not cause any excessive separation and is almost always smaller the time step size.

Other key contact parameters for ANSYS contact pairs that were studied for their effects in this research are the contact algorithm, contact stiffness, and the allowable penetration. ANSYS offers several different contact algorithms. The contact algorithm used in most of the literature in precast concrete panel connections is the penalty method, which is also suggested by the ANSYS guide when modeling bonded contact [11]. The penalty method is a contact algorithm which uses a contact spring to define the relationship between the contacting surfaces. This relationship is defined by the spring stiffness (the contact stiffness) both normal stiffness (FKN) and tangential stiffness (FKT). Another algorithm that was used in some of the literature, and is the default method in ANSYS is the augmented Lagrangian method. According to ANSYS, this

method is an iterative series of penalty methods, usually leads to better conditioning, and is less sensitive to the magnitude of the contact stiffness; however, it may require more iterations than the penalty method [11].

In this analysis, both contact algorithms were used in different models. It was soon found that, in this analysis, the penalty method has caused excessive penetration between the model panels, when compared to models with the same parameters run using the augmented Lagrangian method. Consequently, the augmented Lagrangian method was used in the rest of the analysis.

As mentioned above, both contact algorithms need a normal and tangential contact stiffness to define the relationship between the contacting surfaces. According to ANSYS, a high contact stiffness decreases the amount of contact penetration but at the same time can cause convergence difficulties. Thus, a few trials were attempted to determine the optimum contact stiffness that produces minimal penetration and maintains convergence. ANSYS provides a default value of the normal penalty stiffness that is affected by material properties, element size, and total number of degrees of freedom in the model [11]. However, ANSYS recommends checking the actual used contact stiffness value during postprocessor via element tables in order to verify that the value is appropriate for the analysis. ANSYS also provides the option of defining a normal contact stiffness factor using the real constant FKN, which means defining the actual normal stiffness as a factor of the internally calculated contact stiffness.

Values used for FKN for analysis of precast joints varied significantly in the literature depending on the type and conditions of the connection and the expected behavior based on experimental test results. ANSYS guide suggests that FKN usually ranges between 0.01 and 1 [11]. Some authors used the 0.01 factor recommended by ANSYS [115], [19], while others used lower values to reflect the weaker contact stiffness encountered during experimental tests (a value of 0.0011 was used in reference [70] in some of the models in order to simulate the low contact stiffness encountered in experimental testing between the concrete and grout and the observed failure at that boundary, and a value of 0.0036 was used in [91]).

In this research, different contact stiffness factors were used in different models as part of a contact sensitivity analysis. A starting factor for FKN was 0.5 (half the ANSYS calculated contact normal stiffness). Then, a much lower value of 0.01 was used to simulate a weaker bond at the interface, and a third minimum value of 0.001 was used in some of the models in order to determine the effect of very low contact stiffness on the global behavior of the structure. KEYOPT (10) was set equal to 2, which allows the program to update the contact stiffness automatically. As for the tangential stiffness, ANSYS automatically defines a value that is proportional to the user-input friction coefficient and the normal stiffness. The value of the tangential contact stiffness was not changed in this analysis.

The penetration tolerance factor (FTOLN) in ANSYS is used in conjunction with the augmented Lagrangian method to limit the resulting contact penetration. ANSYS guide states that the penetration tolerance can be defined as a factor (is usually less than 0.2) or as an absolute penetration value. The default value for FTOLN is 0.1 and the penetration tolerance is calculated based on the depth of the underlying model elements, which is defined as the average depth of the contact elements in each pair. In this research, values for FTOLN were varied between 0.0001 and 0.1, as part of the contact sensitivity study, in order to determine the effect of the penetration value on convergence.

Finally, for the coefficient of friction of the contact pairs, a value of 0.7 was used in the model, which was reported in some the relevant literature, although a higher value (equal to 1.0) was used in other studies based on the relevant recommendations of the ACI 318 [3] for friction for concrete placed against hardened concrete.

The following models were created for the simulation of the final segmented structure:

- The first set of models included modeling the final segmented dome panels with contact conditions between all the panels resulting in 30 symmetric contact pairs (60 contact pairs in total). At this stage, the boundary conditions of the dome were modeled as restraining of translation in the X, Y and Z directions of the base of the panels at the foot of the dome. The model is shown in Fig. 50.

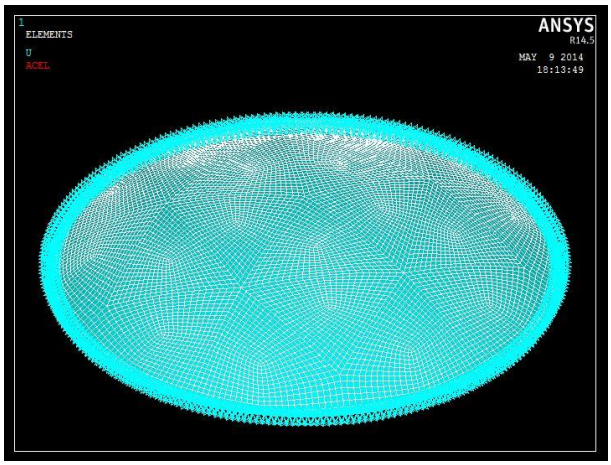

Fig. 50: FE segmented shell model with contact elements between the shell panels

As previously explained, different contact parameters were tried in different runs in order to determine the most suitable set of parameters for the analysis. Table 2 summarizes the different values used for different contact parameters:

Table 2: ANSYS contact parameters

Range for contact stiffness factor	0.001 – 0.5
Range for penetration tolerance factor	0.0001 – 0.1
Contact algorithm	Augmented lagrangian method Pure penalty method
Friction coefficient	0.7
Contact type	Bonded- initial contact
Debonding feature	yes

Maximum contact normal stress (MPa)	2.5
Range for maximum separation at the completion of debonding (m)	0.005 - 0.02
Maximum contact tangential stress (MPa)	4
Range for maximum sliding at the completion of debonding (m)	0.005 - 0.02
Damping coefficient	0.0001
Slip under compression	yes

- The second set of models involved modeling the boundary beam as part of the dome-ring structure using the solid element SOLID65, and with material parameters similar to those discussed in the previous section.

In this model, 10 pairs of asymmetric contact pairs were added to the existing 60 contact pairs to create contact conditions between the base panels of the dome and the boundary beam. In these new contact pairs, the beam areas at the interface were overlaid with target elements, while the base panels contact areas were overlaid with contact elements. The contact parameters used at the stage are the same as those listed in table 2. Fig. 51 shows the geometry of the model, Fig. 52 shows the final meshed model, and Fig. 53 shows all the contact pairs created in this part of the analysis with a translucent model context.

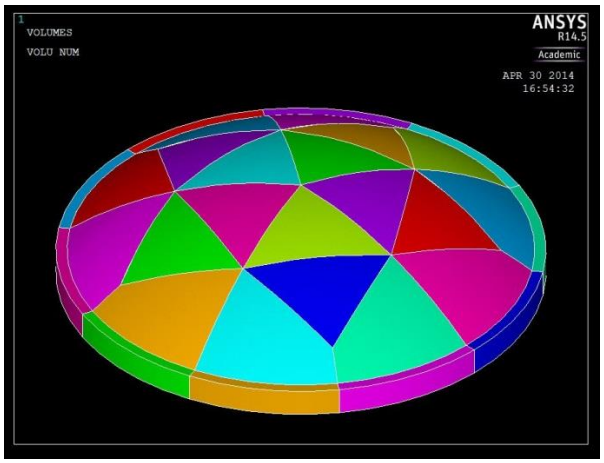

Fig. 51: Geometry of the final FE segmented shell model

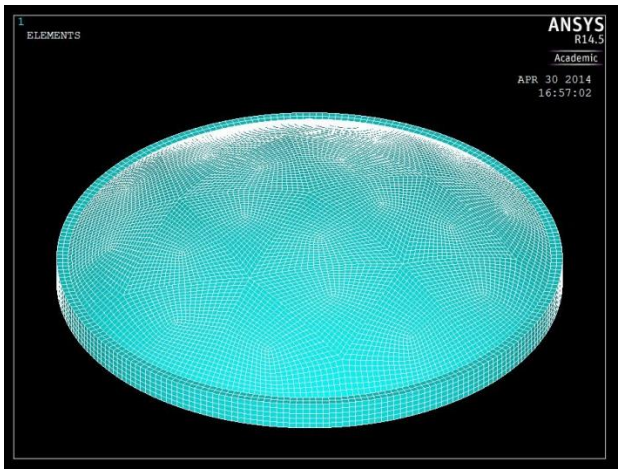

Fig. 52: Final meshed FE segmented shell model

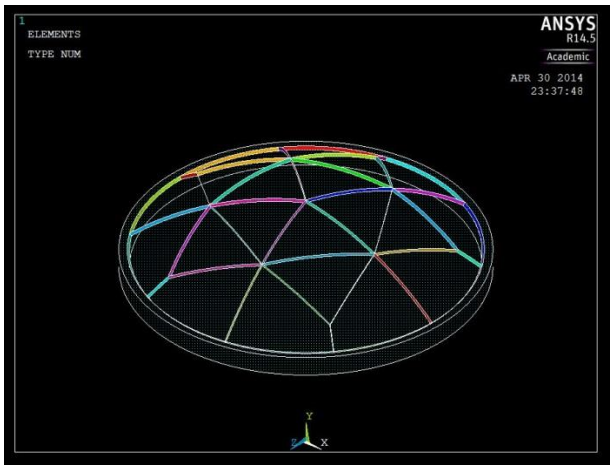

Fig. 53: Contact pairs in final FE segmented shell model

This set of models is considered to be the final form of the structure attempting to simulate all geometry, material and boundary conditions. Consequently, a lot of different material, contact and solution parameters were tried in different runs of this model. The solution parameters were guided by the results achieved through the convergence analysis described previously.

- Another set of models was built to simulate a different loading condition, namely a concentrated vertical load at the dome crown. This loading condition was selected since it represents one of the most critical loading conditions of a spherical shell structure, since it does not produce a uniform stress distribution and usually leads to high local stress concentrations that may accelerate the failure of the shell. The purpose of constructing these models was to determine the failure load of the spherical cap under a concentrated crown load, and compare the results of the numerical model to those of the experimental test performed in the same manner (as explained in section 4). The concentrated load model is shown in Fig. 54.

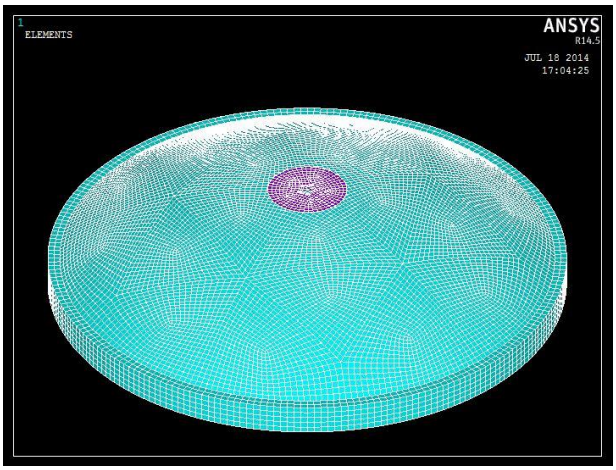

Fig. 54: Concentrated load FE model

The concentrated load models aimed to closely follow the experimental analysis loading conditions. Consequently, the loading was applied to a circular steel plate of a diameter of 4 m and thickness 3 cm centered at the shell crown. These parameters are selected such that the weight per unit area of the numerical model and physical scale model are almost identical, so as not to introduce any extra stress concentrations in the

numerical model. The load was applied as a uniform pressure on the steel plate (as shown in Fig. 55), and, accordingly, the final load was determined as the total load on the steel plate area.

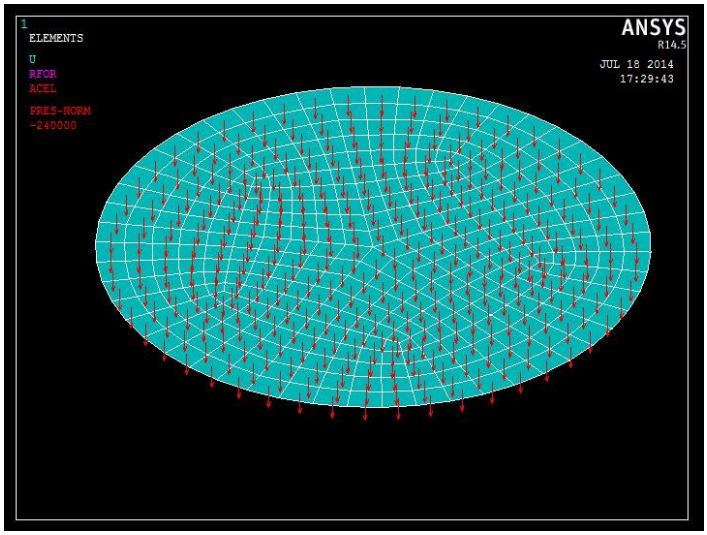

Fig. 55: Uniform pressure load applied to Steel plate at the dome crown

The circular steel plate was created using SHELL181 element on ANSYS. SHELL181 is a nonlinear shell element very similar to SHELL281, except that it is a 4-node element, since it is used in contact with the surface of 8-node solid SOLID65 element. The plate was assigned the same steel material properties.

A contact pair was created between the steel plate and the dome panels at the crown. The contact pair was assigned a rather large stiffness and penetration tolerance (factor of 1 and 0.1 respectively) since the contact conditions at the loading location are generally not of interest. The sole purpose for the contact pair is to assure fast convergence and transfer of the load to the dome.

Beside the segmented dome models, another reference model of a monolithic dome loaded with a concentrated load in the same manner was also built, in order to provide a frame of reference, and give a clear numerical insight into the difference in the behavior between the segmented and monolithic domes under that specific loading condition.

- Since most of the literature on spherical cap buckling used uniform external radial pressure, a similar loading method was necessary for constructing a proper comparison with the calculated values using the documented formulas in the surveyed literature for spherical caps with the same geometrical parameter as that of this study.

Consequently, the same set of models previously created with the segmented spherical cap with and without a ring beam were loaded with a radial pressure load only (no inertia load was applied). The load was applied as a uniform normal pressure on the surface of the dome elements in the finite element model with values close to those predicted by Zoelly's classical buckling load formula [121].

Another reference set of monolithic domes loaded in the same manner (with and without a ring beam) were also created for comparison. Although this loading pattern was applied extensively in the literature and many formulas are provided to predict its value as a fraction of the classical linear buckling load, almost none of the literature studies documented a finite element analysis using a cracked concrete element. Instead, as previously discussed, most of them provided empirical values of a reduction factor for the effect of cracking; these values were sometimes based on experimental analyses or monitoring of the tensile stress levels in the numerical model. Consequently, it was of interest to explore the reduction in the spherical cap's capacity when a smeared crack concrete element is used, and investigate the reliability of the documented empirical factors.

- Finally, a full (and much more expensive in terms of CPU time) model of the spherical cap, the ring beam and the supporting columns was built. This model was created in an attempt to deduce results as close to the actual behavior of the structure as possible, and eliminate the boundary conditions related problems.

Tables 29 – 35 in appendix B present a summary of all the ANSYS models explained in this section and a description of the model parameters with a designated code for each model. The FE model codes shall be used in the next chapters to refer to their corresponding models.

4.3. Design and Construction Plan

The construction procedure of reinforced concrete shells is usually one of the controlling factors of the structural design of the shell [44]. As previously discussed in the literature review, the hectic construction process associated with concrete domes, including extensive formwork, skilled labor and intricate quality control, is one of the reasons for the decline of using concrete domes for covering large spans despite their efficiency in carrying the loads. The value of the proposed structural system is, thus, contingent upon the efficiency with which it is constructed. Detailing the assembly of the dome panels during each stage of the construction until the full shell membrane action takes place is a critical part of this research. Consequently, this section explains the proposed design and construction plan for the segmented dome structure.

This section starts with a conventional preliminary concrete dimensions and reinforcement design for the dome-ring structural system, a design that is used later as guidance for developing the parameters of the scale model of the dome at the experimental analysis stage. The second part of this section presents the suggested construction method of the segmented dome structure. The final part represents a simplified analysis of the behavior of the structure during construction which attempts to take the construction-induced deflections into account during the design stage.

4.3.1. Structural Design of the Prototype Dome-Ring System

Preliminary design of the dome-ring dimensions and reinforcement was guided by different design guides that include *'Concrete Shell Structures - Practice and Commentary'* report by ACI Committee 334 [4], and the design of reinforced concrete shells chapter of '*Design and Analysis of Shell Structures'* by M. Farshad [44] and '*Design and Construction of Concrete Shell Roofs'* by Ramaswamy [94].

Beside the factors explained in the previous section concerning the geometry of the structure and specific to this research, the thickness of the shell structure, in general, is determined by a number of factors, only one of which is the ability to resist service loads. The usually more significant concern, particularly for relatively thin shells, is the resistance to buckling, as discussed in the literature review. Another important factor for the selection of the reinforced concrete shell thickness is the construction requirements.

For the considered span of 25 m, the dome thickness is selected to have a relatively large value of 250 mm, which is mostly larger than the thickness range found in the literature. There are a few reasons that governed that selection; one of which is to account for the possible reduction in the capacity of the dome due to the presence of a large number of connections between the precast panels of the dome which are likely to create weak points in the structure. Another reason is to account of the new construction-induced loads that the structure shall be subjected to. A final factor in the selection, for the purpose of this research, was the feasibility of reproducing the thickness in a 1:10 scale model of the dome with the available resources, as explained in the previous section.

Table 3 lists the geometric and material parameters for the design of the dome, and the nomenclature is shown in Fig. 56.

Table 3: Geometric and material parameters of the shell prototype

Material Parameters	
Concrete average cube compressive strength (Fcu) (MPa)	25
Steel yield strength (Fy) (MPa)	400
Concrete density (kg/m3)	2500

Spherical Shell Parameters	
Radius R (m)	20.59
Half the central angle (φ) (degrees)	37.38
Rise (a) (m)	4.23
span (2r) (m)	25
Surface area of the shell (2 π R a) (m2)	547.04
Shell thickness (mm)	250
Ring Beam Parameters	
Width (B) (mm)	1000
Height (H) (mm)	1500

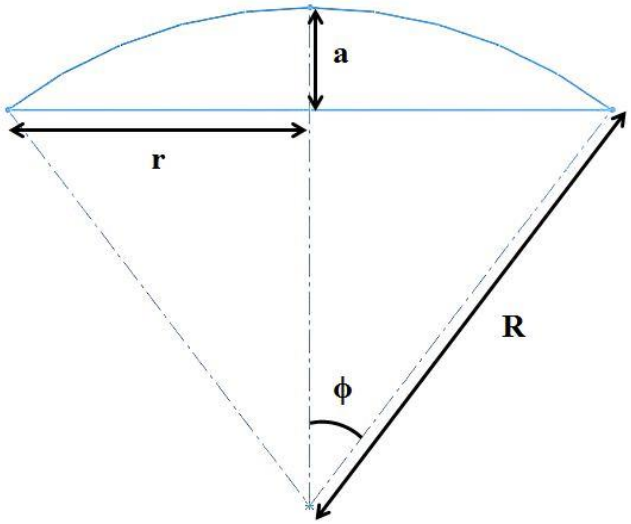

Fig. 56: Shell geometry nomenclature

Table 4 presents the design forces obtained for the structure [44] based on the linear elastic theory of shells. The design forces are calculated based on an ultimate design load of 1.5 of the dome's dead weight plus an assumed live load of 1 kN/m2. The table includes the forces and approximate moments for both the shell and the boundary ring beam.

Table 4: Design forces for the shell prototype

Forces due to dead load	
Dead load per unit of surface (g) (kN/m2)	6.13
Total load due to dead weight (kN)	3354.04
Meridional force (Nφ) (kN/m) (at crown)	-63.12
Hoop force (NΘ) (kN/m) (at crown)	-63.12
Meridional force (Nφ) (kN/m) (at foot)	-70.35
Hoop force (NΘ) (kN/m) (at foot)	-29.98
Horizontal force H (kN/m) (at foot)	-55.90
Forces due to live load	
Live load per unit of surface (g) (kN/m2)	1.00
Total load due to live load (kN)	490.87
Meridional force (Nφ) (kN/m) (constant)	-10.30
Hoop force (NΘ) (kN/m) (at crown)	-10.30
Meridional force (Nφ) (kN/m) (constant)	-10.30
Hoop force (NΘ) (kN/m) (at foot)	-2.71
Horizontal force H (kN/m) (at foot)	-8.18
Total ultimate forces (design forces)	
Dome Forces	
Maximum Meridional force (Nφ) (kN/m) (compression)	-120.96
Maximum Hoop Force (NΘ) (compression)	-110.13
Minimum Hoop Force (NΘ) (Compression)	-49.03
Horizontal force H (kN/m) (at foot)	-96.12
Maximum negative bending moment (at foot) (kN.m/m)*	7.65
Maximum positive bending moment (kN.m/m)*	1.02
Ring beam forces	
Total ultimate vertical Load	5767.37
Horizontal force H (kN/m)	96.12
Axial Force (Tension) (kN)	1201.55
Vertical force V (kN/m)	73.43
Beam own weight (kN/m)	41.39
Total vertical force on ring beam per meter (kN/m)	114.82
Maximum shear force (kN)	563.61
Maximum bending moment at mid-span (+) (kN.m)	473.44
Maximum bending moment over C.L. of column (-) (kN.m)	935.60
Maximum Torsional moment (kN.m)	67.63
Angle between axis of column and section of maximum torsional	9^0 33'

moment	
Total Vertical Load (kN)	9017.81
Load on each supporting column (no. of columns = 8) (kN)	1127.23

*Shell bending moments were approximated using reference [94]

Based on the previous design forces, the dome and ring beam reinforcement was designed, as summarized in table 5. The membrane compressive stresses are well below the allowable limits for the concrete (maximum compressive stress = 0.48 MPa). Consequently, no designed reinforcement for the shell is required. The provided shell reinforcement is for controlling of concrete shrinkage with the volume ratios complying with the ACI recommendations.

Table 5: Reinforcement design for the prototype shell-ring structure

Structural Element	Type of Reinforcement	Reinforcement Rebar
Shell Reinforcement	Hoop and Meridional Reinforcement	Top and bottom reinforcement is provided. Each consists of 5ϕ8 per meter in two directions. Alternatively, and preferably for the reinforcement of the panels of this dome, the same steel area is provided using commercially available welded wire reinforcement.
	Bending reinforcement	Covered by the upper and lower membrane reinforcement
Ring beam reinforcement	Bottom Reinforcement	7Φ25
	Top reinforcement	7Φ25
	Stirrups	Φ10 @ 20 cm
	Longitudinal torsion rebar**	8Φ12

**The torsion longitudinal reinforcement shall be distributed uniformly along the section perimeter (spacing is less than 300 mm in compliance with the Egyptian code design requirements).

4.3.2. Design of the Structural Connections

The panel intermediate joints are designed as moment-resisting connections. Fig. 57 illustrates the detailed design of the connection and the reinforcement across the joints. In the figure, the hatched part represents the grout or cast-in-situ concrete after the assembly of the panels.

The construction of the joint can be summarized as follows: A recess that is 50 cm wide and 10 cm deep is created along all the edges of each panel during casting of the panels (or prefabrication of the molds). Thus, the panel thickness is reduced at that recess to 15 cm, and the total width of the joint is 100 cm (consisting of 50 cm at the edge of each panel of the two interfacing panels at the joint). In the upper 10 cm of the joint, the steel meshes or rebar of the interfacing panels are tied together with a splice length of the entire joint width (100 cm in the prototype). The upper 10 cm of the joint are subsequently cast or grouted to the full nominal cap thickness.

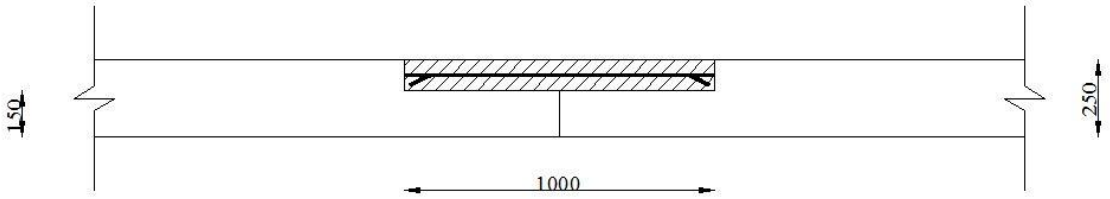

Fig. 57: Design of the panel-panel intermediate joint

The joint between the base panels and the ring beam is designed in a similar manner, using the modified design of the ring beam previously discussed at the beginning of this chapter. As Fig. 58 shows, a moment-resisting joint is created by tying of the steel reinforcement of the base panels, and the specially placed ring beam dowels. This is followed by grouting/casting of the upper parts of the panel edge and the ring beam, denoted by the hatched zone in the figure. In this research, stitches were created in the

beam by casting the beam on multiple stages, as will be discussed in detail in the experimental analysis section of this chapter, thus allowing casting of the parts in contact with the panels simultaneously with casting of the panel joints.

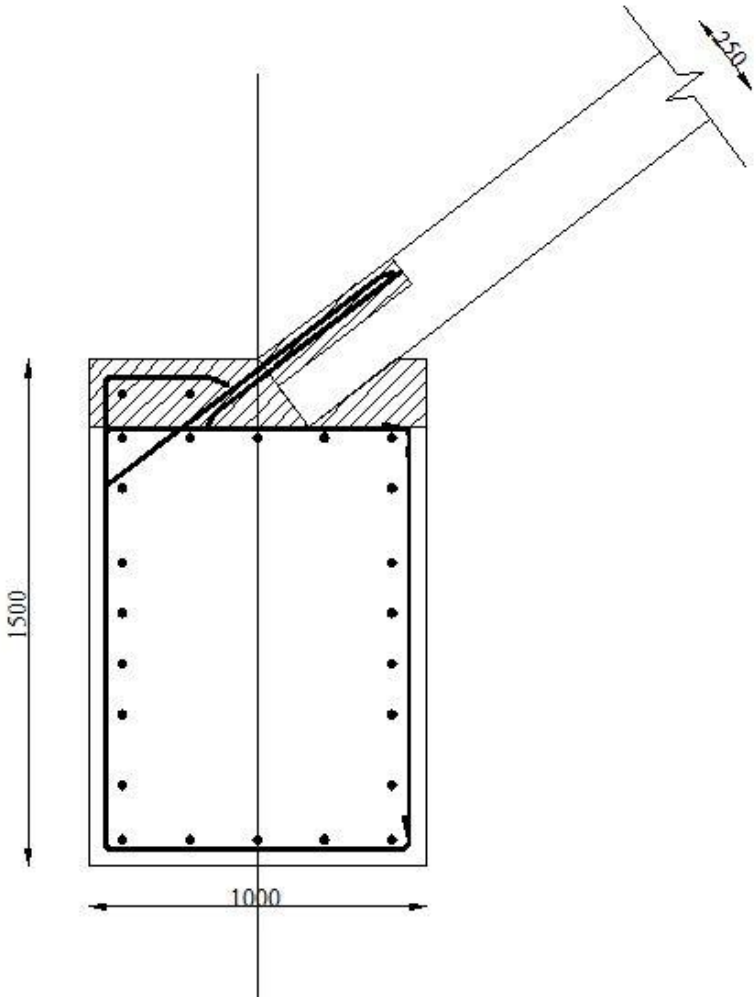

Fig. 58: Design of the panel-ring beam joint

4.3.3. Construction Plan for the Prototype Dome-Ring System

In this section, the logic of the proposed construction sequence is presented, along with the proposed methods for providing temporary support for the construction. A supporting numerical analysis for the structural behavior during construction is also described. It should be noted the same construction procedure was also followed as closely as possible in the experimental analysis of this research, with some inevitable discrepancies that shall be stated where relevant.

The construction logic aims to provide temporary support for the panels until initiation of the shell membrane action. Different options for supporting these panels during construction were investigated through the available literature, commercially available systems, and numerical modeling of the behavior of the panels. The construction procedure was divided into three distinctive stages:

Stage 1: This stage includes assembling row A panels (referred to as the base panels) followed by grouting of the joints between the base panels and the ring beam, and between the base panels themselves. A schematic drawing of the structure at the end of stage 1 is shown in Fig. 57.

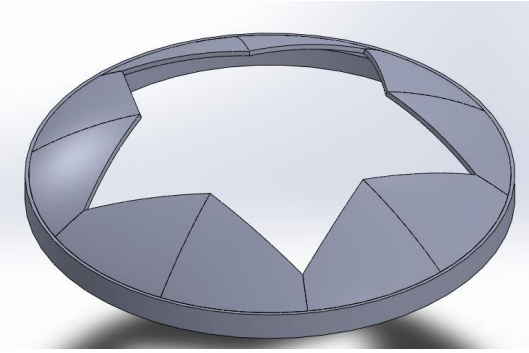

Fig. 59: Structure after construction stage 1

Stage 2: This stage includes assembly of row B panels, which are placed between row A panels, followed by grouting of the joints between row A and row B panels. Fig. 58 shows the structure by the end of stage 2.

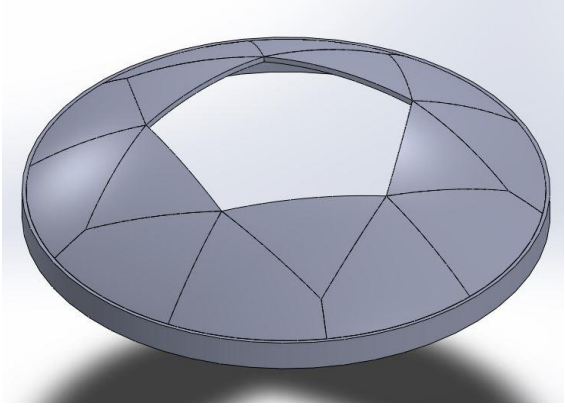

Fig. 60: Structure after construction stage 2

Stage 3: This stage includes assembling row C panels (referred to as the crown panels) followed by grouting the joints between row C and row B panels, and between row C panels themselves. By the end of this stage, the erection of the dome is complete, and the full membrane action takes effect, and the temporary supports can be removed (after hardening of the in-situ joints). The structure at the end of the final stage is shown in Fig. 59. Fig. 60 summarizes the proposed logic for the construction procedure of the dome-ring system supported on columns, while the detailed method used in the experimental analysis is illustrated in section 4 of this chapter.

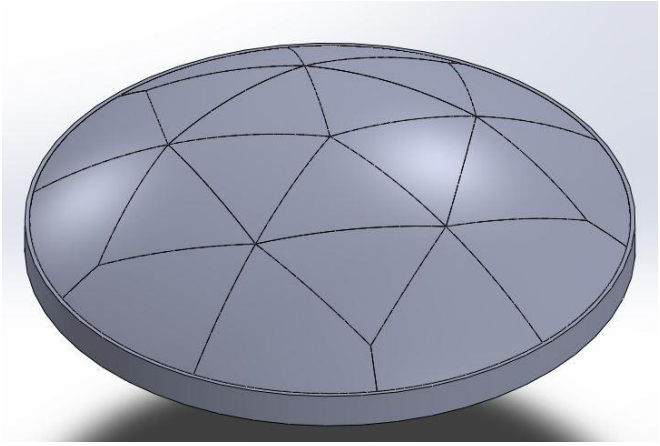

Fig. 61: Structure after construction stage 3

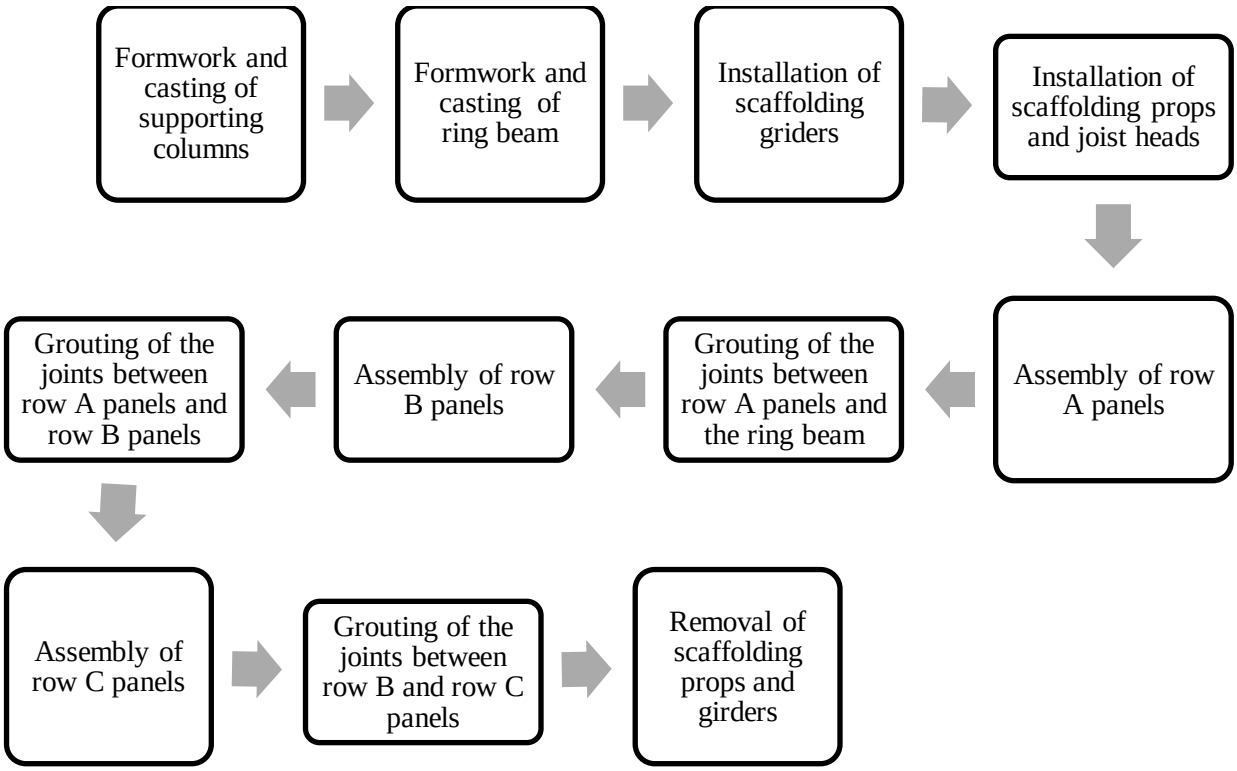

Fig. 62: Proposed construction logic

4.3.4. Numerical Analysis of the Structural Behavior during Construction

After establishing the most suitable element types, material properties, contact conditions and solution control parameters for the structure at hand, as detailed in the previous section, the following analysis was conducted in order to quantifiably look at the behavior of the partial structure under anticipated construction-imposed loads. As previously discussed, the proposed structure shall be constructed by prefabricated concrete panels assembled on-site with as minimal scaffolding as possible. In this part of the analysis, it is attempted to understand the behavior of the structure under the constraints of the proposed supporting method and determine the minimum required supports.

Typically, the analysis at this stage requires several models of the partial structure at the different designated stages of construction. However, for the structural system at hand, the geometric efficiency of the system is accompanied by large reduction in the effort needed to understand the behavior of the structure during construction. Since the structure is composed of only two unique sizes of panels arranged in a pattern that is repetitively symmetric around the central axis, it is only necessary to analyze the behavior of each unique panel, as long as all the identical panels shall be supported in the same manner.

During construction, the behavior of the structure is controlled by a different mechanism than the default membrane action of the full shell structure; namely bending of the panels supported on scaffolding props. The analysis, thus, reduces to determining the minimum supports and most optimum support locations that will prevent rigid body motion and minimize the deflections along the unsupported lengths of the two unique panels. For that purpose, the following finite element models were built on ANSYS:

- A model of panel A only (the base panel) was created using the same geometric and material properties of the dome. The boundary conditions were defined to represent the supporting scaffolding prop heads that are planned to support the assembly of panel A during the construction, which were intuitively selected at the panel edge corners, while the base of the panel was restrained along the whole edge, reflecting that the whole base

is resting on the ring beam. Fig. 61 shows the FE model created for analysis of panel A. The main purpose of the model was to investigate the overall panel bending deflections under its own weight and the applied support restraints.

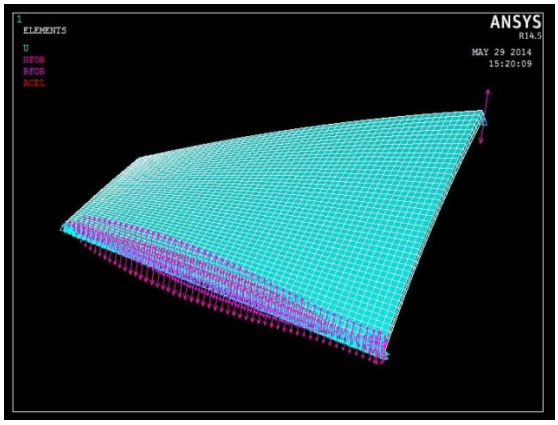

Fig. 63: FE model for the analysis of Panel A behavior during construction

- A similar model was created for panel B and C (identical panels) that are planned to be supported in the same manner during assembly. Although panel B is significantly smaller than panel A (panel's volume is 26% less than that of panel A), panel B has larger unsupported edge length (the largest unsupported edge length of panel B is 16% larger than that of panel A). Consequently, it was necessary to conduct an analysis for panel B, in order to make sure no excessive deflections arise along the panel's largest edge. The properties of the FE models of the individual panels are restated in table 6.

Table 6: Model properties for the analysis of the structure under construction loads

Type of analysis	Large displacement static analysis
Loading	Gravity load (g = 9.81 m/s2)
Boundary conditions	Variable
Element	SOLID65 concrete element
Material properties	Material properties for the concrete: elastic isotropic, nonlinear nonmetal concrete plasticity, isotropic work hardening plasticity Material properties for steel reinforcement: elastic isotropic, isotropic work hardening plasticity.
Contact conditions	Variable (friction type contact or bonded initial contact)
Solution method	Newton-Raphson method with line search and bisection features

4.4. Experimental Analysis

This section presents the planning, fabrication, construction and load testing of a scale model of the segmented precast concrete spherical cap proposed in this study. The section is divided into the following parts:

(1) Model Design

Section dimensions, and material and reinforcement design for the scale model

(2) Mold Design and Fabrication

Design of the molds and formwork for casting different parts of the structure

(3) Casting

Casting process of the supporting structure and the dome panels

(4) Construction

Construction sequence and assembly of the dome panels

(5) Testing

Experimental setup, instrumentation and testing procedure of the dome-ring structure up to failure

4.4.1. Model Design

4.4.1.1. Model Description and Concrete Dimensions

The model is a 1/10-scale reinforced concrete direct model. In order to fulfil the similitude requirements of a true model, characterized by identical strains in the prototype and the model, the model material is concrete designed to be representative of the mechanical properties of the prototype concrete. The stress scale (S_σ) is 1:1 to produce the same stresses and strains of the prototype, although some size effects are to be expected as shall be explained shortly.

The scale model of the shell consists of 20 panels that have two different unique sizes, and are 25 mm thick each. Around the perimeter, each panel has a 50-mm wide, 10-mm deep recess. This recess creates a 10-mm deep, 100-mm wide joint at the interface between each two panels in the shell structure. The panel reinforcement is extended, overlapped and tied together across the joint that is then grouted in place.

A supporting structure for the shell is constructed to reproduce the boundary conditions of the prototype shell as closely as possible. A boundary ring beam (100 x 150 mm) is designed to stiffen the shell ends and provide sufficient constraining. The ring beam section is designed to hold the ends of the shell base panels with extending reinforcement of both the beam and the panel, in order to strengthen the connection that shall later be grouted in place.

Eight columns were constructed along the beam perimeter to provide reasonable spans for the beam and allow for the beam deformation expected in the prototype, and seen to clearly affect the shell failure load in the numerical analysis.

The columns design, though, was not detailed as part of the prototype planning. The only concern is to properly simulate the boundary conditions and allow the beam deformation. Consequently, no failure (buckling of the column) should take place in the test. The columns were designed as short columns, with a height that allows for the ease of instrumentation of the lower surface of the shell (selected as 80 cm). A steel scaffolding bracing system was constructed to restrain the lateral movement of the columns during the test and ensure stability of the supporting structure.

Table 7 summarizes the geometric properties of the shell, the boundary beam and the columns of the scale model, with the nomenclature illustrated in Fig. 62.

Table 7: Geometric properties of the shell scale model

Radius of curvature R (cm)	206
Half the central angle (φ) (degrees)	37.38
Rise (a) (cm)	42
span (2r) (cm)	250
Surface area of the shell (2 π R a) (cm^2)	54700
Number of columns	8
Column height (cm)	80
Shell thickness (mm)	25
Ring beam width (B) (mm)	100
Ring beam depth (H) (mm)	150
Column dimension (square column) (mm)	150

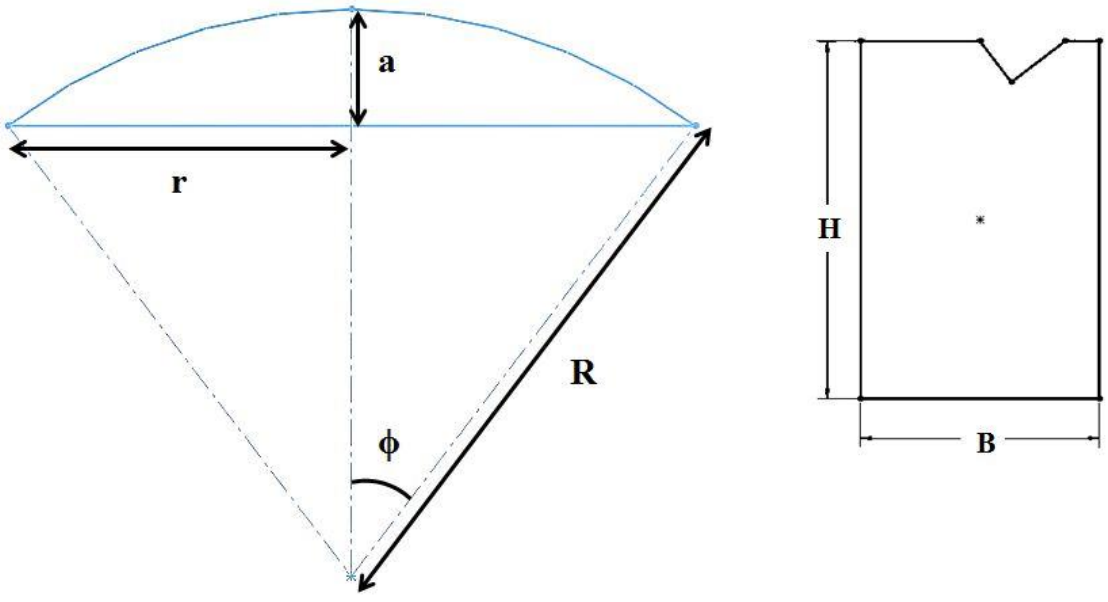

Fig. 64: Shell and ring beam model nomenclature

4.4.1.2. Concrete Material Design

Different material design guides from *'Structural Modeling and Experimental Techniques'* [59] were used as a reference for selecting the model concrete mix proportions. The following points were determined as the design basis for the model concrete:

- Ensuring mechanical properties that are representative of the prototype concrete. The judging property in this research is the compressive strength of standard concrete cubes of 15 X 15 X 15 cm. no tensile strength tests were conducted.
- The largest possible aggregate size was always used in the model in order to minimize the relatively high tensile strength of model concretes, as concluded in the various previous physical modeling studies [59].
- Early strength is an important requirement for the time constraints of this research and reuse of molds. Consequently, water reducing concrete admixtures and other additives were used in the mix.

Table 8 presents the mix proportions for one cubic meter of the concrete used for the supporting structure (columns and ring beam):

Table 8: Concrete mix design for the supporting structure (1 m3)

Concrete Mix Design	
w/c ratio	0.39
Cement (kg)	384
Coarse aggregates (kg) (maximum nominal aggregate size <10 mm)	1242
Fine aggregates (kg)	670
High range water reducing agent (Liters) (~ 1.5% by weight of binder)	7
Silica fume (kg)	16

A series of standard concrete cubes were cast for the purpose of determining the 3-day, 7-day and 14-day compressive strength of the concrete using the ASTM standard

concrete compressive strength test (testing apparatus shown in Fig. 63). Table 9 presents the individual results of compressive strength tests on the support system concrete cubes.

Table 9: Compression test results (supporting structure concrete mix)

Concrete Age	Cube maximum compression force (kN)	Mean Compressive strength (MPa)
3 days	452.8	18.4
	448	
	471.5	
	348.9	
	406.2	
	362.9	
7 days	479.3	24.1
	556.9	
	571.2	
	526.6	
	539.9	
	584.9	
14 days	739.2	30.8
	691.6	
	648	

Fig. 65: Concrete compression test apparatus

The 3-day mean compressive strength of the mix = 18.4 MPa while the 7-day mean compressive strength = 24.1 MPa, and the 14-day mean compressive strength is equal to 30.8 MPa, with a 20% difference from the planned compressive strength for the prototype, which was accepted for the purpose of this study.

The same concrete mix was attempted for casting the dome panels with the difference of using larger quantities of smaller size aggregates (100% passing sieve size 9.5 mm and 50% passing sieve size 4.75 mm). The small aggregate size was needed because of the small panel thickness (2.5 cm) and the small spacing of the reinforcing wire meshes, as will be explained later in the reinforcement design. The mix resulted in a slightly higher 7-day mean compressive strength (3-day strength = 20.5 MPa and 7-day

strength = 25.9 MPa), which was advantageous in this case since an early strength gain was required for the panels. Table 10 presents the maximum compressive cube forces obtained in standard compressive tests:

Table 10: Compression test results (Initial panels concrete mix)

Concrete Age	Cube maximum compression force (kN)	Mean compressive strength (MPa)
3 days	441.1	20.5
	464.4	
	478.5	
7 days	519.7	25.9
	639.9	
	589.1	

However, two trial panels were cast to test the quality of the mix and resulted in an unsatisfactory quality of panels as shown in Fig. 64. This was attributed to the still relatively large proportion of the larger coarse aggregates. The mix was adjusted by increasing the portion of well-graded aggregates passing sieve 4.75 mm, increasing the ratio of fine aggregates in the mix, and also reducing the w/c ratio to provide an even earlier strength gain. The early-strength requirement was more crucial in the panels for the following reasons:

- The panels were removed from the molds after 1-day so that the molds can be reused for casting the next set of panels
- For time constraints, assembly of the panels was started 3 days after casting of the last set of panels.

Fig. 66: Panel cast using initial concrete mix

Table 11 presents the proportions for the new concrete mix designed for casting of the panels:

Table 11: Final concrete mix design for the shell panels (1 m3)

Concrete Mix Proportions	
w/c ratio	0.35
Cement (kg)	384
Coarse aggregates (kg) (maximum nominal aggregate size <10 mm)	1111
Fine aggregates (kg)	763
High range water reducing agent (Liters) (~ 2% by weight of binder)	9.84
Silica fume (kg)	16

Nine initial cubes were cast separately, and then more cubes were cast from the same batches used for casting the panels, in parallel with casting of the panels, as a way to monitor the quality of the mix and ensure homogeneity. It was noted, however, that that technique has resulted in a larger variance of cube strengths due to the slightly differing mixing, casting and curing conditions of each batch. The mean 3-day compressive strength of the concrete cubes = 21.3 MPa and the 7-day strength = 23.1

MPa, and the 14-day strength = 28.0 MPa, which is only 12% higher than the planned prototype compressive strength of 25 MPa. Table 12 presents the individual cube results. The resulting strength was deemed as acceptable and the mix was used for casting the shell panels.

Table 12: Compression test results (final shell panels concrete mix)

Concrete Age	Cube maximum compression force (kN)	Mean compressive strength (MPa)
3 days	470	21.3
	435.8	
	411.7	
	564	
	522	
	453.5	
	494.4	
7 days	583.9	23.1
	491.8	
	570.9	
	425.1	
	563.4	
	494.7	
	495.7	
	498.9	
	556.9	
14 days	527.9	28.0
	661.7	
	698.7	

As previously mentioned, many concrete physical modeling studies referenced in reference [59] have documented differences between prototype and model concretes due to size effects. It was recommended, accordingly, that small standard concrete compression test specimen be used for smaller scale model sizes, generally consistent with the scale of the model. In particular, according to reference [59], ACI Committee

444 (1979) recommended using 50x100 mm cylinders as a standard for model concrete mixes [61]. Although in this research the results of standard test cubes were used in the design, nine 5x5x5 cm cubes were cast in order to test the claimed size effects. However, it was found that the smaller cube sizes did not produce larger compressive strengths. On the contrary, a lower compressive strength was witnessed using the 5 cm cubes. However, that was thought to be related to quality of the cubes. This is explained by the fact that after removing of the cubes from the molds, many of them were noted to have geometrical defects. Initially 18 cubes were cast, and then 9 cubes were considered damaged, while the other 9 were tested producing a significantly lower mean compressive strength than their peers of the 15X15X15 cm cubes (26% difference between the 14-day compressive strengths of both cube sizes). Table 13 presents the maximum compression forces and compressive strengths of the 5X5X5 cm cubes.

Table 13: Compression test results (5 cm cubes)

Concrete Age	Cube maximum compression force (kN)	Mean compressive strength (MPa)
3 days	23.6	10.3
	28.1	
	25.6	
7 days	51.2	18.2
	47.7	
	37.7	
14 days	55.9	20.8
	48.4	
	51.9	

4.4.1.3. Reinforcement Design

The governing factor for designing the model reinforcement was the availability of rebar and wire sizes. It is known to be rare to find the correct number and size of model bars and usually slightly different sizes have to be used. A correctly scaled model force can, however, be produced considering both the reinforcement area and yield strength [60].

A standard tensile test was performed on the steel wires used for the shell reinforcement (testing apparatus shown in Fig. 65). Fig. 66 shows the load-elongation graphs of three different specimens. Each specimen consists of one wire of 1 mm diameter.

Fig. 67: Tension test apparatus

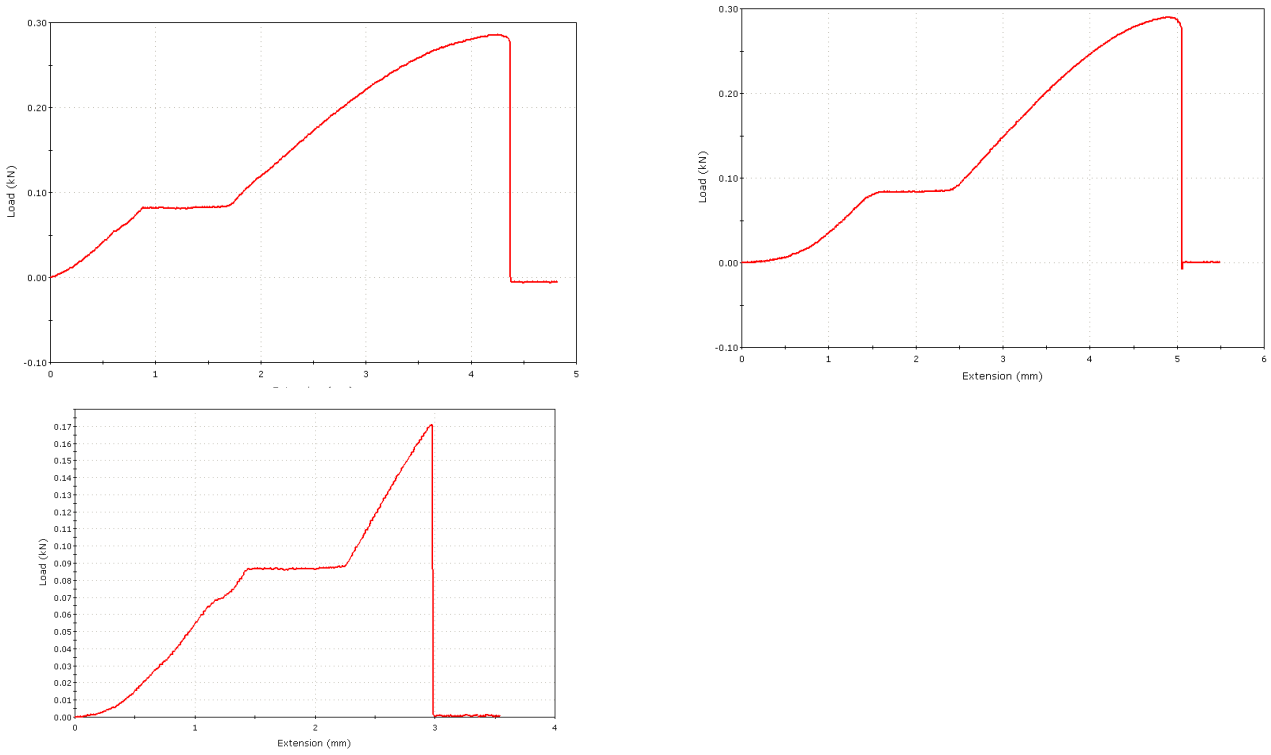

Fig. 68: Load-elongation curves for steel wires used to reinforce the shell panels

From figure 66, the yield tensile force is 83 N, 86N, and 88 N for specimens 1,2 and 3 respectively. This results in a mean tensile yield stress of 109.1 MPa, while the prototype reinforcement is planned as 280 MPa. Table 14 presents the scaling of the model shell reinforcement to produce a correctly scale model force.

Table 14: Comparison between prototype and scale model shell reinforcement

Specimen	Reinforcement Type	No. of rft bars	As	Fy	As*Fy
Shell Prototype	Commercially available deformed bars	Two layers of 5φ8/ 1000 mm	502.7 mm2/1000 mm	280	140756
Sell Model	Commercially available steel welded wire mesh of 1-mm bars and 15-mm spacing	Two layers of welded mesh (~7 bars per layer/ 100 mm)	11 mm2/ 100 mm	109.1	1200.1

A_{steel} scale = 502.7/11 = 45.7 ~ $(6.8)^2$

Force scale = 140756/1200.1 = 117.3 = $(10.8)^2 \sim S_\sigma S_a$

The model wire tensile yield stress is found to be far less than that of the planned prototype reinforcement. Consequently, the reinforcement area was increased to correct for that difference resulting in a $(6.8)^2$ reinforcement area scale, in order to produce an approximately properly scaled model tensile force of $(10.8)^2$.

The following should be noted regarding the model shell reinforcement:

- Although the prototype shell reinforcement is planned as upper and lower layers of steel meshes, the two layers in the model panel were placed in the same location almost in the middle of the panel thickness. This distortion was necessary due to the difficulty of accurately placing an upper and lower layer because of the small panel thickness (2.5 cm).
- Commercially available wire reinforcement bars rarely have the desired yield strength or ductility without proper heat treatment. In this research, as shown in

the wire reinforcement tension tests, the wires lack a sharp yield point and have limited ductility. However, they were not deformed or annealed to match the stress-strain curves of the prototype reinforcing bars. Therefore, although the model tensile force is adjusted to be within acceptable limits, the bond strength of the wire-concrete interface is expected to be significantly lower than the prototype.

- The largest possible splice length of the shell wire mesh reinforcement is used. As will be shown in the design of the panel, each had an edge long joint of 5 cm width and 1 cm depth. The wire mesh of each panel was extended across the joints for 5 cm outside the perimeter of the panel, thus creating a 10 cm reinforcement overlap length at each of the 30 joints across the shell surface.

Scaling of the shell reinforcement was made convenient by the fact that the wire diameter is almost of the required order of magnitude for a 1/10 scale of the prototype reinforcement. However, that was not the case with the boundary beams and columns where slightly larger bars are used in the prototype (16 mm, 18 mm, 20 mm or 25 mm in diameter), but no wires were available to reproduce this size in the model. Consequently, a larger size bars were used (6 mm in diameter) and the overall beam and column steel area had to be adjusted accordingly.

A standard normal tensile test was performed on three different specimens of the model beam and column reinforcement. From Fig. 67 of the load vs. deflection of the three tested specimens, the yield tensile forces for specimens 1, 2 and 3 are 8800 N, 8750 N, and 7700 N respectively. These forces result in a mean yield stress of 297.7 MPa. Given the lower yield stress of the model bars than the planned prototype reinforcement, the same approach was followed with the ring beam longitudinal reinforcement (main reinforcement and torsional longitudinal reinforcement); the reinforcement area in the model was increased to compensate for the low yield stress of the available bars resulting in a $(9.6)^2$ force scale. Table 15 presents a comparison of the longitudinal steel area and reinforcement force in both the model and prototype.

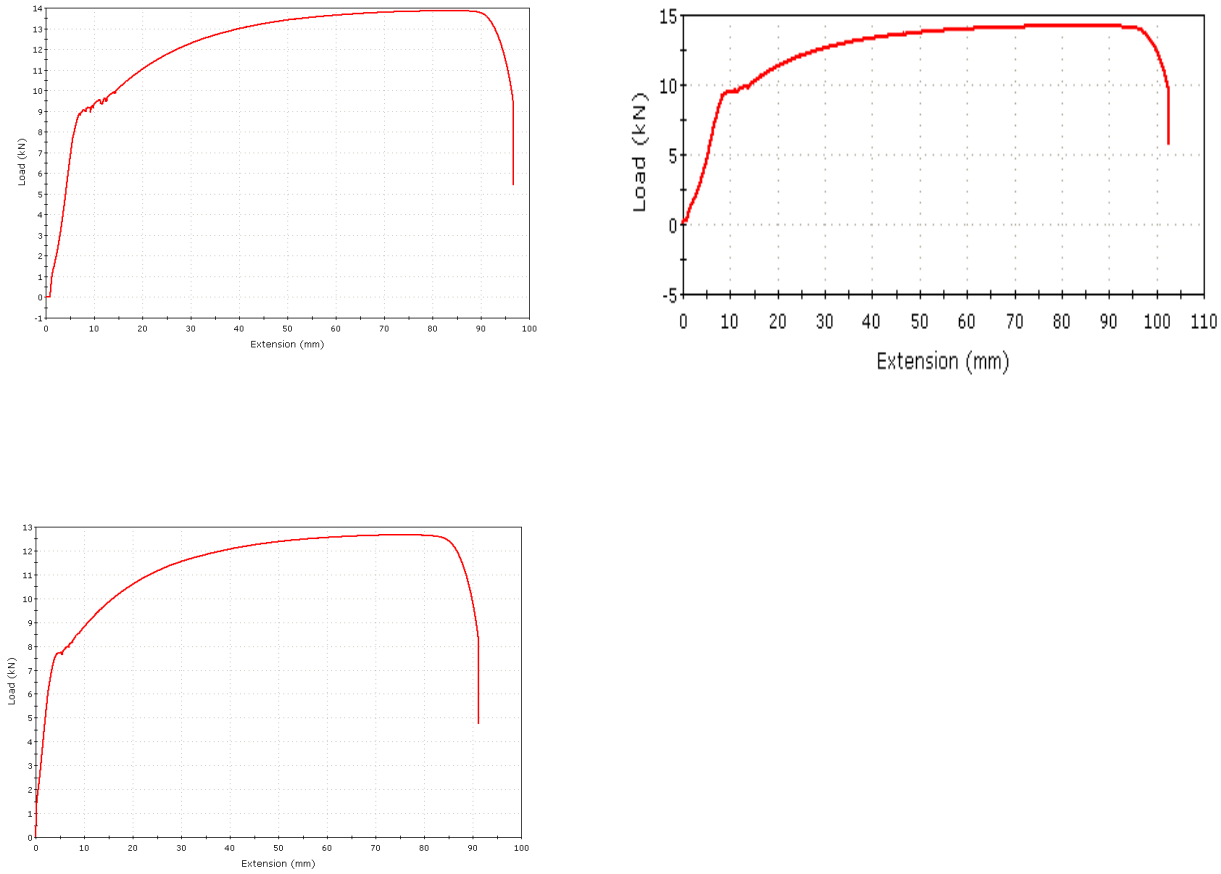

Fig. 69: Load-elongation curves for steel bars used to reinforce ring beam and columns

Table 15: Comparison between prototype and scale model ring beam reinforcement

Specimen	Reinforcement Type	Longitudinal Reinforcement	As (mm^2)	Fy (MPa)	As*Fy
Beam prototype	Commercially available deformed bars	Bottom reinforcement 7Φ25 Upper reinforcement 7Φ25 Torsional longitudinal reinforcement 8Φ12	7777	400	3110805
Beam model	Commercially available smooth bars	Bottom reinforcement 2Φ6 Top reinforcement 2Φ6	113.1	297.7	33669.1

A_{steel} scale = 7777/113.1 = 68.8 ~ $(8.3)^2$

Force scale = 3110805/33669.1 = 92.4 = $(9.6)^2$ ~ $S_\sigma S_a$

As for the beam stirrups, in the prototype beam no stirrups were needed and so minimum stirrups were provided as 5Φ10/m. In the model, a stirrup spacing of 15 cm was provided using the available bars as 6 mm and single stirrups.

The column reinforcement was not a part of the prototype design specifications as planned in the previous section. As previously explained, the main purpose of constructing the columns in the scale model was to reproduce the boundary conditions of the prototype as closely as possible, and allow deformation of the ring beam that is prominent in controlling the failure behavior of the shell. Thus, eight columns are provided around the perimeter of the beam and designed as short columns. Fig. 68 shows the ring beam and column stirrups using Φ6 bars.

Fig. 70: Column (left) and ring beam (right) stirrups

Table 16 presents calculations of all the straining actions of the model shell, beam and columns, similar to those conducted for the prototype, while table 17 presents a summary of the reinforcement of each structural member, as explained earlier in the model material scaling process. The straining actions are calculated based on an ultimate design load of 1.5 times the dead weight of the dome and 1.5 times a live load of 1 kN/m^2.

Table 16: Model shell and ring beam forces

Forces due to dead load	
Dead load per unit of surface (g) (kN/m2)	0.61
Total load due to dead weight (kN)	3.35
Meridional force (Nφ) (kN/m) (at crown)	-0.63
Hoop force (NΘ) (kN/m) (at crown)	-0.63

Meridional force (Nφ) (kN/m) (at foot)	-0.70
Hoop force (NΘ) (kN/m) (at foot)	-0.30
Horizontal force H (kN/m) (at foot)	-0.56
Forces due to live load	
Live load per unit of surface (g) (kN/m2)	1.00
Total load due to live load (kN)	4.91
Meridional force (Nφ) (kN/m) (constant)	-1.03
Hoop force (NΘ) (kN/m) (at crown)	-1.03
Meridional force (Nφ) (kN/m) (constant)	-1.03
Hoop force (NΘ) (kN/m) (at foot)	-0.27
Horizontal force H (kN/m) (at foot)	-0.82
Total ultimate forces	
1. Shell Forces	
Maximum Meridional force (Nφ) (kN/m) (compression)	-2.60
Maximum Hoop Force (NΘ) (compression)	-2.49
Minimum Hoop Force (NΘ) (Compression)	-0.86
Horizontal force H (kN/m) (at foot)	-2.07
Maximum negative bending moment (at foot) (kN.m/m)*	0.0155
Maximum positive bending moment (kN.m/m)*	0.0021
2. Ring beam forces	
Total ultimate vertical Load (kN)	12.39
Horizontal force H (kN/m)	2.07
Vertical force V (kN/m)	1.58
Beam own weight (kN/m)	0.41
Total vertical force on ring beam per meter (kN/m)	1.99
Axial Force (Tension) (kN)	2.58
Maximum shear force (kN)	0.98
Maximum bending moment at mid-span (+) (kN.m)	0.08

Maximum bending moment over C.L. of column (-) (kN.m)	0.16
Maximum Torsional moment (kN.m)	0.01
Angle between axis of column and section of maximum torsional moment	9^0 33'
3. Forces on the support columns	
Total Vertical Load (kN)	15.64
Load on each supporting column (no. of columns = 8) (kN)	1.96
Load on each supporting column including its own weight(kN)	2.05

* bending moment values were based on approximations provided by [94]

Table 17: Summary of the 1/10 scale model reinforcement

Structural Element	Type of Reinforcement	Reinforcement Rebar
Shell Reinforcement	Hoop and Meridional Reinforcement	Two layers of welded wire meshes with 1-mm wire diameter and 15 mm spacing
	Bending reinforcement	Covered by the upper and lower membrane reinforcement
Ring beam reinforcement	Bottom Reinforcement	2ϕ6
	Top reinforcement	2ϕ6
	Stirrups	ϕ6 @ 15 cm
Column Reinforcement	Axial Reinforcement	4ϕ6
	Ties	ϕ6 @ 10 cm

4.4.2. Mold Design and Fabrication

The design and fabrication of the panel molds was one of the most time-consuming and sensitive to quality control tasks of the experimental analysis for the following reasons:

- The panels are initially part of a sphere i.e. they possess a doubly curved form, which is much more difficult to produce than most other forms. The doubly curved form is almost impossible to produce without help of an elaborate 3D model and an equally elaborate smart machining operation to break the complex 3D model into points in the three dimensional coordinate space.
- The structure's geometry is designed to enable reusing of each mold several times during the construction in order to save fabrication costs. This desired quality, however, dictates that panel mold material be durable. It also means that any measurement mistakes in the molds, however small, would echo in several parts of the shell and their effects would be consequently amplified.
- The availability of resources (in this case the fabrication machine, its performance and capacity) was also one of the controlling factors that limited the options for the mold material, the number of produced molds, and the required time for the production of each individual mold.

4.4.2.1. Mold Design

3D models of the panel molds were created using SOLIDWORKS. A total of three mold designs were built. As discussed in the geometric design of the dome, the whole structure requires 20 panels in two unique sizes only. This is divided to 10 identical panels and two sets of 5 panels of the same size but that are mirrors of each other, in terms of the direction of curvature. Thus, the required number of molds to build is three. The three different molds are shown in Fig. 69.

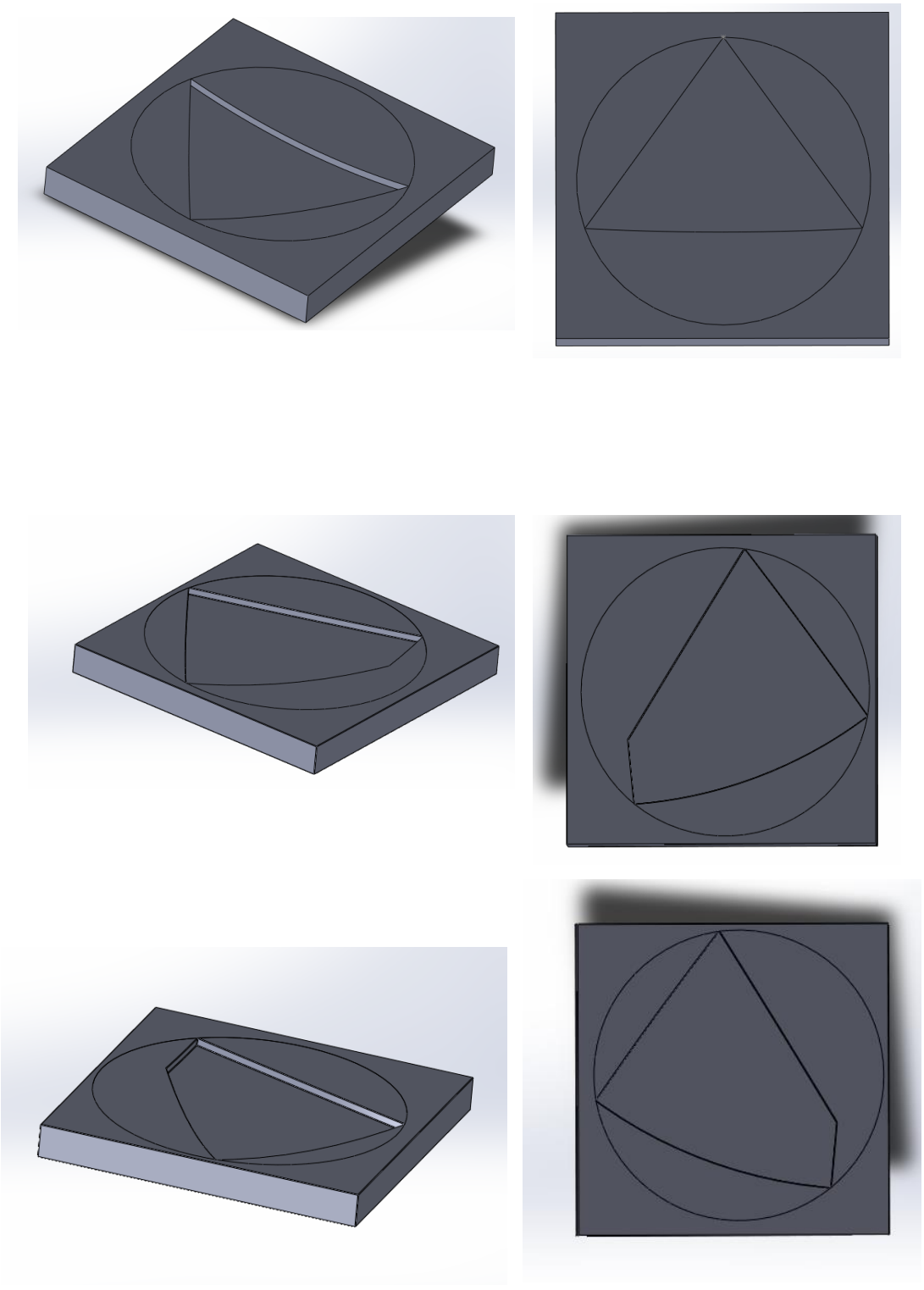

Fig. 71: Mold 3D designs generated using SOLIDWORKS

Ideally, each mold requires two pieces (a positive and a negative piece) to accurately produce the shell panels' upper face and lower face curvature. However, the fabrication time constraints allowed for fabricating the mold beds only, thus accurately producing the shell outer surface curvature, while that of the lower surface was produced and monitored during the casting process using the manual equipment available in the lab, as shall be explained shortly.

4.4.2.2. Mold Fabrication

As previously mentioned, the selected material for fabricating the molds was mostly dictated by the available fabrication method. In the present research, a computerized numerical control (CNC) router machine was used for the fabrication process, shown in Fig. 70. The machine mainly operated on wood and foam type materials with cutting tools of 8 cm length and 6 mm diameter.

Fig. 72: Mold fabrication using CNC router machine

It was decided that foam blocks are the most suitable for the application at hand. The following presents a summary of the fabrication sequence for each mold:

- Blocks of specific sizes of high density foam (36 kg/m3) were custom cut based on the mold design models
- The CNC router machine parameters were set. The cutting and other operation parameters were input using the mold 3D model, and then the machining operation code was posted and imported into the machine software. Usually, pieces of similar cutting requirements are built on two stages: a roughening stage that removes as much volume as possible with a low cut finish quality, then a finishing stage where the surface is smoothed to the desired shape. However, because of the limited time on the machine, only a roughening operation was performed for each mold (see Fig. 71 for mold with rough cutting). Later, the molds were sandpapered manually to produce the desired smooth surface finish.

- The next step was starting of the machining operation. Each operation took, on average, about 50 hours to produce the rough mold shape cut.
- The mold surface was manually treated with sandpaper to produce the desired final smooth surface.

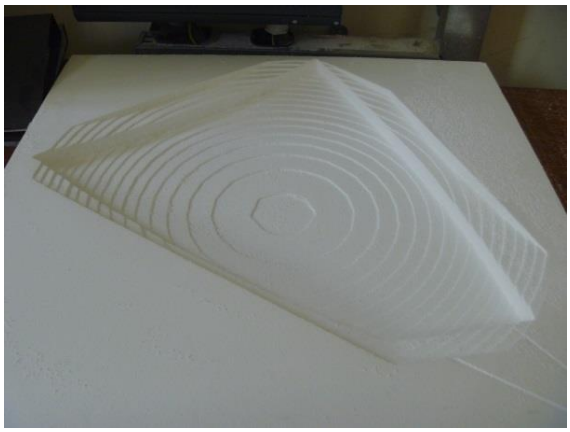

Fig. 73: Mold shape generated through a rough cutting machine operation

- The mold dimensions were checked and adjusted if needed (by lining the mold sides with 0.5 cm-thick pieces). The adjustment was necessary because some discrepancy between the model size of the mold and the produced mold were found in some cases. The reason for that discrepancy could be the sandpapering process that produced slightly larger mold dimensions than the required size (about 0.5-1 cm difference).
- Several pieces of foam of 1-cm depth and 5-cm width were fixed to the mold bed (corresponding to the upper surface of the panel) along the perimeter of each mold, in order to produce the required dimensions for the joints to be grouted in place along the panel edges, as shown in Fig. 72.

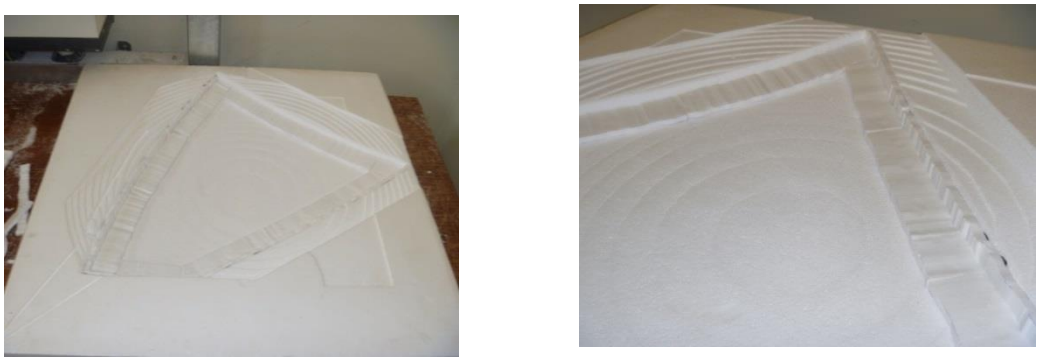

Fig. 74: Lining of the molds to create panel joints

Even though only three molds were needed, four molds were fabricated to reduce the panel casting time in this research. Fabrication of the four molds was completed in about 15 days.

4.4.3. Casting

4.4.3.1. Casting of the Supporting Structure

The supporting structure, consisting of the ring beam and columns, was cast using traditional wooden formwork used in conventional construction. The formwork construction is summarized as follows:

- A supporting frame was built, on which a platform was constructed to the required column height (clear distance of 80 cm) (Fig. 73).
- The platform was used to mark the locations of the columns, create openings for the columns, and support the column forms, as shown in Fig. 74.

Fig. 75: Supporting frame for casting of the columns and ring beam

Fig. 76: Column locations in the supporting platform

- The column reinforcement cages were then placed through the platform with dowels extending through the entire beam depth (Fig. 75).

Fig. 77: Placement of column reinforcement cages

- The beam circular outer and inner forms were then fixed to the platform and the beam main reinforcement bars and stirrup were placed. (Fig. 76)

Fig. 78: Placement of ring beam reinforcement

- Additional dowels were provided at the same stirrup spacing and tied to the beam stirrups (Fig. 77). (These dowels later were bent and overlapped with the shell reinforcement at the interface between the base panels and the ring beam before grouting of the joint.)

Fig. 79: Ring beam dowels

- Additional 4 steel hooks were also tied to the beam reinforcement in four locations around the beam perimeter. These were provided for lifting the structure using the overhead crane.

Building the supporting structure formwork was completed in about 8 hours by 4 construction workers.

In the prototype, the columns shall be supported on appropriately designed footings. However, in this study only the columns were cast. In the test setup section, supporting of the columns in order to simulate the prototype boundary conditions will be discussed.

Casting of the beams and columns was performed simultaneously in order to create a fully monolithic connection between the beam and the supporting columns. The casting sequence is summarized as follows:

- The concrete mix proportions were prepared and mixed in several batches of about 0.08 m^3 each. The total needed concrete volume for the beam and the eight columns was about 0.3 m^3.
- The casting process started with casting of one column, while simultaneously using a vibrator to ensure filling of the whole column height, as shown in Fig. 78.
- The second step was casting of the ring beam section (1/8 of the ring beam) over the already filled column until the next column.

Fig. 80: Casting of columns

- Then the process is repeated for the rest of the columns and beam sections, thus allowing quality control of the columns during at each step, and ensuring a monolithic connection between the ring beam and columns.
- As previously mentioned, the connection between the ring beam and the base shell panels was designed to provide continuity, given that the base part of the shell is where all the tensile stresses initiate and, in the numerical analysis of this research, where a contact gap initiates (between one of the base panels and the ring beam). Thus, the connection was designed to avoid creating a weak point at that location. It has been explained that the design of the ring beam was modified, accordingly, by 'embedding' the base panel inside the beam (see Fig. 40 reshown here).

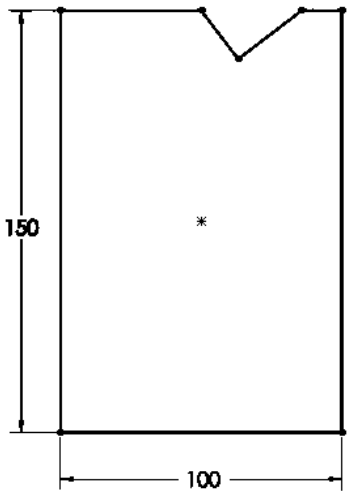

Fig. 40: Adjusted ring beam design

This connection was constructed by casting the ring beam on three stages shown in Fig. 80:

- 13 cm of the 15 cm beam height were cast with the supporting structure at this stage of the construction (shown in Fig. 79 and part A in Fig. 80)
- The top 2-cm of the ring beam in front of the panel (part B in Fig. 80) were cast after assembly of the panels together with the inter-panel joint grouting in the next stage of construction.
- The top 2-cm of the ring beam behind the panel (part C in Fig. 80) were grouted during the very final stage of construction after removal of all formwork, since it was not accessible otherwise.

Fig. 81: Casting of part A of the ring beam

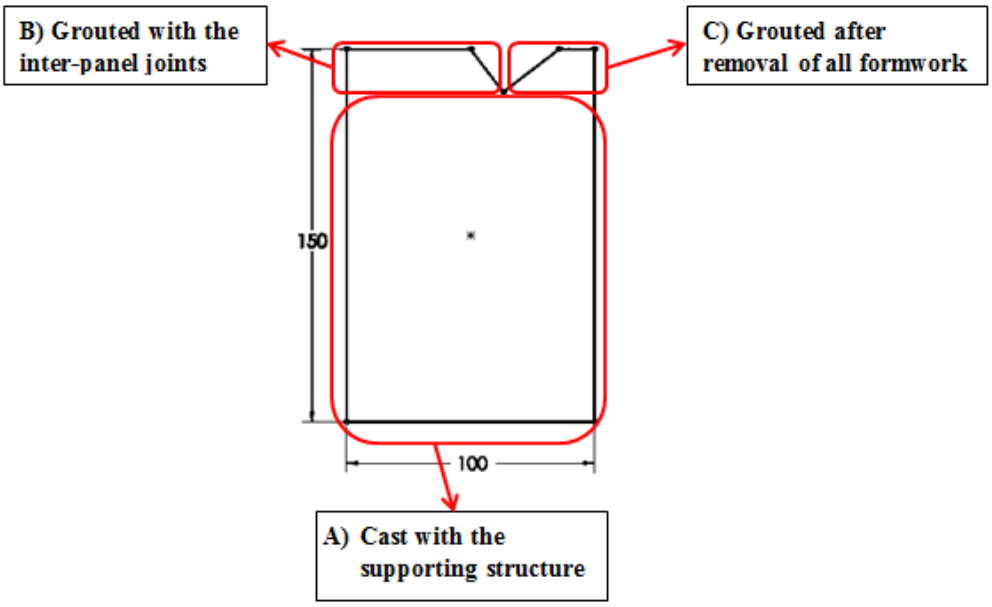

Fig. 82: Three stages of casting of ring beam

After casting of the columns and 13-cm of the ring beam height, this stage of construction was completed. Casting of the supporting structure was completed in about four hours. The upper surface of the ring beam (only exposed surface) was kept moist for about 7 days before any other construction activities took place.

4.4.3.2. Casting of the Shell Panels

The casting plan required 5 days to produce the shell's 20 panels in the four fabricated molds. The following presents a summary of the casting process:

- Wire meshes were cut to the required panel shape. Each mesh extended 5 cm outside the perimeter of the panel as an overlap length across the inter-panel joint (shown in Fig. 81). For the purpose of fitting the wire mesh into the mold, the extra 5-cm mesh length was temporarily bent up during casting of the panel, then straightened again when

Fig. 83: Wire mesh used to reinforce shell panels

the panels were removed out of the molds and prepared for the assembly process.

- The molds, made of high density foam, were painted with a layer of oil, in order to provide insulation and prevent absorption of the concrete water by the foam.
- The wire meshes were placed in the molds. As previously discussed, two layers of wire mesh were installed into each mold resting on the joint foam-spacers (discussed in the fabrication process), hence maintaining the reinforcement layers approximately mid height of the panels (shown in Fig. 82).

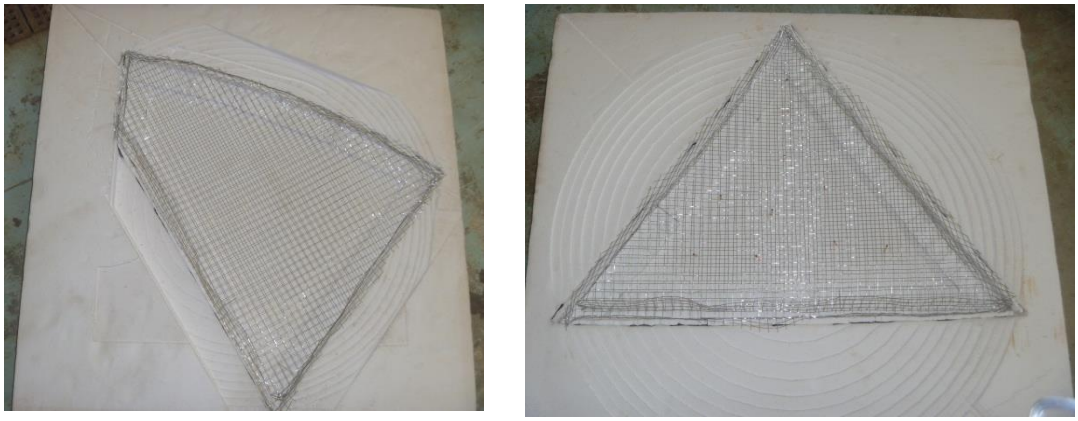

Fig. 84: Placement of wire mesh reinforcement into panel molds

- The wire mesh bent edges were insulted with polyethylene sheets so as to prevent concrete from passing beyond the steel mesh. This problem is illustrated in Fig. 83 of the first batch of panels where the reinforcement was not insulated. The panel boundaries extend after the reinforcement, hence making it impossible for the wire to be straightened back and extended across the inter-panel joints. The panels were recast using the polyethylene sheet insulation (Fig. 84).

Fig. 85: Panels cast without reinforcement insulation

Fig. 86: Panels cast with reinforcement insulation

- Concrete mix proportions were prepared. On average, about 0.03 m3 of concrete were casted per batch. That includes casting of the four panels and two cubes. These cubes were tested for 3-day and 7-day compressive strength, as a way to test the uniformity of the mix quality for each set of panels.

- Concrete materials were mixed and the four panels were cast. Extra care were given to the following:
    - Having a workable concrete mix that easily passes through the 1.5-cm by 1.5 cm mesh squares of the reinforcement.
    - Maintaining workability only exactly as needed and not having a very light and watery mix. This was important because the panel double-curvature was produced and maintained manually. Watery mixes proved to be incoherent causing their water to abandon the concrete and gather in the middle (the low curvature) part of the panel (shown in Fig. 85).

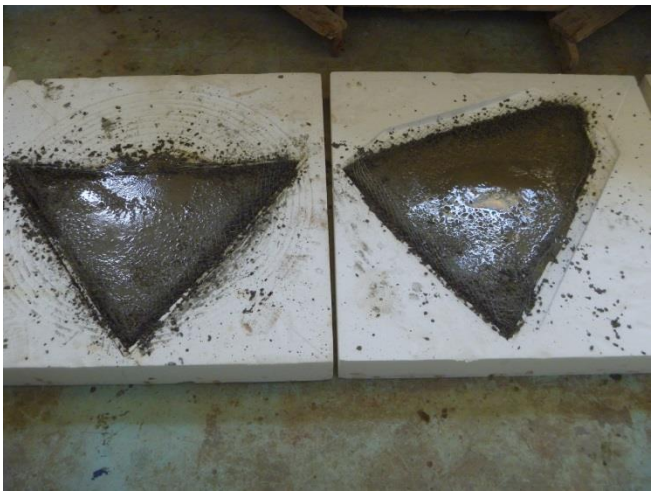

Fig. 87: Departure of water to the low curvature part of the panels

    - As mentioned above, the panel double-curvature was ensured manually (Fig. 86). This was performed by closely smoothing the panel edges to take the edges curvature, and then the middle part was slightly lowered. 2.5-cm thick foam pieces were placed around the center of the panel to guide the surface smoothing to a properly curved lower panel surface.

Fig. 88: Surface finishing of shell panels

- Right after casting each panel, 2.5-cm foam pieces were used to measure the height at different random locations around the panel to make sure the surface has a uniform thickness.

- The panels were unmolded after one day and placed into the curing room for 7 days. The molds were reused for casting the next set of panels. the panels were always kept moist in the laboratory before starting the assembly process.

4.4.4. Construction

As previously mentioned, the assembly process was planned to simulate the prototype suggested construction method as closely as possible. Some deviations were necessary, though, as will be explained where relevant. These deviations were mainly due to some quality problems in the production of the panels and other formwork. In the final chapter of this study, a few recommendations are listed to overcome these problems in future implementations of this system. The following is a summary of the steps taken to erect, assemble and finish the shell system:

4.4.4.1. Scaffolding Design

Prior to the assembly process, a simplified scaffolding system was designed with the help of 3D design software SOLIDWORKS. The scaffolding system consisted of props located at each panel corner location (where the vertices of the panels meet) with girders tying the props together. The SW model defined a. the locations of each prop, and b. the required height of each prop to reproduce the proper panel location and orientation. Fig. 87 shows the simulation in 1D line elements.

A simulation of the assembly process was performed on SW using an assembly type file. This was done in order to ensure the accuracy of the dimensions, panel locations, prop heights, and connectivity with the boundary beam. It should be noted that any dimensional error that would lead to a physical inaccuracy is caught by SOLIDWORKS relations

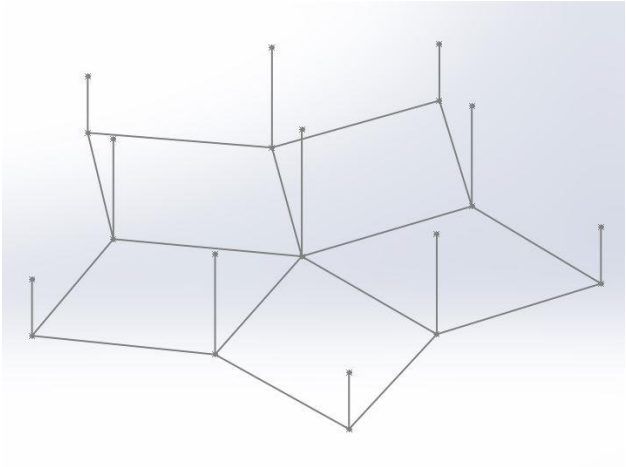

Fig. 89: Scaffolding simulation model

manager and the problem is reported by the program for adjustment. Fig. 88 illustrates the assembly stages previously explained in the construction plan section, and the main model construction stages are summarized in the chart of Fig. 89.

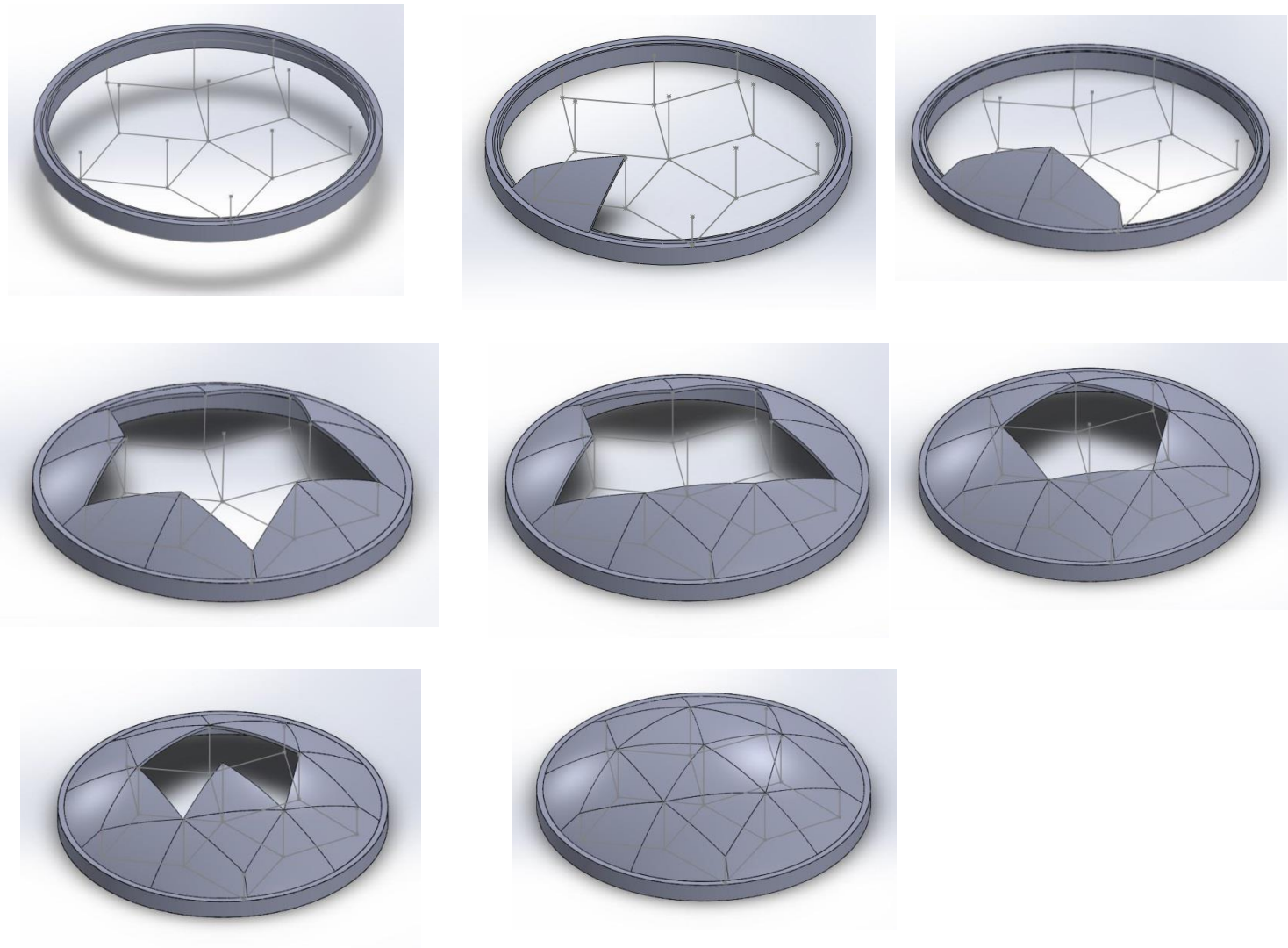

Fig. 90: Assembly sequence of scale model simulated using SOLIDWORKS assembly

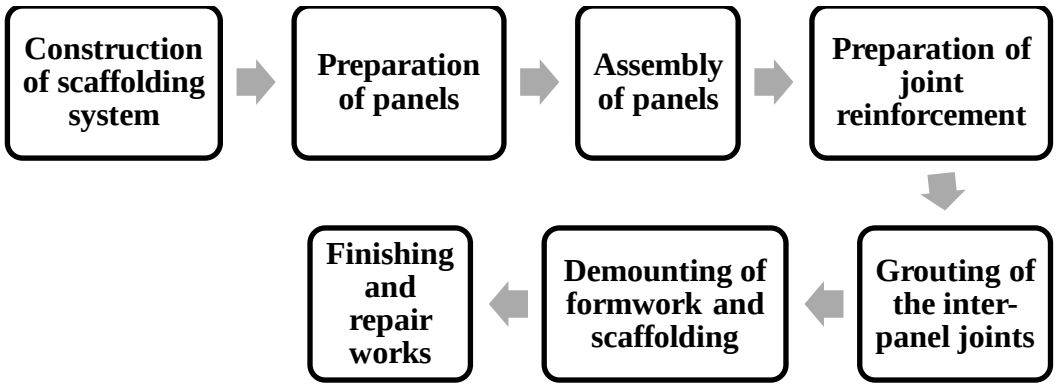

Fig. 91: Construction stages of scale model

4.4.4.2. Construction of Scaffolding

The model assembly started with setting out the origin and main orthogonal axes for the shell's circular base. Those were used to define the coordinates of the points that determine the locations of the props (panel corners). A framework consisting of vertical props (shown in Fig. 90) and horizontal girders tying the props was then built using the available wooden props (same as those used for creating the columns and beam formwork and used in low-key conventional construction).

Fig. 92: Construction of scaffolding props

Numerous problems were faced during building of the scaffolding, mainly because the low quality and associated inaccuracies of manual scaffolding systems. It should be noted that while that system was more economical and convenient for the laboratory experiment conditions, more elaborate versions of commercially available

girders and props with customized heights are recommended for the assembly of the prototype structure.

- The panels were prepared for assembly by removing of the polyethylene insulation sheet used to protect the reinforcement mesh, and re-straightening the edges of the mesh along the perimeter of each panel, in preparation for joining with other panels
- The panels were then assembled on three stages, as previously explained in the construction plan section: row A panels, row B panels and row C panels. Fig. 91 illustrates the assembly sequence.

Fig. 93: Assembly sequence of scale model

As illustrated in the design of panels and mold fabrication, a 10-mm deep, 100-mm wide recess exists along the interface between each two panels (50-mm recess in each panel). This means that 15 mm of the panel edge height is to be placed directly against the edges of other panels, while the top 10 mm are to be grouted later to provide a continuous connection.

However, during the assembly process some unplanned for intermediate spaces were found between the panels, as shown in the assembly sequence pictures (Fig. 91). These were in the range of 1 cm and as high as 4 cm in some instance. These spaces were traced back to have been caused by the following:

During casting of the panels, the bent wire meshes along the edges of each panel did not closely follow the edge. The bending and sheet covering of the steel wires, thus, left a space of about 0.5-2 cm at the edge that was, as a result, trimmed of the panel dimension resulting in smaller size panels. The error was covered up during the casting because of the insulation sheets used for the reinforcement that defined the edges of the panels based on the limits of the bent wire mesh (see Fig. 92), and was only clearly visible during the assembly. A few recommendations are later presented in order to overcome that problem in the prototype structure and in future similar model studies.

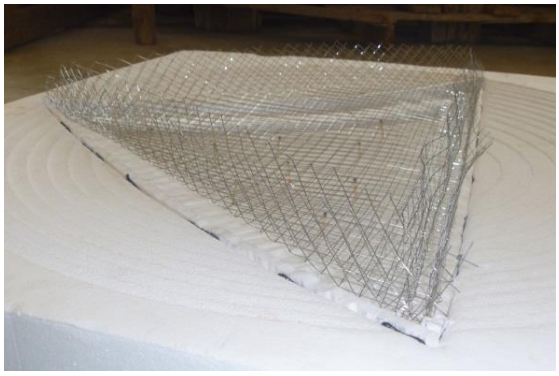

Fig. 95: Dimension discrepancy due to bent reinforcement curvature

Fig. 94: Plywood sheet placed in between panels to overcome dimension discrepancies

In this study, the problem was overcome using 3 mm-thick plywood sheets of enough width to cover the discontinuity between the panels (shown in Fig. 93). These

sheets were extended between the props wherever needed providing a bed for casting the discontinuity in place together with the planned 10-mm deep joint at the interface.

Each assembly stage then proceeded with fixing the props to the horizontal girders on the platform and an initial assembly of the panels. This was followed up by extending customized widths of plywood sheets between the prop heads where needed, or an adjustment of the location of the props, if needed. The same process was repeated for each stage until all of the 20 panels were in place. During the assembly, extra care was given to ensuring as uniform a joint width between all the panels as much as possible, and performing any necessary location adjustments to achieve that. The mean width of all the joints was about 110 mm (instead of the planned 100 mm).

- The joint reinforcement was then prepared. That included two different tasks:
    - Tying of four wire meshes (two from each panels) extending across the joint at the interface using tying wires. The overlapping length is equal to 100 mm (almost equal to the joint width). In some instances, it was difficult to completely straighten the wire mesh and nails were used to fix it to the underlying plywood sheet as a means to eliminate the mesh bending (as shown in Fig. 94). In all the joints, however, the joint grouting was intentionally increased in thickness over that of the surrounding panels in order to ensure sufficient cover over the wires. The same technique may be needed for the prototype structure as well.

Fig. 96: Straightening of wire mesh reinforcement

- The beam dowels (see subsection 4.4.3) were bent and placed inside the joint between the base panels and the ring beam to ensure continuity of the connection. The overlapping reinforcement length is 100 mm between the panel reinforcement wire mesh and the beam dowels (see Fig. 95).


Fig. 97: Bending of beam dowels into intermediate joints with base panels

- The next step was grouting of all the joints. Grouting was done using available non-shrinkage cement-based grout. The process is divided into two different tasks:
  - Casting of the top 2-cm of the ring beam (shown in Fig. 96) which embeds the base panels into the beam section (see subsection 4.4.3). As previously explained, casting of that part was performed together with casting of the inter-panel joints as an attempt to provide the joint with better resistance to initiation of separation at that location and, consequently, failure. However, it should be noted that another weak point may have been created by applying that technique; the contact between the two parts of the beam (the upper 2-cm and the lower 13 cm) which was monitored during the load test.

Fig. 98: Casting of top 2 cm of the ring beam (Part B)

- Grouting of the joints between the shell panels (30 joints in total) (Fig. 97). During the grouting process, the amount of water added to the grout powder was kept to a minimum (the minimum recommended by the commercial brand's technical brochure) which was 3 litres/ 25 kg. The water was added on multiple stages, the grout mixed and the flowability of the grout monitored. Addition of more water was ceased once the grout reached a paste consistency, rather than a flowable consistency. The requirement for that specific consistency stems from the geometry of the curved shell where, if the grout mix is extra flowable, it will slide down the curved surface and settle at the bottom part of the joint length.

Casting of the lower panel joints was completed first and, after one day, casting of the rest of the joints was done. The reason for that was also to provide a boundary of hardened grout as a base for the upper joints (of row B and C panels), thus also helping to partially restrain the grout from departing through the lower joints.

Fig. 99: Grouting of inter-panel joints

- Three days after casting the joints, the beam and column formwork were demounted, simultaneously removing the panels scaffolding system that was only fixed to the beam formwork platform, as shown in Fig. 98.

Fig. 100: Demounting of all formwork and scaffolding

- Two days were then dedicated to finishing and repairing of the structure, which included the following:
    - Grouting of the final part of the ring beam (part C; top 2 cm behind the panels and only accessible after removal of all formwork) thus completing the connection between the beam and the base panels, and embedding the base panels into the beam (see Fig. 99).

Fig. 101: Grouting of the final part of the ring beam (Part C)

    - Repairing of column honeycombing using the same non-shrinkage cement-based grout. Two columns were diagnosed with honeycombing, with one severely compromised (shown in Fig. 100). The grout was used to provide a high-strength and fast repair for the compromised columns.

Fig. 102: Honeycombing found in two of the model columns

- All eight columns were plastered with cement mortar in order to provide a smooth surface finish, as shown in Fig. 101.

Fig. 103: Plastering of all model columns

- As previously explained, the beam was cast on three different stages for connection purposes. After removal of all formwork, a crack was observed between the upper (2 cm) and lower (13 cm) portion of the beam. At this stage, the crack was repaired using cement mortar (see Fig. 102). It was anticipated that that part may originate a weak point as the torsional moment resultant onto beam increases, and it was, thus, monitored closely during the test.

Fig. 104: Ring beam joint cracks

- A concrete cutter was used to trim extra hardened grout observed on the lower surface of the shell (Fig. 103) between the panels, in order to ensure as uniform a thickness as possible for the entire shell.

Fig. 105: Superfluous hardened grout on the lower surface of the shell

The finished structure is shown in Fig. 104, prior to testing preparations.

Fig. 106: Finished shell model

4.4.5. Testing

In this study, the load test of the shell structure is an inelastic, static, ultimate strength test. The inelasticity refers to the nonlinearity of the concrete material preserved by using the same material in both model and prototype structure with a stress scale of 1: 1. This requirement is paramount for the accuracy of an ultimate strength loading test of reinforced concrete structures [59]. The static characteristic refers to the static type of loading i.e. applied very slowly to the structure during the test, as opposed to dynamic load tests. Finally, the major purpose of the test is to determine the failure load (ultimate strength) and failure mode of the structure.

4.4.5.1. Test Setup

After completion of the construction, the model was prepared for the load test as explained in the following steps:

4.4.5.1.1. Model surface preparation

The main parts of the structure to be monitored were painted with a white plastic paint; that includes the upper and lower surface of the shell, and all sides of the boundary ring beam. The purpose of this procedure is to highlight any hair cracks that initiate during the test so that they are both visible and catchable on a recording medium.

4.4.5.1.2. Construction of bracing system

A bracing system was designed, manufactured and installed for the purpose of adjusting the boundary conditions of the structure to closely simulate those of the prototype.
As explained in the previous sections, the ring beam supporting the shell is subjected to a horizontal thrust that must be met with a sufficient horizontal reaction at the base of the structure. In the prototype structure, the column footing shall be designed to withstand the horizontal force and prevent any displacement at the column base (a fixed boundary condition). However, in the model no foundation system is constructed and, hence, a bracing system that withstands the horizontal forces was a must, if similitude conditions were to be maintained between the model and the prototype. A set of 8 deformed steel bars of grade 360 and 12 mm diameter, and set of 8 steel angles were used to manufacture a belt to tie the structure's column s. Manufacturing of the system proceeded as follows:

- The steel bars were cut to a length of 2.8 m (slightly larger than the shell diameter measured between the ends of each two interfacing columns)
- At the mechanical engineering workshop, each bar was threaded for a length of 7.5 cm on each end, and each steel angle was drilled to create two holes of 10 mm diameter at a distance slightly larger than the column dimension.
- Each set of two bars were fixed to the sides of each two interfacing columns using two steel angles, thus creating tension struts at the column bases which produce sufficient reaction force to the anticipated horizontal thrust and prevent displacement of the column bases (see Fig. 105).

Fig. 107: Model column bracing system

4.4.5.1.3. Instrumentation

In this study, only the deflections and the strains were measured, and in as many locations as the lab facilities made possible. It should be kept in mind that the main purpose of the study was the identification of the failure load and failure mode of the shell, rather than an elaborate determination of the stress/strain distributions across the surface of the shell, which would require a larger number of strain gage channels than available, and perhaps a different distribution map of the gages.

- **Strain gages**

Fig. 106 presents a distribution map of the strain gages used to record the strains developed on the lower surface of the shell during the test. 13 strain gages of the one-element type and of a length of 60 mm were used. The strain gage locations shown in Fig. 106 were based on the following:

  - Strain gages 1- 6 were placed to determine both meridional and circumferential strains along half a meridian of the shell
  - Strain gages 7-10 were placed in a repeated location symmetrically across the whole cap surface in order to investigate the symmetry of strains around the whole surface.
  - Strain gage 11 was placed near an observed imperfection in the scale model, which consisted of a panel with a slightly smaller thickness along one edge than the adjacent panel. This has resulted in a visible change in the radius of curvature of the shell at that location and a misaligned connection that is identified as an imperfection which may trigger failure.
  - Strain gages 12 and 13 were placed on two locations normal to each other on the ring beam in order to measure the strains in two perpendicular directions.

The different locations of strain gages are shown with color codes in Fig. 106 and illustrated in the figure legend, while Fig. 107 shows some of the strain gages on the actual structure.

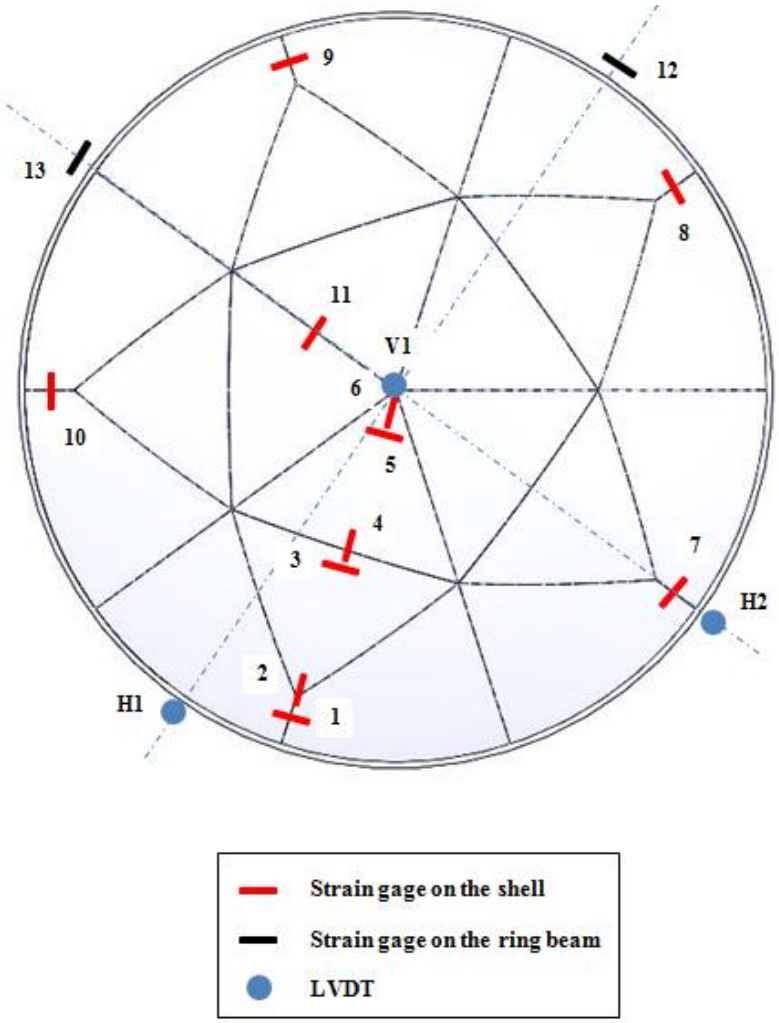

Fig. 108: Strain gage locations map

Fig. 109: Strain gages placed on the shell model

- **Linear variable differential transformers (LVDTs)**

It was of interest to measure the displacement at multiple locations of the shell, specifically for comparison against the finite element model data. The following LVDTs locations were selected based on the maximum displacement locations recorded through the results of the finite element analysis:

Fig. 110: Vertical LVDT (1V)

- 1V at the crown of the shell; being the location of maximum vertical displacement in all FE models of ideal shells (Fig. 108).
- 1H and 2H are two perpendicular locations at the top part of the ring beam where maximum horizontal displacement is expected (Fig. 109).

Fig. 111: Horizontal LVDTs measuring the displacement of the ring beam

LVDT locations are also shown in Fig. 106. Finally, two cameras were set up at different locations to video record the entire test. These recordings were later processed and utilized for interpretation of the shell behavior and failure mode, as shall be discussed in the results chapter.

4.4.5.2. Loading

All the tests in this study were performed using slowly applied loads. Initially, the planned loading was gravity distributed load on the upper surface of the shell. However, as it will be shown in the results chapter, the test was terminated after reaching the maximum load with no signs of failure or significant strains. That allowed performing

more tests on the same specimen with more critical loading conditions until failure was achieved. The three different types of loading are:

- **Test 1:** Axisymmetric uniformly distributed gravity load on the upper surface of the shell
- **Test 2:** Unsymmetrical uniformly distributed gravity load on one half of the surface of the shell
- **Test 3:** Vertical point load at the crown of the shell

The following subsections illustrate the procedure for each test.

4.4.5.2.1. **Test 1:** Axisymmetric uniformly distributed gravity loading test

The load type in this test is static uniform vertical load. This type of load was selected since the study's interest is to determine the capacity of the shell as a multiple (factor) of its weight. The loading system consisted of sand bags of calibrated weights applied incrementally and uniformly to the shell upper surface. This loading method was selected for the following reasons:

- It readily provides a vertical load when applied to the surface of the shell, thus solving the load direction problem
- It makes it possible to apply many bags to cover the entire surface and provide as close to a uniform distribution of the load on the shell surface as possible, without manufacturing of complex loading systems that may be difficult to produce with the available lab facilities.
- The availability of the loading material.

The drawback of the selected manual loading system is that it dictates manual recording of strain and displacement readings. Given that the load is not connected to a load cell that directly measures the load value so it can be paired with the corresponding recorded strain gage readings, the process had to proceed manually. This was performed by applying the load both uniformly and on increments referred to as loading steps. After application of the designated load of each loading step, the strain gage and LVDTs

readings were recorded and associated with that specific loading point. The process was then repeated for the next load steps.

The loading was designed to reproduce a uniform load distribution with 16 sand bags with axisymmetric distribution over the upper surface of the shell. Each sand bag is calibrated at 20 kg in weight, resulting in a total of 0.35 tons for each loading point, which is almost equal to the weight of the model (~0.37 tons).

The loads were applied slowly in order to minimize any dynamic effects. Although the each load step was planned as 16 bags of 20 kg (0.35 tons), during each loading step the strain and displacement readings were taken twice; once after placement of 10 bags, then a second reading at the end of the load step, after placing of the 16 bags. Fig. 110 illustrates the loading of test 1.

Fig. 112: Axisymmetric loading of test 1

4.4.5.2.2. **Test 2:** Unsymmetrical uniformly distributed gravity loading test

The second loading condition was created during the unloading of test 1 loads. The unsymmetrical distributed load was produced by unloading only one half of the shell surface (shown in Fig. 111), resulting in a load value that is the same as the maximum load per unit area applied in the previous test, however on only one half of the structure.

Fig. 113: Unsymmetrical loading of test 2

4.4.5.2.3. **Test 3:** Vertical point load at the crown of the shell

The third load test consisted of a vertical concentrated load at the crown of the shell, which is considered one of the most critical loading conditions for spherical shells. Although this loading test was not what the shell was initially planned to undergo, it was performed for the following reasons:

- Since the shell survived the maximum load applied in test 1, the capacity of the shell was not identified. Thus, a test that presents more critical loading had to be performed to achieve failure and, thus, quantify the structure's capacity.
- After reaching the maximum prepared load in test 1, no more loading was physically feasible. This was due to sliding of the sand bags, especially those on the curved sides of the shell. Therefore, a new loading method had to be introduced to increase the loads.

- This loading method offered a convenient way of applying higher loads that were easily measured using the available load cell, thus guaranteeing achieving of failure. The capacity of the laboratory load cell is 60 tons.

In preparation for the test, the structure was transported using the lab overhead crane to the loading location, which is under a steel frame to which the load cell is attached. The following steps summarize loading process of test 3:

- After transporting of the structure under the lab steel frame, the columns bracing system was reinstalled.
- The location of the lab steel frame girder was adjusted to the required elevation and the load cell was fixed directly above the crown of the shell.
- A steel plate (40X40X4 cm) was placed under the load cell on top of the shell crown, and a sand bag of about the same surface area was placed under the steel plate (shown in Fig. 112), in order to avoid punching of the shell and guarantee the transfer of the load to the rest of the shell.

Fig. 114: Loading setup for test 3

- The same strain gage and LVDT locations were maintained, and they were reconnected to the computer and checked for signal transfer.
- A loading period of 1000 seconds was designated in order to ensure slow load application rate.
- The structure, strain readings and LVDT readings were monitored during the loading procedure. The test was terminated at the onset of failure initiation marked by an observed large displacement and accompanying large cracks.

The results of the loading test are presented and discussed in the next section.

5. RESULTS AND DISCUSSION

This chapter discusses the results of the numerical and experiment analysis of this study. The first section presents the results of a parametric geometric analysis of the structure, which follows from the selected geometry and aims to graphically clarify certain relationships between the division pattern and frequency of the structure, and relevant construction considerations. The second section presents the results of the structural analysis of the spherical cap proposed system. The section discusses the results of different modeling parameters, material properties, boundary and loading conditions of the numerical analysis, and the correlation with the results of the experimental analysis and relevant studies in the literature. The final section presents the results related to the construction process of the structure, including both prefabrication and erection, relevant to the prototype and/or the scale model of the structure.

5.1. Geometric Analysis

This part of the analysis has focused on the geometric parameters of the proposed structure and clarifying different relationships between geometric division of the structure, size and weight of panels to be handled, and the span of the structure. As previously discussed, a MATLAB code was created for the purpose of determining the size and number of panels to be handled which correspond to the user's input span, division frequency and dome configuration (DS/DD). The same code was then modified to graph relationships between these parameters which can be of help to show quick estimates of different parameters controlling the design and construction efficiency of the structure.

As previously explained, the division frequency in spherical division refers to the number of divisions of each spherical polygon's edge. In this study, the division frequencies considered to be appropriate for the structure are referred to as 8v and 4v as explained in the methodology. The other division pattern, which is technically not a division frequency and is also considered in this analysis, is referred to as 'LCD', which is the name of the triangle resulting from that pattern (the Least Common Denominator), as explained in reference [90]. Each of these division pattern result in a different number of divisions, i.e. a different number of panels to be handled for the construction. In addition, every single division frequency results in a different number of panels for the shallower dome (DS) and the deeper dome (DD). Discussing the complete geometric parameters and class II division technique for each of these divisions is seen to be out of the context of this study and can be found in detail in reference [90]. However, the important factors that may directly affect the efficiency of the construction process are outlined here.

5.1.1. Division Properties

Table 18 presents the number of unique panels which result from each division frequency. The number of unique panels is helpful in determining the number of molds that need to be fabricated for precasting the structure's panels (although it should be noted that some of the same size panels are right hand- and left hand- versions of each other and may require two different molds. The reusability of each mold can be determined then from table 19 which presents the total number of panels to be fabricated and handled for the construction, for each division frequency and each structural configuration.

Table 18: Number of unique panels for each division frequency

Division Frequency	8v	4v	LCD	2v
Number of Unique Panels	4	2	1	1

Table 19: Total number of panels for each division frequency

Division Frequency		8v	4v	LCD	2v
Number of Panels	DS	80	20	10	5
	DD	240	60	30	15

As table 18 shows, the 2v division presents the advantage of only one division size, which means that only one mold is reused 5 times for the fabrication of DS panels, and 15 times for DD panels. However, this advantage also means that it produces the least number of panels, and consequently, largest panel size. The large panel size can pose challenges on the construction if the span is relatively large. Hence, 2v division may only be appropriate for very small spans. The detailed relationships between the span, the panel size and weight are presented shortly.

The LCD division also presents the advantage of only one panel size for the entire structure and is only half the size of that of 2v division (resulting in 10 and 30 panels for DS and DD), which gives this division more application for larger span than 2v.

However, it should be noted that the LCD-divided structure is composed of one triangle size but has a right-hand and left-hand version. This means, for conventional molding techniques, that each structure requires the fabrication of two molds.

As the division frequency increases, more unique panels are produced requiring more molds. At the same time, a larger division frequency means a larger number of smaller size panels to be handled for the construction. The suitability of each division frequency to a particular application shall entirely depend on the structural span and the thickness selected for the panels as discussed in the next subsections.

5.1.2. Panel Properties

Fig. 113 and Fig. 114 present the average panel sizes (frequencies 8v and 4v produce different but very similar unique panel sizes) for spans between 10 and 50 m for DS and DD, respectively. Each figure includes three different plots for 8v, 4v and LCD divisions, and clearly shows the large increase in the panel size (expressed in area units) as the span increases for each division frequency, particularly for lower divisions LCD and 4v.

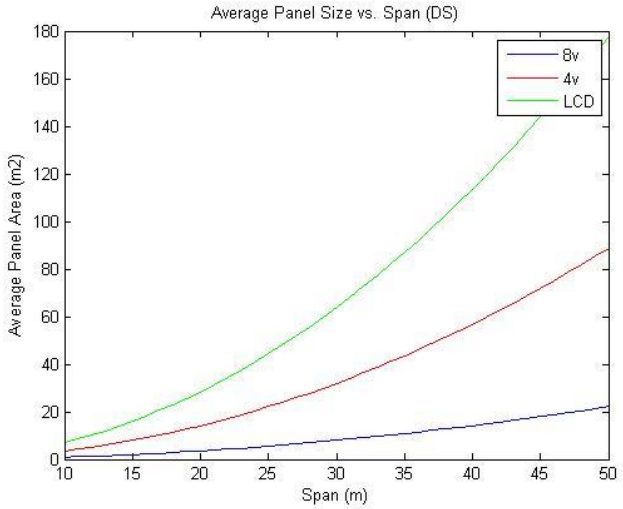

Fig. 115: Average panel area vs. span for shallow dome (DS)

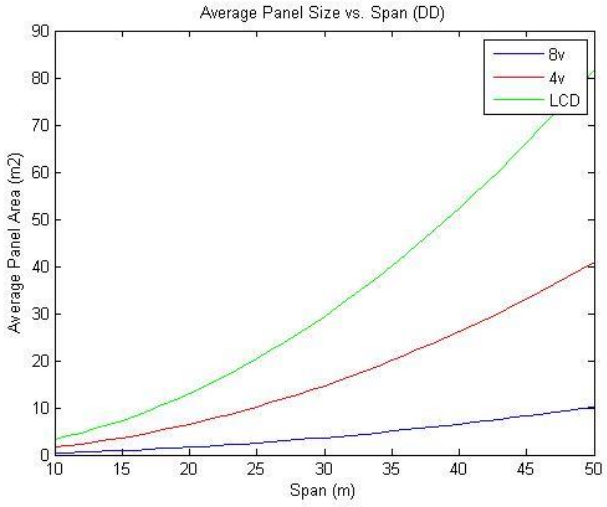

Fig. 116: Average panel area vs. span for deep dome (DD)

Of more practical convenience, Fig. 115, Fig. 116 and Fig. 117 were constructed for the same group of spans between 10 and 50 vs. the weight of the average panel (expressed in tons), as this mostly poses the governing factor for the size of the precast elements to be handled in precast concrete structures. The plot was created for dome thicknesses between span/80 and span/260, and the weights were determined based on normal-weight concrete of density equal to 2500 kg/m3. Fig. 115, Fig. 116 and Fig. 117 present the relationships for divisions LCD, 4v and 8v, respectively.

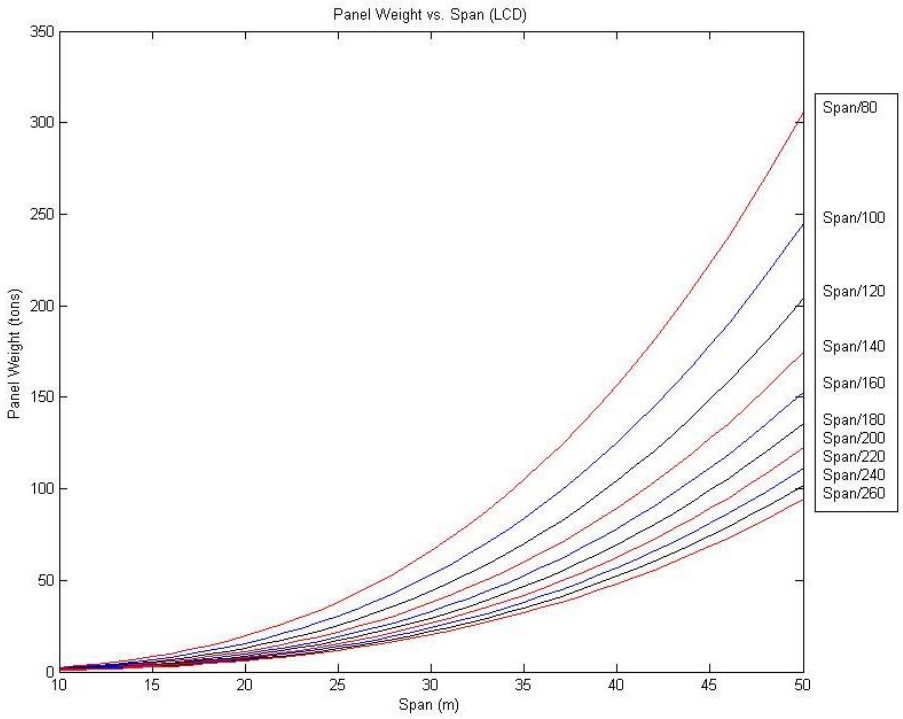

Fig. 117: Panel weight vs. span for LCD division

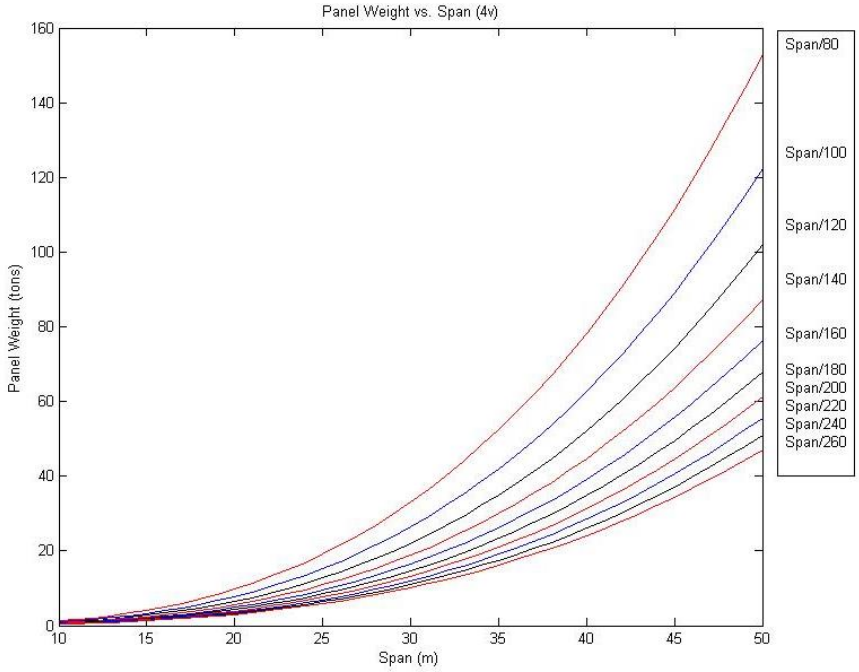

Fig. 118: Panel weight vs. span for 4v division frequency

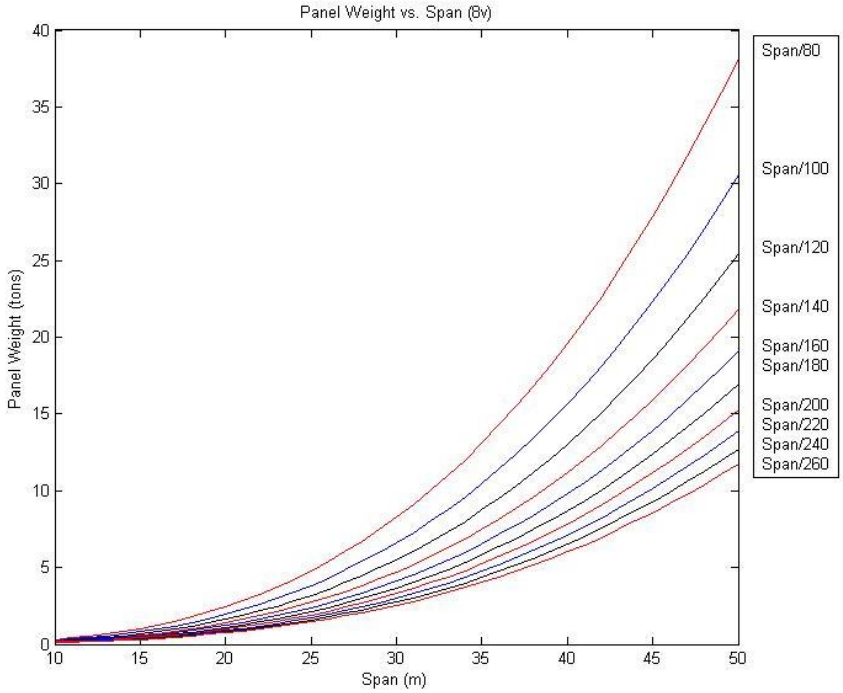

Fig. 119: Panel weight vs. span for 8v division frequency

As shown in Fig. 115, for LCD division the panel weight reaches unrealistically high values for large spans, and even for very small panel thicknesses. Consequently, this division pattern may be suitable for smaller spans up to 20 m only. Division frequency 4v, in Fig. 116, allows for slightly larger spans and thickness ranges than LCD, but is also seen to reach unrealistically large weights for larger spans. The 8v division, while it produces the largest number of unique panels, appears to be favorable when considering the construction process, and seems to be the only suited division frequency for large spans; however, for spans approaching 50 m, it is seen that thicknesses as small as span/260 reaches about 12 tons.

For the present study, the prototype structure is selected to have a span of 25 m, and a relatively large thickness of 25 cm (span/100), and is constructed using a 4v division frequency. These parameters result in a relatively large panel weight of about 15 tons. Division frequency 4v was selected to be suitable for the construction since it only produces two different panel sizes (and requires three different molds). A relatively large thickness was used in order to be on the conservative side for structural analysis purposes, however, smaller thicknesses and, thus, weights may be applicable.

It should be noted that the produced plots and span recommendations in this section only consider the construction efficiency with no regard for the structural behavior. In the next sections, the structural behavior of the selected prototype is analyzed in detail. A future recommendation may be to apply the same analysis to structures of larger spans and smaller thicknesses, in order to further validate the previously produced plots and integrate the structural capacity with the design of the geometric parameters.

5.2. Structural Analysis

This section presents the results of the numerical and experimental analysis of the structural behavior of the proposed structural system under various loading conditions and modeling parameters. As explained in the methodology section of this study, using finite element modeling, the structure is first investigated in its monolithic form with no divisions using different solution parameters, material properties and boundary conditions. The purpose of that initial stage is to determine the adequacy of the constructed finite element model, given that finite element modeling of concrete spherical caps is very scarce in the literature. The resulting values are, thus, compared to those of other experimental or analytical studies using spherical caps possessing the same geometric parameter, and made of concrete or other materials.

At the same time, the built models with the different parameters are compared to each other to present the general patterns of how the behavior of concrete spherical caps is affected by the different solution parameters, material properties and boundary conditions, particularly using the general purpose finite element program ANSYS. This section also presents the results of integrating the effects of constructing the structure using precast panels in the FE model, through the use of contact elements in the ANSYS program. The sensitivity of contact conditions is also explored through a parametric study whose results are presented in the same section.

Finally, the results of the ultimate load test performed on a 1:10 scale model of the proposed prototype structure are presented. The analysis attempts to draw conclusions about the behavior of the segmented structure and the effect of introducing the in-situ stitches, and compare them to the corresponding FE models with the same loading conditions.

5.2.1. Failure Loads of Gravity Loaded Models

Table 20 presents the failure loads of the benchmark models of the gravity-loaded structure. The table refers to each model using the model codes previously discussed in the methodology chapter and summarized in Appendix B with their detailed properties. In table 20, only the main relevant model parameters are highlighted. As previously discussed, the models in this part of the analysis are loaded with large gravitational acceleration, and the failure load is then calculated as a portion of the applied gravity load as force per unit area of the shell surface. The fifth column of table 20 presents a normalized value of the failure load as a multiple of the shell weight. The sixth column presents another normalized value of the failure load as a ratio of the failure load predicted by the linear elastic finite element analysis.

Table 20: Failure loads of gravity loaded FE models

Gravity Loading					
Model Code	Analysis type	Boundary	Failure Load (N/m2)	Failure load (multiple of weight)	Ratio of Linear Elastic Failure Load
MDS01	Linear Elastic	Clamped	3.9E+06	663.7	1.00
MDS07	Nonlinear Elastic	Ring beam	2.9E+06	470.4	0.71
MDS09	Nonlinear Inelastic	clamped	6.2E+05	102.9	0.16
MDS16	Nonlinear Inelastic	Ring beam	3.4E+05	55.4	0.08
MDS17	Small displacement inelastic – concrete crushing enabled	Ring beam	2.1E+05	34.0	0.05
MDS19	Nonlinear Inelastic	Ring beam - with contact elements	3.1E+05	51.6	0.08
SDS03	Nonlinear Inelastic	Clamped	5.8E+05	102.8	0.15
SDS17	Nonlinear Inelastic	Ring beam – with contact elements – debonding with concrete properties	2.5E+05	44.5	0.07
SDS19	Nonlinear Inelastic	Ring beam – with contact elements - debonding with steel properties	2.6E+05	46.6	0.07

SDS20	Nonlinear Inelastic - concrete cracking disabled	Ring beam – with contact elements debonding with concrete properties	5.9E+05	102.2	0.15

Table 20 shows that a large reduction of the spherical cap capacity from the value predicted by the linear elastic analysis after considering the effects of different nonlinearities associated with the structural behavior of the proposed system. It is shown, as expected, that as a result of a linear elastic analysis, the structure fails by a loss of stability at the very high value of 663.7 times its own weight under gravity loading. This high value is expected due to the relatively large thickness of the shell, purposefully selected to conservatively account for the anticipated capacity reduction due to the introduced in-situ joints between the structure's panels, and a few other reasons previously discussed in this paper. Fig. 118 shows the first eigenvalue buckling mode of the clamped structure (MDS01) as an non-axisymmetric buckling which initiates near the crown, with the contours representing the value of the total displacement sum at each node.

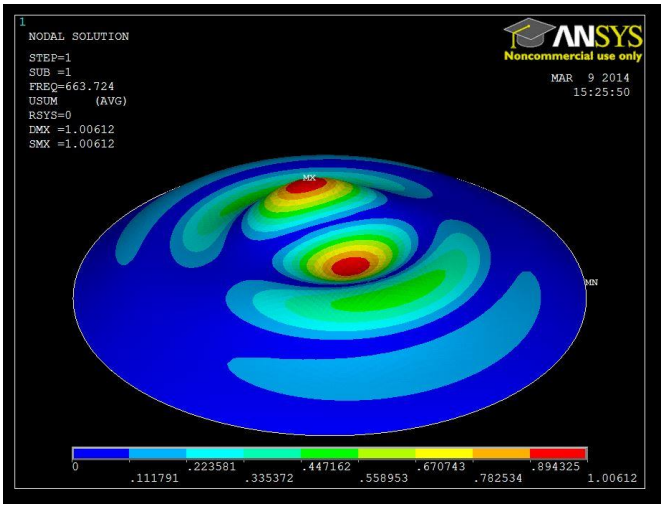

Fig. 120: Total displacement of MDS01

When the geometric nonlinearity is included in the analysis, along with changing the clamped boundary to a line ring beam hinged at 8 locations around the perimeter, and using the same elastic isotropic material properties, the structure fails at a load value of about 71% of the linear elastic failure load value, which, in theory, is consistent with the capacity reduction of shells loaded by normal pressure. At that point, the structure also fails by losing its stability. After using the stabilization command on ANSYS to track the post-failure behavior, it is seen that the structure completely reverses its form exhibiting a classic snap-through buckling mode of failure as seen in Fig. 119 of MDS07. Fig. 119 shows a maximum central vertical displacement value of 8.8 m; slightly larger than twice the shell height (equal to 4.23 m).

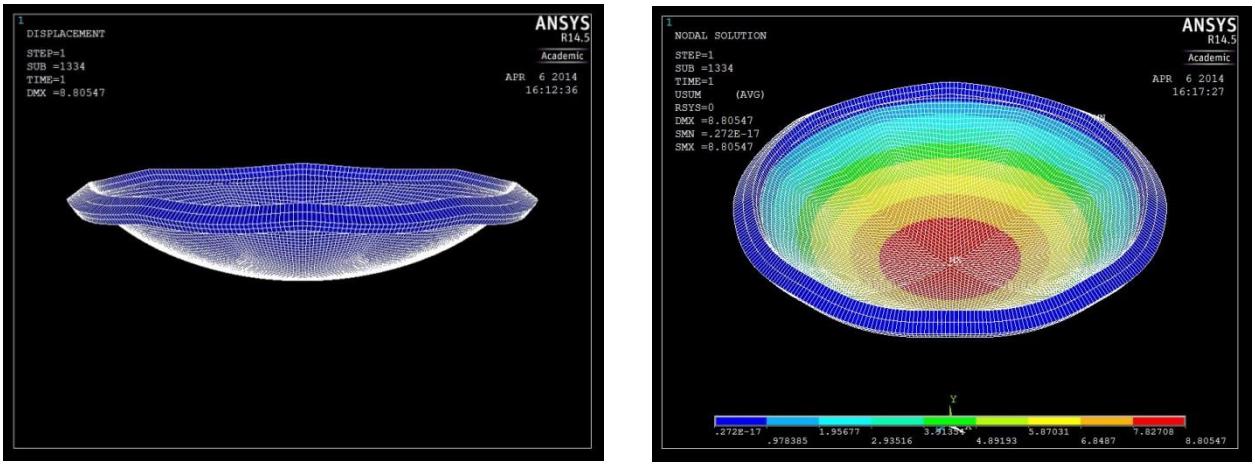

Fig. 121: Snap-through buckling of MDS07

The elastic instability load-deflection path of MDS07 is illustrated in Fig. 120 which presents the normalized load (multiples of weight) vs the central deflection of the spherical cap. The initial linear part presents the typical initial behavior of spherical caps under uniform loads, then at a load value of 470.4 times the cap weight, the structure exhibited a loss of stability at which the load deflection path shows an increase of displacement with no load increase (unstable path). Finally, after the cap completely snaps through, the structure exhibits a stable behavior again with a linear load-displacement relationship. It should be noted though that, while nonlinear stabilization on

ANSYS is able achieve convergence for an unstable structural behavior, it cannot exactly track the load-deflection path where the structure has come to have a negative stiffness (unstable increase of the displacement accompanied by a reduction in the load). Consequently, the use of nonlinear stabilization serves to only confirm the initiation of a structural instability, but is not reliable for judging the postbuckling load-deflection path.

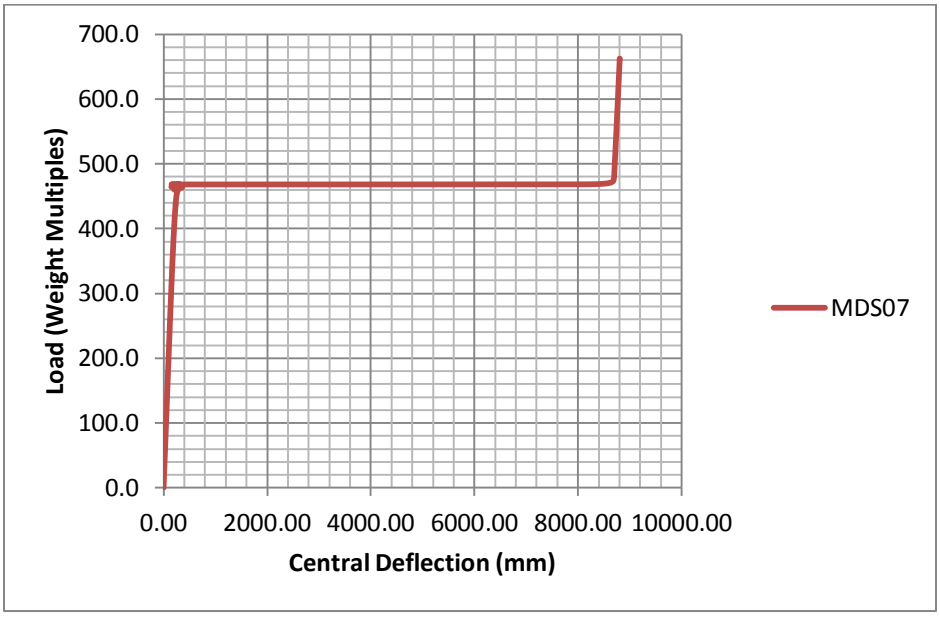

Fig. 122: Load-deflection path of MDS07

Drastic reduction of the structure's capacity to only 16% of the linear elastic failure load was observed when SHELL281 element with linear elastic material properties is replaced by SOLID65 concrete solid element which possesses linear isotropic properties, nonlinear isotropic rate-independent elasticity and concrete material properties. The analysis shows, however, that the structure did not fail by a loss of stability, but rather by a material failure. Fig. 121 shows a comparison between the load-deflection path of MDS07 and MDS09 where both show an almost identical load path till failure of MDS09 at 102.9 times the weight of the structure. The linear load displacement path of MDS09 in the figure illustrates that failure has occurred at a very low displacement.

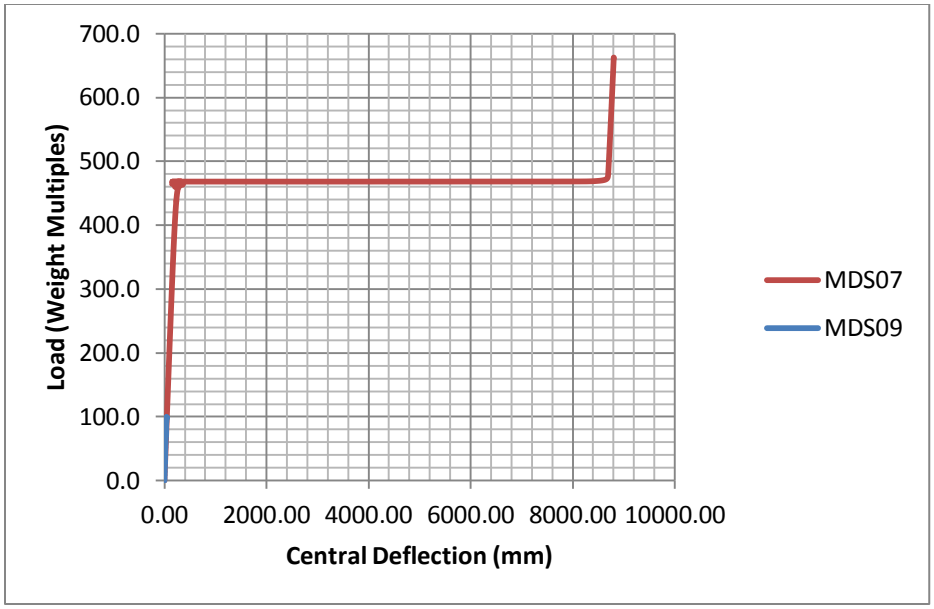

Fig. 123: Comparison between the load-deflections paths of MDS07 and MDS09

An approximate value of the load at which the concrete reaches its crushing stress is calculated using the membrane theory. As shown in the design methodology, for the present spherical cap parameters, the largest compression membrane force is the meridional force at the foot of the cap and is calculated using Eq. (39) [94] as follows:

$$N\phi = gR\frac{1}{1+cos\phi} \tag{39}$$

Where g is the weight per unit area of the shell surface

Substituting for the meridional force with the resulting membrane stresses ($N\phi = \sigma h$) and for the weight per unit area, the following formula results:

$$\sigma = \gamma R\frac{1}{1+cos\phi}$$

For the parameters of the present shell (R = 20.59 m and ϕ = 37.38 at the foot), this reduces to:

$$\sigma = 11.473\,\gamma$$

Where σ is in N/m2 while γ is in N/m3

For an average concrete unit weight of 2400 kg/m3, the concrete material reaches its crushing stress (assumed to be 90% fc and equals 22.5 MPa) at a gravitational acceleration of 83.3 g. If the compressive strength (equal to 25 MPa) is considered as the crushing stress, as is the case in the finite element model, the structure fails at 92.6 g, or 92.6 times the structure's weight, which is close to but slightly less than (about 90% of) the gravity load at which the solution stops converging in the FE model of MDS09 (102.9 times the weight of the shell).

The value of stress that follows from Eq. (39) is important given that most of the models in this study are loaded with vertical gravity dead loads. It was used throughout the analysis as a general means to determine where failure has occurred in relation to the maximum concrete compressive stresses, since a material failure was expected. However, the following should be noted:

- Due to the different behavior of concrete under tension and compression, a material-initiated failure in the concrete shell may be not governed by the compressive strength of concrete, but rather by the much lower tensile strength resulting in cracks that gradually reduce the capacity of the section to zero. In spherical caps, that effect is mostly dominant in the region adjacent to the edge ring, where a bending field is generated between the shell foot and the ring beam. Consequently, that effect may be reasonably anticipated to affect the capacity of the structure. The calculated value herein is consequently only used as a measure for the reasonability of the failure loads for models where a loss of stability was not observed, and particularly for models where the concrete cracking was disabled, and clamped models where no deformable body (ring beam) was provided at the boundary.

- f_c is the ultimate compressive strength of concrete under a uniaxial stress state. In the general multi-axial concrete stress state in the model, failure governed by a failure envelope for multi-axial stress states, which defaults to Willam and Warnke's constitutive model for the triaxial behavior of concrete [116]. In compression, given that concrete crushing is disabled, failure of the concrete material is judged by observing the value of von Mises equivalent stress reaching the maximum stress value that was input through the multilinear stress-strain curve for the rate-independent plasticity. The von Mises equivalent stress is calculated in Eq. (40) in reference [8]:

$$\sigma_e = \left(\frac{1}{2}\left[(\sigma_1 - \sigma_2)^2 + (\sigma_2 - \sigma_3)^2 + (\sigma_3 - \sigma_1)^2\right]\right)^{\frac{1}{2}} \tag{40}$$

  Where σ_1, σ_2, and σ_3 are the principal stresses of the material
  As previously discussed in the methodology, enabling concrete crushing results in an even lower load at which the solution stops converging, and is usually attributed to local stress concentrations in the FE model, rather than an actual failure. In tension, on the other hand, the concrete failure is governed by the Willam and Warnke failure envelope, as pointed out, in which concrete cracks when any of the three principal stresses exceeds the tensile strength of the concrete [8].

As Fig. 122 shows, the value of von Mises equivalent stresses of model MDS09 are shown to be maximum near the edges, with the maximum stresses at 25 MPa; equal to the maximum stress of the concrete stress-strain curve. It is also seen that, at the failure load, the maximum total displacement of the structure is relatively small (about 4.4 cm as shown in Fig. 123) supporting the observation that failure has occurred due to a material failure rather the a loss of stability accompanied by significantly large displacements, as that of the elastic model.

The arc-length method was tried for solving the same model. As discussed in the methodology chapter. The arc-length method is designated by ANSYS to be able to track

post-instability paths of structures where a zero or negative stiffness obstructs convergence of the solution. This method was used for the MDS09 model as another check to verify that termination of the solution was not due to a loss of stability. However, when the solution using the arc-length method stopped converging at the same failure load value as previously obtained using the default Newton-Raphson method.

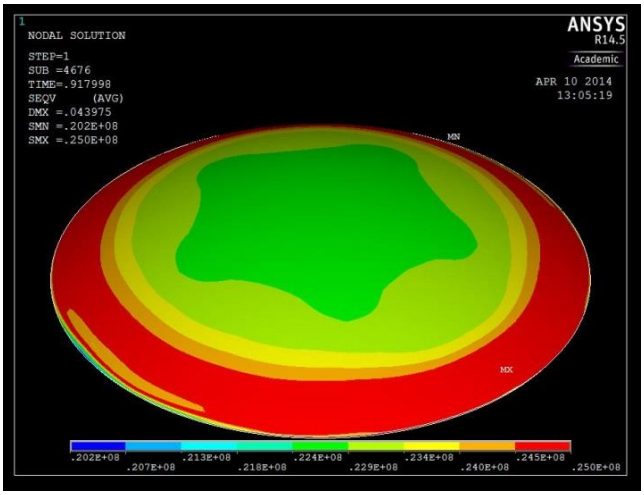

Fig. 124: Equivalent von Mises stresses of MDS09

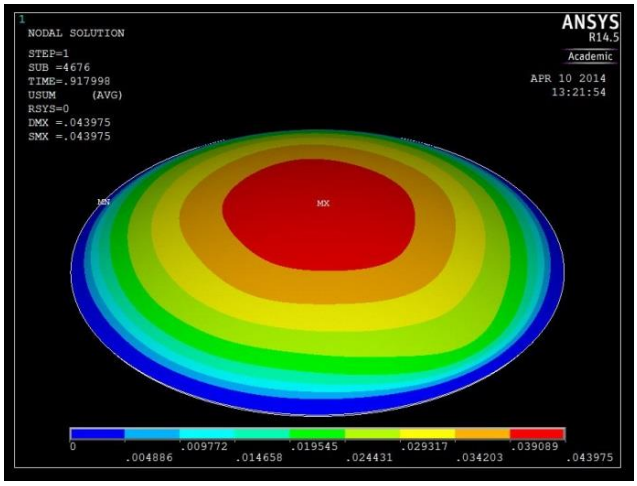

Fig. 125: Total displacement of MDS09

In the clamped structure MDS09, very low tensile stresses were observed in the model. The case is significantly different when the ring beam is modeled as the boundary

for the structure. For model MDS16, for example, the failure load of the ring beam bounded model is reduced to half of that of the clamped concrete model (8% of the linear elastic failure load and 55.4 times the weight of the shell). The nodal displacement of MDS16 shows a larger maximum displacement, with a maximum central displacement value of about 7.6 cm (almost twice that of MDS09) as shown in Fig. 124 which presents a plot of the vertical displacement.

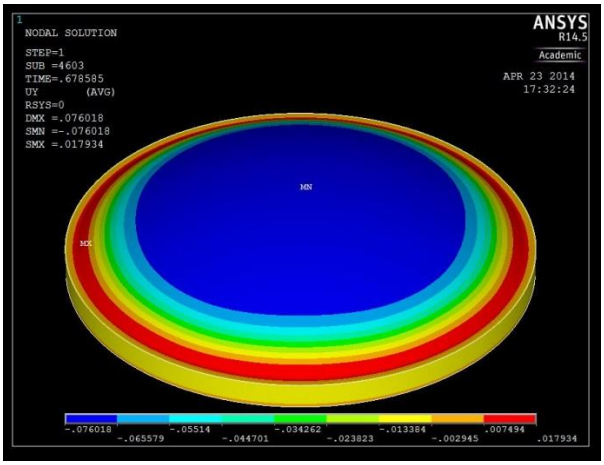

Fig. 126: Vertical displacement of MDS16

Fig. 125 of model MDS16 at the load where the solution terminated shows extensive cracking at the region between the cap and the bounding ring beam. While the final stresses at the cracked region appear to be very low, relatively high stresses are observed immediately adjacent to it, as shown in the von Mises equivalent stresses plot in Fig. 126, where the stresses at the cracked region appear to be as low as 0.7 MPa, while the adjacent von Mises stresses have reached the maximum stress value of 25 MPa.

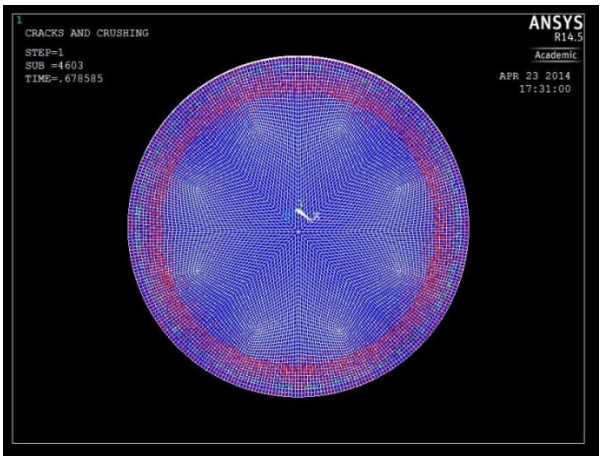

Fig. 127: Cracking of MDS16

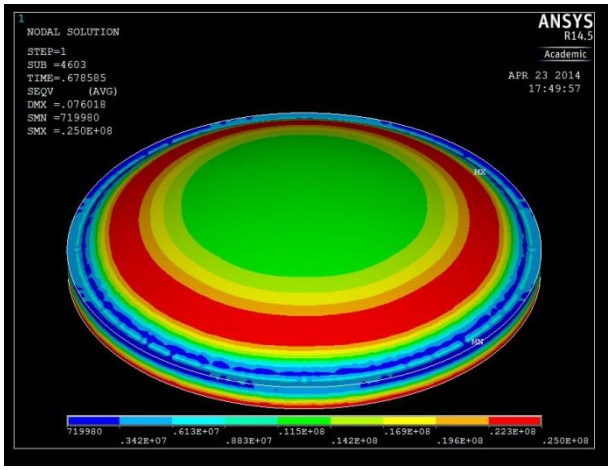

Fig. 128: Equivalent von Mises stresses of MDS16

The displacement pattern exhibits a consistent pattern with that of von Mises stresses; Fig. 124 shows that the large vertical central vertical displacement in the negative y direction is not localized at the crown, but rather the large displacement zone is observed to occur immediately adjacent to the ring-cap intermediate region followed by an inflection point and an increasing positive displacement in the positive y direction with a maximum of 1.8 cm at the cap-ring transition. Consequently, it is seen that the high stresses region in Fig. 126 coincides with the start of the large central deflection. This pattern shows to be consistent, in principle, with Bushnell [23] who he concluded that buckling of (relatively deep) ring-bounded spherical caps is an edge phenomenon.

Fig. 127 presents a comparison between the central vertical displacement between MDS09 and MDS16 which reveals that failure of MDS09 occurs suddenly after an almost linear load-deflection path, while the path of MDS16 is initially linear, then the structure is seen to exhibit an increasing displacement for smaller load steps, and closely approaches a neutral equilibrium position at the failure load. Consequently, it can be seen that while the presence of the ring beam results in significant tensile stresses, the structure also approaches an unstable equilibrium at the failure load, which could suggest that the edge-induced stresses result in an early loss of stability of the structure.

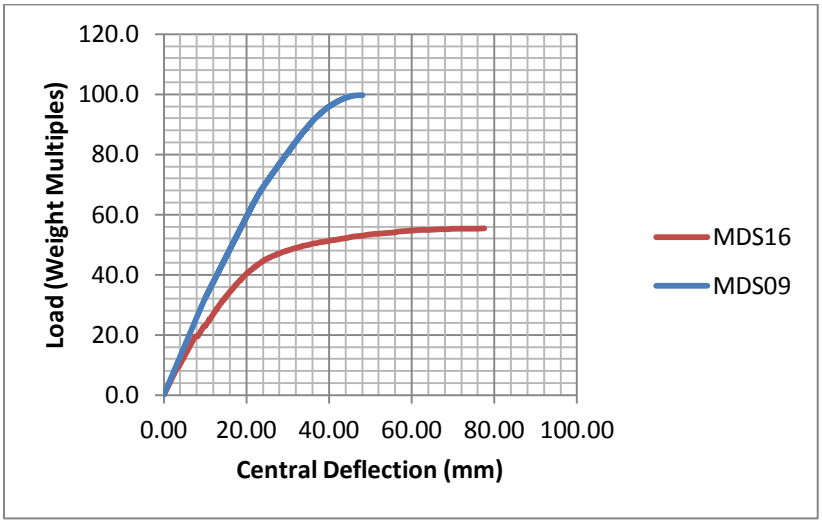

Fig. 129: Comparison between the load-deflection paths of MDS16 and MDS09

A significant lateral displacement is also observed at the shell-ring intermediate region, as shown in Fig. 128, where the horizontal z direction (UZ) has a maximum value of 4.6 cm.

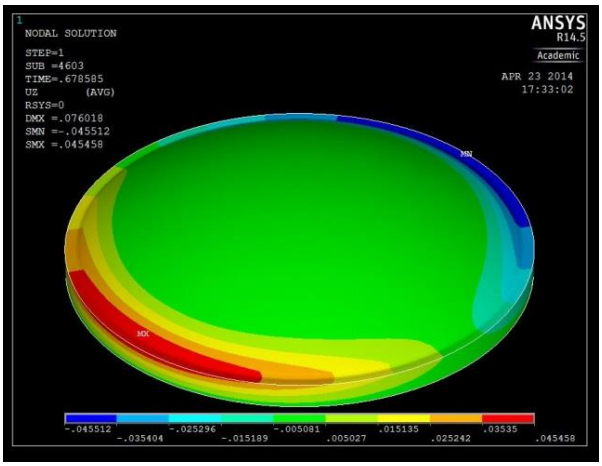

Fig. 130: Lateral displacement of MDS16

It should be noted though that local high stresses are observed at the bottom of the ring beam. These stresses are not representative of those anticipated in the real structure and are mainly due to the restraining of the lower surface of the beam. consequently, as previously discussed in the methodology chapter, a boundary sensitivity study was conducted using different boundary conditions to the ring beam so as to eliminate the effects of local stress concentrations on the convergence of the solution, while aspiring to model the conditions as close to the real structure as possible.

Boundary Sensitivity Study

The different boundary cases are outlined in table 21 with the corresponding load levels at which the solution has lost convergence and terminated. In most of these models, a very early loss of convergence was observed due to high stress concentrations resulting from restraining limited regions of the lower edge of the ring beam.

Table 21: Boundary sensitivity models

Model Code	Analysis Type	Boundary	Failure Load (N/m2)	Failure load (multiple of weight)	Ratio of Linear Elastic Failure Load
MDS11	Nonlinear Inelastic	Ring beam is restrained against UX, UY, UZ at 8 locations (4 nodes at each location)	4.7E+04	7.8	0.01
MDS12	Nonlinear Inelastic	Ring beam restrained against UX, UY, UZ at 8 column locations of 750X1000 mm column (20 nodes at each location)	7.3E+04	12.1	0.02
MDS13	Nonlinear Inelastic	Ring beam restrained against UX, UY, UZ at 8 column locations of 750X1000 mm column (20 nodes at each location) while the rest of the beam lower edge is restrained against UY only.	9.6E+04	15.9	0.02
MDS14	Nonlinear Inelastic	Beam lower edge is restrained against UY, while one column location is restrained in UX, UY, UZ	7.1E+04	11.7	0.02
MDS10	Nonlinear Inelastic	Beam is BEAM189 line element restrained against UX, UY, UZ at 8 locations	2.9E+05	45.6	0.07
MDS16	Nonlinear Inelastic	Beam lower edge is completely restrained in UX, UY, UZ	3.4E+05	55.4	0.08

Fig. 129 shows the very high stress concentration observed at the restrained locations of the beam lower edge in MDS11 resulting in an early loss of convergence at a value of 1% of linear elastic failure load (about 7.8 times the weight of the cap), while the rest of the structure exhibits much lower stresses.

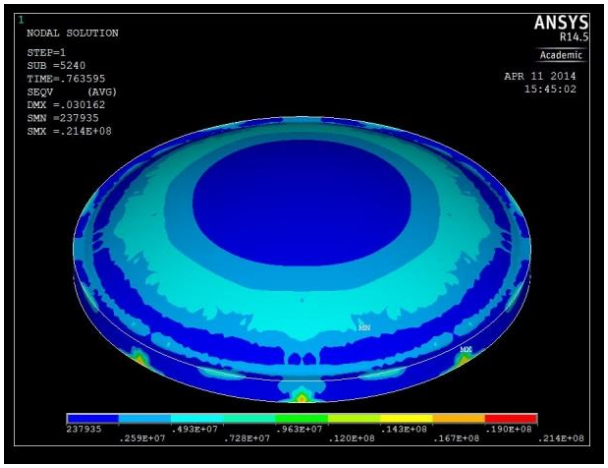

Fig. 131: Equivalent von Mises stresses of MDS11

Although increasing the size of the restrained region has helped with extending convergence, it also shows a much lower failure load of less than 2% of the linear elastic failure load, and similar stress and cracking concentrations as shown in Fig. 130 and Fig. 131 of MDS12. Fig. 131 shows a close-up of the von Mises stresses at the restrained locations which have reached the maximum value of 25 MPa.

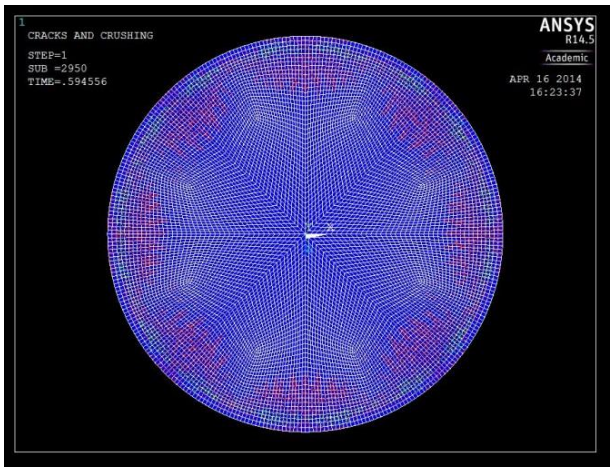

Fig. 132: Cracking of MDS12

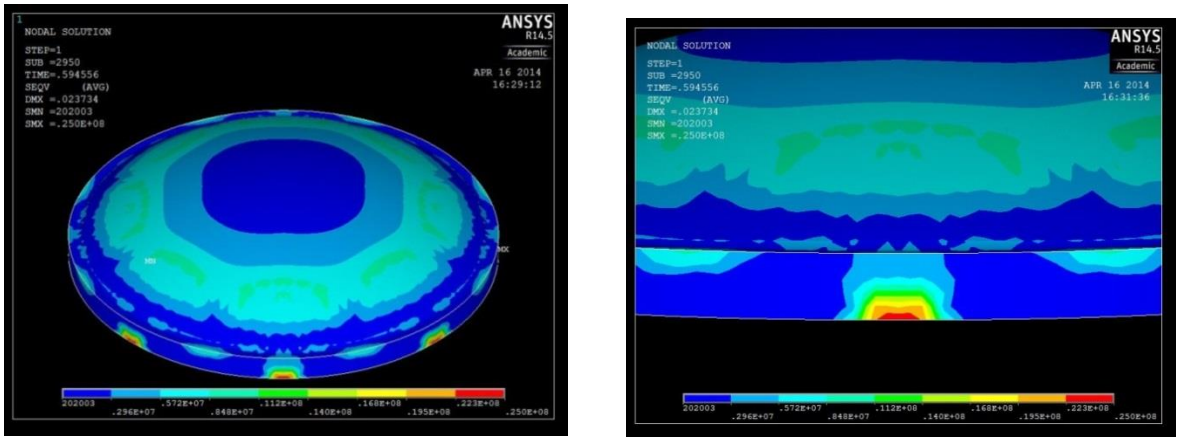

Fig. 133: Equivalent von Mises stresses of MDS12

Another boundary condition, seen in model MDS13 and has resulted in a slightly larger failure value than MDS12, is when the whole boundary was restrained against UY beside restraining the column locations against UX, UY, UZ, but the value was still very low. A different boundary was applied in MDS14 by restraining the whole lower boundary against UY, while only one column location was restrained against UX, UY, UZ. This case was implemented in order to explore the effect of allowing the beam edge to expand laterally while preventing rigid body motion by hinging the beam at one location only. While this case may allow a theoretically closer boundary to the ring beam

restrained by deformable columns that may drift laterally, numerically it has resulted in severe convergence difficulties during the entire solution, not just closer to the failure value. These difficulties are explained by the large displacement that results from each load step because the structure is almost free to displace laterally. Consequently, a very small load step was needed for achieving convergence, and eventually, as the load increased, the minimum load step allowed by ANSYS was not sufficient to achieve convergence and the solution terminated even though the highest von Mises stresses have a maximum value of 18 MPa only (at the restrained region) as shown in Fig. 132. Fig. 133 shows the total displacement of the model nodes to be larger than any of the ring beam bounded models yet, with a maximum total displacement of 11.4 cm at most of the shell surface and the most free-to-displace-laterally side of the ring beam.

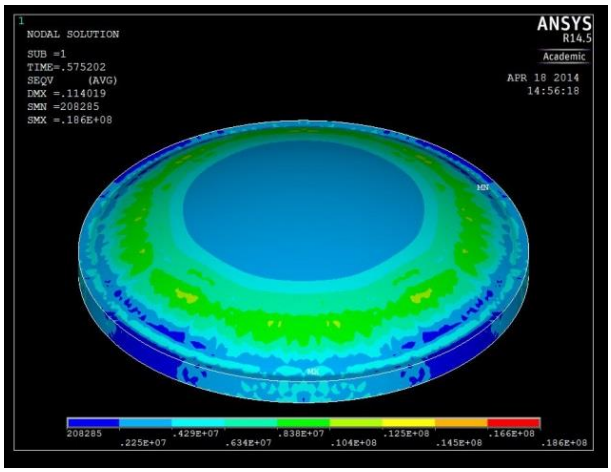

Fig. 134: Equivalent von Mises stresses of MDS13

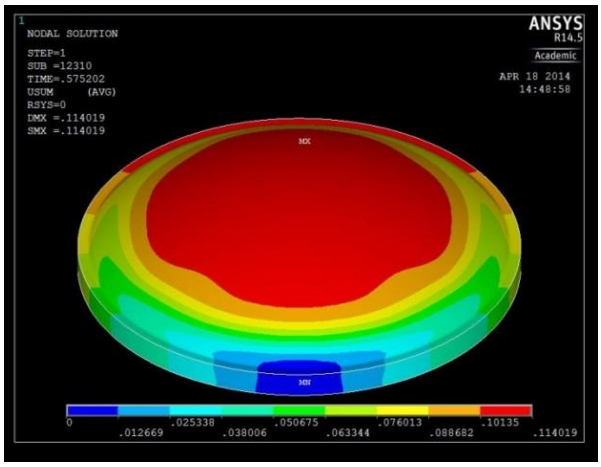

Fig. 135: Total displacement of MDS13

Another much more expensive model (whose results are not reported here), in which the columns were modeled at their exact locations and sizes corresponding to those of the prototype, was built. In that model, the ring beam is thus restrained in the proper way closely following the real beam boundary conditions with a deformable body built of reinforced concrete SOLID65 elements, and is fixed at the base. However, a very small load step and a huge number of equilibrium iterations were needed for the solution convergence in that particular model. Initial examining of the model unconverged load substeps has revealed, as expected, that the faced convergence difficulties were due to the cracking in the tension zones of the ring beam (the lower parts of the mid span). That observation is coupled with the fact that most reinforced concrete beam analyses seen in the literature have modeled the steel reinforcement in the tension region separately and in due detail to overcome these effects (mostly using LINK8 elements with steel material properties). Consequently, it was decided that the possible enhanced accuracy of the solution with regard to the behavior of the shell structure when modeling the full structure is extremely exceeded by the significant increase of the size of the model and the time elapsed during the solution, given that most of the convergence difficulties were caused by cracking of the lower ring beam regions under tension.

The undermined value of modeling the full real life boundary of shell structures may also be supported by the fact that most of the analytical studies in the surveyed literature have considered the shell edge to be clamped. Some of the numerical studies considered to boundary to be hinged or free to displace radially [119]; however, they did not resort to modeling the ring beam in the numerical model. In studies where the effect of the boundary was of interest, experimental modeling of a scale model of the structure was used and the boundary tailored to properly follow the prototype boundary conditions.

A similar approach was consequently followed in this study where the finite element models of the structure hereafter included only the shell and the ring beam with a completely restrained lower boundary; thus providing a more proper simulation of the stresses at the intermediate region between the shell and supporting deformable body than that of the clamped edge, while avoiding wasting resources on the resulting stresses in the ring beam itself. At the same time, the efficiency of this modeling approach is compared with the experimental analysis of the scale model which models the structure in its entirety; shell, ring beam and columns restrained at the base, as shall be discussed shortly.

The effect of modeling the ring beam at the boundary was quantitatively assessed in the finite element analysis through using the nonlinear elastic model with shell elements for the cap and beam line elements for the ring beam (MDS07). Another attempt to include the effects of the boundary coupled with material plasticity was MDS10 where the spherical cap was modeled using SHELL281 elements and the beam using BEAM189 line elements, as those of the elastic analysis. However, SHELL281 elements were composed of three layers of concrete-steel- concrete to represent a middle layer of the reinforcement. The concrete layers of the shell were assigned a von Mises multilinear isotropic hardening plasticity stress-strain curve, identical to that used in the concrete models, and the steel layer was also assigned the same bilinear isotropic hardening plasticity of the steel reinforcement in the solid elements model. The use of nonlinear line elements of the beam has largely reduced the effect of stress concentrations at beam restraining locations (8 hinged locations around the perimeter), resulting in a

much higher failure load of 7% of the linear elastic clamped shell failure load, which is very close to the results of MDS16 where the lower beam edge is completely restrained (about 8% of the liner elastic clamped shell failure load).

Consequently, MDS10 is seen to provide some confidence in the ability of the solid elements modelling approach with the lower edge of the ring beam fully restrained to approximate the load level at which the stresses reach their maxima and the solution stops converging. However, the modeling approach of MDS10 was not used in the rest of the analysis since the use of solid elements was essential in order to model the behavior at the interface between the cap panels, represented in the FE model as the interfacing areas of the panel solid elements. The use of 'areas' as the contacting surfaces in a contact analysis is highly desirable for achieving convergence and almost exclusively implemented in all the surveyed relevant literature.

The use of MDS10 was, however, helpful in providing an approximation of the stresses in the ring beam that is not possible to deduce from the models where the whole ring beam boundary is restrained. Fig. 134 shows the deflection of MDS10 (scaled by 20) which clearly shows the deflections of the ring beam at the failure. It's worth remembering here that the beam is modeled as a line element; however, the beam section is viewed in its actual input dimensions using the ESHAPE command on ANSYS. Fig. 135 shows the von Mises equivalent stresses in the beam which are shown to the reach the maximum value of 25 MPa at mid spans and over the supports (in both tension and compression regions). These stresses are possible to see in MDS10 since no concrete properties (cracking in particular) can be assigned to the line element.

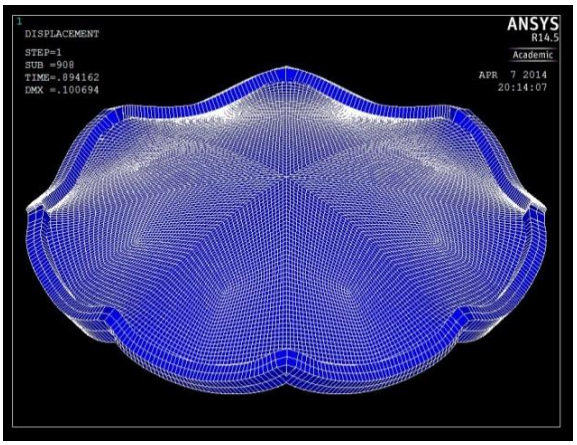

Fig. 136: Deflection shape of MDS10

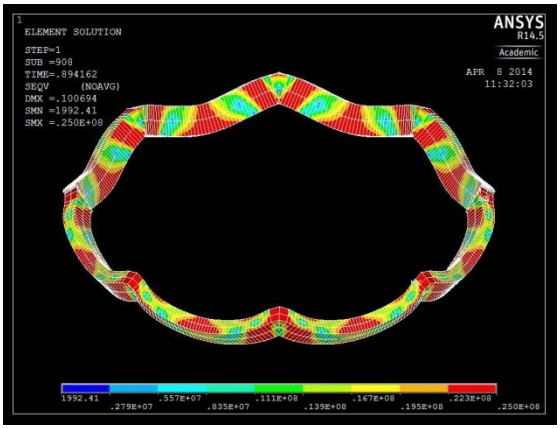

Fig. 137: Equivalent von Mises stresses of MDS10 ring beam

Before moving on to modeling the effects of the segmentation of the structure using contact elements on ANSYS, the effect of concrete crushing on the capacity of the structure was worth exploring, although not implemented in the rest of the analysis. When concrete crushing is activated in the model by inserting a value for the crushing stress (input as 25 MPa in the analysis), ANSYS displays a warning message at the beginning of the analysis reporting that inaccurate results may be reported when concrete crushing and a large displacement analysis are used. Hence, a linear (small displacement) analysis was used in the concrete crushing model; thus limiting the effects of nonlinearity

to material plasticity, cracking and crushing. The model (MDS17) showed earlier loss of convergence than MDS16, which has exactly the same model properties other than the ability of concrete to crush in compression. The loss of convergence occurred at 5% of the linear elastic failure load (34 times the weight of the shell), which represents 61% of the failure load of MDS16. Examining von Mises stresses of MDS17, shown in Fig. 136, displays the overall low stresses in the whole structure, while very high local stresses arise immediately adjacent to the lower restrained boundary with the largest value at 24.4 MPa at the last converged load substep. In that case, it is seen that the local large stress concentrations at the restrained nodes do not represent a real failure of the structure.

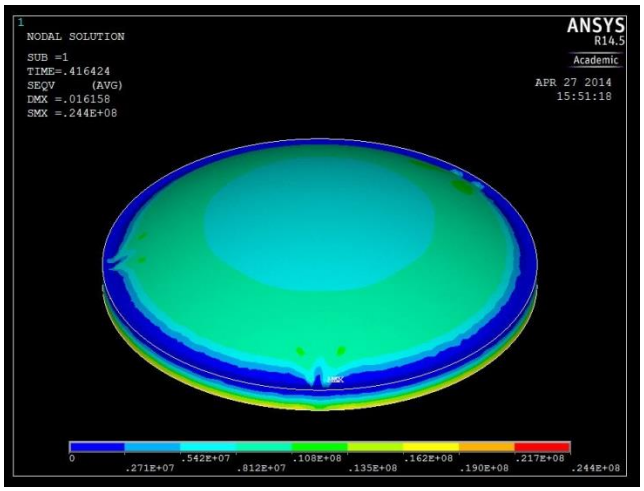

Fig. 138: Equivalent von Mises stresses of MDS17

The analysis then moved to assessing the difference in the behavior of the spherical cap model when it is composed of individual panels with contact elements at the interface between these panels, and between the base panels and the ring beam. The first step of that analysis was assessing the behavior when contact conditions are provided between the spherical cap, as a whole, and the ring beam. In MDS19 where that approach was implemented, the loss of convergence was observed at a lower value than MDS16 where the same properties are used, with the exception of coupling the cap base and the ring beam DOFs at the interface. The failure of MDS19 is observed to occur at about 93% of failure in MDS16 (51.6 times the weight of the shell) with a very close

load-deflection path as seen in Fig. 137, suggesting some capacity reduction due to the presence of contact conditions between the shell and the ring beam with the maximum normal tracking stress for debonding equal to 2.5 MPa (chosen to represent the concrete tensile capacity as previously discussed in the methodology).

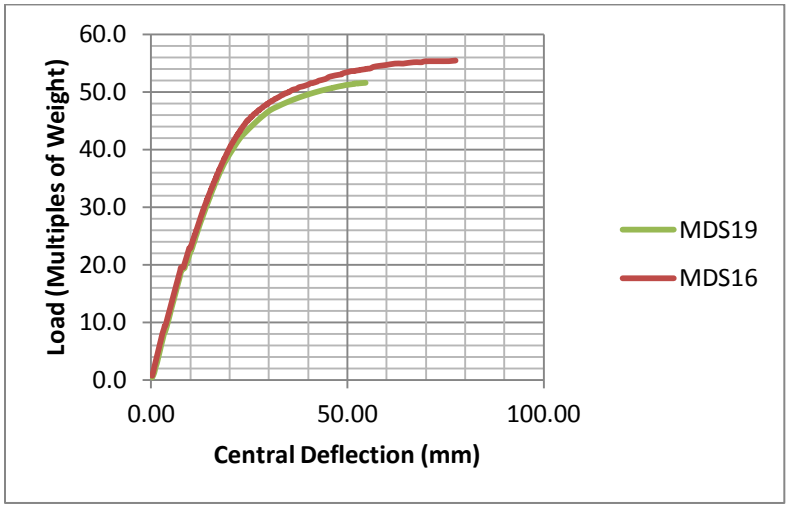

Fig. 139: Comparison between the load-deflection paths of MDS16 and MDS19

In principle, at the maximum normal stress the debonding process follows a linear function that ends with the completion of debonding at a maximum normal separation value selected between 0.5 and 2 cm in this study (1 cm in MDS19). However, it should be noted that in MDS19, and all the models in this study, the bonding with adjacent structural members provides the only boundary condition to each of the contacting members. Consequently, a complete debonding of the contacting surfaces will directly result in a large rigid body motion that cannot be tracked with the solution methods of the present model. Hence, only the initiation of debonding and partial normal separation values approaching those of the complete debonding value can be tracked. In MDS19, for instance, Fig. 138 shows the contact gap development at the cap-ring beam interface with a maximum value of 0.53 cm. It may be suggested that the initiation of contact debonding is what obstructed the convergence of the solution, suggesting a failure at the cap-ring joint. However, von Mises equivalent stresses, as shown in Fig. 139, also show reaching

the maximum stress value of 25 MPa at a similar location to that of MDS16, with the same displacement pattern and inflection point across the meridian, as illustrated in Fig. 140.

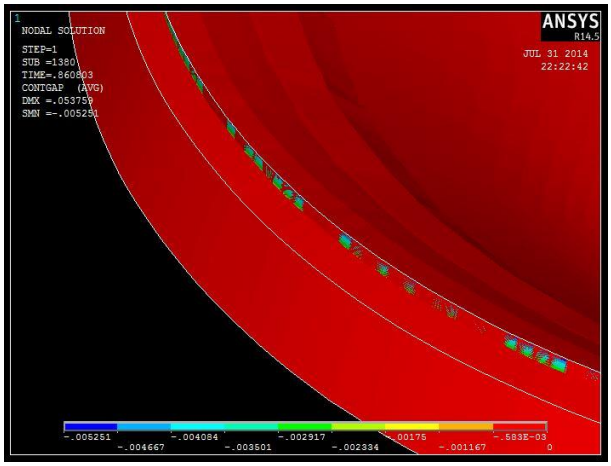

Fig. 140: Contact gap in MDS19

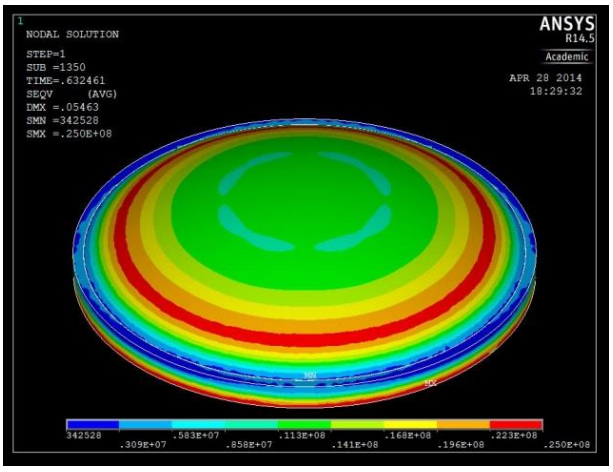

Fig. 141: Equivalent von Mises stresses of MDS19

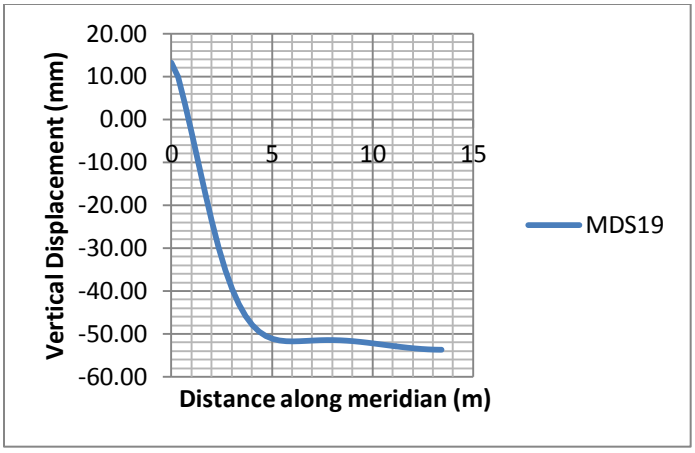

Fig. 142: Vertical displacement across the meridian of MDS19

The maximum stress region is, however, smaller than that of MDS16, which could suggest that the initiation of debonding at the cap-ring interface caused the stresses to drop at the immediately adjacent regions. That observation may also be supported by observing the stress state ratio plot from ANSYS, which represents the ratio of the actual stresses to the maximum stresses of the model, and is shown in Fig. 141. Fig. 141 shows a stress state ratio between 93% and 104% of the whole structure with the exception of the cap-ring intermediate region where the stress state ratio has dropped to as low as 6.5%.

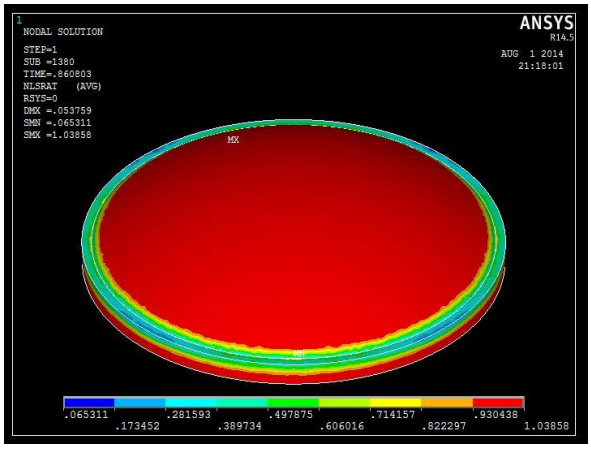

Fig. 143: Stress-state ratio of MDS19

The following model SDS03, which explores the effect of segmenting the whole structure into individual panels supported by a bonded contact at the interface, shows an interesting observation. The model, clamped at the boundary with no ring beam, showed a failure load at exactly the same load value of the clamped model MDS09 in which the cap is modeled monolithically with no contact. This observation is consistent with the analytical description of the shallow clamped spherical cap where compressive stresses are dominant over the structure; consequently, the contact surface, which debonds at a tension of 2.5 MPa, has no effect on the behavior of the structure in that case.

Although the segmented model SDS03 shows a very similar displacement pattern to that of the monolithic cap MDS09, the central deflection is about 20% higher than that of MDS09, as shown in Fig. 142, and the von Mises stress pattern is significantly different.

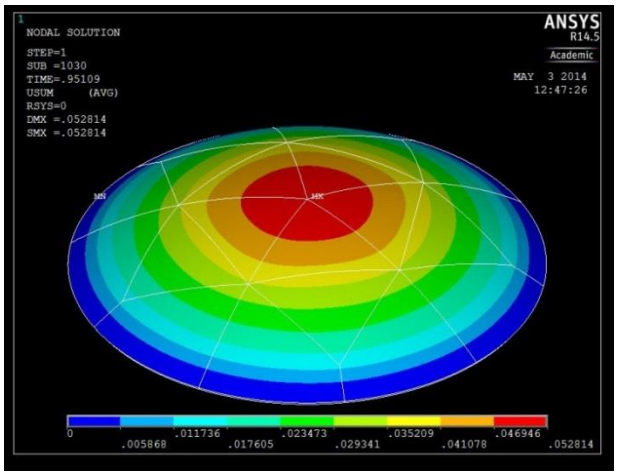

Fig. 144: Total displacement of SDS03

As Fig. 143 of SDS03 von Mises stresses shows, the stresses are largest around the crown (25 MPa), then they reduce gradually toward the foot to about 19 MPa. This pattern is different from the previously discussed MDS09 where von Mises stresses were largest at the foot. This change in the stress distribution could reasonably be attributed to the contact at the panels interface: Since the cap edge is clamped and the structure is mainly under membrane compression, the compression forces result in contact

penetration between the panels (which is mainly a numerical concern in the context of the analysis). Additionally, since the lower edge is supported and cannot displace, the largest penetration, accompanied by large contact stresses to reduce the penetration and achieve convergence, occurs at the crown where the corners of the least supported panels meet, which could explain the large crown stresses seen in Fig. 143, along with the large crown displacement (deflection shape shown in Fig. 144). This observation may be supported by examining the unconverged load step in which a large penetration and material disintegration is observed around the crown of the cap (Fig. 145). Another observation that supports this conclusion is the relatively high stress concentrations seen at each contact corner location in the model when compared to the rest of the panel body, as seen in Fig. 143.

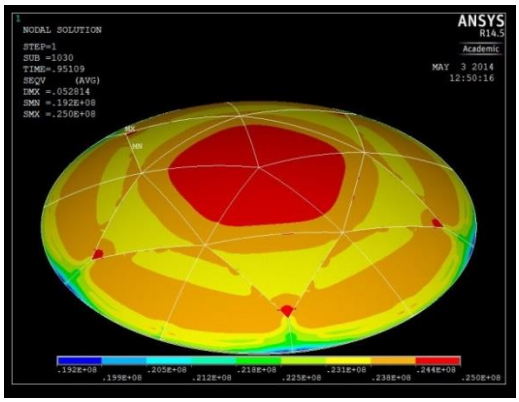

Fig. 145: Equivalent von Mises stresses of SDS03

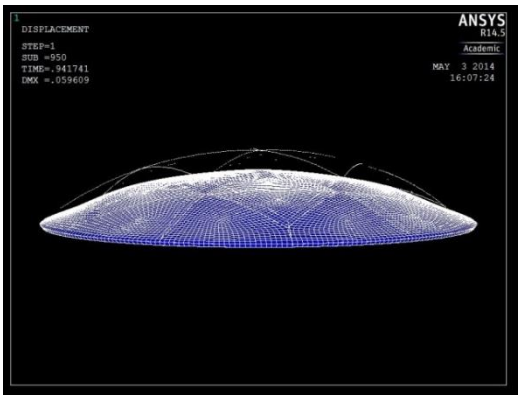

Fig. 146: Deformed shape of SDS03

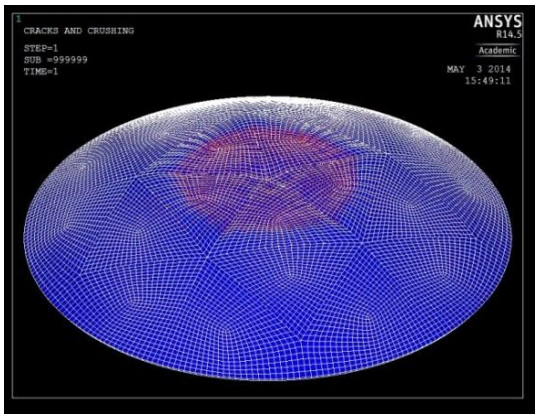

Fig. 147: Unconverged load substep of SDS03

As seen from the failure load value, though, these effects resulted in no change in the capacity of the clamped structure. The case is different when a ring beam is provided at the boundary as the case of SDS17 where the failure load is observed to be about 80% of that of the monolithic cap bounded by a ring beam in MDS16. This value corresponds to 44.5 the weight of the shell which is 7% of the linear elastic buckling load value.

Fig. 146 of the load-deflection path of SDS17 and MDS16 shows that both models initially follow the same almost linear path. However, SDS17 completely loses convergence at the load level where MDS16 starts exhibiting increasing displacement for small loads (approaching a zero stiffness), which caused the small reduction in the failure load. This might be attributed to contact related convergence difficulties that accompany the structure's sudden large displacements.

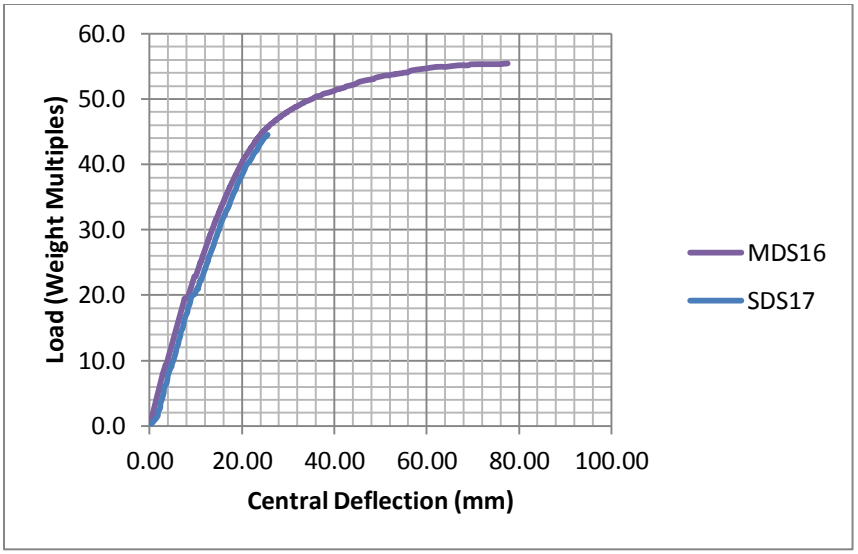

Fig. 148: Comparison between the load-deflection path of MDS16 and SDS17

For that reason, SDS17 is seen to not display any large displacement or large stresses at the last unconverged load substep, but rather, local stress concentrations and cracking around the interface between the base panels and the ring beam as shown in Fig. 147 of the cracks and Fig. 148 of von Mises strains.

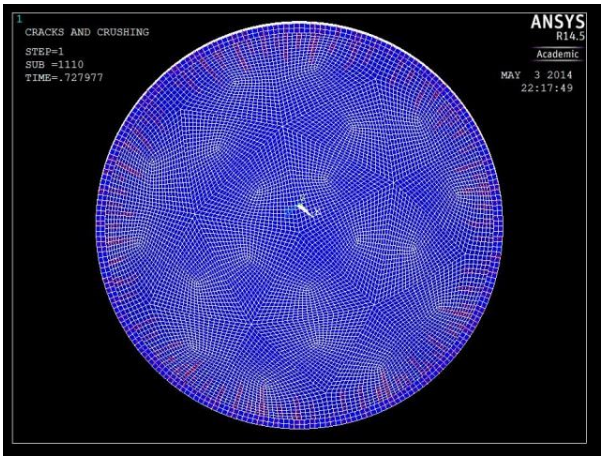

Fig. 149: Cracking of SDS17

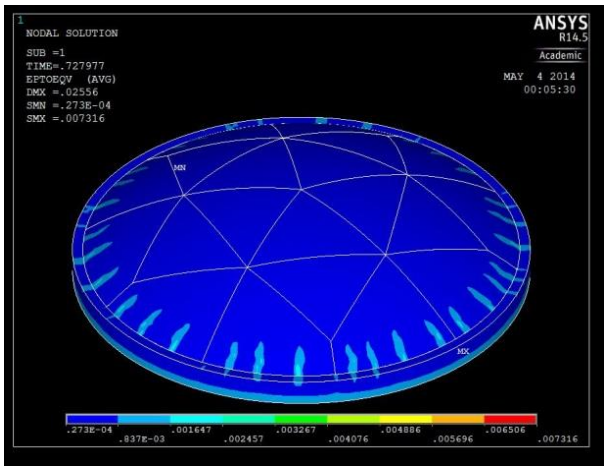

Fig. 150: Equivalent von Mises strains of SDS17

This observation suggests that the loss of convergence was initiated by large tensile stresses at the cap-ring interface that resulted in large tracking stresses at the contact interface at that location. This conclusion is supported by examining the stresses across the surface of the cap in Fig. 149, which did not exceed a value of 10 MPa except at some locations adjacent to cap-ring intermediate region. Examining the Newton-Raphson residual forces, which are the result of a nonlinear diagnostic tool on ANSYS which shows the element locations where a large residual force is located leading to the loss of convergence, it is seen that the large residual is also found at a location near the cap-ring intermediate region, suggesting an initiation of failure at that location (see Fig. 150).

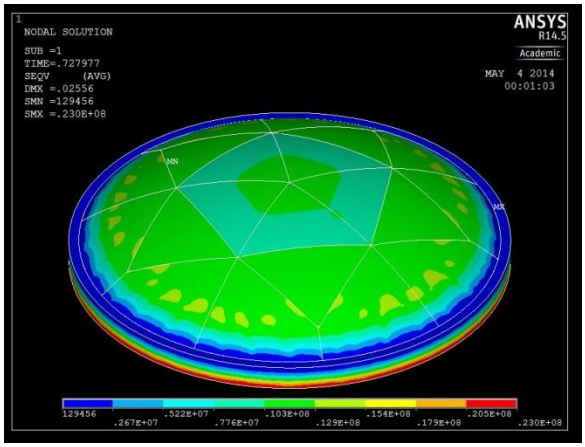

Fig. 151: Equivalent von Mises stresses of SDS17

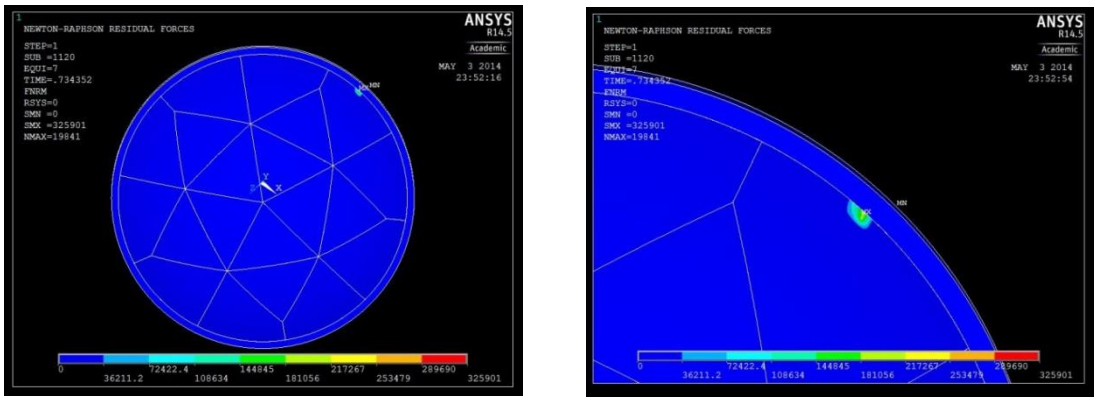

Fig. 152: Newton-Raphson residual forces of SDS17

Consequently, it was of interest to this analysis to verify the effect of modeling the ring beam and the introduced tensile region at the cap-ring interface on the behavior of the segmented structure. SDS20 was built for that purpose retaining all the parameters of SDS17 while disabling concrete cracking. The model results were to reflect on how the low concrete tensile capacity affects the failure load, particularly at the cap-ring intermediate region since the whole cap is otherwise under compression. As shown in table 20 , SDS20 showed a failure load that is almost identical to the clamped-boundary models, both monolithic and segmented (MDS09 and SDS03), which supports the results of the previous models and suggests that the early failure is caused by concrete cracking

at the cap-ring intermediate region. The even earlier loss of convergence in models with contact conditions between the cap and the ring (SDS17 failed at 80% of MDS16) suggests that the contact conditions may have accelerated that failure.

It is observed, however, that while the failure load value is the same, the load deflection path of SDS20 is visibly different. As shown in Fig. 151 and previously discussed, MDS09 displacement is almost linear up to sudden failure. On the other hand, in SDS20, the first part of the path is initially linear with a larger stiffness (slower rate of displacement) than MDS09. As the load approaches the failure load, though, the stiffness of the structure is seen to gradually decrease, and large displacements are observed before the structure fails.

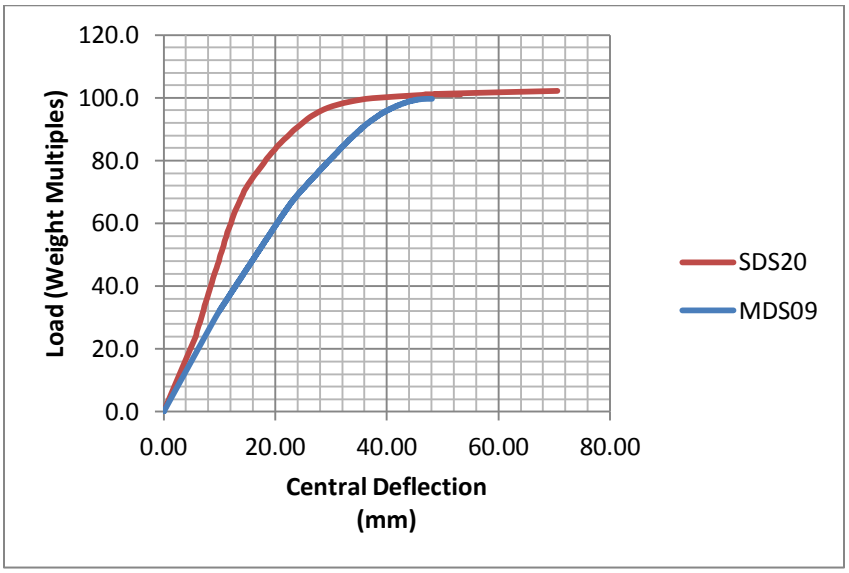

Fig. 153: Comparison between the load deflection paths of SDS20 and MDS09

Adding SDS17 and MDS08 to the comparison further clarifies the interaction of concrete cracking and the presence of the ring beam on the structure's failure. As shown in Fig. 152, the presence of concrete cracking in all models in the figure (MDS09, MDS16, SDS17) results in a reduced structural stiffness. This reduction is very significant in ring beam-bounded models (MDS16, SDS17) where the tensile cap-ring intermediate region plays an important role in reducing the capacity.

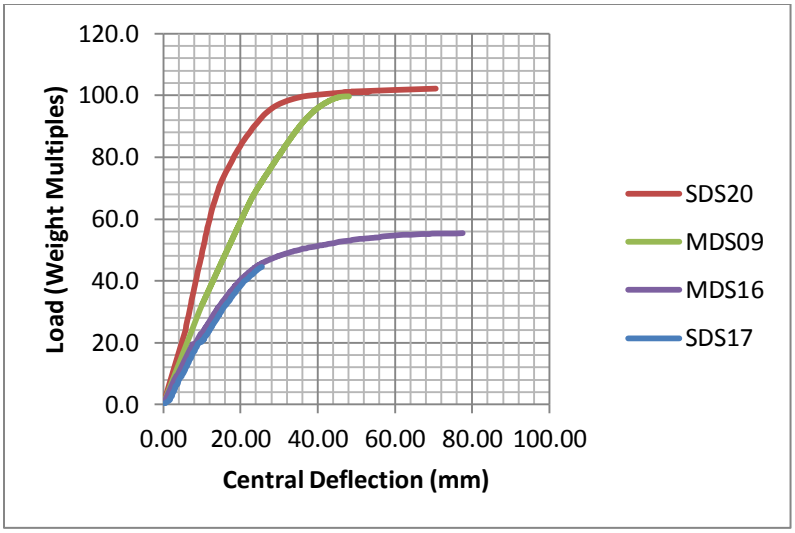

Fig. 154: Load deflection paths of SDS20, MDS09, MDS16 and SDS17

Finally, as previously noted, SDS17 is noted in the figure to lose convergence earlier than the identical but monolithic MDS16, raising the concern of an earlier failure due to segmentation of the structure.

In order to answer the question of whether the traction force at the contact is responsible the loss of convergence, larger debonding stress values are provided in SDS19. In particular, the steel limits for tensile and shear stresses are used as the limit for debonding, thus loosely simulating the action of connecting the panels with steel bars which have a normal yield stress of 400 MPa (represented by the maximum normal stress for debonding) and shear stress capacity of 240 MPa (represented by the maximum tangential stress for debonding). This change results in an increase of the failure load by only 5% over that of SDS17, although the overall displacement rate is slightly larger (as shown in Fig. 153).

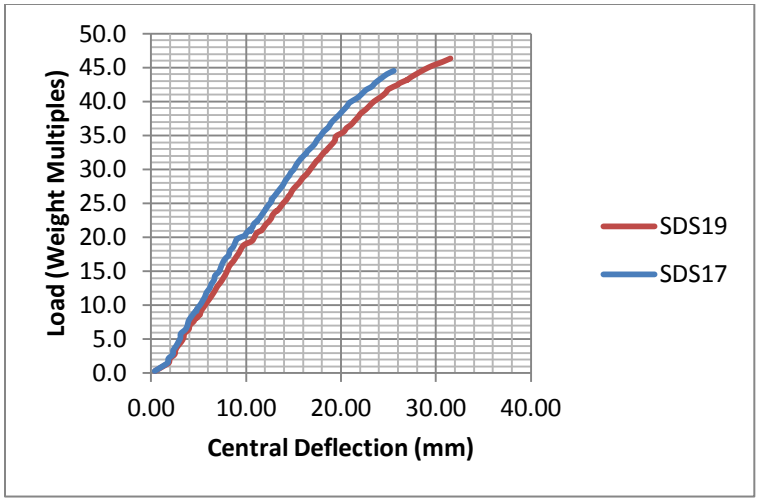

Fig. 155: Comparison between the load-deflection paths of SDS19 and SDS17

It's worth noting that the failure load value of SDS19 is still 84% of the failure value of the monolithic cap of MDS16, which suggests that the low tensile capacity of the connection is not solely responsible for the reduction in the load value at which convergence is lost and the solution is terminated. Other factors may, therefore, include the contact parameters themselves, particularly the contact stiffness and contact penetration tolerance. A contact sensitivity study was conducted to explore the effects of the major contact parameters on the convergence of the solution, and determine the optimum range for the values of these parameters.

Contact Sensitivity Study

The most important parameters in the contact analysis on ANSYS, as discussed in the methodology, are the contact stiffness and the contact penetration tolerance. These two parameters are controlled by two ANSYS constant values which are the contact stiffness factor FKN and the contact penetration tolerance factor FLON. These values were thus adjusted within the ranges discussed in the literature and recommended by ANSYS in order to observe their effects on the behavior of the structure. The aim is to provide the smallest contact stiffness needed for achieving convergence which is, at the same time, large enough to reduce the contact penetration to an acceptable level. Tables 22 and 23 summarize the different models used toward that end. Table 22 presents the different contact stiffness values used for the same penetration tolerance values for both the clamped and the ring beam bounded models. Columns 4, 5, 6 and 7 present the corresponding failure load values of each model and the maxima of the contact stiffness value itself, which is extracted through the element table results on ANSYS.

Table 22: Effect of contact stiffness factor FKN on the failure load

Gravity Loading - Clamped Models						
FLON	Model Code	Contact Stiffness factor (FKN)	Failure Load (N/m2)	Failure load (multiple of weight)	Max FKN	Min FKN
0.001	SDS05	0.001	2.6E+05	46.8	2.25E+08	-2.36E+07
	SDS07	0.01	6.2E+05	110.2	1.13E+09	-2.96E+07
	SDS01	0.5	6.5E+05	115.0	2.25E+09	-2.88E+07
0.01	SDS08	0.001	3.0E+05	53.7	2.25E+08	-2.36E+07
	SDS10	0.005	6.4E+05	113.2	1.13E+09	-2.96E+07
Gravity Loading - Boundary Ring Beam Models						
FLON	Model Code	Contact Stiffness factor (FKN)	Failure Load (N/m2)	Failure load (multiple of weight)	Max FKN	Min FKN
0.001	SDS12	0.005	2.3E+05	40.7	1.13E+09	-2.05E+07
	SDS17	0.01	2.5E+05	44.5	2.25E+09	-2.32E+07
	SDS15	0.5	2.6E+05	46.3	1.13E+11	-2.48E+07

Table 23: Effect of penetration tolerance factor FLON on the failure load

Gravity Loading – Clamped Models				
FKN	Model Code	Contact Penetration factor (FLON)	Failure Load (N/m2)	Failure load (multiple of weight)
0.001	SDS05	0.001	2.6E+05	46.8
	SDS08	0.01	3.0E+05	53.7
0.01	SDS07	0.001	6.2E+05	110.2
	SDS02	0.1	6.0E+05	107.0
Gravity Loading – Boundary Ring Beam Models				
FKN	Model Code	Contact Penetration factor (FLON)	Failure Load (N/m2)	Failure load (multiple of weight)
0.01	SDS16	0.0001	1.1E+05	19.3
	SDS17	0.001	2.5E+05	44.5
	SDS14	0.01	2.4E+05	43.0

Table 22 values show that for the clamped boundary models and an FLON value of 0.001, Increasing the value of FKN 10 times from 0.001 to 0.01 results in increasing the failure load to 2.4 times its value, while at the same time an increase of 50 times of FKN to 0.5 does not result in any significant change in the failure load value (a 4% increase only). These results suggest that a value of 0.5 FKN is too high and consequently unneeded in the analysis, while a value of 0.001 is too low and has resulted in early convergence loss. A similar result is observed for an FLON value of 0.01, where increasing FKN to 5 times its value from 0.001 to 0.005 has a resulted in an increase of the failure load to twice its value. The observation that an FKN value of 0.001 is too low is also supported by experimenting with different FLON values for the same FKN, as shown in table 23. In the clamped models of table 23, it is shown that an increase of 10 times of FLON from 0.001 to 0.01 for an FKN value of 0.001 has resulted in only 15% increase in the failure load value. On the other hand, for a higher FKN value equal to 0.01, an increase of 100 times of FLON value has, in fact, resulted in a slight reduction in the failure load value, which suggests that using a high penetration tolerance value may result in an early loss of convergence.

A suggested range of FKN then was between 0.005 and 0.05, while FLON was to be kept lower than 0.1. These ranges were tried in different runs of the ring beam-bounded models; however, the results were different than those of the clamped models. As seen in table 22, for a FLON value of 0.001, increasing FKN twice from 0.005 to 0.01 has resulted in an increase of 9% only in the failure load, and even when FKN was increased to 0.5; an unusually high value, no significant increase was noticed in the failure load. Based on that observation, a value of 0.01 for FKN was mostly used in the rest of the analysis. It's also worth noting that using a value of 0.05 does not result in a failure load increase, but helps to accelerate convergence, so it was also used in some of the contact analysis models.

A convenient range is also suggested for FLON through the contact sensitivity analysis. As shown in table 23, a value of 0.0001 is too low and results in a much earlier loss of convergence than a value 0.001. At the same time, a value of 0.01 is not seen to enhance convergence. Consequently, values between 0.001 and 0.005 for FLON were used for the rest of the analysis.

Experimental Analysis Results

The results of tests 1 and 2 of the experimental analysis serve only to generally evaluate the integrity of the structure under uniform gravity loads and investigate whether a significant capacity reduction could be caused by the presence of joints and observed imperfections on the surface of the shell. As previously discussed in the methodology, the structure was loaded by calibrated sand bags uniformly across the entire surface of the shell on multiple load steps, originally planned to continue up to failure. However, the test had to be terminated since loading of the cap became very inefficient as more sand bags were added in each load step. The final applied uniform gravity load on the shell surface presented a pressure of 6.31 kN/m^2, and the corresponding central displacement of the crown measured by the LVDT was almost zero during the entire test. Small lateral displacement was recorded by the horizontal LVDTs with the maximum at about 0.6 mm (corresponding to 6 mm in the prototype), and generally all the recorded strains were insignificant.

The second test was performed during unloading of the first test sand bags by only unloading one half of the cap, as previously discussed in the methodology. The purpose was to observe the stresses of the segmented cap and behavior of the joints under loads which induce non-uniform stresses. At that point, very small strains and displacements were recorded as well. Consequently, the cap was fully unloaded and the third concentrated load test was performed up to failure of the structure, as shall be discussed shortly.

5.2.2. Failure Loads of Normal pressure models

The purpose of this part of the analysis was to establish a comparison between the obtained failure loads using the numerical modeling techniques of this study and the corresponding results throughout the literature. Normal pressure loading of spherical caps represents the bulk of the research work on spherical shells in the literature. Consequently, even though the loading condition is different from that performed in the experimental analysis of this study, a benchmark analysis where the results of the finite element models were compared to the values documented in the literature and the closed-form solution was necessary. According the Eq. (3) by Zoelly [121], the linear elastic buckling load is calculated as:

$$P_{cr} = \frac{2E}{\sqrt{3(1-v^2)}}\left(\frac{h}{R}\right)^2 \tag{3}$$

This value, as discussed in the literature review, is regarded as an upper limit value and a reference for comparison between failure load results obtained analytically or experimentally, which are usually a fraction of this value.

For the parameters of the present spherical cap, the upper critical load value under normal pressure is calculated to be 3.8 MPa. This value is used in the following subsections as a reference for comparing the different values obtained for models loaded with normal pressure. The ratio of the failure load to the upper critical buckling load also presents a normalized value for the buckling of spherical caps used in all the relevant literature for comparing the results of different studies, therefore that ratio is also used for comparison against the literature data.

Based on Eq. (1) in reference [87], the maximum allowable pressure on the shell when considering the material limits is presented as:

$$p_y = 2\frac{\sigma_y t}{R} \tag{1}$$

For a concrete crushing stress of 25 MPa, and assuming that no tensile effects are present in the shell, the maximum allowed pressure for the shell of the present study is equal to about 0.61 MPa, which is only about 16% of the pressure leading to instability (based on the linear elastic buckling formula by Zoelly [121]). Consequently, a material failure is expected for the shell of this study. Given that the cap is bounded by a ring-beam which introduces a bending field at the cap-ring intermediate region, the low tensile capacity of the concrete is expected to reduce the structure's capacity even further. Consequently, after establishing the failure load results of the elastic shell and comparing them to the values documented in the literature, the effects of concrete plasticity and cracking, and the joints between the panels of the segmented structure are investigated.

Table 24 presents the buckling values of spherical caps, obtained from previous research, with the same geometric parameter as the cap of this study. As previously discussed in the literature review, most of the research work between the 1940s and 1970s aimed to establish a relationship between the failure load of spherical caps and the geometric parameter λ, which was found to be calculated in most of the literature as Eq. (7) [23], which results in a value of 10.74 for the shell of this study. The following should be noted about table 24:

- Although the failure load values in the table correspond to almost the same geometric parameter of the shell in this study, most of the surveyed studies have conducted their work on relatively thinner shells than the structure of this study. Consequently, even though the shell geometric parameter is the same, the failure loads of the shell in this study should be expected to generally exhibit less sensitivity to form imperfections which are established to radically reduce the shell capacity, and lead to sudden instability failures.
- The failure loads in table 24 do not represent a comprehensive overview of all the surveyed studies in the literature, but rather, the reported values merely include the results of studies and recommended guidelines that are either relevant to the present work, or are presented as a generalized formula for the failure of spherical caps.

- The values presented in the table 24 are derived either analytically or experimentally, or are empirical guiding formulas presented for design purposes. For the experimental values in particular, the values were obtained from graphs presented by the authors, or compiled and quoted in other studies by different authors. Consequently, the values extracted from the graphs are prone to slight variations due to subjective interpretation of the results. Conservatively, it can be established that experimental results summarized in table 24 are for shells of geometric parameters between 10 and 11.
- As previously discussed in the literature, most spherical caps stability experimental work was performed on elastic shells, while very few experiments were performed on mortar or concrete shells. Consequently, most of the values in the table are derived based on experiments on shells which failed by buckling elastically. The table indicates which experiments or design equations are particular to concrete shells.

Table 24: Buckling load values of spherical caps in the surveyed literature

Source	Derivation Method	Normalized Buckling Load (P/Pcr)
Zoelly (1915) [121]	Theoretical	1.00
T. von Karman and H. S. Tsien (1939) [113]	Theoretical	0.31
Kaplan and Fung (1954) [72]	Experimental	0.35
B. Budiansky (1959) [21]	Theoretical	0.82
Homewood, Brine, and Johnson (1961) [63]	Experimental	0.18
Seaman (1962) [99]	Experimental	0.50
Seaman (1962) [99]	Experimental	0.30
Volmir (1963) [112]	Theoretical	0.26
ACI 344 (1970) [5]- concrete shells	Empirical	0.04
Vandepitte, Rathe and Weymeis (1979) [109] - concrete shells	Experimental	0.46
Gonçalves (1992) [49]	Theoretical	0.06
Farshad (1992) [44] - concrete shells	Empirical	0.04
Ventsel and Krauthammer (2001) [110]	Empirical	0.25
Marcinowski (2007) [83]	Theoretical	0.13

Khakina and Zhou (2011) [76]	Theoretical	0.58

The table reestablishes the large scatter of shell buckling values stated widely in the literature. Based on the data provided in the table, a mean value of 0.307 of the classical buckling load is found for the shell, based solely on the value of the geometric parameter. The standard deviation of the data is 0.215, with 64.3% of the data within one standard deviation from the mean.

The lowest values found in the table are the empirical equations presented as design guidelines for concrete shells in [44] and [5]. Consequently, they present, by definition, a conservative value for design purposes. When these two values are excluded, the mean rises to 0.355 with a slightly smaller standard deviation of 0.206, where 66.7% of the data lie within one standard deviation.

An interesting observation is that when the experimentally and numerically derived data are compared, very close mean values are found (0.362 for analytically derived values and 0.357 for experimentally obtained values). This may be due to the fact that most of surveyed analytical studies were focused on deriving formulas that can predict buckling loads which match those of experimental analyses, and most of them, in fact, have shown compatibility with one or more sets of data by the author or other authors of similar studies.

Another observation is that the scatter of the tabulated experimental results appears to much smaller than usually documented in various studies on shells of different geometric parameters (the standard deviation of the experimental values is 0.114). This observation could suggest that shells with relatively large geometric parameters (λ = 10.74 for the table data) may be less sensitive to imperfections when compared to shells of smaller geometric parameters.

Within the five experimental values presented in the table, only one value was obtained by experiments conducted on concrete shells [109] with a buckling load value of

about 0.46 of the classical buckling load. Two other values in the table refer to concrete spherical caps; these values present empirical formulas recommended for the design of concrete domes in [44] and [5]. Both values give failure loads of about only 0.04 of the classical buckling load, and are lower than any other values found in the surveyed literature.

Table 25 presents a summary of the failure load values of the spherical cap of this study obtained using finite element models on ANSYS and various modeling parameters. The main analysis parameters are stated in the table, while the detailed parameters can be found in tables 29 – 35 in appendix B of this paper. Column 5 of table 25 presents a normalized value for the failure load as a ratio of the linear elastic buckling load value.

Table 25: Failure load values of normal pressure loaded models

Normal Pressure Loading				
Model Code	Analysis type	Boundary	Failure Load (N/m2)	Failure load (ratio of classic buckling load)
MDS24	Nonlinear Elastic	Clamped	3.2E+06	0.83
MDS26	Nonlinear Inelastic	Clamped	6.0E+05	0.16
MDS23	Nonlinear Inelastic	ring beam	3.2E+05	0.08
SDS23	Nonlinear Inelastic	clamped	5.8E+05	0.15
SDS22	Nonlinear Inelastic	ring beam	2.8E+05	0.07

Table 25 shows that the nonlinear elastic buckling load of the shell, when modeled using SHELL281 and clamped boundary conditions is 83% of the linear elastic buckling load. This value is almost the same as that calculated analytically by Budiansky [21] for nonlinear elastic buckling. The postbuckling shape was tracked using nonlinear stabilization on ANSYS, showing, in Fig. 154, a snap-though buckling where the cap is deflected into an inverted form and the maximum vertical displacement is equal to 8.2 m (almost twice as the cap's height).

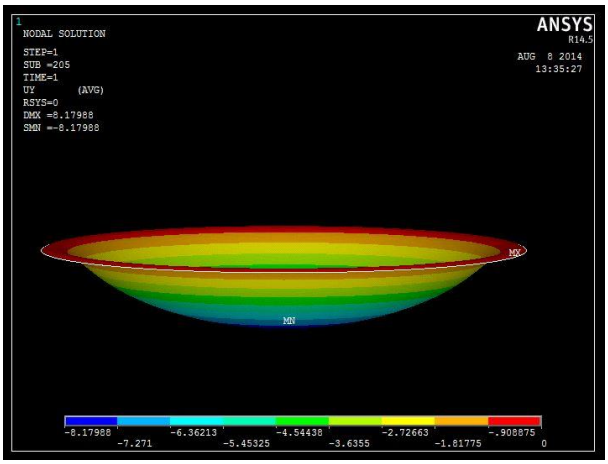

Fig. 156: Snap-through buckling of MDS24

Fig. 155 shows the load central deflection path for MDS24, which shows a linear relationship typical of the perfect spherical shell up until buckling occurs where the structure undergoes a large displacement for very small load steps until it is inverted and then it starts carrying loads again, as seen in the very last part of the path. It should be noted, as previously mentioned, that the postbuckled load deflection path produced using nonlinear stabilization on ANSYS is not necessarily accurate, since nonlinear stabilization is stated to not be able to track negative stiffness portions of the curve. However, only the load at which buckling starts is of significance in this study.

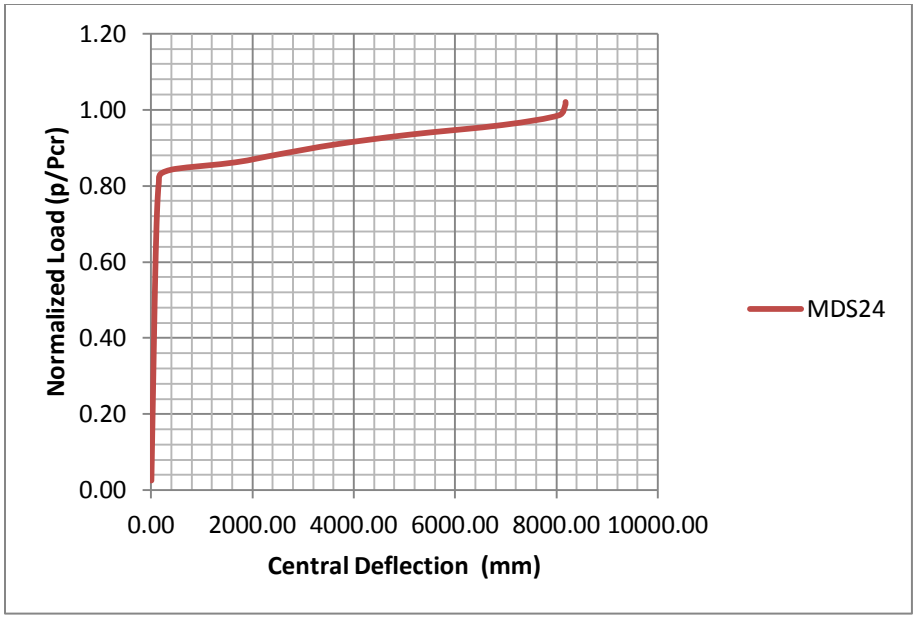

Fig. 157: Load-deflection path of MDS24

When the shell is modeled using concrete elements with plasticity and cracking properties (MDS26), the failure load drops to only 16% of the P_{cr}. This value is seen to be exactly the same as the maximum allowable pressure provided by Eq. (1) and considering the material limits only, which clearly supports the material failure assumption. A comparison between the load deflection paths of MDS26 and MDS24 (Fig. 156) shows that the structure fails long before it's nonlinear elastic buckling load and with very small displacements, further supporting the initial prediction of a material induced failure.

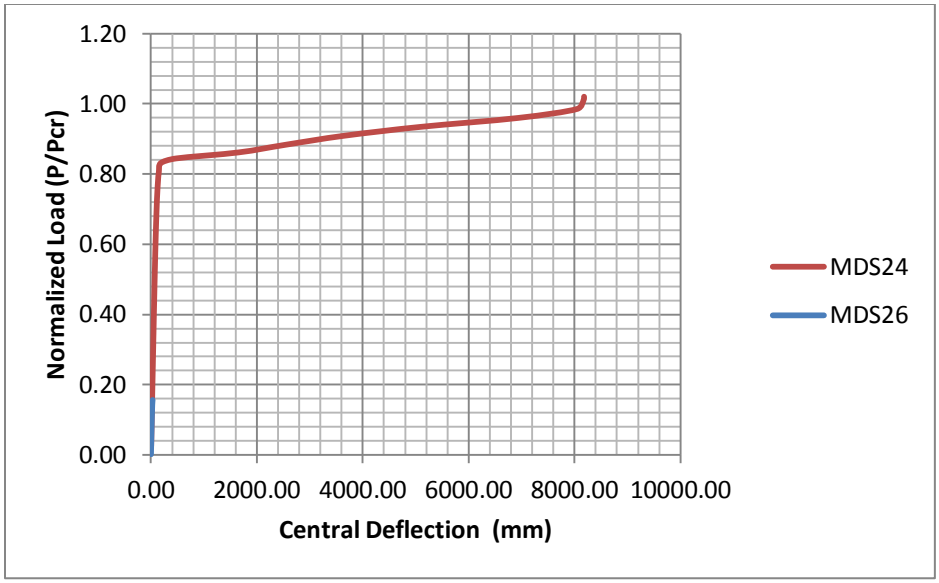

Fig. 158: Load-deflection paths of MDS24 and MDS26

Fig. 157 shows that most of the cap shows von Mises stresses approaching the maximum allowed value (between 23 and 25 MPa). The stress-state ratio plot in Fig. 158 clarifies that the maximum stresses are found, not at the crown, but rather at the intermediate region between the clamped boundary and the crown zone.

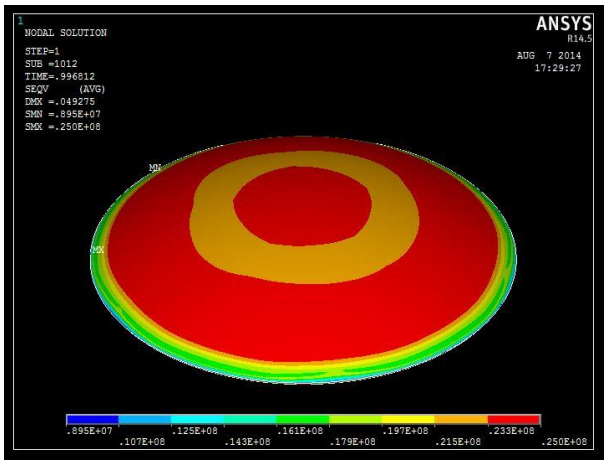

Fig. 159: Equivalent von Mises stresses of MDS26

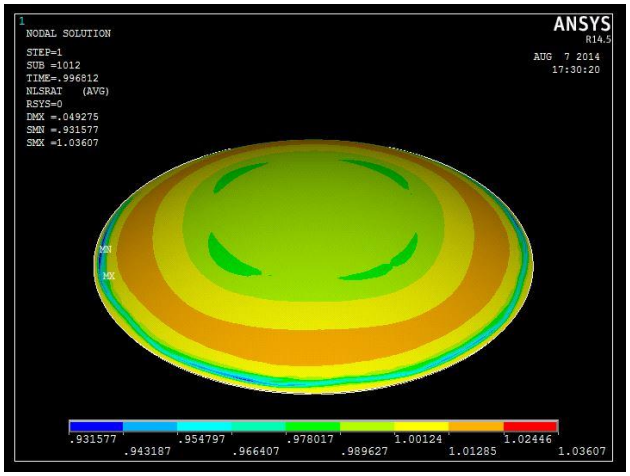

Fig. 160: Stress-state ratio of MDS26

The vertical displacement pattern of MDS26 is consistent with the stress distribution where the maximum displacement appears to not be at the crown, but rather at the intermediate region between the crown zone and the clamped boundary, as shown in Fig. 159.

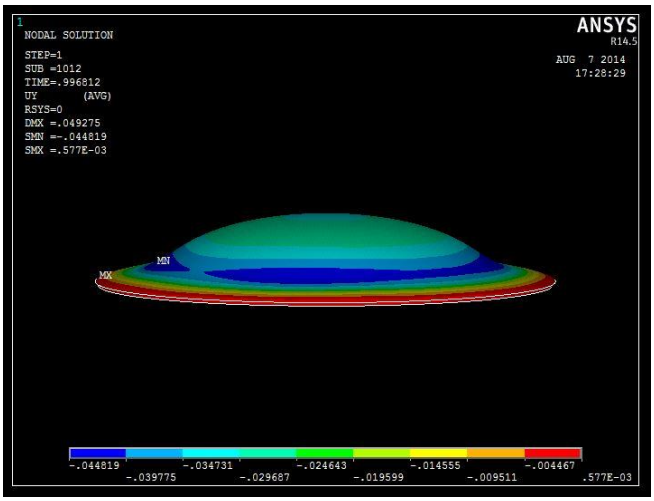

Fig. 161: Vertical displacement of MDS26

The reduction in capacity pattern of the normal pressure loaded models was previously seen in gravity loaded models, and seems to be accompanied by the same

displacement patterns. The ring beam-bounded cap of MDS23 shows a reduction in the failure load to half of MDS26 (8% of P_{cr}). Fig. 160 presents a comparison of the load deflection paths of MDS26 and MDS23 that shows the lower stiffness of MDS23 which is seen to quickly approach zero toward the failure load value with an even larger deflection than MDS26.

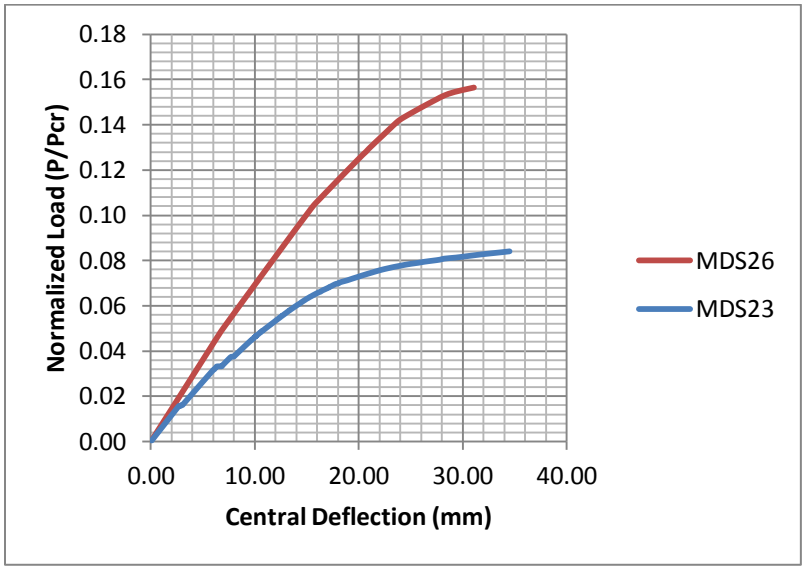

Fig. 162: Load-deflection paths of MDS23 and MDS26

The stress state ratio in Fig. 161 shows that most of the cap has a stress ratio between 0.92 and 1.1, which means that the stresses in most of the cap have reached or are approaching the material failure stresses. The exception is the tensile region between the ring beam and the cap which displays stress ratios between 0.06 and 0.63, which is consistent with the expected cracking at that region.

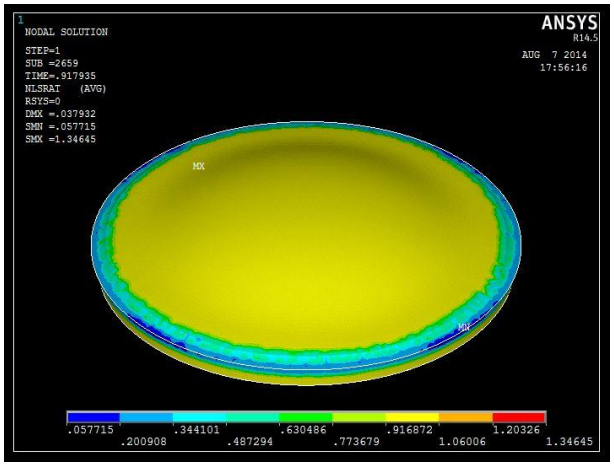

Fig. 163: Stress-state ratio of MDS23

When the cap was modeled segmentedly using panels in contact, similar patterns and failure loads are observed; however, slightly lower than those of the caps modeled monolithically, with clamped boundary model SDS23 failure load at 97% of MDS26 (15% of Pcr) and SDS22 at 88% of MDS23 (7% of Pcr).

The load-deflection paths of SDS23 and SDS22 are compared to those of MDS26 and MDS23, respectively, as shown in Fig. 162 and Fig. 163. The figures show similar load-deflection paths with a generally stiffer response in the monolithic models. The presence of contact between the panels has resulted in some discontinuities in the path as clearly seen in SDS23.

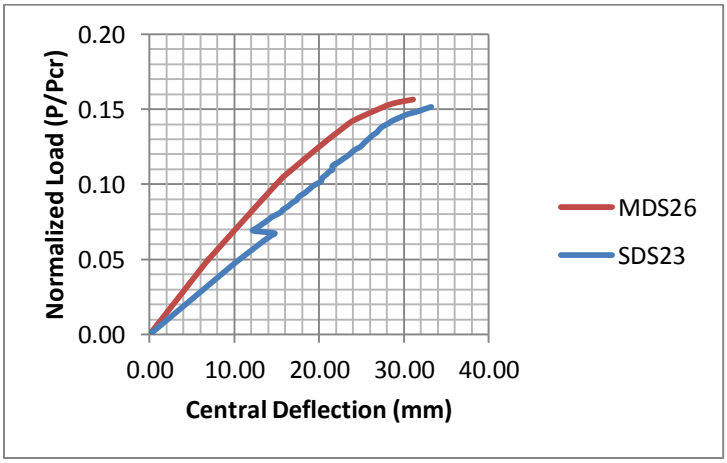

Fig. 164: Comparison between the load-deflection paths of MDS26 and SDS23

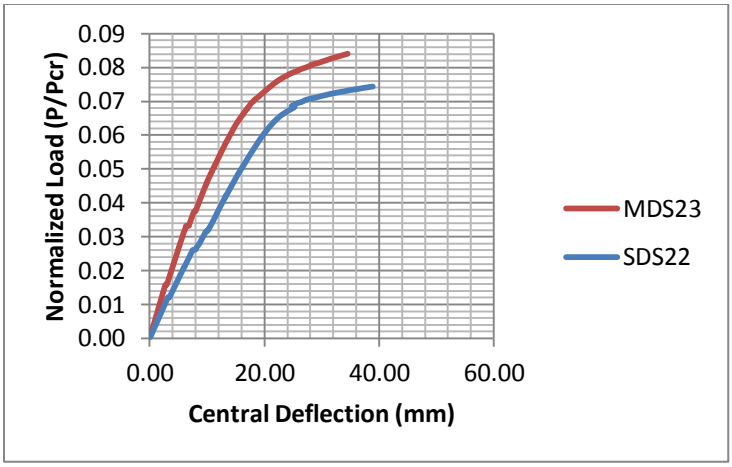

Fig. 165: Comparison between the load-deflection paths of MDS23 and SDS22

The distributions of von Mises stresses and stress-state ratios of SDS23 appears to be very similar to those of MDS26 with the exception of some asymmetric local stress concentrations at some contact locations as seen in Fig. 164 and Fig. 165. The earlier loss of convergence of SDS23 could be attributed to the very high stress-state ratios seen in the cap elements immediately adjacent to the contact elements of the base panels as seen in Fig. 165.

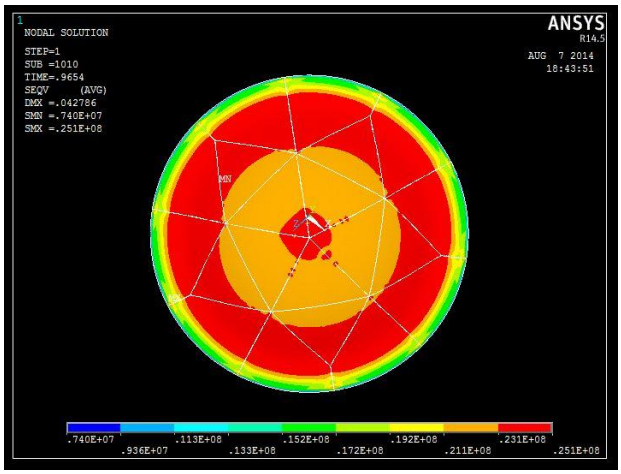

Fig. 166: Equivalent von Mises stresses of SDS23

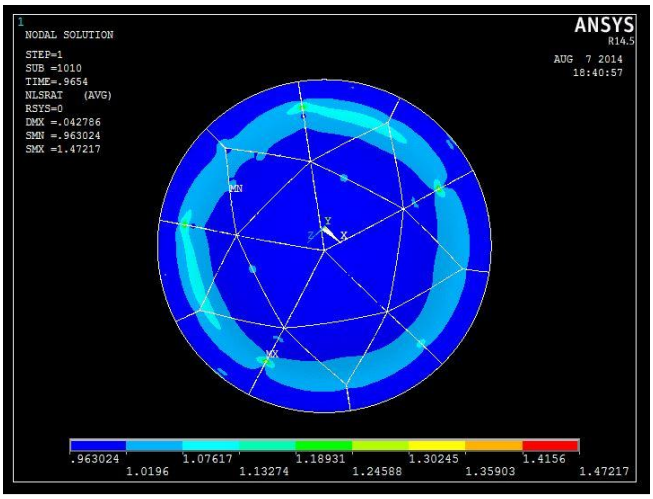

Fig. 167: Stress-state ratio of SDS23

Similar local stress concentrations near some contact locations are also observed in ring beam-bounded model SDS22, as shown in Fig. 166 of the von Mises plot. However, the largest stresses are only at 23 MPa, which could indicate that loss of convergence might not have been caused by a material instability. In this case, the failure could have been initiated by a debonding of contact, as seen in the contact status plot in Fig. 167, which shows the contact condition as 'near contact' with the largest contact gap at the contact between the base panels and the ring beam, as shown in Fig. 168, and equal to 5.3 mm (completion of contact debonding occurs at a gap of 5 mm). As previously mentioned, the panels are only supported by bonded contact with adjacent panels; consequently, complete debonding will result in a large rigid body motion that is expected to cause a loss of convergence.

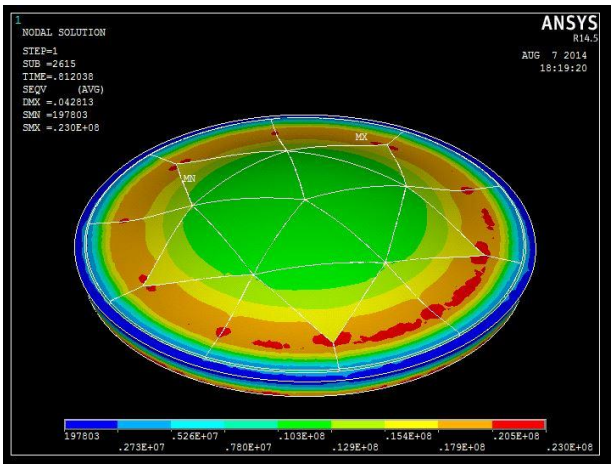

Fig. 168: Equivalent von Mises stresses of SDS22

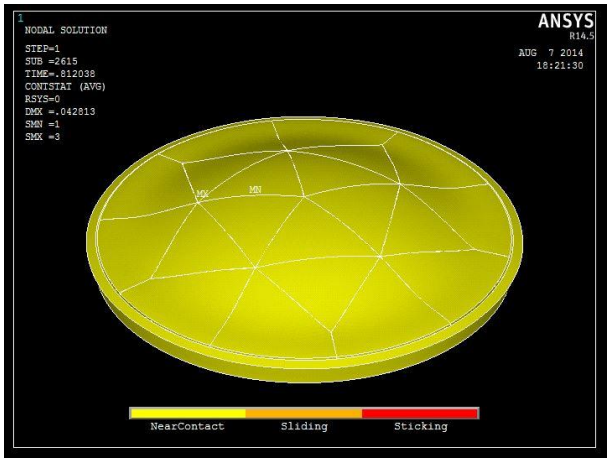

Fig. 169: Contact status of SDS22

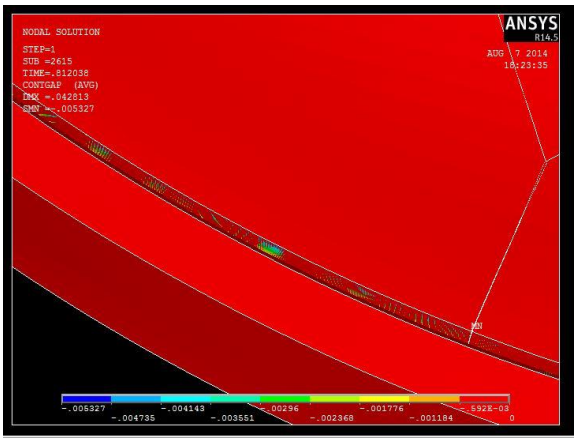

Fig. 170: Development of contact gap of SDS22

Based on the results of the previous models, it is seen the large drop in the capacity of concrete spherical caps, when modeled with material plasticity and concrete cracking, is found to be consistent with the recommended empirical formulas for the design of concrete caps, particularly those by Farshad [44] and ACI 344 committee report [5], which provide values that are about 4% of the linear elastic buckling load. The failure loads of the spherical cap of this study under normal pressure were found to be equal to 8% and 7% of the linear elastic buckling load for monolithic and segmented caps, respectively. It should be kept in mind, though, that the very low design values provided in the formulas are considered to take into account the anticipated capacity reduction caused by geometric imperfections. That effect was not considered in the models of the present study. However, it is anticipated that relatively small geometric imperfections (of thickness and radius of curvature variations) may not contribute to a significant capacity reduction since the failure of the cap was caused by either a material failure or a connection debonding failure. The relatively large thickness of the shell in this study suggests that, under uniform loading conditions, a material failure mode precedes an imperfection-induced loss of stability.

5.2.3. Failure of concentrated load models

In this part of the analysis, the behavior of the structure under a concentrated point load at the crown is studied through a finite element model, and compared to the results of the experimental analysis performed on a 1:10 scale model of the full prototype structure consisting of the spherical cap panels, the ring beam and the supporting columns.

Table 26 presents the results of the FE models where the cap was loaded by a concentrated load at the crown. As previously mentioned, the loading in the finite element models was applied as a uniform pressure over a steel plate modeled by SHELL181 at the crown, in order to closely follow the loading of the experimental model and avoid early loss of convergence due to the high stress concentration at the loading point. The actual failure load values of the monolithic cap model MDS25 and segmented cap model SDS25 are shown in column 4 of the table in Newtons.

Table 26: Failure loads of models loaded with concentrated loads

Concentrated Loading			
Model Code	Analysis type	Boundary	Failure Load (N)
MDS25	Nonlinear Inelastic	ring beam	6.06E+06
SDS25	Nonlinear Inelastic	ring beam	4.16E+06

As the results of MDS25 and SDS25 show, there is a significant reduction of the structural capacity due to the segmentation of the cap under the concentrated loading condition. The results show that the segmented cap of SDS25 failed at about 69% of the failure load of the monolithic cap of MDS25.

This reduction can be explained by the fact that the concentrated loading at the crown results in non-uniform stress distributions across the surface of the shell. While the monolithic shell deflects as one unit under the concentrated load reducing the effect of local stress concentrations to some extent, the effect appears to be escalated in the segmented cap where the panels are not fully acting together in the model. This effect can be seen in Fig. 169 of SDS25 where the central panels appear to be deflecting in isolation

under the concentrated load, while the rest of the shell appears to be unaffected (the displacement is scaled by 20 for clarity).

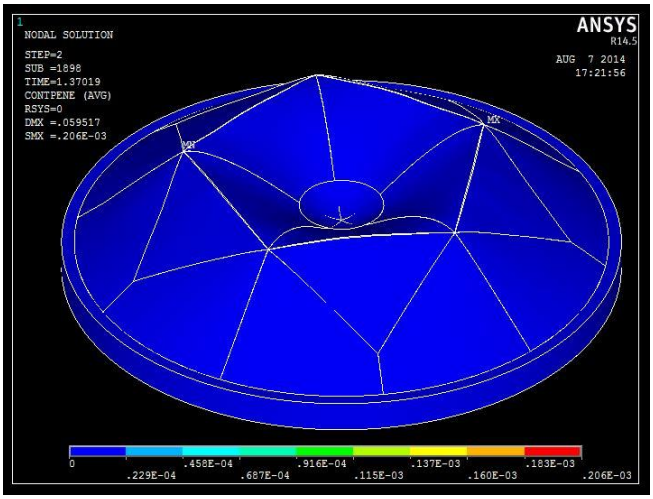

Fig. 171: Deflection of the central panels of SDS25

This conclusion can also be supported by the mostly insignificant capacity reduction due to segmentation in models loaded uniformly, whether by normal pressure or global gravitational acceleration.

The deflection of MDS25 shows what resembles a snap-through of the central region around the loaded area accompanied by a significant upward vertical displacement of the immediately adjacent region (the red region in Fig. 170). The load displacement path in Fig. 171 shows, however, that the inverted central region represents a stable equilibrium position as indicated by the load carrying capacity apparent in the last portion of the load-deflection path in Fig. 171.

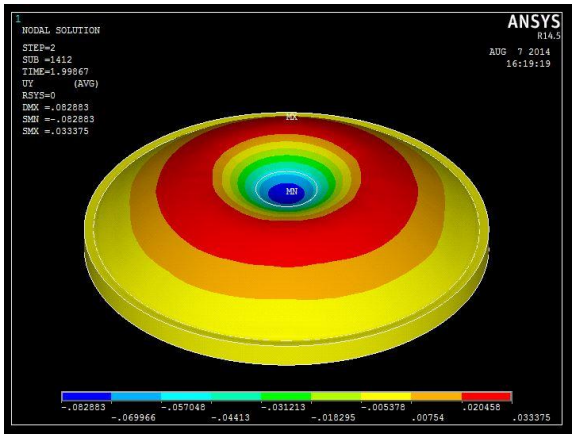

Fig. 172: Vertical displacement of MDS25

The loss of convergence of MDS25, thus, appears to not have been caused by large displacement, but rather by the stresses at the central region at the crown reaching the maximum stresses, which is shown in Fig. 172 of the stress-state ratios. It's worth noting that the failure of MDS25 was accompanied by an extensive cracking around the entire surface of the shell as seen in Fig. 173.

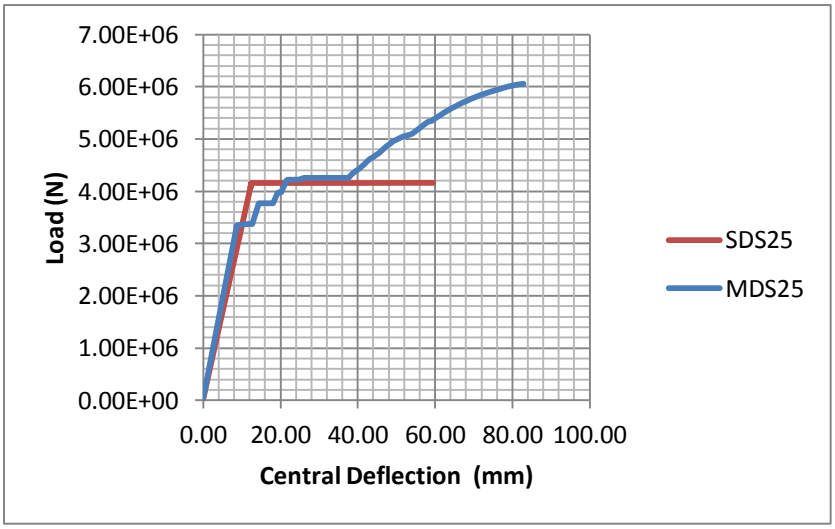

Fig. 173: Comparison between the load-deflection paths of MDS25 and SDS25

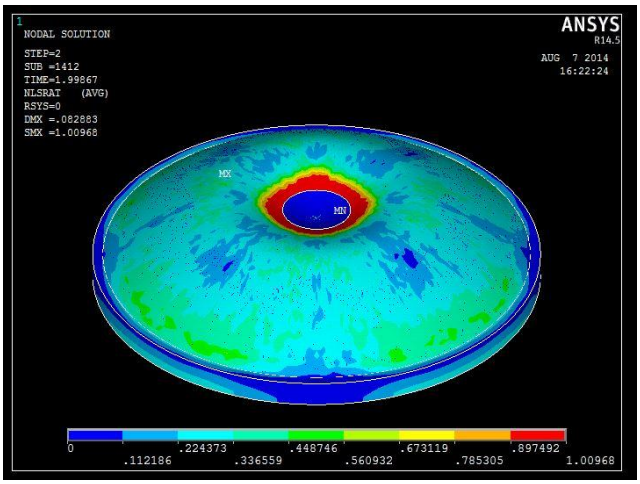

Fig. 174: Stress-state ratio of MDS25

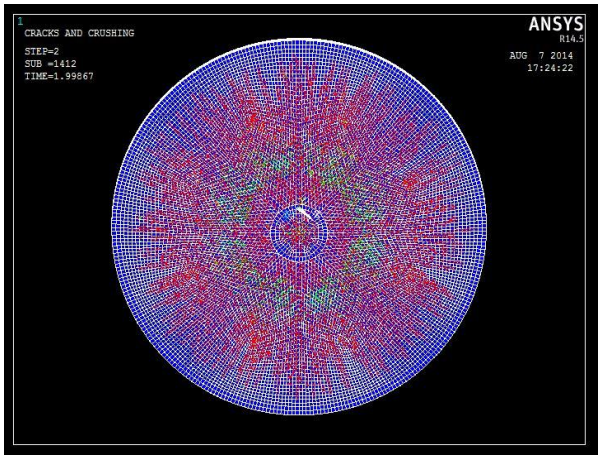

Fig. 175: Cracking of MDS25

On the other hand, the load-deflection path of SDS25 shows a linear pattern until the failure load point where a zero stiffness response is observed, indicating a large displacement at no increase of the load. This observation supports the previous observation of the central panels working in isolation in resisting the load. The straight line portion of the load-deflection curve indicates the large displacement of the central panels of SDS25 which are only supported by the contact with the adjacent panels. Accordingly, large local strains are seen at these contact locations as shown in the von Mises equivalent strains plot in Fig. 174.

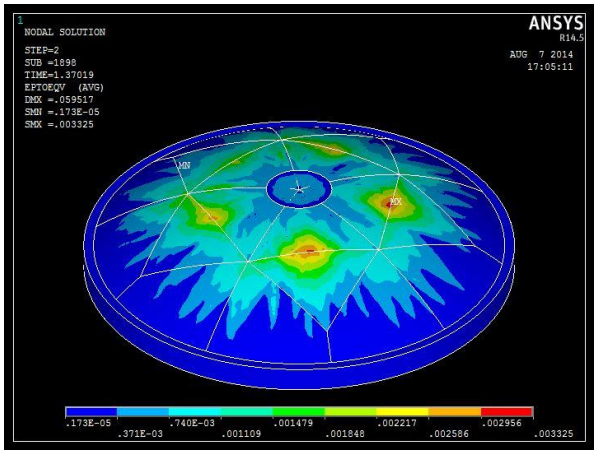

Fig. 176: Equivalent von Mises strains of SDS25

The stress state ratios of SDS25 (Fig. 175) also show a central region of about the same size as MDS25 to have reached the maximum stresses. In addition, some asymmetric stress concentrations are seen at the elements around the contact region between the central panels and the rest of the cap.

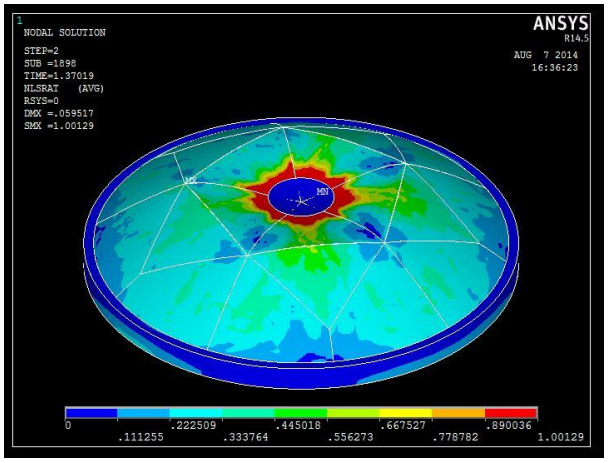

Fig. 177: Stress-state ratio of SDS25

Experimental Analysis Results

As previously discussed, test 3 of the experimental analysis was an ultimate load test which included applying a compressive concentrated load at the crown measured by a load cell up to failure of the cap. The loading was distributed on a central region at the crown of about the same area as the steel plate area in the finite element model. This was accomplished by placing a sand bag topped by a 3 cm thick steel plate on which the load is applied. The test was terminated after a large displacement and large cracks were observed on the surface of the cap.

The failure mode of the experimental model was observed to be generally consistent with the failure of the FE model SDS25. At the failure load, the central cap panels showed a large displacement under no further load increase, leading to sudden slight flattening of the shell crown region, which can be seen in Fig. 176. This flattening was accompanied by large cracks at the boundary of the flattened region and other meridional cracks that extend to the ring beam. Most of the large cracks appear to have occurred between the edge of the panel and the grout of the joint adjacent to the panel, as seen in Fig. 177 and Fig. 178.

Fig. 178: Flattening of the central region of the experimental model

Fig. 179: Cracks at the interface of the panel and the grout at the joint

Fig. 180: Meridional cracks at the intermediate joints

The cracking pattern of the cap appears to be generally consistent with the stress concentrations seen in the FE model. As mentioned above, the largest cracks are seen at two locations; the joints adjacent to the central panels between the panel edges and the grout, and meridional cracks which extend from the corners of the central panels, through the joint between the two adjacent base panels, as seen in Fig. 179 and Fig. 180. It is, however, seen that the FE model shows extensive cracking across the entire surface of the shell (see Fig. 181). This clearly indicates that the panel-grout interface is the weakest point of the structure since the panels themselves appear to be mostly unaffected.

Fig. 181: Cracking pattern of the experimental model

Fig. 182: Central crack of the experimental model

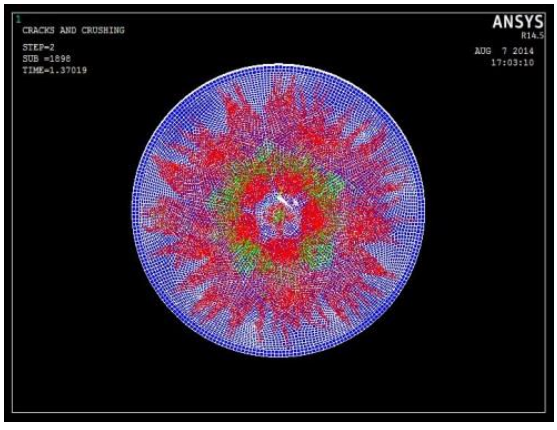

Fig. 183: Cracking of the FE model SDS25

Some asymmetric cracks are observed at locations of geometric imperfections. For example, while the large hoop crack around the central panels is mostly at the panel-grout interface, a large transverse crack is observed across the surface of the panel itself, as seen in Fig. 182. This particular panel is one which was designated to have the smallest average thickness of the cap panels. It was discussed in the methodology chapter to have led to extra flattening of that part of the cap and was expected to constitute a weak point of the shell surface that shall be monitored during the test.

Fig. 184: Cracks in the imperfect panel

Another weak point is in the boundary ring beam which had shown some honeycombing after removing the formwork, and was treated with mortar. At the structural failure, one of the meridional joint cracks is seen to have extended though the ring beam, at the location where honeycombing was previously observed, right at the face of the column as seen in Fig. 183.

Fig. 185: Transverse crack in the ring beam

In general, though, most of the cracks are seen to have extended through the entire thickness of the intermediate joints and can be clearly seen on the lower surface of the cap, as noted in Fig. 184.

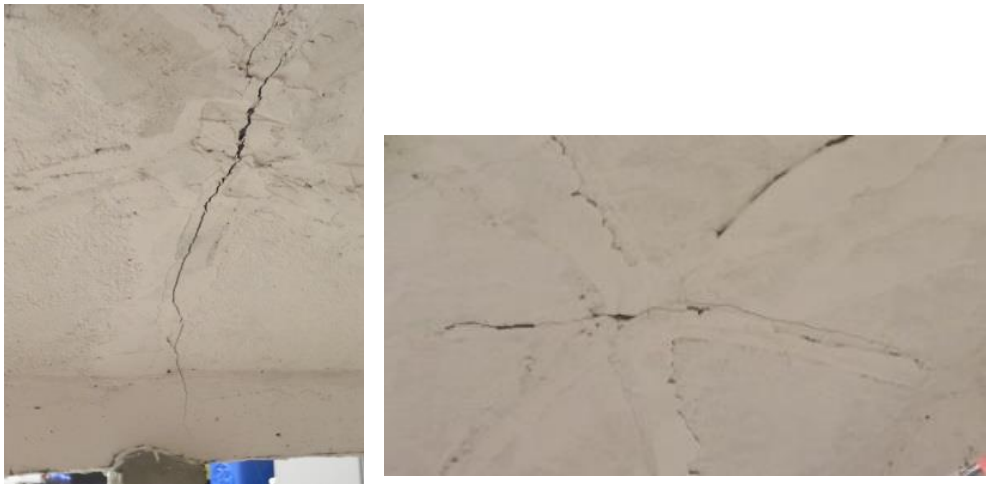

Fig. 186: Structural cracks on the lower surface of the cap

Table 27 presents a comparison between the failure load of the experimental model and the corresponding FE model in Newtons. The table shows that the experimental failure load is 77% of the failure load of the FE model. A comparison between the load-central deflection paths of both models, seen in Fig. 185, shows that the experimental model exhibits a lower stiffness than that of the numerical model throughout the entire loading process. The kinks observed in the load deflection path of the experimental model are due to the presence of the sand bag directly under the applied load which, as the load increased, was compacted resulting in the jumps seen in the figure. At a load of about 77% of the failure load of the numerical model, the experimental model undergoes a similar large displacement under almost no load increase, represented by the horizontal part of the load-deflection path. Subsequently, while the FE model fails at that stage due to the material reaching the maximum stresses causing convergence difficulties, the experimental model undergoes an unbounded displacement at the crown, as seen in the negative stiffness part of the path, before unloading of the structure.

Table 27: Comparison between the failure load of the experimental model and FE model (SDS25)

Model	Failure Load (N)
FE Model (SDS25)	4.16E+06
Experimental (Scaled)	3.21E+06

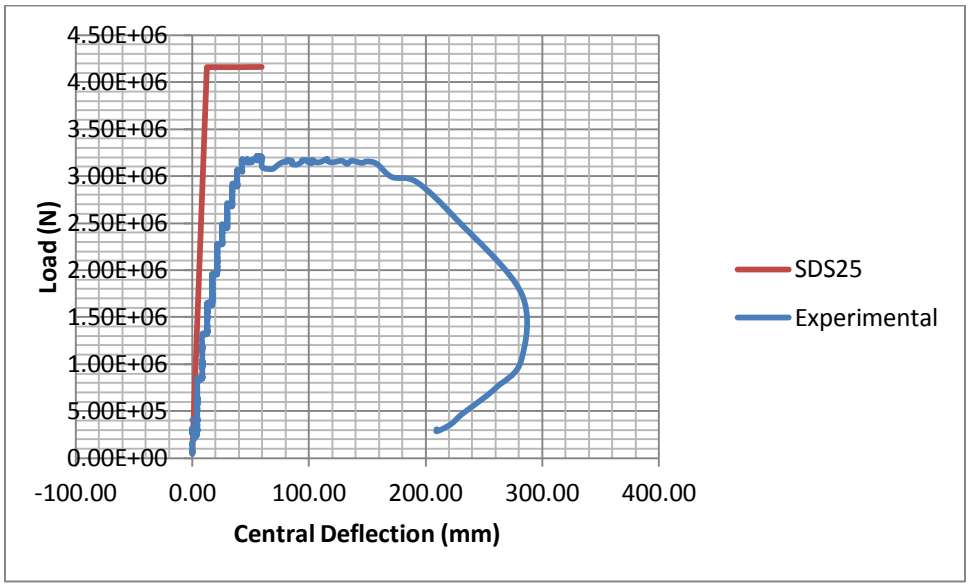

Fig. 187: Load-deflection paths of the experimental model and FE model SDS25

The lower stiffness of the physical model, when compared to the FE model, could be attributed, in part, to the differences in the boundary conditions between the experimental and numerical model. As previously discussed, in the numerical model, the lower nodes of the ring beam are completely restrained against translation in the x, y and z directions. In the physical model, however, the ring beam is supported on eight columns that are braced at the base. Consequently, the fact that the ring beam is supported by deformable bodies that allow the beam to expand radially has resulted in larger lateral displacements at the foot of the cap, as seen in Fig. 186, thus increasing the overall downward vertical displacement. This could suggest that the idealized boundary in the numerical model overestimates the capacity of the structure.

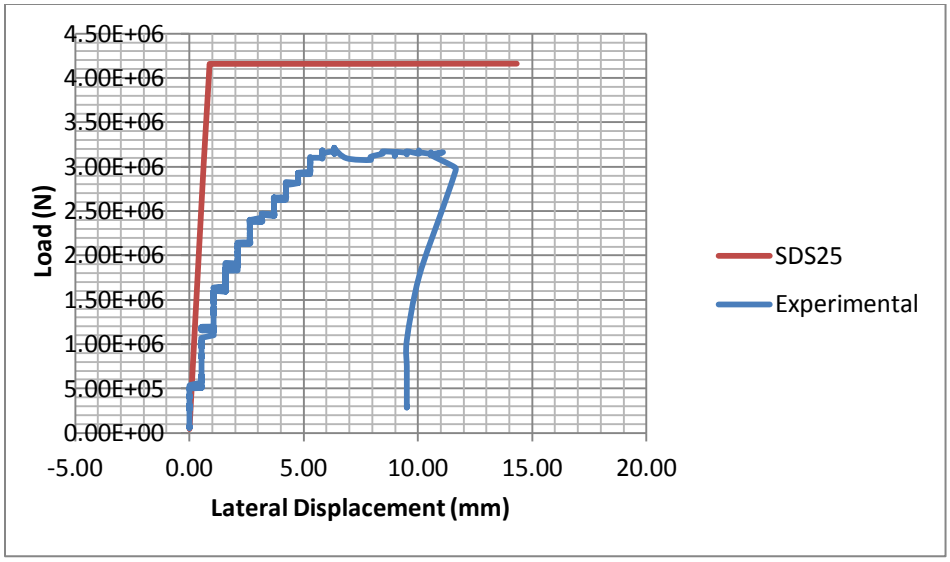

Fig. 188: Lateral displacement of the experimental model and FE model SDS25

Another possible indication of the lower failure load of the experimental model could be that the capacity of the joints between the panels is overestimated in the numerical model when modeled using contact elements. In particular, the contact stiffness factor or debonding stresses at the contact may need to have lower values in order to properly reflect the actual capacity of the joint. This conclusion may be supported by the distribution of the stresses at failure in the FE model (see Fig. 174) where no significant discontinuities are observed at the meridional joints between the base panels where most of the large cracks in the physical model are observed.

Finally, the failure of the experimental model is seen to exhibit an almost symmetric behavior with the largest cracks seen at the same joint locations around the entire surface of the cap, rather than asymmetric deflections initiated at imperfect geometry locations. This observation suggests that the failure load of the shell, which has a relatively large thickness, may not be significantly affected by geometric imperfections. The only significant form effects are those caused by the inherit discontinuities in the structure introduced by the joints between the precast shell panels. These joints seem to only significantly affect the structural capacity when the structure is loaded non-

uniformly leading to non-uniform stress distributions that give rise to localized large stress concentrations at the weaker points of the structure, which are, in the case of the physical model, the panel-grout interface at the joints.

5.3. Construction analysis

This section presents particularly relevant results regarding the prefabrication and assembly of the proposed structural system. The section discusses the resulting quality of the model precast panels produced in the experimental analysis process, and previously touched upon in the methodology chapter of this paper. Furthermore, the results of the finite element analysis of the behavior of the structure during construction is discussed in order to present a general idea of the construction induced loads and anticipated deflections using the proposed construction method.

5.3.1. Panel Properties

The most important parameters of the prefabrication process are the panel thickness, curvature and size. Deviations in the curvature of the lower surface of the panel were expected to occur in the prefabrication of the experimental model due to the fact that no positive mold piece was used to control the lower surface curvature, but rather, it was only controlled manually using concrete surface smoothing tools, and spacers inserted during casting to ensure a uniform thickness. After demolding of all the panels, the uniformity of the panels' thickness was measured and the average panel thickness was calculated.

Based on 20 thickness measurements (from the 20 panels), the average thickness of the panels was found to be 2.61 cm with a standard deviation of 0.29 cm, where 55% of the panel thicknesses (based on the measurements population) lie within one standard deviation from the mean, and 95% lie within two standard deviations. The calculated average thickness is 1.1 mm different from the planned thickness of 2.5 cm, with an acceptable scatter of the data, particularly considering that the economical molding and casting methods used for the panel prefabrication are generally expected to produce low quality specimens.

Other thickness measurements of the panels were taken in order to determine the thickness uniformity of each individual panel. This was performed by taking a sample of 10 measurements (in addition to the previously measured thickness) at different locations

along the edge of the panels which had the largest and smallest recorded thickness in the previously recorded measurements. The measurements taken for the largest thickness panel, measured to be 3.24 cm, and the smallest thickness panel, measured to be 2.09 cm, are shown in table 28.

Table 28: Sample of the thicknesses of largest- and smallest-thickness panels

Thicknesses of largest thickness panel	Thicknesses of smallest thickness panel
2.090	1.750
2.655	2.420
2.900	2.005
1.828	2.235
2.080	2.750
2.460	3.055
3.400	2.180
2.740	1.965
2.280	2.360
2.670	2.635
3.240	2.090

From the data in the table, the average thickness of the largest-thickness panel is found to be equal to 2.58 cm with a standard deviation of 0.47 cm, and that of the smallest-thickness panel is calculated as 2.31 cm with standard deviation of 0.36 cm. Although the most extreme average thicknesses appear to only differ from the planned thickness by a maximum of about 2 mm, the standard deviation of the thickness measurements within the panel itself is seen to be quite high, which indicates a significantly varying thickness along the edges of individual panels, and suggests the need for better quality control over the prefabrication process.

Another problem that was faced due to the inaccurate panel fabrication, which was referred to in the methodology chapter, is the size of the panels. As previously explained, during the assembly process, the size of the panels was founded to be smaller the planned size which resulted in unplanned-for gaps between the cap panels. These

gaps were traced back to have been caused by the bent steel meshes and their insulation sheets along the edges of each panel, which have resulted in a reduction, significant in some instances, of the size of the panel in the order of 0.5 -2 cm. Although these gaps were easily overcome in the physical mode by using plywood sheets to fill the gaps, they are unacceptable in the prototype structure since they can constitute weak points and result in significant form imperfections at the joints. Consequently, accurate panel sizes with very low manufacturing tolerances are essential for the efficiency of the proposed structure.

5.3.2. Construction Loads Analysis

As previously discussed in the methodology chapter, the construction process utilizes a scaffolding framework for supporting the panels during the assembly. More specifically, vertical props are provided at the locations of panel corners and to the specific heights of these corners dictated by the spherical cap's geometry. These props are supported by girders, all resting on a working platform. The details of the assembly process, which was mostly followed for the assembly of the physical model's panels as well, were discussed in the methodology. The two concerns for the construction induced loads analysis were preventing rigid body motion and limiting the bending deflections of the panels.

Typically, for a construction loads analysis, the partial structure would be analyzed for each different construction stage. However, the symmetry of the structure of this study, and the selected symmetric supporting conditions for the panels reduces the problem to analyzing only two panels. The FE models of these individual panels, referred to as P1 and P2, provide estimates for the mid-edge deflection of each panel, in order to determine whether extra temporary supports will be needed during the construction.

The analysis of the base panel P1, represents row A panels with the largest overall size, was performed using the same element, material and geometric properties of all previous FE models, with the two free corners and the lower boundary restrained against vertical translation, representing the restraining provided by the vertical props and the boundary ring beam. The lower boundary of the panel was also restrained against

horizontal displacement in order to ensure numerical stability of the model. However, a more elaborate boundary with contact friction between the base of the panel and the ring beam may provide a better simulation of the real life boundary of the panel during construction. This modeling alternative is discussed in the recommendations chapter.

Fig. 187 shows the total displacement plot of P1, which shows a maximum total displacement of about 3 mm around the upper corner of the panel. The largest component of this displacement is horizontal, due to the fact that the panel, at that location, is only supported against vertical displacement. The horizontal displacement, however, may be restrained during the construction through the prop heads at the upper corner, which can be designed to provide some lateral restraining. When the horizontal displacement is prevented at the upper corner, the maximum deflection drops to about 1 mm, around the mid-span of the panel's unsupported length, which is 0.01% of the unsupported span, as shown in Fig. 188.

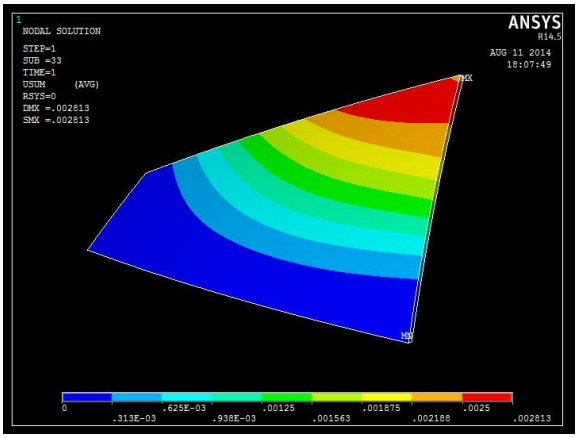

Fig. 189: Total deflection of panel P1

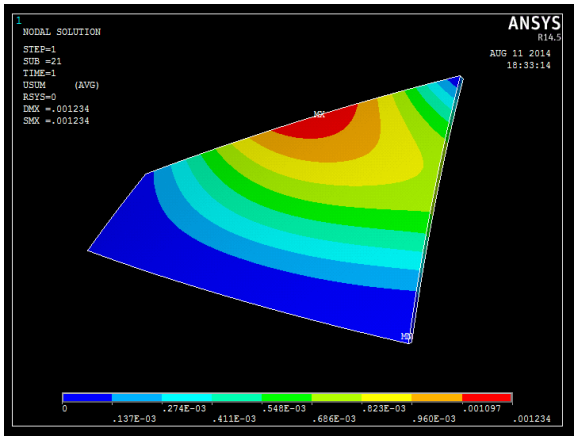

Fig. 190: Total deflection of panel P1 with horizontal restraining at the upper corner

Panel P2 model represents an analysis of row B and C panels during the construction. The 10 structural panels of this type are all supported at the corner locations by the vertical props. In model P2, the three corners were restrained against vertical translation, and additionally, the lower two corners were restrained against horizontal displacement. Although P2 panel is smaller than P1 panel in the overall size, as previously discussed, it has the largest unsupported length, and is supported only at the three corners, which has resulted in a significantly larger bending deflection, as seen in Fig. 189 which shows a maximum total displacement of about 2.3 cm, toward the upper panel corner. The vertical component of this displacement is the largest component, as seen in Fig. 190 of the vertical displacement, where the maximum vertical displacement at the same location is 2.2 cm, which is 0.3% of the unsupported span. For relatively large spans, this may suggest the need for extra temporary supports mid the unsupported edge of panel P2.

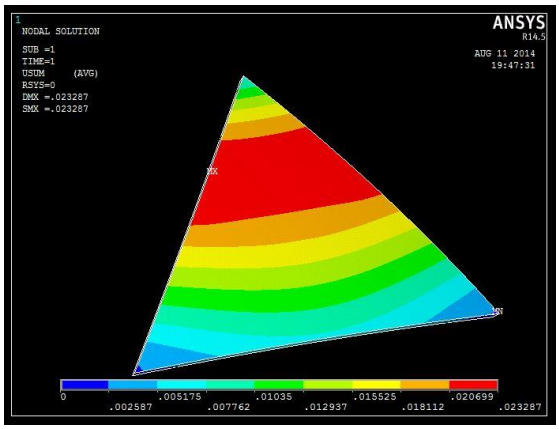

Fig. 191: Total deflection of panel P2

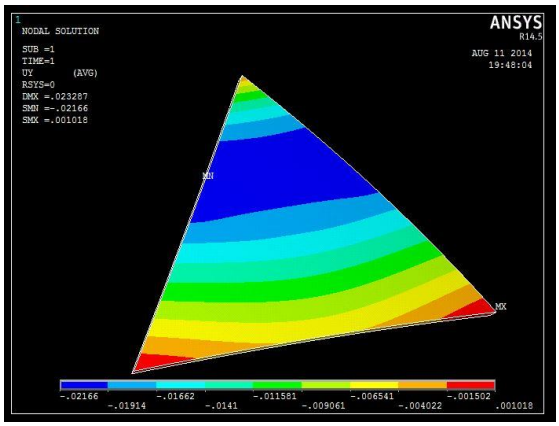

Fig. 192: Vertical deflection of panel P2

As previously discussed, temporary horizontal restraining of the panels may be provided using the heads of the vertical props. During the experimental analysis of this study, only vertical supports were provided for the temporary supporting of the panels under their own weight during assembly, before the joints were grouted. However, a larger scale, or maybe a full scale, model of the individual panels may be needed to properly simulate the effects of the construction-induced loads, provide an accurate estimate of the expected panel deflections, and determine whether more temporary scaffolding is needed to avoid excessive deflections during the construction.

6. CONCLUSIONS

In this study, a segmental precast concrete spherical cap-ring beam structural system is proposed. In the beginning of the study, the structure's geometry is optimized with the purpose of optimizing the efficiency of the prefabrication and construction process. The second part of the study investigates the structural behavior using both numerical and experimental modeling techniques where the effects of segmenting the structure into panels on the capacity and failure mode of the structure are investigated. The behavior of the structure during construction was also investigated with a proposed assembly sequence, finite element models of the partial structure and application of the proposed method for the construction of the physical model. The efficiency of the proposed construction method, both prefabrication and assembly, is an inherit quality of precast concrete construction on account of the higher quality produced using prefabrication techniques and eliminating the need for elaborate formwork on-site. This study adopts a geometry and connection design that adds to the efficiency of prefabrication through maximum reusability of molds and minimum different panel sizes, and conducts a structural analysis which demonstrates that the structural capacity of the dome does not exhibit a significant reduction due to segmentation, particularly under uniform loading conditions. The conclusions to follow were made through the present study regarding the geometry, structural behavior and construction of the proposed structural system.

6.1. **Geometric Design**

It is concluded that the available literature on spherical subdivision techniques, however limited, presents feasible opportunities for application in precast concrete spherical cap construction. Considering the fact that uniform panel sizes pose the largest obstacle for the application of precast techniques for concrete shell construction, the discussed geometries in this study are seen as prospects for modularization and widespread application of efficient precasting of concrete domes through the spherical division techniques which provide the least number of unique panels, and consequently require the least number of molds and allow for maximum reusability.

It is concluded that, using the data generated by the MATLAB code developed in this study and from the construction point of view, the structural system and its variations may only be applicable for a specific range of spans, after which the panels become too heavy to handle during construction. Further validation of the applicability of the design to that specific span range requires an integration of the structural behavior of each particular thickness-to-span ratio, as recommended in the next chapter.

6.2. **Structural Behavior**

Under uniform loading conditions, the spherical cap of this study does not seem to exhibit a significant reduction in the capacity when composed of panels connected by joints with debonding capabilities. However, under loads which create non-uniform stress distributions, local stress concentrations are seen to arise at the inter-panel joints, in both the experimental and numerical models, possibly accelerating the structural failure and leading to a reduction in the spherical cap's overall capacity. As anticipated, the intermediate joints between the panels represent the weakest points of the structure, specifically at the interface of the panel edge and the grout or cast-in-situ concrete at the joint. This has to be taken into consideration when determining the appropriate shell thickness and calculating the capacity of the structure for design purposes.

It is also concluded that the use of a moment-resisting connection is appropriate for the joints in the proposed design, for both the panel intermediate joints and the joints between the base panels and the ring beam. While the panels' intermediate joints are, under uniform loading conditions, expected to have compressive stresses and, thus, act efficiently with a small effect on the structure's continuity, the case is different for the base panel-ring beam joint where tensile stresses inevitably arise, and dictate the presence a tensile joint. It is also seen in the experimental test that, at failure, while a large sudden displacement was observed at the crown and multiple cracks were observed at the joints on both the top and bottom surfaces, the panels did not completely detach. This is attributed to the tied steel reinforcement across the joints which result in a ductile joint. The ductility of the joint is mostly significant in controlling the failure process so that the shell stays as one unit at the onset of failure, with no sudden detachment and collapse of panels due to the cracks at the joint.

6.3. **Finite Element Modelling:**

Modeling of idealized boundary conditions of spherical caps in finite element models may lead to an overestimation of the load-carrying capacity of the structure, and in some instances, it is seen to significantly alter the overall stress distribution and the failure mode of the structure. For the particular results of this study, it is seen that inclusion of the actual boundary in the FE model could result in a better correlation with the experimental results and more proper prediction of the structural capacity. However, it is also concluded that such models require extensive modeling resources and may not always be feasible or justifiable. Ultimately, though, it is concluded that modeling of the boundary ring beam in the FE model is essential for concrete spherical caps. The presence of the ring beam in most of the models was shown to cut the failure load in half, which eventually provided a closer estimate to the failure load of the physical model.

The parameters of the contact pairs at the joints have a significant effect on the failure load of the structure in the FE model. In particular, improper values of the contact stiffness factor and the penetration tolerance factor could lead to an earlier loss of convergence leading to an early termination of the solution that does not represent an actual structural failure. Although there are common values for these parameters that were seen in the surveyed literature to be used in joints of precast concrete structural members, a contact sensitivity analysis should be performed for each different structural application in order to determine the most optimum contact parameters for the particular structure to be studied.

For the models of this study, while the use of ANSYS bonded contact elements combined with a debonding feature was determined to be suitable for simulating the behavior of the joints, the particular contact parameters and debonding stress limits used in this study may be partially responsible for the overestimation of the failure load of the structure when compared to the results of the experimental model. Another limitation is the linear debonding of the cohesive zone material which could be replaced by a more elaborate nonlinear debonding pattern to simulate the behavior of the joint grout.

6.4. **Prefabrication and Construction**

The most important parameters to control for proper prefabrication of the structure panels are the panel thickness, curvature and edge lengths, which are inherently defined by the shape of the mold. However, while small deviations in the panel thickness and curvature may be acceptable, the edge length has to be manufactured with an extremely high accuracy and very low tolerance. This is due to the fact that the panel edges have to be perfectly aligned in order to create a closed joint bed for the in-situ casting/grouting of the intermediate joint. Based on the experimental analysis of this study, it is seen that failing to produce accurate panel edge lengths certainly compromises the efficiency of the construction.

The proposed construction procedure of this study, which adopts the use of temporary vertical scaffolding with customized heights to support the panel corners, is shown to be suitable for relatively smaller spans where bending deflections of the unsupported panel lengths are considered insignificant. However, extra temporary supports may be needed mid the unsupported panel lengths wherever the deflections are judged to be unacceptably large for the particular design application.

7. RECOMMENDATIONS

In this chapter, further research required for the validation of particular parts of this study is outlined. The suggestions include points relevant to the geometry, structural behavior and/or construction of the proposed structure. Particular recommendations for the duplication of the experimental analysis part of the study are also presented, with a focus on the problems faced during the prefabrication and assembly phases of the analysis.

- The first part of this research included a geometrical parametric study where the different sizes, division frequencies, and configurations of the proposed structure are investigated. However, the structural analysis was performed on only one instance of that structure, using one thickness, span, and division frequency. It is recommended for future research to explore the differences in capacity for different ranges of these parameters, since they may have a significant effect on the structural capacity. A series of models should be built with different radius-to-thickness ratios, spans, and division frequencies in order to gain insight onto the relationship between the stability of the structure and the number of prefabricated panels used in the construction. Eventually, the optimum span range and thickness range for the proposed structure should be determined based on the analysis.
- As briefly mentioned in the results chapter, although the discussed geometric division patterns produce a minimal number of unique sized panels, sometimes these panels are mirrors of one another, which means that while the size is the same, two versions of the shape exist with a different curvature direction. Consequently, using conventional molds, these panels require two molds each; for the right-hand and left-hand side shapes. An alternative to conventional molding techniques that may be suitable for prefabricating the panels is the use of flexible panel molds which produce double-curvature panel shapes using adjustable props which define the points of the doubly-curved surface. Hence, this flexible mold may be adjusted to create different curvature profile, and in this case mold the same shape with two different curvature directions. The development and use of flexible molds are discussed in [52], [95],

[96] and [97], and is seen as a possible opportunity for optimizing the prefabrication of the structural panels in this study.

- The created numerical code for calculating the panel sizes and number of panels for the user selected geometry serves only to provide a quick preliminary estimate. The code needs further development in order to provide detailed information about the panel parameters and other geometric data relevant to the construction process. It should also be noted that the code was mainly based on the division coordinates provided in reference [90]. For a more generalized code, the process of the division technique of the sphere should be integrated within the code.
- In the construction analysis part of this research, the partial structure was analyzed through the use of individual panels with idealized boundary conditions. However, a more elaborate representation of the partial structure and its temporary boundary conditions may be needed for a deeper understanding of the behavior of the panels under temporary construction loads and other accidental loads that may be expected during construction. These models need to closely simulate the partial restraining of the curved base panels through friction with the ring beam and other vertical supports of the scaffolding, in order to ensure stability of the temporarily supported panels under the expected loads which might have significant horizontal components.
- A transient analysis of the structure should be performed in order to determine the structural behavior and failure behavior under extreme loading conditions, such as earthquake loads. The purpose is to verify the stability of the structure and the capacity and joints under dynamic loads, and the ductility of the joints, in case of failure.
- Modeling of the intermediate joints between the panels may be conducted using different methods in order to find the modeling method which most simulates the behavior of the precast joints in concrete shell structures. In this study, ANSYS contact elements were used to simulate the joint with a debonding cohesive zone material model which allows partial panel detaching at the joints. Other methods were seen in different parts of the literature in the simulation of the behavior of different joints between concrete structural members. One of the common modeling techniques

that is seen to be worth investigating for the proposed structure was found in a collaborate research project between the university of Arizona, Lehigh University, and the university of California, San Diego titled "Development of A Seismic Design Methodology for Floor Diaphragms" where the behavior of different connections between precast concrete diaphragm panels was studied, and force-displacement backbone curves were developed [45], [46]. According to that study, finite element models of the joints between the precast panels used both contact elements and nonlinear springs. The spring elements were intended to fully capture the nonlinear behavior of the reinforcement and the surrounding concrete across the joint, and the spring properties were obtained from the results of previous experimental tests in the same research study.

Although the test conditions and most specimens are significantly different from the model in this study, one of the connections between the diaphragm panels was based on only reinforcement bars across the joint without mechanical connectors, and the specimen was subjected to in plane tensile force, shear force and combined tensile-shear. That particular case is seen to be similar to the model at hand and suggests that the use of nonlinear spring elements with force-displacement curves may be applied to the structural system of this study. One concern, however, may be the large modeling effort due to the large number of springs that needs to be modeled at the joints.

- If the modeling technique of this study is to be applied, a recommendation would be to experiment with different debonding material behaviors and stress values, since the debonding pattern and stresses used in this study may have been responsible for overestimation of the spherical cap capacity when compared to the physical model results. The modeling of a more elaborate debonding behavior, along with elaborate boundary conditions, is anticipated to improve the correlation between the FE and experimental model results.

- The following recommendations are made for the future duplication of the experimental analysis of this study:
    - In order to avoid the size discrepancy seen in the panels of the experimental analysis, higher quality molds should be manufactured using more-suited materials. A steel mold fabricated with a low manufacturing tolerance is recommended for ensuring an accurate panel size.
    - In any case, proper concrete filling of the whole mold must be checked. If that seems to be obstructed with the bent steel meshes extending at the edges of the panels and their insulation sheets, as it was seen in this experiment, the steel meshes or insulation sheets may be hammered to the sides of the mold in order to make sure the concrete flow is not obstructed.
    - A positive mold piece should be manufactured for each mold in order to ensure accurate and uniform panel thickness and proper curvature.
    - In this study, conventional wooden props were used for creating the scaffolding frame for supporting the construction, and have required extra falsework to properly support the planned temporary props. As a recommendation for the assembly process, more elaborate forms of commercially available scaffolding should be considered in order to avoid the use of extra props and ensure the stability of the scaffolding system.
    - The size effects of modeling the concrete material should be studied, particularly for experimental models of relatively small scales. These effects were not studied here in due detail, and may result in discrepancies between the strength, particularly the tensile strength, of the prototype and model concrete, as discussed in reference [61].
    - In some instances, the use of sand bags for ultimate load testing of the concrete shell physical model may not present an efficient loading method, particularly if the shell structure has a relatively large thickness and is anticipated to withstand large loads. A more efficient gravity loading method should be considered, such as whiffle-tree systems which simulate uniform gravity loads through links which

produce an even load distribution onto multiple points across the surface of the structure.

While this study presents a proposal of the geometry, structural analysis and construction procedure of the segmented precast spherical cap, much research is still needed to create more uniform designs and structural configuration varieties, develop more efficient construction methods, and determine more suited modeling techniques to best simulate the structural behavior under different loading conditions.

8. REFERENCES

[1] Anonymous. “Precast shells form barrel vaulted roof.” *Engineering News-Record 198(7),* 1977, pp. 50.

[2] *Monolithic Dome*. Available: www.monolithic.org.

[3] ACI Committee. *Building code requirements for structural concrete (ACI 318-05) and commentary (ACI 318R-05)*. 2005.

[4] ACI Committee 334. *Concrete shell structures practice and commentary*. ACI Journal Proceedings. 1964.

[5] ACI Committee 344. *Design and construction of circular prestressed concrete structures*. ACI Journal Proceedings. 1970.

[6] S. Adeeb, B. W. Scholefield, T. Brown, N. Shrive, J. Kroman, V. Perry and G. Tadros. “Modelling, testing, and construction of the first ductal® canopy in the world.” *Canadian Journal of Civil Engineering 32(6),* pp. 1152-1165. 2005.

[7] H. A. Ameen. “The impact of diameter, number of ribs, percentage of steel, compressive strength and cover thickness on the large concrete dome.” *American Journal of Industrial and Scientific Research*. 2010. Available: http://scihub.org/AJSIR/PDF/2010/3/AJSIR-1-3-472-495.pdf. DOI:10.5251/ajsir.2010.1.3.472.495.

[8] ANSYS Inc.,"ANSYS mechanical APDL theory reference," in *ANSYS User's Manual*, Release 14.5. 2012.

[9] ANSYS Inc., "ANSYS mehcanical APDL material reference," in *ANSYS User's Manual*, Release 14.5. 2012.

[10] ANSYS Inc., "Element reference," in *ANSYS User's Manual*, Release 12.1. 2009.

[11] ANSYS Inc., "Contact technology guide," in *ANSYS User's Manual*, Release 12.0. 2009.

[12] ANSYS Inc., "Structural analysis guide," in *ANSYS User's Manual*, Release 12.0. 2009.

[13] ANSYS Inc., "ANSYS Mechanical," Release 14.5.

[14] R. R. Archer. “On the numerical solution of the nonlinear equations for shells of revolution.” *J.Math.Phys 41(3),* pp. 165-178. 1962.

[15] M. Bangash. Concrete and concrete structures: Numerical modelling and applications. London, UK: Elsevier Applied Science, 1989.

[16] A. F. Barbosa and G. O. Ribeiro. “Analysis of reinforced concrete structures using ANSYS nonlinear concrete model.” *Computational Mechanics*, International Center for Numerical Methods in Engineering, Barcelona, Spain, 1998.

[17] R. J. Bellinfante, "Buckling of Spherical Caps Under Uniform External Pressure," *Douglas Aircraft Co. Rpt. no. SM-38938,* 1962.

[18] D. P. Billington. *The tower and the bridge*. Princeton University Press, 1983.

[19] T. R. Brackus, P. J. Barr and W. Cook. “Live-load and shear connection testing of full-scale precast bridge panels.” *J. Bridge Eng. 18(3),* pp. 210-219. 2011.

[20] B. Budiansky and J. Fitch. “Buckling and postbuckling behavior of spherical caps under axisymmetric load.” *AIAA Journal 8(4),* pp. 686-693. 1970.

[21] B. Budiansky. “Buckling of clamped shallow spherical shells.” *Harvard University, Cambridge, MA* 1959.

[22] N. Burger and D. P. Billington. “Felix candela, elegance and endurance: An examination of the xochimilco shell.” *Journal-International Association for Shell and Spatial Structures 152* pp. 271. 2006.

[23] D. Bushnell. *Computerized Buckling Analysis of Shells,* the Netherlands: Springer, 1985.

[24] D. Bushnell. “Analysis of buckling and vibration of ring-stiffened, segmented shells of revolution.” *Int. J. Solids Structures 6(1),* pp. 157-181. 1970.

[25] D. Bushnell. “Buckling of spherical shells ring-supported at the edges.” *AIAA Journal 5(11),* pp. 2041-2046. 1967.

[26] D. Bushnell. “Nonlinear axisymmetric behavior of shells of revolution.” *AIAA Journal 5(3),* pp. 432-439. 1967.

[27] D. Bushnell. “Symmetric and nonsymmetric buckling of finitely deformed eccentrically stiffened shells of revolution.” *AIAA Journal 5(8),* pp. 1455-1462. 1967.

[28] D. Bushnell. Buckling of spherical shells ring-supported at the edges. *AIAA Journal 5(11),* pp. 2041-2046. 1967.

[29] CAE Associates, "Fatigue and Fracture Seminar: ANSYS cohesive zone modeling," 2011. Available:

https://caeai.com/sites/default/files/CAE_Fatigue_and_Fracture_Seminar_-_CZM_For_Web.pdf.

[30] A. B. Caseman. Influence of the assumed deflected shape in applying the energy method to determine the elastic buckling pressure of thin shallow spherical shells. *ProQuest Dissertations and Theses* 1961. Available: http://search.proquest.com.library.aucegypt.edu:2048/docview/302077094?accountid=8423.

[31] Z. Chang, M. A. Bradford and R. I. Gilbert. "Short-term behaviour of shallow thin-walled concrete dome under uniform external pressure." *Thin-Walled Structures 49(1),* pp. 112-120. 2011.

[32] Z. Chang, M. A. Bradford and R. Ian Gilbert. "Limit analysis of local failure in shallow spherical concrete caps subjected to uniform radial pressure." *Thin-Walled Structures 48(6),* pp. 373-378. 2010. Available: http://dx.doi.org/10.1016/j.tws.2010.01.014. DOI: 10.1016/j.tws.2010.01.014.

[33] W. L. Chen. Effect of geometrical imperfection on the elastic buckling of shallow spherical shells. Massachusetts Institute of Technology, Cambridge, MA, 1959.

[34] J. Chilton. *Heinz Isler: The Engineer's Contribution to Comtemporary Architecture.* London: Thomas Telford Publishing, 2000.

[35] J. D. Clinton. *Advanced Structural Geometry Studies. Part 1: Polyhedral Subdivision Concepts for Structural Applications.* National Aeronautics and Space Adminsitration, Washington D.C., 1971.

[36] F. Colin. *Candela: The shell builder*. New York: Reinhold Pub. Corp., 1963.

[37] F. X. Crowley. Precast 150 ft diameter dome. *66(9),* pp. 698-702. 1969.

[38] Dassault Systèmes SolidWorks Corp., SolidWorks 2012, Massachusetts, USA.

[39] E. Den Hartog. "Prefabrication of concrete shells." M.S. thesis, Delft University of Technology, 2008.

[40] P. Desayi and S. Krishnan. "Equation for the stress-strain curve of concrete." *ACI Journal Proceedings*. 1964.

[41] P. Desideri. *Pier Luigi Nervi.* Zurich: Artemis, 1982.

[42] E. Dulácska. "Buckling analysis of reinforced concrete shells," in *Inelastic Behaviour of Plates and Shells; IUTAM Symposium*, 1985.

[43] K. Elliott. *Precast Concrete Structures.* Boston, MA: Butterworth-Heinemann, 2002.

[44] M. Farshad. *Design and Analysis of Shell Structures.* Boston: Kluwer Academic, 1992.

[45] R. B. Fleischman. "Seismic design methodology for precast concrete diaphragms part 2: Research program." *PCI Journal.* 2005.

[46] R. B. Fleischman, C. J. Naito, J. Restrepo, R. Sause and S. Ghosh. "Seismic design methodology for precast concrete diaphragms part 1: Design framework." *PCI Journal 50(5),* pp. 68. 2005.

[47] J. Gere and S. Timoshenko. *Mechanics of materials*. Boston: PWS Pub. Co., 1997.

[48] G. C. Giuliani and M. E. Giuliani. "Fifty years experience in concrete shell design, fabrication and erection." *Journal of the International Association for Shell and Spatial Structures 53(172),* pp. 83-98. 2012.

[49] P. B. Gonçalves and J. G. Croll. "Axisymmetric buckling of pressure-loaded spherical caps." *J. Struct. Eng. 118(4),* pp. 970-985. 1992.

[50] P. H. Griggs. "Buckling of reinforced concrete shells." *Journal of the Engineering Mechanics Division 97(3),* pp. 687-700. 1971.

[51] E. Grigolyuk and Y. A. Lopanitsyn. "The axisymmetric postbuckling behaviour of shallow spherical domes." *J. Appl. Math. Mech. 66(4),* pp. 605-616. 2002.

[52] S. Grünewald, B. Janssen, H. Schipper, K. Vollers and J. Walraven. "Deliberate deformation of concrete after casting." Delft University of Technology. 2012.

[53] G. Günschel, *Große Konstrukteure 1: Freyssinet, Maillart, Dischinger, Finsterwalder.* Berlin: Verlag Ullstein., 1996 (in German).

[54] A. Guran and L. P. Lebedev. "Basic concepts in the stability theory of thin-walled structures," in *Shell-Like Structures.* H. Altenbach and V.A. Eremeyev, Ed. Shell-like Structures, Springer-Verlag Berlin Heidelberg, 2011. DOI: 10.1007/978-3-642-21855-2_11.

[55] A. Habib and L. J. SENG. "Hyperbolic paraboloid shell roof using triangular flat elements." *Journal of Ferrocement 23(4),* pp. 309-317. 1993.

[56] E. Hamed, M. A. Bradford and R. Ian Gilbert. "Nonlinear long-term behaviour of spherical shallow thin-walled concrete shells of revolution." *Int. J. Solids Structures 47(2),* pp. 204-215. 2010.

[57] E. Hamed, M. Bradford, R. Gilbert and Z. Chang. “Analytical model and experimental study of failure behavior of thin-walled shallow concrete domes.” *J. Struct. Eng. 137(1),* pp. 88-99. 2011. Available: http://dx.doi.org/10.1061/(ASCE)ST.1943-541X.0000274. DOI: 10.1061/(ASCE)ST.1943-541X.0000274.

[58] E. Hamed, M. A. Bradford, R. I. Gilbert and Z. Chang. “Creep testing and analysis of shallow concrete domes,” presented at 21st Australasian Conference on the Mechanics of Structures and Materials, ACMSM21, December 7 - December 10, 2010.

[59] H. G. Harris and G. M. Sabnis. "Inelastic models," in *Structural Modeling and Experimental Techniques*, Second Edition. CRC Press LLC, 1999, Available: http://dx.doi.org/10.1201/9781420049589.ch4. DOI: doi:10.1201/9781420049589.ch4.

[60] H. G. Harris and G. M. Sabnis. "Inelastic models," in *Structural Modeling and Experimental Techniques*, Second Edition. CRC Press LLC, 1999, Available: http://dx.doi.org/10.1201/9781420049589.ch5. DOI: doi:10.1201/9781420049589.ch5.

[61] H. G. Harris and G. M. Sabnis. "Size effects, accuracy, and reliability in materials systems and models," in *Structural Modeling and Experimental Techniques*, Second Edition. CRC Press LLC, 1999, Available: http://dx.doi.org/10.1201/9781420049589.ch9. DOI: doi:10.1201/9781420049589.ch9.

[62] F. J. Heger. “Concrete domes for water and wastewater tanks.” *ACI Struct. J. 87(4),* pp. 445-452. 1990.

[63] R. Homewood, A. Brine and A. E. Johnson Jr. “Experimental investigation of the buckling instability of monocoque shells.” *Exp. Mech. 1(3),* pp. 88-96. 1961.

[64] N. Huang. “Unsymmetrical buckling of thin shallow spherical shells.” *Journal of Applied Mechanics 31(3),* pp. 447-457. 1964.

[65] Huber, Hunt & Nichols, Inc., Indianapolis, Indiana, "Concrete geodesic dome made history," The Aberdeen Group, 1987.

[66] M. K. Hurd. “Geodesic dome of polystyrene and concrete.” *Concrete Construction - World of Concrete 33(11),* 1988.

[67] R. Huston and H. Josephs. "Buckling of spherical shells," in *Practical Stress Analysis in Engineering Design*, 3rd ed., Boca Raton, FL: CRC Press, Taylor & Francis Group, 2008, Available: http://dx.doi.org/10.1201/9781420017823.ch31. DOI: doi:10.1201/9781420017823.ch31.

[68] Working Group No. 5, S. J. Medwadowski. *Recommendations for reinforced concrete shells and folded plates*. International Association for Shell and Spatial Structures, 1979.

[69] H. Isler. “The Stability of Thin Concrete Shells” in *Buckling of shells.* Springer Berlin Heidelberg, 1982, pp. 645-672. DOI: 10.1007/978-3-642-49334-8_23.

[70] J. L. Julander. “Finite element modeling of full depth precast concrete transverse bridge deck connections.” M.S. thesis, Utah State University, Logan, UT, 2009.

[71] D. Kachlakev, T. Miller, S. Yim, K. Chansawat and T. Potisuk. “Finite element modeling of concrete structures strengthened with FRP laminates, Final Report SPR 316,” Oregon Dept. of Transportation, Research Unit, Salem, OR, 2001.

[72] A. Kaplan and Y. C. Fung. “A nonlinear theory of bending and buckling of thin elastic shallow spherical shells.” *U. S. National Advisory Committee for Aeronautics, Washington (Technical Note 3212),* 1954.

[73] A. Kaplan. “Buckling of spherical shells (computer capabilities and experimental techniques),” in *Symposium on Thin Shell Structures: Theory, Experiments, and Design Proceedings*, 1974, pp. 247-288.

[74] E. N. Kaplunovich and C. Meyer. “Shell construction with precast elements.” *Concr. Int. 4(4),* pp. 37-43. 1982.

[75] H. B. Keller and A. W. Wolfe. “On the nonunique equilibrium states and buckling mechanism of spherical shells.” *Journal of the Society for Industrial & Applied Mathematics 13(3),* pp. 674-705. 1965.

[76] P. Khakina and H. Zhou. “A reduction factor for buckling load of spherical cap shells.” *Research Journal of Applied Sciences, Engineering and Technology 3(12),* pp. 1437-1440. 2011.

[77] K. Kloppel and O. Jungbluth. “Buckling problem of thin spherical shells.” *Stahlbau 22(6),* pp. 121-133. 1953.

[78] L. Kollár. Modified proposal for the text of the recommendations. *Personal Communication to S. J. Medwadowski.* 1993.

[79] L. Kollár and E. Dulácska. *Buckling of shells for engineers.* Chichester: John Wiley, 1984.

[80] M. A. Krenzke and T. J. Kiernan. “The effect of initial imperfections on the collapse strength of deep spherical shells,” David Taylor Model Basin Report 1757, Department of the Navy, 1965.

[81] M. A. Krenzke and T. J. Kiernan. “Tests of stiffened and unstiffened machined spherical shells under external hydrostatic pressure,” David Taylor Model Basin, Washington DC, 1963.

[82] W. A. Litle, F. J. Forcier and P. H. Griggs. “Can plastic models represent the buckling behavior of reinforced concrete shells?” *ACI Special Publication 24.* 1970.

[83] J. Marcinowski. “Stability of relatively deep segments of spherical shells loaded by external pressure.” *Thin-Walled Structures 45(10),* pp. 906-910. 2007.

[84] MathWorks, MATLAB, ver. 8.1 R2013a, 2013.

[85] S. J. Medwadowski. “Buckling of concrete shells: An overview.” *Journal of the International Association for Shell and Spatial Structures 45(1),* pp. 51-63. 2004.

[86] P. Moncarz, M. Griffith and P. Noakowski. “Collapse of a reinforced concrete dome in a wastewater treatment plant digester tank.” *J. Perform. Constr. Facil. 21(1),* pp. 4-12. 2007. Available: http://dx.doi.org/10.1061/(ASCE)0887-3828(2007)21:1(4). DOI: 10.1061/(ASCE)0887-3828(2007)21:1(4).

[87] B. Pan and W. Cui. “An overview of buckling and ultimate strength of spherical pressure hull under external pressure.” *Mar. Struct. 23(3),* pp. 227-240. 2010.

[88] R. Parmerter. “Buckling of clamped shallow shells under unifrom pressure.” Ph.D. thesis, California Institute of Technology, Pasadena, California, 1963.

[89] B. Peerdeman. “Analysis of thin concrete shells revisited: Opportunities due to innovations in materials and analysis methods.” M.S. thesis, Delft University of Technology, the Netherlands, 2008.

[90] E. S. Popko. *Divided Spheres: Geodesics and the Orderly Subdivision of the Sphere.* Boca Raton, FL: CRC Press Taylor & Francis Group, 2012.

[91] S. D. Porter, J. L. Julander, M. W. Halling, P. J. Barr, H. Boyle and S. Xing. “Flexural testing of precast bridge deck panel connections.” *J. Bridge Eng. 16(3),* pp. 422-430. 2010.

[92] A. H. Qader, V. Agarwal and A. M. Ibrahim. “Nonlinear behavior of continuous composite steel concrete beam with external prestress.” *International Journal of Innovative Technology and Exploring Engineering (IJITEE)* 3 (7), pp. 76-82. 2013.

[93] F. Queiroz, P. Vellasco and D. Nethercot. “Finite element modelling of composite beams with full and partial shear connection.” *Journal of Constructional Steel Research 63(4),* pp. 505-521. 2007.

[94] G. S. Ramaswamy, *Design and Construction of Concrete Shell Roofs.* New York: McGraw-Hill, 1968.

[95] H. Schipper, S. Grunewald, P. Eigenraam, P. Raghunath and M. Kok. "Optimization of the flexible mould process for the production of double-curved concrete elements," presented at CIC 2014: The 1st Concrete Innovation Conference, Oslo, Norway, 11-13 June 2014. 2014.

[96] R. Schipper and B. Janssen. "Manufacturing double-curved elements in precast concrete using A flexible mould-first experimental results," in *Proceedings of Fib Symposium*, Prague, 2011.

[97] R. Schipper and B. Janssen. "Manufacturing double curved precast concrete panels." *Concrete Plant International 4* pp. 32-38. 2011.

[98] A. C. Scordelis. "Nonlinear material, geometric and time-dependent analysis of reinforced and prestressed concrete shells." *Journal of the International Association for Shell and Spatial Structures 31(102-103),* pp. 57-70. 1990.

[99] L. Seaman. "Nature of buckling in thin spherical shells." Sc.D. thesis, Massachusetts Institute of Technology, Cambridge, MA, 1962. Available: http://search.proquest.com.library.aucegypt.edu:2048/docview/302258954?accountid=8423.

[100] S. R. Sullivan. "Behavior of transverse joints in precast deck panel systems." M.S. thesis, College of Engineering and Technology of Ohio University, Athens, OH, 2003.

[101] H. Takeuchi, S. Taketomi, S. Samukawa and A. Nanni. "Renovation of concrete water tank in chiba prefecture, Japan." *Pract. Period. Struct. Des. Constr. 9(4),* pp. 237-241. 2004. Available: http://dx.doi.org/10.1061/(ASCE)1084-0680(2004)9:4(237). DOI: 10.1061/(ASCE)1084-0680(2004)9:4(237).

[102] G. Thurston. "Comparison of experimental and theoretical buckling pressures for spherical caps," in *Collected papers on instability of shell structures*. NASA Langley Research Center, Langley Station, VA, 1962, pp. 515-521.

[103] G. A. Thurston. "A numerical solution of the nonlinear equations for axisymmetric bending of shallow spherical shells." *Journal of Applied Mechanics 28(4),* pp. 557-562. 1961.

[104] G. A. Thurston and F. A. Penning. "Effect of axisymmetric imperfections on the buckling of spherical caps under uniform pressure." *AIAA Journal. 4(2),* pp. 319-327. 1966.

[105] S. Tillman. "On the buckling behaviour of shallow spherical caps under a uniform pressure load." *Int. J. Solids Structures 6(1),* pp. 37-52. 1970.

[106] H. S. Tsien. “A theory for the buckling of thin shells.” *Journal of the Aeronautical Sciences (Institute of the Aeronautical Sciences) 9(10)*, pp. 373-384. 1942. Available: http://arc.aiaa.org/doi/abs/10.2514/8.10911. DOI: 10.2514/8.10911.

[107] A. Van der Neut. “The elastic stability of a thin spherical shell.” Thesis, Delft University, the Netherlands, 1932.

[108] D. Vandepitte and G. Lagae. "Buckling of spherical domes made of microconcrete and creep buckling of such domes under long-term loading," in *Inelastic Behaviour of Plates and Shells.* IUTAM Symposium, Rio de Janeiro, Brazil August 5–9, 1985, 1986, pp 291-311. DOI: 10.1007/978-3-642-82776-1_14.

[109] D. Vandepitte, J. Rathe and G. Weymeis. “Experimental investigation into the buckling and creep buckling of shallow spherical caps subjected to uniform radial pressure,” in *proceedings of the International Association for Shell and Spatial Structures Congress*, 1979.

[110] E. Ventsel and T. Krauthammer. "Buckling of shells," in *Thin Plates and Shells Theory: Analysis, and Applications*. New York: Marcel Dekker, Inc., 2001. Available: http://dx.doi.org/10.1201/9780203908723.ch19. DOI: 10.1201/9780203908723.ch19.

[111] R. Vidjeapriya, A. Bahurudeen and K. Jaya. “Nonlinear analysis of exterior precast beam-column J-bolt and cleat angle connections.” *International Journal of Civil & Structural Engineering 4(1)*, pp. 87-97. 2013.

[112] A. Volmir. “Stability of elastic systems.” *Gos. Izd-vo Fiz.-Mat. Lit-ry*, Moscow, 1963 (in Russian).

[113] T. Von Karman and H. S. Tsien. “The buckling of spherical shells by external pressure.” *Journal of the Aeronautical Sciences (Institute of the Aeronautical Sciences) 6(2)*, pp. 43-50. 1939. Available: http://arc.aiaa.org/doi/abs/10.2514/8.1019. DOI: 10.2514/8.1019.

[114] H. J. Weinitschke. “The effect of asymmetric deformations on the buckling of shallow spherical shells.” *Journal of the Aerospace Sciences 29(9)*, pp. 1141-1142. 1962. Available: http://arc.aiaa.org/doi/abs/10.2514/8.9733. DOI: 10.2514/8.9733.

[115] Z. G. Wells, P. J. Barr and P. H. James. “Performance of posttensioned curved-strand connections in transverse joints of precast deck panels.” *J. Bridge Eng. 18(10)*, pp. 1062-1073. 2012.

[116] K. Willam and E. Warnke. “Constitutive model for the triaxial behavior of concrete,” presented at Association of Bridge and Structural Engineers, Seminar on Concrete Structure Subjected to Triaxial Stresses, Paper III-1, Bergamo, Italy. 1975.

[117] W. Wunderlich and U. Albertin. “Buckling behaviour of imperfect spherical shells.” *Int. J. Non-Linear Mech. 37(4),* pp. 589-604. 2002.

[118] S. Yamada, K. Uchiyama and M. Yamada. “Experimental investigation of the buckling of shallow spherical shells.” *Int. J. Non-Linear Mech. 18(1),* pp. 37-54. 1983.

[119] M. S. Zarghamee and F. J. Heger. “Buckling of thin concrete domes.” *ACI Journal* 80(6), pp. 487-500. 1983.

[120] D. Zhang, R. Fleischman, C. Naito and R. Ren. “Experimental evaluation of pretopped precast diaphragm critical flexure joint under seismic demands.” *J. Struct. Eng. 137(10),* pp. 1063-1074. 2010.

[121] R. Zoelly. “On the problem of buckling of the spherical shell.” Dissertation, Zurich, 1915 (in German).

APPENDIX A: MATLAB CODE FOR CALCULATING THE GEOMETRUC PARAMETERS OF THE STRUCTURE

The attached MATLAB code calculates the number of panels, the side lengths of the triangular panels and the average panel area for each selected spherical cap configuration, span and division frequency

GeomGen

```
%Calculates the average area of the panels for the selected geometry
%calculates the number of panels required for the selected geometry
function PanelArea=GeomGen(span,depth,freq)
format short
span=input('Span of the dome= ');
depth=input('Depth of the dome (s/d)= ','s');
freq=input('Frequency of division (8v,4v.LCD,2v)= ','s');
Coord =[0.52573149 0.4013448 0.4013448 0.27326675 0.26803508 0.13726462
0.13238474 0 0 0.52573149 0.26803508 0.26803508 0 0 0.52573149 0 0
0.52573149 0 0; 0 -0.0997286 0.0997286 0 0.19473891 0.0997286
0.28122769 0.19473891 0.35682236 0 -0.19473891 0.19473891 0 0.35682236
0 0 0.35682236 0 -0.35682236 0.35682236; 0.85065057 0.9104815 0.9104815
0.9619383 0.9435221 0.98550121 0.95046582 0.98085511 0.93417226
0.85065057 0.9435221 0.9435221 1 0.93417226 0.85065057 1 0.93417226
0.85065057 0.93417226 0.93417226];

if strcmp(freq,'8v')
    m=1;
    n=7;
    weights=[8;12;8;4];
    panelperdia=32;
    elseif strcmp(freq,'4v')
        m=10;
        n=12;
        weights=[4;4];
        panelperdia=8;
        elseif strcmp(freq,'LCD')
            m=15;
            n=15;
            weights=1;
            panelperdia=4;
            elseif strcmp(freq,'2v')
                m=15;
                n=15;
                weights=1;
                panelperdia=2;
else
    m=0;
    n=0;
    weights=0;
end
```

```
counter=0;
    for i=m:2:n
    a=acos((((Coord(1,i+1)-Coord(1,i))^2+(Coord(2,i+1)-Coord(2,i))^2+
(Coord(3,i+1)-Coord(3,i))^2)/2)-1)/-1);
    b=acos((((Coord(1,i+2)-Coord(1,i+1))^2+(Coord(2,i+2)-
Coord(2,i+1))^2+ (Coord(3,i+2)-Coord(3,i+1))^2)/2)-1)/-1);
    c=acos((((Coord(1,i+2)-Coord(1,i))^2+(Coord(2,i+2)-Coord(2,i))^2+
(Coord(3,i+2)-Coord(3,i))^2)/2)-1)/-1);
    E=4*atan(sqrt(tan((a+b+c)/4)*tan((b+c-a)/4)*tan((a+c-
b)/4)*tan((a+b-c)/4)));

    counter= counter+1;
    sidea(counter)=a;
    sideb(counter)=b;
    sidec(counter)=c;
    ExcessVec(counter)=E;
    end

MeanExcess=(ExcessVec*weights)/sum(weights);

shallowangle=37.37738;
deepangle=63.43495;

if strcmp(depth,'s')
    Rad=span/(2*sin(shallowangle*pi/180));
    diaperdome=2.5;
elseif strcmp(depth,'d')
        Rad=span/(2*sin(deepangle*pi/180));
        diaperdome=7.5;
else
    Rad=0;
    diaperdome=0;
end

disp('The arc lengths of triangles are: ');
m=size(sidea,2);
for i=1:m
    disp(['triangle' num2str(i) '  ' 'a=' num2str(sidea(1,i)*Rad) ' b='
num2str(sideb(1,i)*Rad) ' c=' num2str(sidec(1,i)*Rad)]);
end

PanelArea= MeanExcess*Rad^2;
disp(['The average area of the triangular panel= '
num2str(PanelArea)]);

Numberofpanels=panelperdia*diaperdome;
disp(['The number of panels for the dome= ' num2str(Numberofpanels)]);
```

APPENDIX B: LABELS AND CORRESPONDING PROPERTIES OF ANSYS MODELS

Table 29: Linear Elastic Analysis Models

FE Model Code	Type of Analysis	Loading	Boundary Conditions	Element and Material Properties	Contact Conditions	Solution Method
MDD01	Linear elastic analysis	Vertical gravity load (g= 9.81 m/s2)	All DOFs are restrained (UX, UY, UZ, ROTX, ROTY, ROTZ)	Model was created using SHELL281 elements and linear elastic material properties	No contact	ANSYS Eigenvalue buckling analysis method
MDD02	Linear elastic analysis	Vertical gravity load (g= 9.81 m/s2)	Translational DOFs are restrained (UX, UY, UZ)	Model was created using SHELL281 elements and linear elastic material properties	No contact	ANSYS Eigenvalue buckling analysis method
MDD03	Linear elastic analysis	Vertical gravity load (g= 9.81 m/s2)	A 500X1500 mm boundary ring beam hinged at 8 locations around the perimeter of the structure	Model was created using SHELL281 and BEAM189 elements, and linear elastic material properties	No contact	ANSYS Eigenvalue buckling analysis method
MDD04	Linear elastic analysis	Vertical gravity load (g= 9.81 m/s2)	No ring beam was used. The dome was hinged at 8 locations around the perimeter	Model was created using SHELL281 elements and linear elastic material properties	No contact	ANSYS Eigenvalue buckling analysis method

MDD05	Linear elastic analysis	Normal pressure = 1 N/m2	All DOFs are restrained (UX, UY, UZ, ROTX, ROTY, ROTZ)	Model was created using SHELL281 elements and linear elastic material properties	No contact	ANSYS Eigenvalue buckling analysis method
MDS01	Linear elastic analysis	Vertical gravity load (g= 9.81 m/s2)	All DOFs are restrained (UX, UY, UZ, ROTX, ROTY, ROTZ)	Model was created using SHELL281 elements and linear elastic material properties	No contact	ANSYS Eigenvalue buckling analysis method
MDS02	Linear elastic analysis	Vertical gravity load (g= 9.81 m/s2)	Translational DOFs are restrained (UX, UY, UZ)	Model was created using SHELL281 elements and linear elastic material properties	No contact	ANSYS Eigenvalue buckling analysis method
MDS03	Linear elastic analysis	Vertical gravity load (g= 9.81 m/s2)	A 500X1500 mm boundary ring beam hinged at 8 locations around the perimeter of the structure	Model was created using SHELL281 and BEAM189 elements, and linear elastic material properties	No contact	ANSYS Eigenvalue buckling analysis method
MDS04	Linear elastic analysis	Vertical gravity load (g= 9.81 m/s2)	No ring beam was used. The dome was hinged at 8 locations around the perimeter	Model was created using SHELL281 elements and linear elastic material properties	No contact	ANSYS Eigenvalue buckling analysis method
MDS05	Linear elastic analysis	Normal pressure = 1 N/m2	All DOFs are restrained (UX, UY, UZ, ROTX, ROTY, ROTZ)	Model was created using SHELL281 elements and linear elastic material properties	No contact	ANSYS Eigenvalue buckling analysis method

Table 30: Nonlinear Elastic Analysis Models

FE Model Code	Type of Analysis	Loading	Boundary Conditions	Element and Material Properties	Contact Conditions	Solution Method
MDS06	Nonlinear static analysis	Vertical gravity load (g= 6500 m/s2)	A 500X1500 mm boundary ring beam hinged at 8 locations around the perimeter of the structure	Model was created using SHELL281 and BEAM189 elements, and linear elastic material properties	No contact	Newton-Raphson method with Line search and bisection features. Nonlinear stabilization was used to track the final buckling shape of the structure
MDS07	Nonlinear static analysis	Vertical gravity load (g= 6500 m/s2)	A 750X1500 mm boundary ring beam hinged at 8 locations around the perimeter of the structure	Model was created using SHELL281 and BEAM189 elements, and linear elastic material properties	No contact	Newton-Raphson method with Line search and bisection features. Nonlinear stabilization was used to track the final buckling shape of the structure

Table 31: Nonlinear Inelastic Analysis Models (Monolithic Dome)

FE Model Code	Type of Analysis	Loading	Boundary Conditions	Element and Material Properties	Contact Conditions	Solution method
MDS08	Large displacement static analysis	Vertical gravity load(g=1000 m/s2)	Translational DOFs are restrained (UX, UY, UZ)	Model was created using SOLID65 elements. Material properties for the concrete are: elastic isotropic, nonlinear nonmetal concrete plasticity, isotropic work hardening plasticity Material properties for steel reinforcement: elastic isotropic, isotropic work hardening plasticity	No contact	Newton-Raphson method with Line search and bisection features
MDS09	Large displacement static analysis	Vertical gravity load(g=1100 m/s2)	Translational DOFs are restrained (UX, UY, UZ)	Model was created using SOLID65 elements. Material properties for the concrete are: elastic isotropic, nonlinear nonmetal concrete plasticity, isotropic work hardening plasticity Material properties for steel reinforcement: elastic isotropic, isotropic work hardening plasticity	No contact	Newton-Raphson method with Line search and bisection features

MDS10	Large displacement static analysis	Vertical gravity load(g=500 m/s2)	A 750X1500 mm boundary ring beam hinged at 8 locations around the perimeter of the structure	Model was created using nonlinear layered SHELL281 and BEAM189 elements, and nonlinear isotropic hardening plasticity (concrete and steel plasticity)	No contact	Newton-Raphson method with Line search and bisection features
MDS11	Large displacement static analysis	Vertical gravity load(g=100 m/s2)	A 750X1500 mm boundary ring beam hinged at 8 locations around the perimeter of the structure	Model was created using SOLID65 elements. Material properties for the concrete are: elastic isotropic, nonlinear nonmetal concrete plasticity, isotropic work hardening plasticity Material properties for steel reinforcement: elastic isotropic, isotropic work hardening plasticity	No contact	Newton-Raphson method with Line search and bisection features
MDS12	Large displacement static analysis	Vertical gravity load(g=200 m/s2)	750X1500 ring beam hinged at column locations (4 by 5 nodes)	Model was created using SOLID65 elements. Material properties for the concrete are: elastic isotropic, nonlinear nonmetal concrete plasticity, isotropic work hardening plasticity Material properties for steel reinforcement: elastic	No contact	Newton-Raphson method with Line search and bisection features

			at each location	isotropic, isotropic work hardening plasticity		
MDS13	Large displacement static analysis	Vertical gravity load(g=200 m/s2)	8 locations hinged 750X1500 ring beam, restrained UY for the whole boundary	Model was created using SOLID65 elements. Material properties for the concrete are: elastic isotropic, nonlinear nonmetal concrete plasticity, isotropic work hardening plasticity Material properties for steel reinforcement: elastic isotropic, isotropic work hardening plasticity	No contact	Newton-Raphson method with Line search and bisection features
MDS14	Large displacement static analysis	Vertical gravity load(g=200 m/s2)	restrained UY for the whole boundary, one column location restrained in UX, UY, UZ	Model was created using SOLID65 elements. Material properties for the concrete are: elastic isotropic, nonlinear nonmetal concrete plasticity, isotropic work hardening plasticity Material properties for steel reinforcement: elastic isotropic, isotropic work hardening plasticity	No contact	Newton-Raphson method with Line search and bisection features
MDS15	Large displacement static analysis	Vertical gravity load(g=200 m/s2)	restrained UY for the whole boundary, one column	Model was created using SOLID65 elements. Material properties for the concrete are: elastic isotropic, nonlinear nonmetal concrete plasticity, isotropic work hardening plasticity Material	No contact	Newton-Raphson method with adaptive descent and

			location restrained in UX, UY, UZ	properties for steel reinforcement: elastic isotropic, isotropic work hardening plasticity		pressure load stiffness
MDS16	Large displacement static analysis	Vertical gravity load(g=800 m/s2)	whole beam lower boundary is restrained in UX UY UZ	Model was created using SOLID65 elements. Material properties for the concrete are: elastic isotropic, nonlinear nonmetal concrete plasticity, isotropic work hardening plasticity Material properties for steel reinforcement: elastic isotropic, isotropic work hardening plasticity	No contact	Newton-Raphson method with adaptive descent and pressure load stiffness
MDS17	Small displacement static analysis	Vertical gravity load(g=800 m/s2)	whole beam lower boundary is restrained in UX UY UZ	Model was created using SOLID65 elements. Material properties for the concrete are: elastic isotropic, nonlinear nonmetal concrete plasticity, isotropic work hardening plasticity Material properties for steel reinforcement: elastic isotropic, isotropic work hardening plasticity. crushing of the concrete is enabled	No contact	Newton Raphson method with adaptive descent
MDS18	Large displacement static	Vertical gravity load(g=80	whole beam lower boundary is	Model was created using SOLID65 elements. Material properties for the concrete are: elastic isotropic, nonlinear	No contact	Newton-Raphson method with

	analysis	0 m/s2)	restrained in UX UY UZ	nonmetal concrete plasticity, isotropic work hardening plasticity Material properties for steel reinforcement: elastic isotropic, isotropic work hardening plasticity		Line search and bisection features. pressure load stiffness is included
MDS19	Large displacement static analysis	Vertical gravity load(g=800 m/s2)	whole beam lower boundary is restrained in UX UY UZ	Model was created using SOLID65 elements. Material properties for the concrete are: elastic isotropic, nonlinear nonmetal concrete plasticity, isotropic work hardening plasticity Material properties for steel reinforcement: elastic isotropic, isotropic work hardening plasticity.	Asymmetric contact between boundary beam and dome. Bonded (initial) contact with FKN = 0.01, pene tolerance = 0.001, contact algorithm is the augmented lagrangian, maximum friction stress = 4 MPa. Mixed-mode debonding with a CZM material model, maximum normal stress = 2.5 MPa, maximum tangential stress = 4 MPa. separation and sliding at completion of debonding = 0.005, damping coefficient = 0.0001	Newton-Raphson method with Line search and bisection features. pressure load stiffness is included
MDS20	Large displacement static analysis	Vertical gravity load(g=800 m/s2)	whole beam lower boundary is restrained in	Model was created using SOLID65 elements. Material properties for the concrete are: elastic isotropic, nonlinear nonmetal concrete plasticity, isotropic	Asymmetric contact between boundary beam and dome. Bonded (initial) contact with FKN = 0.01, pene tolerance =	Newton-Raphson method with adaptive

			UX UY UZ-CONTACT ELEMENTS between beam and dome	work hardening plasticity Material properties for steel reinforcement: elastic isotropic, isotropic work hardening plasticity.	0.001, contact algorithm is the augmented lagrangian, maximum friction stress = 4 MPa. Mixed-mode debonding with a CZM material model, maximum normal stress = 2.5 MPa, maximum tangential stress = 4 MPa, separation and sliding at completion of debonding = 0.005, damping coefficient = 0.0001	descent
MDS21	Large displacement static analysis	Vertical gravity load (g=700 m/s2)	whole beam lower boundary is restrained in UX UY UZ-CONTACT ELEMENTS between beam and dome	Model was created using SOLID65 elements. Material properties for the concrete are: elastic isotropic, nonlinear nonmetal concrete plasticity, isotropic work hardening plasticity Material properties for steel reinforcement: elastic isotropic, isotropic work hardening plasticity.	Asymmetric contact between boundary beam and dome. Bonded (initial) contact with FKN = 0.001, pene tolerance = 0.01, contact algorithm is augmented lagrangian, maximum friction stress = 4 MPa Mixed-mode debonding with a CZM material model, maximum normal stress = 2.5 MPa, maximum tangential stress = 4 MPa. separation and sliding at completion of debonding = 0.005, damping coefficient = 0.0001,	Newton-Raphson method with Line search and bisection features

					slip under compression is allowed.	
MDS22	Large displacement static analysis	Vertical gravity load(g=600 m/s2)	whole beam lower boundary is restrained in UX UY UZ	An extra refined mesh was employed. Model was created using SOLID65 elements. Material properties for the concrete are: elastic isotropic, nonlinear nonmetal concrete plasticity, isotropic work hardening plasticity Material properties for steel reinforcement: elastic isotropic, isotropic work hardening plasticity	No contact	Newton-Raphson method with Line search and bisection features

Table 32: Nonlinear Inelastic Analysis Models (Segmented Dome)

FE Model Code	Type of Analysis	Loading	Boundary Conditions	Element and Material Properties	Contact Conditions	Solution Method
SDS01	Large displacement static analysis	Vertical gravity load (g= 1100 m/s2)	Translational DOFs are restrained (UX, UY, UZ)	Model was created using SOLID65 elements. Material properties for the concrete are: elastic isotropic, nonlinear nonmetal concrete plasticity, isotropic work hardening plasticity Material properties for steel reinforcement: elastic	Symmetric contact between dome panels. Bonded (initial) contact with FKN = 0.5, pene tolerance = 0.001, contact algorithm is the augmented lagrangian, maximum friction stress = 4 MPa Mixed-mode debonding with a CZM material model, maximum normal	Newton-Raphson method with Line search and bisection features

				isotropic, isotropic work hardening plasticity.	stress = 2.5 MPa, maximum tangential stress = 4 MPa, separation and sliding at completion of debonding = 0.01, damping coefficient = 0.0001	
SDS02	Large displacement static analysis	Vertical gravity load (g= 1100 m/s2)	Translational DOFs are restrained (UX, UY, UZ)	Model was created using SOLID65 elements. Material properties for the concrete are: elastic isotropic, nonlinear nonmetal concrete plasticity, isotropic work hardening plasticity Material properties for steel reinforcement: elastic isotropic, isotropic work hardening plasticity.	Symmetric contact between dome panels. Bonded (initial) contact with FKN = 0.01, pene tolerance = 0.1, contact algorithm is the augmented lagrangian, maximum friction stress = 4 MPa Mixed-mode debonding with a CZM material model, maximum normal stress = 2.5 MPa, maximum tangential stress = 4 MPa, separation and sliding at completion of debonding = 0.01, damping coefficient = 0.0001	Newton-Raphson method with Line search and bisection features
SDS03	Large displacement static analysis	Vertical gravity load (g= 1100 m/s2)	Translational DOFs are restrained (UX, UY, UZ)	Model was created using SOLID65 elements. Material properties for the concrete are: elastic isotropic, nonlinear nonmetal concrete plasticity, isotropic work hardening plasticity Material properties for	Symmetric contact between dome panels. Bonded (initial) contact with FKN = 0.01, contact algorithm is the penalty method, maximum friction stress = 4 MPa. Mixed-mode debonding with a CZM material model, maximum normal	Newton-Raphson method with Line search and bisection features

				steel reinforcement: elastic isotropic, isotropic work hardening plasticity.	stress = 2.5 MPa, maximum tangential stress = 4 MPa, separation and sliding at completion of debonding = 0.01, damping coefficient = 0.0001	
SDS04	Large displacement static analysis	Vertical gravity load (g= 1100 m/s2)	Translational DOFs are restrained (UX, UY, UZ)	Model was created using SOLID65 elements. Material properties for the concrete are: elastic isotropic, nonlinear nonmetal concrete plasticity, isotropic work hardening plasticity Material properties for steel reinforcement: elastic isotropic, isotropic work hardening plasticity.	Symmetric contact between dome panels. Bonded (initial) contact with FKN = 0.01, pene tolerance = 0.001, contact algorithm is the augmented lagrangian method, maximum friction stress = 4 MPa. Mixed-mode debonding with a CZM material model, maximum normal stress = 2.5 MPa, maximum tangential stress = 4 MPa. separation and sliding at completion of debonding = 0.01, damping coefficient = 0.0001	Newton-Raphson method with Line search and bisection features
SDS05	Large displacement static analysis	Vertical gravity load (g= 1100 m/s2)	Translational DOFs are restrained (UX, UY, UZ)	Model was created using SOLID65 elements. Material properties for the concrete are: elastic isotropic, nonlinear nonmetal concrete plasticity, isotropic work hardening plasticity Material properties for	Symmetric contact between dome panels. Bonded (initial) contact with FKN = 0.001, pene tolerance = 0.001, contact algorithm is the augmented lagrangian method, maximum friction stress = 4 MPa. Mixed-mode debonding with a CZM material	Newton-Raphson method with Line search and bisection features

				steel reinforcement: elastic isotropic, isotropic work hardening plasticity.	model, maximum normal stress = 2.5 MPa, maximum tangential stress = 4 MPa, separation and sliding at completion of debonding = 0.01, damping coefficient = 0.0001	
SDS06	Large displacement static analysis	Vertical gravity load (g= 1100 m/s2)	Translational DOFs are restrained (UX, UY, UZ)	Model was created using SOLID65 elements. Material properties for the concrete are: elastic isotropic, nonlinear nonmetal concrete plasticity, isotropic work hardening plasticity Material properties for steel reinforcement: elastic isotropic, isotropic work hardening plasticity.	Symmetric contact between dome panels. Bonded (initial) contact with FKN = 0.001, contact algorithm is the penalty method, maximum friction stress = 4 MPa Mixed-mode debonding with a CZM material model, maximum normal stress = 2.5 MPa, maximum tangential stress = 4 MPa, separation and sliding at completion of debonding = 0.01, damping coefficient = 0.0001	Newton-Raphson method with Line search and bisection features
SDS07	Large displacement static analysis	Vertical gravity load (g= 1100 m/s2)	Translational DOFs are restrained (UX, UY, UZ)	Model was created using SOLID65 elements. Material properties for the concrete are: elastic isotropic, nonlinear nonmetal concrete plasticity, isotropic work hardening plasticity Material properties for steel reinforcement: elastic	Symmetric contact between dome panels. Bonded (initial) contact with FKN = 0.01, contact algorithm is the penalty method, maximum friction stress = 4 MPa Mixed-mode debonding with a CZM material model, maximum normal stress = 2.5 MPa, maximum tangential	Newton-Raphson method with Line search and bisection features

				isotropic, isotropic work hardening plasticity. CZM with normal stress = 2.5 MPa andtangential = 4 MPa, max separation/sliding = 0.01, damping coefficient =0.0001, FKN = 0.01 (PENE TOLERANCE = 0.001) algorithm: augmented lagrangian, slip under compression is permitted	stress = 4 MPa, separation and sliding at completion of debonding = 0.01, damping coefficient = 0.0001	
SDS08	Large displacement static analysis	Vertical gravity load (g= 1100 m/s2)	Translational DOFs are restrained (UX, UY, UZ)	Model was created using SOLID65 elements. Material properties for the concrete are: elastic isotropic, nonlinear nonmetal concrete plasticity, isotropic work hardening plasticity Material properties for steel reinforcement: elastic isotropic, isotropic work hardening plasticity.	Symmetric contact between dome panels. Bonded (initial) contact with FKN = 0.001, pene tolerance = 0.01, the contact algorithm is the augmented lagrangian, maximum friction stress = 4 MPa Mixed-mode debonding with a CZM material model, maximum normal stress = 2.5 MPa, maximum tangential stress = 4 MPa, separation and sliding at completion of debonding = 0.01, damping coefficient = 0.0001	Newton-Raphson method with Line search and bisection features
SDS09	Large	Vertical	Translational	Model was created using	Symmetric contact between dome	Newton-

	displacement static analysis	gravity load (g= 1100 m/s2)	DOFs are restrained (UX, UY, UZ)	SOLID65 elements. Material properties for the concrete are: elastic isotropic, nonlinear nonmetal concrete plasticity, isotropic work hardening plasticity Material properties for steel reinforcement: elastic isotropic, isotropic work hardening plasticity.	panels. Bonded (initial) contact with FKN = 0.001, pene tolerance = 0.01, contact algorithm is the augmented lagrangian, maximum friction stress = 4 MPa Mixed-mode debonding with a CZM material model, maximum normal stress = 2.5 MPa, maximum tangential stress = 4 MPa, separation and sliding at completion of debonding = 0.01, damping coefficient = 0.0001, slip under compression is allowed	Raphson method with Line search and bisection features
SDS10	Large displacement static analysis	Vertical gravity load (g= 1100 m/s2)	Translational DOFs are restrained (UX, UY, UZ)	Model was created using SOLID65 elements. Material properties for the concrete are: elastic isotropic, nonlinear nonmetal concrete plasticity, isotropic work hardening plasticity Material properties for steel reinforcement: elastic isotropic, isotropic work hardening plasticity.	Symmetric contact between dome panels. Bonded (initial) contact with FKN = 0.005, pene tolerance = 0.01, contact algorithm is the augmented lagrangian, maximum friction stress = 4 MPa Mixed-mode debonding with a CZM material model, maximum normal stress = 2.5 MPa, maximum tangential stress = 4 MPa, separation and sliding at completion of debonding = 0.01, damping coefficient = 0.0001	Newton-Raphson method with Line search and bisection features

SDS11	Large displacement static analysis	Vertical gravity load (g= 800 m/s2)	750X1500 mm beam with a lower boundary restrained in UX, UY, UZ	Model was created using SOLID65 elements. Material properties for the concrete are: elastic isotropic, nonlinear nonmetal concrete plasticity, isotropic work hardening plasticity Material properties for steel reinforcement: elastic isotropic, isotropic work hardening plasticity.	Symmetric contact between dome panels, and asymmetric contact between the lower panel edges and the boundary beam. Bonded (initial) contact with FKN = 0.01, pene tolerance = 0.001, contact algorithm is the augmented lagrangian, maximum friction stress = 4 MPa Mixed-mode debonding with a CZM material model, maximum normal stress = 2.5 MPa, maximum tangential stress = 4 MPa. separation and sliding at completion of debonding = 0.005, damping coefficient = 0.0001	Newton-Raphson method with Line search and bisection features
SDS12	Large displacement static analysis	Vertical gravity load (g= 800 m/s2)	750X1500 mm beam with a lower boundary restrained in UX, UY, UZ, and asymmetric contact	Model was created using SOLID65 elements. Material properties for the concrete are: elastic isotropic, nonlinear nonmetal concrete plasticity, isotropic work hardening plasticity Material properties for steel reinforcement: elastic isotropic, isotropic work	Symmetric contact between dome panels, and asymmetric contact between the lower panel edges and the boundary beam. Bonded (initial) contact with FKN = 0.005, pene tolerance = 0.001, contact algorithm is the augmented lagrangian, maximum friction stress = 4 MPa	Newton-Raphson method with Line search and bisection features

			between the lower panel edges and the ring beam	hardening plasticity.	Mixed-mode debonding with a CZM material model, maximum normal stress = 2.5 MPa, maximum tangential stress = 4 MPa. separation and sliding at completion of debonding = 0.005, damping coefficient = 0.0001	
SDS13	Large displacement static analysis	Vertical gravity load (g= 600 m/s2)	750X1500 mm beam with a lower boundary restrained in UX, UY, UZ, and asymmetric contact between the lower panel edges and the ring beam	Model was created using SOLID65 elements. Material properties for the concrete are: elastic isotropic, nonlinear nonmetal concrete plasticity, isotropic work hardening plasticity Material properties for steel reinforcement: elastic isotropic, isotropic work hardening plasticity. Crushing is enabled.	Symmetric contact between dome panels, and asymmetric contact between the lower panel edges and the boundary beam Bonded (initial) contact with FKN = 0.01, pene tolerance = 0.001, the contact algorithm is the augmented lagrangian, maximum friction stress = 4 MPa Mixed-mode debonding with a CZM material model, maximum normal stress = 2.5 MPa, maximum tangential stress = 4 MPa, separation and sliding at completion of debonding = 0.005, damping coefficient = 0.0001	Newton-Raphson method with Line search and bisection features

SDS14	Large displacement static analysis	Vertical gravity load (g= 600 m/s2)	750X1500 mm beam with a lower boundary restrained in UX, UY, UZ, and asymmetric contact between the lower panel edges and the ring beam	Model was created using SOLID65 elements. Material properties for the concrete are: elastic isotropic, nonlinear nonmetal concrete plasticity, isotropic work hardening plasticity Material properties for steel reinforcement: elastic isotropic, isotropic work hardening plasticity.	Symmetric contact between dome panels, and asymmetric contact between the lower panel edges and the boundary beam Bonded (initial) contact with FKN = 0.01, contact algorithm is the penalty method, maximum friction stress = 4 MPa Mixed-mode debonding with a CZM material model, maximum normal stress = 2.5 MPa, maximum tangential stress = 4 MPa, separation and sliding at completion of debonding = 0.005, damping coefficient = 0.0001	Newton-Raphson method with Line search and bisection features
SDS15	Large displacement static analysis	Vertical gravity load (g= 600 m/s2)	750X1500 mm beam with a lower boundary restrained in UX, UY, UZ, and asymmetric contact between the	Model was created using SOLID65 elements. Material properties for the concrete are: elastic isotropic, nonlinear nonmetal concrete plasticity, isotropic work hardening plasticity Material properties for steel reinforcement: elastic isotropic, isotropic work hardening plasticity.	Symmetric contact between dome panels, and asymmetric contact between the lower panel edges and the boundary beam Bonded (initial) contact with FKN = 0.5, pene tolerance = 0.001, the contact algorithm is the augmented lagrangian, maximum friction stress = 4 MPa Mixed-mode debonding with a CZM	Newton-Raphson method with Line search and bisection features

			lower panel edges and the ring beam		material model, maximum normal stress = 2.5 MPa, maximum tangential stress = 4 MPa, separation and sliding at completion of debonding = 0.005, damping coefficient = 0.0001	
SDS16	Large displacement static analysis	Vertical gravity load (g= 600 m/s2)	750X1500 mm beam with a lower boundary restrained in UX, UY, UZ, and asymmetric contact between the lower panel edges and the ring beam	Model was created using SOLID65 elements. Material properties for the concrete are: elastic isotropic, nonlinear nonmetal concrete plasticity, isotropic work hardening plasticity Material properties for steel reinforcement: elastic isotropic, isotropic work hardening plasticity.	Symmetric contact between dome panels, and asymmetric contact between the lower panel edges and the boundary beam Bonded (initial) contact with FKN = 0.01, pene tolerance = 0.0001, the contact algorithm is the augmented lagrangian, maximum friction stress = 4 MPa Mixed-mode debonding with a CZM material model, maximum normal stress = 2.5 MPa, maximum tangential stress = 4 MPa. separation and sliding at completion of debonding = 0.005, damping coefficient = 0.0001	Newton-Raphson method with Line search and bisection features

SDS17	Large displacement static analysis	Vertical gravity load (g= 600 m/s2)	750X1500 mm beam with a lower boundary restrained in UX, UY, UZ, and symmetric contact between the lower panel edges and the ring beam	Model was created using SOLID65 elements. Material properties for the concrete are: elastic isotropic, nonlinear nonmetal concrete plasticity, isotropic work hardening plasticity Material properties for steel reinforcement: elastic isotropic, isotropic work hardening plasticity.	Symmetric contact between dome panels, and symmetric contact between the lower panel edges and the boundary beam Bonded (initial) contact with FKN = 0.01, pene tolerance = 0.001, contact algorithm is the augmented lagrangian, maximum friction stress = 4 MPa Mixed-mode debonding with a CZM material model, maximum normal stress = 2.5 MPa, maximum tangential stress = 4 MPa, separation and sliding at completion of debonding = 0.005, damping coefficient = 0.0001	Newton-Raphson method with Line search and bisection features
SDS18	Large displacement static analysis	Vertical gravity load (g= 600 m/s2)	750X1500 mm beam with a lower boundary restrained in UX, UY, UZ, and symmetric contact between the	Model was created using SOLID65 elements. Material properties for the concrete are: elastic isotropic, nonlinear nonmetal concrete plasticity, isotropic work hardening plasticity Material properties for steel reinforcement: elastic isotropic, isotropic work	Symmetric contact between dome panels, and symmetric contact between the lower panel edges and the boundary beam Bonded (initial) contact with FKN = 0.01, pene tolerance = 0.001, contact algorithm is the augmented lagrangian, maximum friction stress = 4 MPa	Newton-Raphson method with Line search and bisection features

			lower panel edges and the ring beam	hardening plasticity.	Mixed-mode debonding with a CZM material model, maximum normal stress = 2.5 MPa, maximum tangential stress = 4 MPa, separation and sliding at completion of debonding = 0.02, damping coefficient = 0.0001	
SDS19	Large displacement static analysis	Vertical gravity load (g= 600 m/s2)	750X1500 mm beam with a lower boundary restrained in UX, UY, UZ, and symmetric contact between the lower panel edges and the ring beam	Model was created using SOLID65 elements. Material properties for the concrete are: elastic isotropic, nonlinear nonmetal concrete plasticity, isotropic work hardening plasticity Material properties for steel reinforcement: elastic isotropic, isotropic work hardening plasticity.	Symmetric contact between dome panels, and symmetric contact between the lower panel edges and the boundary beam Bonded (initial) contact with FKN = 0.01, pene tolerance = 0.001, contact algorithm is the augmented lagrangian, maximum friction stress = 4 MPa Mixed-mode debonding with a CZM material model, maximum normal stress = 400 MPa, maximum tangential stress = 240 MPa, separation and sliding at completion of debonding = 0.01, damping coefficient = 0.0001	Newton-Raphson method with Line search and bisection features

SDS20	Large displacement static analysis	Vertical gravity load (g= 2000 m/s2)	750X1500 mm beam with a lower boundary restrained in UX, UY, UZ, and symmetric contact between the lower panel edges and the ring beam	Model was created using SOLID65 elements. Material properties for the concrete are: elastic isotropic, nonlinear nonmetal concrete plasticity, isotropic work hardening plasticity. Concrete cracking is disabled. Material properties for steel reinforcement: elastic isotropic, isotropic work hardening plasticity.	Symmetric contact between dome panels, and symmetric contact between the lower panel edges and the boundary beam Bonded (initial) contact with FKN = 0.05, pene tolerance = 0.005, contact algorithm is the augmented lagrangian, maximum friction stress = 4 MPa Mixed-mode debonding with a CZM material model, maximum normal stress = 400 MPa, maximum tangential stress = 240 MPa, separation and sliding at completion of debonding = 0.005, damping coefficient = 0.0001	Newton-Raphson method with Line search and bisection features

Table 33: Normal Pressure Loading

FE Model Code	Type of Analysis	Loading	Boundary Conditions	Element and Material Properties	Contact Conditions	Solution Method
SDS21	Large displacement static analysis	Normal pressure = 3E+05 N/m2 + (g = 9.81 m/s2)	750X1500 mm beam with a lower boundary restrained in UX, UY, UZ, and symmetric contact between the lower panel edges and the ring beam	Model was created using SOLID65 elements. Material properties for the concrete are: elastic isotropic, nonlinear nonmetal concrete plasticity, isotropic work hardening plasticity. Material properties for steel reinforcement: elastic isotropic, isotropic work hardening plasticity.	Symmetric contact between dome panels, and symmetric contact between the lower panel edges and the boundary beam Bonded (initial) contact with FKN = 0.05, pene tolerance = 0.005, contact algorithm is the augmented lagrangian, maximum friction stress = 4 MPa Mixed-mode debonding with a CZM material model, maximum normal stress = 400 MPa, maximum tangential stress = 240 MPa, separation and sliding at completion of debonding = 0.005, damping coefficient = 0.0001	Newton-Raphson method with Line search and bisection features
SDS22	Large displacement static analysis	Normal pressure = 3.5E+05 N/m2 (no inertia)	750X1500 mm beam with a lower boundary restrained in	Model was created using SOLID65 elements. Material properties for the concrete are: elastic isotropic, nonlinear nonmetal concrete plasticity,	Symmetric contact between dome panels, and symmetric contact between the lower panel edges and the boundary beam Bonded (initial) contact with FKN =	Newton-Raphson method with Line search and

			UX, UY, UZ, and symmetric contact between the lower panel edges and the ring beam	isotropic work hardening plasticity. Material properties for steel reinforcement: elastic isotropic, isotropic work hardening plasticity.	0.05, pene tolerance = 0.005, contact algorithm is the augmented lagrangian, maximum friction stress = 4 MPa Mixed-mode debonding with a CZM material model, maximum normal stress = 400 MPa, maximum tangential stress = 240 MPa, separation and sliding at completion of debonding = 0.005, damping coefficient = 0.0001	bisection features
SDS23	Large displacement static analysis	Normal pressure = 6E+05 N/m2 (no inertia)	Translational DOFs are restrained (UX, UY, UZ)	Model was created using SOLID65 elements. Material properties for the concrete are: elastic isotropic, nonlinear nonmetal concrete plasticity, isotropic work hardening plasticity. Material properties for steel reinforcement: elastic isotropic, isotropic work hardening plasticity.	Symmetric contact between dome panels, and symmetric contact between the lower panel edges and the boundary beam Bonded (initial) contact with FKN = 0.05, pene tolerance = 0.005, contact algorithm is the augmented lagrangian, maximum friction stress = 4 MPa. Mixed-mode debonding with a CZM material model, maximum normal stress = 400 MPa, maximum tangential stress = 240 MPa,	Newton-Raphson method with Line search and bisection features

					separation and sliding at completion of debonding = 0.005, damping coefficient = 0.0001	
MDS23	Large displacement static analysis	Normal pressure = 3.5E+05 N/m2 (no inertia)	750X1500 mm beam with a lower boundary restrained in UX, UY, UZ	Model was created using SOLID65 elements. Material properties for the concrete are: elastic isotropic, nonlinear nonmetal concrete plasticity, isotropic work hardening plasticity. Material properties for steel reinforcement: elastic isotropic, isotropic work hardening plasticity.	No Contact	Newton-Raphson method with Line search and bisection features
MDS24	Large displacement static analysis	Normal pressure = 3.5E+06 N/m2 (no inertia)	A 750X1500 mm boundary ring beam hinged at 8 locations around the perimeter of the structure	Model was created using SHELL281 and BEAM189 elements, and linear elastic material properties	No Contact	Newton-Raphson method with Line search and bisection features
MDS26	Large displace	Normal pressure =	Translational DOFs are	Model was created using SOLID65 elements. Material	No Contact	Newton-Raphson

	ment static analysis	6E+06 N/m2 (no inertia)	restrained (UX, UY, UZ)	properties for the concrete are: elastic isotropic, nonlinear nonmetal concrete plasticity, isotropic work hardening plasticity. Material properties for steel reinforcement: elastic isotropic, isotropic work hardening plasticity.		method with Line search and bisection features

Table 34: Concentrated Loading

FE Model Code	Type of Analysis	Loading	Boundary Conditions	Element and Material Properties	Contact Conditions	Solution Method
SDS24	Large displacement static analysis	Concentrated vertical load = 3000000 N +(g = 9.81 m/s2)	750X1500 mm beam with a lower boundary restrained in UX, UY, UZ, and symmetric contact between the lower panel edges and the ring beam	Model was created using SOLID65 elements. Material properties for the concrete are: elastic isotropic, nonlinear nonmetal concrete plasticity, isotropic work hardening plasticity Material properties for steel reinforcement: elastic isotropic, isotropic work hardening plasticity.	Symmetric contact between dome panels and symmetric contact between the lower panel edges and the boundary beam. Bonded (initial) contact with FKN = 0.05, pene tolerance = 0.005, the contact algorithm is the augmented lagrangian, Maximum friction stress = 4 Mpa. Mixed-mode debonding with a CZM material model, maximum	Newton-Raphson method with Line search and bisection features

					normal stress = 2.5 MPa, maximum tangential stress = 4 MPa. separation and sliding at completion of debonding = 0.005, damping coefficient = 0.0001, slip flag off	
SDS25	Large displacement static analysis	Two load steps of Pressure on an circular steel plate of D =4 m, t =3 cm. each step = 240000 N/m2 (+ g = 9.81 m/s2)	750X1500 mm beam with a lower boundary restrained in UX, UY, UZ, and symmetric contact between the lower panel edges and the ring beam	Model was created using SOLID65 elements. Material properties for the concrete are: elastic isotropic, nonlinear nonmetal concrete plasticity, isotropic work hardening plasticity Material properties for steel reinforcement: elastic isotropic, isotropic work hardening plasticity.	Symmetric contact between dome panels and symmetric contact between the lower panel edges and the boundary beam. Bonded (initial) contact with FKN = 0.05, pene tolerance = 0.005, the contact algorithm is the augmented lagrangian, Maximum friction stress = 4 Mpa. Mixed-mode debonding with a CZM material model, maximum normal stress = 2.5 MPa, maximum tangential stress = 4 MPa. separation and sliding at completion of debonding = 0.005, damping coefficient = 0.0001, slip flag off	Newton-Raphson method with Line search and bisection features
MDS25	Large displacement static analysis	Two load steps of Pressure on an circular	750X1500 mm beam with a lower boundary restrained in UX,	Model was created using SOLID65 elements. Material properties for the concrete are: elastic isotropic, nonlinear	No contact	Newton-Raphson method with Line search

		steel plate of D =4 m, t =3 cm. each step = 240000 N/m2 (+ g = 9.81 m/s2)	UY, UZ, and symmetric contact between the lower panel edges and the ring beam	nonmetal concrete plasticity, isotropic work hardening plasticity Material properties for steel reinforcement: elastic isotropic, isotropic work hardening plasticity.		and bisection features

Table 35: Unsymmetric Loading

FE Model Code	Type of Analysis	Loading	Boundary Conditions	Element and Material Properties	Contact Conditions	Solution Method
SDS27	Large displacement static analysis	Unsymmetric gravity loading on only one half of the dome (g = 500 m/s2)	750X1500 mm beam with a lower boundary restrained in UX, UY, UZ, and symmetric contact between the lower panel edges and the ring beam	(Fy = 400 MPa) Model was created using SOLID65 elements. Material properties for the concrete are: elastic isotropic, nonlinear nonmetal concrete plasticity, isotropic work hardening plasticity Material properties for steel reinforcement: elastic isotropic, isotropic work hardening plasticity.	Symmetric contact between dome panels and symmetric contact between the lower panel edges and the boundary beam. Bonded (initial) contact with FKN = 0.05, pene tolerance = 0.005, the contact algorithm is the augmented lagrangian, Maximum friction stress = 4 Mpa. Mixed-mode debonding with a CZM material model, maximum normal stress = 2.5 MPa, maximum tangential stress = 4 MPa. separation and sliding at completion of debonding = 0.005, damping coefficient = 0.0001, slip flag off	Newton-Raphson method with Line search and bisection features